

MEASUREMENT OF HIGH- Q^2 NEUTRAL CURRENT CROSS-SECTIONS
WITH LONGITUDINALLY POLARISED POSITRONS WITH THE ZEUS
DETECTOR

by

Trevor P. Stewart

A thesis submitted in conformity with the requirements
for the degree of Doctor of Philosophy
Graduate Department of Department of Physics
University of Toronto

Copyright © 2012 by Trevor P. Stewart

Abstract

Measurement of High- Q^2 Neutral Current Cross-sections with Longitudinally
Polarised Positrons with the ZEUS Detector

Trevor P. Stewart

Doctor of Philosophy

Graduate Department of Department of Physics

University of Toronto

2012

The cross sections for neutral current (NC) deep inelastic scattering (DIS) in e^+p collisions with a longitudinally polarised positron beam are measured at high momentum transfer squared ($Q^2 > 185 \text{ GeV}^2$) at the ZEUS detector at HERA. The HERA accelerator provides $e^\pm p$ collisions at a centre-of-mass energy of 318 GeV, which allows the weak contribution to the NC process to be studied at high Q^2 . The measurements are based on a data sample with an integrated luminosity of 135.5 pb^{-1} collected with the ZEUS detector in 2006 and 2007. The single differential NC cross sections $d\sigma/dQ^2$, $d\sigma/dx$ and $d\sigma/dy$ and the reduced cross section $\tilde{\sigma}$ are measured. The structure function $x\tilde{F}_3$ is determined by combining the e^+p NC reduced cross sections with the previously measured e^-p [1] measurements. The interference structure function $xF_3^{\gamma Z}$ is extracted at $Q^2 = 1500 \text{ GeV}^2$.

The cross-section asymmetry between the positive and negative polarisation of the positron beam is measured and the parity violation effects of the electroweak interaction are observed.

The predictions of the Standard Model of particle physics agree well with the measurements.

Acknowledgements

This thesis would not have been possible were it not for the help of many people.

Firstly, I would like to thank my supervisor, John Martin, who made it possible for me to study particle physics and join the ZEUS collaboration. I've been lucky to work with such a supportive and patient supervisor, who never gave up on me when progress on the analysis was slow. I would also like to thank Sampa Bhadra and Halina Abramowicz for help and advice on the analysis.

A special thanks needs to go to Sergey Fourletov, who introduced me to the ZEUS analysis environment and the software tools needed to perform this analysis. Thank you for the uncountable hours of conversation.

I would like to thank the NC e^+p analysis team. Working with Friederike Januschek has been a pleasure. This analysis would not have been possible without her hard work and dedication. I would also like to thank Jolanta-Sztuk-Dambietz and Monica Turcato for guiding us through through this analysis.

Life at DESY would not have been the same were it not for the many friends that I made. Thank you for the lunchtime conversations and thoroughly enjoyable evenings Cecilia, Patrick, Jason, Jerome, Dan, Naomi, Umer, Tom, Aileen, Homer, Tim, John, Billy, Katie, Matt, Katherine and Sarah. To those that I've missed here, I'm sorry and thank you.

Thank you to my friends in Toronto Pier-Olivier, Dominique, Sing, Bin, Saminder and Jaspreet for putting up with my ramblings and questions about ZEUS, especially as none of you work on the experiment.

Lastly, I would like to thank my family. To my twin brother Travis, who allowed me to bounce ideas off of him for years, rarely complaining, I say thank you. Finally, without the love and encouragement from my mother and father, Daniel (Danny) and Sandra, this thesis would not have been possible. Thank you.

Contents

List of Tables	ix
List of Figures	xi
1 Deep Inelastic Scattering	1
1.1 Introduction	1
1.2 The standard model	1
1.3 Theory of Deep Inelastic Scattering	3
1.3.1 Historical Overview	3
1.3.2 Deep Inelastic Scattering	4
1.4 The quark parton model	7
1.4.1 Identification of the parton as a quark	10
1.5 QCD and the QCD-improved quark parton model	11
1.5.1 Quantum chromodynamics	12
1.5.2 Asymptotic freedom and confinement	14
1.5.3 Factorization and DGLAP	15
1.5.4 Sum rules	17
1.6 Parton distribution functions	19
1.7 Electromagnetic and weak interaction	21
1.7.1 Electroweak theory	21
1.7.2 The NC cross-section	25
1.8 NC DIS Measurements	27

2	HERA and the ZEUS Detector	28
2.1	HERA collider	28
2.1.1	The bunch structure	31
2.1.2	Luminosity	32
2.1.3	HERA-II upgrade	32
2.1.4	Polarisation measurement	35
2.2	The ZEUS detector	37
2.2.1	The microvertex detector	40
2.2.2	The central tracking detector	42
2.2.3	The forward/rear tracking detector	44
2.2.4	The uranium-scintillator calorimeter	47
2.2.5	The hadron electron separator	51
2.2.6	The presampler	53
2.2.7	Luminosity measurement	53
2.2.8	The trigger	55
3	Data, Monte Carlo and Analysis Environment	59
3.1	Data sample	59
3.2	Monte Carlo and simulation	60
3.2.1	NC MC sample	60
3.2.2	Background Monte Carlo	64
3.2.3	Event reconstruction and software environment	65
4	Event Reconstruction	70
4.1	Event characteristics	70
4.1.1	Event topology	70
4.1.2	Event observables	72
4.2	Reconstruction of kinematic variables	73
4.2.1	Electron method (EL)	75
4.2.2	Jacquet-Blondel method (JB)	75

4.2.3	Double-Angle method (DA)	76
4.2.4	Resolution and comparison of reconstruction methods	76
4.3	Offline event reconstruction	77
4.3.1	Calorimeter pre-corrections	81
4.3.2	Calorimeter alignment	82
4.3.3	Tracking and event vertex reconstruction	82
4.3.4	Electron identification	85
4.3.5	Hadronic final state reconstruction	91
5	Corrections to DATA and MC samples	99
5.1	F_L correction	100
5.2	Polarisation	100
5.2.1	Running Periods	102
5.3	Trigger Rates	103
5.3.1	RISOE Correction	103
5.4	Track Veto Efficiency	105
5.5	Track matching efficiency	110
5.6	Electron energy measurement	113
5.6.1	Electromagnetic energy scale pre-correction	113
5.6.2	Dead material and non-uniformity corrections	114
5.6.3	Energy scale and resolution	115
5.7	Z_{vtx} re-weighting	118
5.7.1	Introduction	118
5.7.2	The Z_{vtx} distribution	118
5.7.3	NC event selection	120
5.7.4	Efficiencies	121
5.7.5	Fitting	123
5.7.6	Reweighting	123

6	Data Selection	128
6.1	NC event characteristics	128
6.2	Background Characteristics	130
6.2.1	Photoproduction	130
6.2.2	Elastic QEDC	131
6.2.3	Beam-gas Interactions	132
6.2.4	Cosmic and halo muons	133
6.3	Trigger preselection	134
6.3.1	First level trigger	135
6.3.2	Second level trigger	136
6.3.3	Third level trigger	137
6.4	Data quality requirements	138
6.5	Event Selection	138
6.5.1	Positron selection	139
6.5.2	Vertex	142
6.5.3	Detector Geometry	143
6.5.4	Background rejection	144
6.5.5	Phase space and MC validity:	146
6.6	Final data and MC samples	147
7	Cross-Section Measurement and Systematic Uncertainties	153
7.1	Bin Selection	153
7.1.1	Bin definition for $\frac{d\sigma}{dQ^2}$	155
7.1.2	Bin definition for $\frac{d\sigma}{dx}$	156
7.1.3	Bin definition for $\frac{d\sigma}{dy}$	156
7.1.4	Bin definition for the reduced cross-section	159
7.2	Unfolding the cross-section	159
7.2.1	Bin-by-bin unfolding	162
7.2.2	Background subtraction	163
7.2.3	Radiative corrections	163

7.2.4	Bin centring correction	163
7.2.5	Unfolded cross-section	164
7.3	Systematic uncertainties	165
7.3.1	Reconstruction of the scattered electron	166
7.3.2	Reconstruction of the hadronic system	168
7.3.3	Background estimation	168
7.3.4	Effect of MC corrections	169
8	Results	171
8.1	Unpolarised cross-sections	171
8.1.1	Single differential cross-sections	172
8.1.2	Reduced cross-sections	178
8.1.3	$\boldsymbol{x}\tilde{F}_3$	179
8.2	Polarised cross-sections	187
8.2.1	Single differential cross-sections	187
8.2.2	Reduced cross-sections	190
9	Summary and conclusions	197
A	Cross section tables	200
A.1	List of included systematics	200
A.2	Tables of cross-sections	202
	Bibliography	236

List of Tables

1.1	The three generations of leptons and their electric charge in the SM.	2
1.2	The three generations of quarks and their electric charge Q in the SM.	2
1.3	The gauge bosons of the SM with their electric charge Q and mass.	3
1.4	The weak isospin T and its third component T_3 , hypercharge Y and electric charge e_f for each fermion of the SM.	23
1.5	The vector coupling v and axial coupling a for each fermion to the Z^0 boson.	25
2.1	Electron and proton beam energies and currents for HERA-I and HERA-II.	30
2.2	Instantaneous and integrated luminosity values for various running periods at HERA and ZEUS. LER and MER refer to low and medium proton energy runs, respectively, in order to measure the structure function F_L	33
3.1	Summary of the luminosity and polarisation for each run period.	60
3.2	Summary of the NC DIS MC.	64
3.3	Summary of the PHP MC.	65
5.1	Normalisation between data and MC before the application of the corrections outlined in chapter 5.	99
5.2	The parameters of the fourth degree polynomial fit to the loose track veto efficiency correction as a function γ_h for each running period.	108

5.3	The parameters of the fourth degree polynomial fit to the semi-loose track veto efficiency correction as a function γ_h for each running period.	108
5.4	The parameters of the fourth degree polynomial fit to the tight track veto efficiency correction as a function γ_h for each running period. . .	109
5.5	Summary of the factors used to scale and smear the MC for the RCAL and BCAL.	117
5.6	Parameters for the fit to the Z_{vtx} efficiency for each running period. .	122
5.7	Parameters for the fit to the data Z_{vtx} distribution.	124
6.1	Summary of the number of DATA, NC DIS MC, PHP MC events and the normalisation for each running period.	147

List of Figures

1.1	Feynman diagram of electron-proton NC and CC DIS.	5
1.2	Scaling test for νW_2 as a function of Q^2 from ep scattering at the MIT-SLAC experiment[18].	8
1.3	The inelastic ep divided by the Mott cross-section for fixed values of W as a function of Q^2 [14]. The elastic ep cross-section divided by the Mott cross-section is shown as the dashed-dotted line.	9
1.4	Ratio of the structure function F_1 and $2xF_2$ confirms the prediction $2xF_1(x)/F_2(x) = 1$ for spin-1/2 partons[22].	11
1.5	The 3 fundamental QCD vertices: gluon emission (left), three gluon vertex (middle) and four gluon vertex (right).	12
1.6	The first three jet event seen by the TASSO collaboration[24] providing support for the existence of the gluon.	13
1.7	Feynman diagrams of virtual quark (left) and gluon (right) loops. . .	13
1.8	Splitting functions P_{ij} give the probability of a parton i with momentum fraction ξ , reducing its momentum to x , emitting a second parton j with momentum $z = \frac{x}{\xi}$	16
1.9	The measured F_2^γ as a function of Q^2 at fixed values of x from ZEUS (filled squares), H1 (filled circles and triangles), BCDMS (open triangles), E665 (open squares) and NMC (open diamonds). The yellow band represents the SM predictions and associated uncertainty with ZEUS NLO PDF fit, and the red curve the SM predictions from H1 PDF 2000. Scaling violation can be clearly seen at high and low x . . .	18

1.10	The leading order QCD contributions to the NC DIS cross-section. QCD Compton (QCDC) (left) and boson gluon fusion (BGF) (right).	20
1.11	The proton valence quarks (u_v , d_v), sea quarks (S) and gluon (g) PDFs from the HERAPDF1.5 fit for $Q^2 = 10 \text{ GeV}^2$ (top) and $Q^2 = 10000 \text{ GeV}^2$ (bottom).	22
2.1	An aerial view of DESY and the HERA collider. The dashed rings indicate the locations of the PETRA pre-accelerator and the HERA collider. The ZEUS experiment is located at the right small circle, while H1 is located at the left small circle.	29
2.2	A schematic view of the HERA collider (top right) and pre-accelerator system (bottom left).	30
2.3	A schematic diagram of a typical HERA bunch structure.	31
2.4	A schematic view of HERA showing the location of the spin rotators, polarimeters and experiments. The black arrows indicate whether the electron polarisation is transverse or longitudinal to the direction of motion.	35
2.5	Schematic view of ZEUS detector along the beam.	37
2.6	Schematic $x - y$ view of ZEUS detector.	38
2.7	The ZEUS coordinate system.	39
2.8	Schematic view of the MVD in the $y - z$ plane.	41
2.9	Left: cross-sectional ($x - y$) view of the BMVD. Right: isometric view of the FMVD.	41
2.10	Two BMVD half-modules showing their orientation to construct a MVD module.	42
2.11	CTD octant with 9 superlayers.	44
2.12	A close-up view of a single CTD cell showing the relative location of sense and field shaping wires.	45
2.13	Schematic view of the tracking chambers showing the positions of the MVD (green), CTD (blue), FTD (purple), STT (orange) and RTD (red).	46

2.14	A schematic view of a FTD/RTD drift chamber showing the orientation of the sense wires in each plane.	46
2.15	The 2 STT modules. Each module consisting of 4 superlayers.	47
2.16	A simplified diagram of the CAL sections in the $x - z$ plane. The polar angles shown correspond to the boundaries between CAL sections. . .	51
2.17	An isometric view of a FCAL module showing the towers and cells. The wavelength shifters and light-guides that transmit the light signal from each cell to the photomultipliers run parallel to the module sides.	52
2.18	A schematic view of the ZEUS luminosity system. The bright green rectangles represent the location of the SPEC detector, while the turquoise rectangles represent the location of the PCAL detector.	54
2.19	A schematic view of the ZEUS trigger system. The rates shown on the left hand side represent typical events rates for each trigger level. . .	56
3.1	Feynman diagrams for a) the leading order process b) and c) gluon emission d) the boson gluon fusion (BGF) process.	61
3.2	Feynman diagrams for a) ISR b) FSR c) vertex correction d) self-energy.	67
3.3	The η_{max} distribution found in data and MC. The long tail at low values of η_{max} is due to diffractive events.	68
3.4	Feynman diagrams for the QEDC Compton process.	68
3.5	Feynman diagrams representing direct (left) and resolved (right) photoproduction.	69
3.6	The ZEUS software framework.	69
4.1	Event topology of NC DIS events for different Q^2 and x values. The thin red arrows point in the direction of the scattered electron and the thick blue arrow corresponds to the angle of the scattered quark. The arrow length is proportional to the energy.	71

4.2	Isolines of observable quantities in the $x - Q^2$ plane: θ_e (top left), E'_e (top right), $p_{t,h}$ and δ_h (middle left), E_h (middle right) and γ_h (bottom left).	74
4.3	Bias of Q^2 : $\frac{Q_{gen}^2 - Q_{reco}^2}{Q_{gen}^2}$ for each reconstruction method in bins of Q^2 and x . The red filled circles are EL, the blue open circles are JB and the yellow histogram is DA.	78
4.4	Bias of x : $\frac{x_{gen} - x_{reco}}{x_{gen}}$ for each reconstruction method in bins of Q^2 and x . The red filled circles are EL, the blue open circles are JB and the yellow histogram is DA.	79
4.5	Bias of y : $\frac{y_{gen} - y_{reco}}{y_{gen}}$ for each reconstruction method in bins of Q^2 and x . The red filled circles are EL, the blue open circles are JB and the yellow histogram is DA.	80
4.6	Track helix in the $x - y$ plane for a positively charged track.	83
4.7	A schematic diagram of the cell-island algorithm in two dimensions. The size of a circle corresponds to the energy deposit in the cell. . . .	87
4.8	The difference between the reconstructed and generated polar angle of the scattered electron using only calorimeter information (left) and using calorimeter and tracking information (right). The plots are made with NC DIS MC events passing the event selection.	92
4.9	The γ_h distribution before (top) and after (after) applying the back-splash correction. The points are data and the yellow histogram is NC DIS MC and PHP MC.	96
4.10	γ_{max} as a function of γ_h . The closed black circles correspond to MC for 1997-1998 and the open black circles correspond to 1995-1996 MC. . .	97
4.11	The hadronic energy scale determined from $P_{t,h}/P_{t,DA}$ versus γ_h (top) and θ_e (bottom). The data and MC are shown as blue and red dots, respectively. The data and MC ratios are shown below each plot. . .	98

5.1	The y_{DA} distribution. The points are data, the blue hashed histogram is NC DIS MC with F_L included and the red hashed histogram is NC DIS MC without F_L . The ratio of data and MC is shown below, with the blue points with F_L and the red points without F_L	101
5.2	The event rate (the number of events per pb^{-1}) as a function of run number. The black points are the data, the black line is the average rate, the light blue line is the rate predicted from MC (with F_L and polarisation corrections only). The dark blue vertical line indicates the switch from RH to LH and the red vertical line indicates the shutdown in 2007 separating the LH1 and LH2 run periods.	102
5.3	The efficiency of the CAL_EM C variable for FLT 40 (top) and RCAL_EM C (bottom) for FLT 30. The black points are data and the yellow histogram is MC. The ratio of data to MC is shown below. The drop in efficiency for the data FLT 30 is due to the RISOE bug.	104
5.4	The rate for FLT 30 for NC DIS events as a function of run number. The double line structure (red box) is due to the RISOE bug.	105
5.5	Definition of track classes.	106
5.6	Track classes in data and MC (fraction of events). The points are data and the yellow histogram NC DIS MC. The ratio of MC to data is shown below.	107
5.7	The track veto efficiency correction ($\frac{\text{TVE}_{DATA}}{\text{TVE}_{MC}}$) as a function of γ_h for the ALL running period. The loose track veto is shown as the open red points, the semi-loose track veto open blue points and the tight track veto open purple points.	109
5.8	The TME as a function of E_e (top) and θ_e (bottom). The points are data and the yellow histogram is MC. The ratio of data and MC is shown below.	112

5.9	The E_e (top) and δ_{tot} (bottom) distributions before applying electron energy scale and resolution corrections. The black points are data, the yellow histogram is NC DIS MC plus PHP MC and the red histogram is PHP MC. The ratio of data to MC is shown below.	116
5.10	E_e/E_{DA} distributions for the RCAL (top left) and BCAL (bottom left). The blue points are data and the red points are NC DIS MC. The ratios of data and MC for the RCAL and BCAL are shown on the top right and bottom right for the RCAL and BCAL, respectively.	117
5.11	The resolution distributions for the RCAL (top left) and BCAL (bottom left). The blue points are data, and the red points are NC DIS MC. $\sqrt{\sigma_{data}^2 - \sigma_{MC}^2}$ is shown for the RCAL (top right) and BCAL (bottom right).	118
5.12	The E_e (top) and δ_{tot} (bottom) distributions after applying electron energy scale and resolution corrections. The black points are data, the yellow histogram is NC DIS MC plus PHP MC and the red histogram is PHP MC. The ratio of data to MC is shown below.	119
5.13	Z_{vtx} efficiencies for ALL (top left), RH (top right), LH1 (bottom right) and LH2 (bottom left) running periods. The black line is the fit to efficiency.	122
5.14	Fits to the Z_{vtx} distribution in data after the efficiency from MC has been applied for ALL (top left), RH (top right), LH1 (bottom right) and LH2 (bottom left) running periods. The black line is the fit to the entire Z_{vtx} distribution.	124
5.15	The Z_{vtx} distributions for the range $ Z_{vtx} < 100\text{cm}$ before Z_{vtx} re-weighting (left) and after Z_{vtx} re-weighting (left) for the ALL, RH, LH1 and LH2 running periods. The data is shown as points, the yellow histogram is the NC DIS MC plus PHP MC and the red histogram is the contribution from the PHP MC. The ratio of data to MC is shown below each Z_{vtx} distribution.	126

5.16	The Z_{vtx} distributions for the range $ Z_{vtx} < 30$ cm before Z_{vtx} re-weighting (left) and after Z_{vtx} re-weighting (left) for the ALL, RH, LH1 and LH2 running periods. The data is shown as points, the yellow histogram is the NC DIS MC plus PHP MC and the red histogram is the contribution from the PHP MC. The ratio of data to MC is shown below each Z_{vtx} distribution.	127
6.1	A typical NC event in the ZEUS detector. The $x - y$ -view is on the left and the $z - r$ -view is on the right. Lines emerging from the event vertex represent the tracks, while the red block depict energy deposits in the CAL.	129
6.2	A typical PHP event in the ZEUS detector. The low energy deposits in the EMC section of the CAL can fake a NC event.	131
6.3	An elastic QEDC event in the ZEUS detector. The electron and photon are in the RCAL and balanced in P_T . Note the lack of energy deposits in the FCAL. Due to the distinct signature of elastic QEDC they can be easily rejected.	132
6.4	A cosmic muon event in the ZEUS detector. The muon enters the top of the detector, depositing energy in the BAC and BMUON chambers before passing through the central tracking region and out the other side of the detector.	133
6.5	A halo muon event in the ZEUS detector. The muon passes through the calorimeter parallel to the beams and and is not balanced in P_T	134
6.6	The grand probability (top) and the electron energy (bottom) of the scattered electron candidate. The points are data, the yellow histogram is NC DIS MC plus PHP MC and the red histogram is PHP MC. The vertical line indicates the cut value.	141

6.7	The isolation energy (bottom) of the scattered electron candidate. The points are data, the yellow histogram is NC DIS MC plus PHP MC and the red histogram is PHP MC. The vertical line indicates the cut value.	142
6.8	The track momentum (top) and the DCA (bottom) of the scattered electron candidate. The points are data, the yellow histogram is NC DIS MC plus PHP MC and the red histogram is PHP MC. The vertical line indicates the cut value.	148
6.9	The DME (top) and the position on the RCAL surface (bottom) of the scattered electron candidate. The points are data, the yellow histogram is NC DIS MC plus PHP MC and the red histogram is PHP MC. The vertical line indicates the cut value, events between the vertical lines are excluded. The effect of the chimney cut can be seen as the region with no event entries.	149
6.10	The difference of total energy and the longitudinal momentum, δ_{tot} (top) and $y_{JB}(1 - x_{DA})^2$ (bottom), where the points are data, the yellow histogram is NC DIS MC plus PHP MC and the red histogram is PHP MC. The vertical line indicates the cut value.	150
6.11	The ratio $\frac{P_T}{\sqrt{E_T}}$ (top) and $\frac{P_T}{E_T}$ (bottom), where the points are data, the yellow histogram is NC DIS MC plus PHP MC and the red histogram is PHP MC. The vertical line indicates the cut value.	151
6.12	Distributions of some of the important variables from the NC DIS event selection. Data is represented by the black points, the yellow filled histogram is DIS NC MC and PHP MC and the dark blue filled histogram is PHP MC.	152
7.1	The acceptance (filled in squares), purity (open circles) and efficiency (crosses) for the cross-section $\frac{d\sigma}{dQ^2}$	156

7.2	The acceptance (filled in squares), purity (open circles) and efficiency (crosses) for the cross-section $\frac{d\sigma}{dx}$ for $Q^2 > 185 \text{ GeV}^2$ (top) and $Q^2 > 3000 \text{ GeV}^2$ (bottom).	157
7.3	The acceptance (filled in squares), purity (open circles) and efficiency (crosses) for the cross-section $\frac{d\sigma}{dy}$ for $Q^2 > 185 \text{ GeV}^2$ (top) and $Q^2 > 3000 \text{ GeV}^2$ (bottom).	158
7.4	The acceptance (filled in squares), purity (open circles) and efficiency (crosses) for the reduced cross-section as a function of x in bins of Q^2	160
8.1	The $P_e = 0$ cross-section $d\sigma/dQ^2$ for $y < 0.9$ and $y(1-x)^2 > 0.004$ (top) and the ratio to the SM prediction (bottom). The closed circles represent the measured values, the inner error bars show the statistical uncertainty and the outer bars show the statistical and systematic uncertainties added in quadrature. The curves show the SM predictions evaluated using the HERAPDF1.5 (black solid line), ZEUSJETS (black dashed line), CTEQ6M (red dashed line) and MSTW2008 (green dashed line) PDFs. The shaded band on the bottom plot shows the uncertainties from the HERAPDF1.5 PDFs.	173
8.2	The systematic uncertainties for $d\sigma/dQ^2$. The coloured markers represent each systematic uncertainty, the red line shows the total statistical uncertainty.	174
8.3	The $P_e = 0$ cross-sections $d\sigma/dx$ for $Q^2 > 185 \text{ GeV}^2$ (top left), $d\sigma/dy$ for $Q^2 > 185 \text{ GeV}^2$ (top right), $d\sigma/dx$ for $Q^2 > 3000 \text{ GeV}^2$ (bottom left) and $d\sigma/dy$ for $Q^2 > 3000 \text{ GeV}^2$ (bottom right). The closed circles represent the data points, the inner error bars show the statistical uncertainty and the outer bars show the statistical and systematic uncertainties added in quadrature. The curves show the SM predictions evaluated using the HERAPDF1.5 PDFs.	175

8.4	The ratios of the $P_e = 0$ cross-sections $d\sigma/dx$ for $Q^2 > 185 \text{ GeV}^2$ (top left), $d\sigma/dy$ for $Q^2 > 185 \text{ GeV}^2$ (top right), $d\sigma/dx$ for $Q^2 > 3000 \text{ GeV}^2$ (bottom left) and $d\sigma/dy$ for $Q^2 > 3000 \text{ GeV}^2$ (bottom right) to the SM predictions evaluated using HERAPDF1.5 PDFs. The closed circles represent the measured values, the inner error bars show the statistical uncertainty and the outer bars show the statistical and systematic uncertainties added in quadrature. The shaded band shows the uncertainties from the HERAPDF1.5 PDFs.	176
8.5	The systematic uncertainties for $d\sigma/dx$ for $Q^2 > 185 \text{ GeV}^2$. The coloured markers represent each systematic uncertainty, the red line shows the total statistical uncertainty.	177
8.6	The systematic uncertainties for $d\sigma/dx$ for $Q^2 > 3000 \text{ GeV}^2$. The coloured markers represent each systematic uncertainty, the red line shows the total statistical uncertainty.	178
8.7	The systematic uncertainties for $d\sigma/dy$ for $Q^2 > 185 \text{ GeV}^2$. The coloured markers represent each systematic uncertainty, the red line shows the total statistical uncertainty.	179
8.8	The systematic uncertainties for $d\sigma/dy$ for $Q^2 > 3000 \text{ GeV}^2$. The coloured markers represent each systematic uncertainty, the red line shows the total statistical uncertainty.	180
8.9	The reduced cross-section of $e^\pm p$ NC DIS with unpolarised e^\pm beams as a function of x for fixed Q^2 values. The blue closed circles represent the measured values, the inner error bars show the statistical uncertainty and the outer bars show the statistical and systematic uncertainties added in quadrature, although the errors are too small to be visible in most cases. The previously measured $e^- p$ reduced cross-sections are shown as red open circles. The blue and red curves show the SM predictions evaluated using the HERAPDF1.5 PDFs for e^+ and e^- , respectively.	181

8.10	The ratio of the reduced cross-section of e^+ as a function of x at fixed values of Q^2 to the SM prediction evaluated using the HERAPDF1.5 PDFs. The points represent the measured values, the inner error bars show the statistical uncertainty and the outer bars show the statistical and systematic uncertainties added in quadrature. The shaded band shows the uncertainties from the HERAPDF1.5 PDFs.	182
8.11	The systematic uncertainties for for the reduced cross-section in terms of $x - Q^2$ bin number. The coloured markers represent each systematic uncertainty, the red line shows the total statistical uncertainty.	183
8.12	The structure function $x\tilde{F}_3$ as a function of x at fixed values of Q^2 . The points represent the measured values, the inner error bars show the statistical uncertainty and the outer bars show the statistical and systematic uncertainties added in quadrature. The solid curves show the SM prediction using the HERAPDF1.5 PDFs.	184
8.13	The structure function $xF_3^{\gamma Z}$ as a function of x at $Q^2 = 1500 \text{ GeV}^2$. The points represent the measured values, the inner error bars show the statistical uncertainty and the outer bars show the statistical and systematic uncertainties added in quadrature. The solid curve shows the SM prediction using the HERAPDF1.5 (black solid line), ZEUSJETS (black dashed line), CTEQ6M (red dashed line) and MSTW2008 (green dashed line) PDFs.	186

8.14 The cross-section $d\sigma/dQ^2$ for $y < 0.9$ and $y(1-x)^2 > 0.004$ for positive (top) and negative (bottom) polarisation. The closed circles represent the measured values, the inner error bars show the statistical uncertainty and the outer bars show the statistical and systematic uncertainties added in quadrature. The curves show the SM predictions evaluated using the HERAPDF1.5 PDFs. The inset shows the ratio to the SM prediction. The shaded bands on the inset show the uncertainties from the HERAPDF1.5 (black solid line), ZEUSJETS (black dashed line), CTEQ6M (red dashed line) and MSTW2008 (green dashed line) PDFs. 188

8.15 The measured ratio of the $d\sigma/dQ^2$ cross-sections for positive and negative polarisation (top) and the polarisation asymmetry A^+ as a function of Q^2 . The closed circles represent the measured values, where only the statistical uncertainties are considered as the systematic uncertainties are assumed to cancel. The curves show the SM predictions evaluated using the HERAPDF1.5 PDFs. 189

8.16 The cross-sections $d\sigma/dx$ for $Q^2 > 185 \text{ GeV}^2$ (top left), $d\sigma/dy$ for $Q^2 > 185 \text{ GeV}^2$ (top right), $d\sigma/dx$ for $Q^2 > 3000 \text{ GeV}^2$ (bottom left) and $d\sigma/dy$ for $Q^2 > 3000 \text{ GeV}^2$ (bottom right) for positive polarisation. The closed circles represent the data points, the inner error bars show the statistical uncertainty and the outer bars show the statistical and systematic uncertainties added in quadrature. The curves show the SM predictions evaluated using the HERAPDF1.5 PDFs. 191

8.17 The cross-sections $d\sigma/dx$ for $Q^2 > 185 \text{ GeV}^2$ (top left), $d\sigma/dy$ for $Q^2 > 185 \text{ GeV}^2$ (top right), $d\sigma/dx$ for $Q^2 > 3000 \text{ GeV}^2$ (bottom left) and $d\sigma/dy$ for $Q^2 > 3000 \text{ GeV}^2$ (bottom right) for negative polarisation. The closed circles represent the data points, the inner error bars show the statistical uncertainty and the outer bars show the statistical and systematic uncertainties added in quadrature. The curves show the SM predictions evaluated using the HERAPDF1.5 PDFs. 192

8.18 The ratio of the positive and negative polarised cross-sections $d\sigma/dx$ for $Q^2 > 185 \text{ GeV}^2$ (top left), $d\sigma/dy$ for $Q^2 > 185 \text{ GeV}^2$ (top right), $d\sigma/dx$ for $Q^2 > 3000 \text{ GeV}^2$ (bottom left) and $d\sigma/dy$ for $Q^2 > 3000 \text{ GeV}^2$ (bottom right). The closed circles represent the data points, the inner error bars show the statistical uncertainty and the outer bars show the statistical and systematic uncertainties added in quadrature. The curves show the SM predictions evaluated using the HERAPDF1.5 PDFs. The shaded bands on the plot show the uncertainties from the HERAPDF1.5 PDFs. 193

8.19 The reduced cross-section for e^+p NC DIS with polarised e^+ beams as a function of x for fixed Q^2 values. The blue closed (red open) circles represent the measured values for positive (negative) polarisation, the inner error bars show the statistical uncertainty and the outer bars show the statistical and systematic uncertainties added in quadrature, although the errors are too small to be visible in most cases. The blue and red curves show the SM predictions evaluated using the HERAPDF1.5 PDFs at the measured polarisation value. 195

8.20	The ratios of the reduced cross-section with polarised e^+ beams as a function of x at fixed values of Q^2 to the SM predictions evaluated using the HERAPDF1.5 PDFs. The points represent the measured ratios, the inner error bars show the statistical uncertainty and the outer bars show the statistical and systematic uncertainties added in quadrature. The shaded band shows the uncertainties from the HERAPDF1.5 PDFs.	196
9.1	Parton densities for the u_v (top left), d_v (top right) valence quarks, the sea quarks (bottom left) and the gluon (bottom right). The fractional error is shown as the purple band below each distribution.	199

Chapter 1

Deep Inelastic Scattering

1.1 Introduction

The goal of this thesis is to measure the high- Q^2 NC DIS cross-sections and investigate electroweak effects for positron-proton collisions collected in 2006/2007 with the ZEUS detector at HERA. This is a major high statistics analysis, completing the high- Q^2 DIS measurements at ZEUS, with important implications for PDF fits and constraining electroweak couplings. Combining the results with the previously measured electron-proton [1] NC DIS measurements, the structure functions $x\tilde{F}_3$ and $xF_3^{\gamma Z}$ are extracted. The parity violating nature of the electroweak interaction is investigated by comparing separate samples with a negative and positive polarised positron beam.

In this introductory chapter a theoretical and historical overview is presented in order to place the measurements in context.

1.2 The standard model

The Standard Model (SM) of particle physics describes the electromagnetic, strong and weak forces (it does not describe gravity), which mediate the interactions between the known subatomic particles. Central to the SM is that matter consists of a small set of point-like spin-1/2 particles called fermions, which interact through the exchange of gauge bosons of spin-1.

First Generation	Second Generation	Third Generation	Q
electron (e)	muon (μ)	tau τ	-1
electron neutrino (ν_e)	muon neutrino (ν_μ)	tau neutrino ν_τ	0

Table 1.1: The three generations of leptons and their electric charge in the SM.

First Generation	Second Generation	Third Generation	Q
up (u)	charm (c)	top (t)	+2/3
down (d)	strange (s)	bottom (b)	-1/3

Table 1.2: The three generations of quarks and their electric charge Q in the SM.

The fermions that make up matter can be placed into one of two groups: leptons and quarks, each with three “generations” of increasing mass. Leptons that have mass have a charge (Q), while the electrically neutral leptons, the neutrinos, have zero mass in the SM (neutrino oscillation results actually indicate that neutrinos have a very small non-zero mass [2] [3]). The three generations differ from each other in lepton family number (L), as well as mass. Each lepton has an anti-particle partner with the same mass but opposite Q and L. The leptons are summarized in table 1.1. Quarks differ from leptons in that they have fractional charge, and carry a “colour” charge of either red (r), green (g) or blue (b). There are six “flavours” of quarks, up (u), down (d), strange (s), charm (c), bottom (b) and top (t). As with leptons, each quark has an anti-particle partner. Hadrons are composite particles made of quarks bound by the strong force. Hadrons are categorized into two families: baryons (composed of three quarks, e.g., the proton) and mesons (made of a quark and anti-quark pair, e.g., π^0). The quarks are summarized in table 1.2.

The gauge bosons that mediate the electromagnetic, weak, and strong interactions are summarised in table 1.3. The photon mediates the electromagnetic interaction and couples to all electrically charged particles. The W^\pm and Z^0 bosons mediate the weak interactions and couple to all fermions. The electron-quark interaction studied in this thesis is mediated by the γ or the Z^0 and W^\pm bosons. The gluons, which mediate the strong interaction, themselves carry colour charge. Gluons only couple with other coloured particles, i.e., quarks and other gluons.

Interaction	Gauge Boson	Q	Mass
Electromagnetic	photon (γ)	0	0
Weak	Z^0, W^\pm	$0, \pm 1$	91.2/80.4 GeV
Strong	gluon (g)	0	0

Table 1.3: The gauge bosons of the SM with their electric charge Q and mass.

1.3 Theory of Deep Inelastic Scattering

1.3.1 Historical Overview

Atomic substructure was proposed by several scientists such as William Prout [4], Norman Lockyer [5] and Sir William Crookes [6], based on the relative weights of the elements and spectroscopic measurements. J. J. Thomson's discovery of the electron in 1897 suggested that atoms have substructure [7]. Thomson proposed his "plum-pudding" model of the atom which hypothesized negatively charged electrons embedded in a uniform mass of positive charge. In 1909, H. Geiger and E. Marsden [8], working under a research program initiated by Rutherford, scattered α particles off a thin gold foil. The plum-pudding model predicted that the α particles should be deflected relatively little during their passage through the gold foil. What was observed was that most α particles did indeed pass through the foil undeflected, but some were scattered at very large angles. In 1911, Rutherford explained this observation by postulating that the mass of the atom is concentrated in a tiny positively charged nucleus, surrounded by orbiting electrons [9]. This result not only demonstrated the structure of the atom, but showed that scattering experiments using a well understood point-like particle could be used to reveal the structure of matter. The discovery of the neutron by Chadwick [10] in 1932 (through scattering experiments) completed the picture of the atom: a nucleus consisting of protons and neutrons orbited by electrons, all of which were thought to be fundamental.

Measurements of the anomalous magnetic moment of the proton in the 1930s and the discovery of new particles in cosmic ray events and hadron-hadron collisions in the 1940s and 1950s hinted at proton substructure. Experiments by R. W. McAllister and R. Hofstadter in 1956 [11] elastically scattered 185 and 236 MeV electrons from

hydrogen atoms and showed that the proton is not point-like but has a spacial charge distribution with a root-mean-square radius of $(0.74 \pm 0.24) \times 10^{-13}$ cm. This result supported a Thomson-like model of proton structure rather than Rutherford-like.

By the mid-1960s a vast proliferation of particles had been discovered. Measurements from the MIT-SLAC collaboration in 1969 [13] provided a breakthrough in understanding the structure of the proton and understanding the wide variety of observed particles. These results showed that the proton does not have a Thomson-like smooth charge distribution but in fact is composed of point-like particles. This result and its implications are discussed in section 1.4.

1.3.2 Deep Inelastic Scattering

Deep inelastic scattering (DIS) refers to the scattering of a lepton from a nucleon with a large momentum transfer. At HERA beams of electrons (e^-) or positrons (e^+) are brought into collision with a beam of protons. For the sake of simplicity, unless otherwise stated, the incoming and scattered lepton will be referred to as an electron and the nucleon as a proton. Electron substructure has not been observed [15] so far, thus the electron can be treated as a point-like particle. If the gauge boson exchanged between the electron and the proton has a sufficiently short wavelength to resolve features smaller than the proton the process is called “deep”. If the struck quark is knocked out of the proton and the proton breaks up, then the collision is called “inelastic”. The quarks and gluons that remain in the broken-up proton are referred to as the “proton remnant”. The DIS process can be divided into two categories: Neutral Current (NC) DIS where a neutral γ or Z^0 is exchanged and Charged Current (CC) DIS where a charged W^\pm is exchanged. The scattered lepton in NC DIS is an electron, while for CC DIS it is a neutrino.

Kinematics

The analysis discussed in this thesis focuses on NC DIS. The typical final state topology of a NC DIS event consists of the following: a scattered electron, the proton

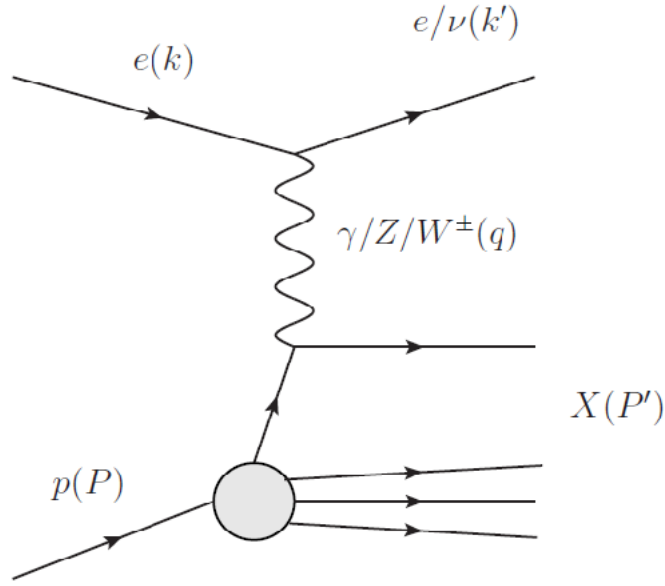


Figure 1.1: Feynman diagram of electron-proton NC and CC DIS.

remnant travelling in same direction as the incoming proton, and one or more jets (a jet is a narrow cone of hadrons and other particles emanating from the struck quark) travelling roughly in the direction of the scattered quark. NC (CC) DIS of electron-proton scattering, $ep \rightarrow e'X$ ($ep \rightarrow \nu'X$), is shown in figure 1.1, where e and e' (ν) are the incoming and outgoing electrons (neutrino) with four-momentum k and k' , respectively. The incoming proton is represented by p with four-momentum P and the hadronic final state is represented by X with a four momentum P' . The exchanged virtual gauge boson has four-momentum $q = k - k'$.

The following Lorentz-invariant variables are most often used to describe the kinematics of DIS:

$$Q^2 = -q^2 = (k - k')^2 \quad (1.1)$$

$$s = (k + P)^2 \quad (1.2)$$

$$x = \frac{Q^2}{2P \cdot q} \quad (1.3)$$

$$y = \frac{P \cdot q}{P \cdot k} \quad (1.4)$$

$$W^2 = (P + q)^2. \quad (1.5)$$

Q^2 is the negative squared four-momentum of the exchanged gauge boson. It gives

a length scale, Δx , at which the proton is probed by the exchanged gauge boson carrying a momentum Δp . The Heisenberg uncertainty relation allows a relationship between Q^2 and the wavelength of the exchanged gauge boson, λ , given by:

$$\Delta p \Delta x \approx \hbar \rightarrow \sqrt{Q^2} \approx \frac{\hbar}{\lambda}. \quad (1.6)$$

With increasing Q^2 , the proton is probed at smaller scales by a shorter wavelength gauge boson. The minimum distance scale probed at HERA experiments is $\approx 10^{-18}$ m.

The variable x (equation 1.3) is interpreted as the fraction of proton momentum carried by the struck quark (discussed further in section 1.4). It can take values between 0 and 1. The inelasticity y (equation 1.4) is a measure of the fraction of the electron energy transferred to the proton. It can take values between 0 and 1. The variable s (equation 1.2) is the centre-of-mass energy squared. W (equation 1.5) is the invariant mass of the hadronic final state. W can vary between the mass of the proton, m_p , and the center-of-mass energy, \sqrt{s} .

The variables Q^2 , x and y are properties of each event, while s is set by the incoming electron and proton beam energies ($E_p = 920$ GeV and $E_e = 27.56$ GeV) to $\sqrt{s} = 318$ GeV. The values of Q^2 , x and y are not independent and are related by the equation:

$$Q^2 = sxy, \quad (1.7)$$

neglecting the mass of the proton and electron. Only two of the variables Q^2 , x and y are needed to describe DIS events.

1.4 The quark parton model

The cross-section for ep inelastic scattering in the laboratory frame, assuming only photon exchange, can be written as follows [16]:

$$\frac{d^2\sigma}{d\Omega dE'} = \frac{4\alpha^2 E'^2}{Q^4} (2W_1(Q^2, \nu) \sin^2 \frac{\theta}{2} + W_2(Q^2, \nu) \cos^2 \frac{\theta}{2}), \quad (1.8)$$

where E' and θ are the scattered electron energy and angle respectively, α is the QED coupling constant, ν is the energy loss of the electron and $d\Omega$ is an element of solid angle. W_1 and W_2 are the structure functions, which are unknown and expected to depend on the target particle and on Q^2 and ν .

In 1967 an MIT-SLAC collaboration began investigating inelastic ep scattering [13] [14] using the two-mile 20 GeV electron linear accelerator at SLAC and a fixed proton target. The collaboration made two surprising observations: “Bjorken scaling” of the structure functions and, later, small violations of this scaling behaviour, as discussed in section 1.5.3.

The first observation had been predicted by Bjorken [17] on the basis of current algebra that in the limit of $\nu \rightarrow \infty$ and $Q^2 \rightarrow \infty$, with ν/Q^2 fixed, the structure functions, W_1 and νW_2 , will only depend on the dimensionless ratio x :

$$\nu W_2(\nu, Q^2) \rightarrow F_2(x) \quad (1.9)$$

$$2M_p W_1(\nu, Q^2) \rightarrow F_1(x), \quad (1.10)$$

where M_p is the proton mass and $x = Q^2/2M_p\nu$ is the Bjorken scaling variable, the same variable defined in equation 1.3. This phenomena is known as “Bjorken scaling” and was observed [18] by the MIT-SLAC collaboration for $Q^2 > 1 \text{ GeV}^2$ and $W > 2 \text{ GeV}$, as shown in figure 1.2.

The Hofstadter results from elastic scattering of electrons off protons [11] had shown the proton to have a smooth charge distribution with a size of $\approx 1 \text{ fm}$. Most models of the proton prior to the MIT-SLAC experiments predicted that the cross-

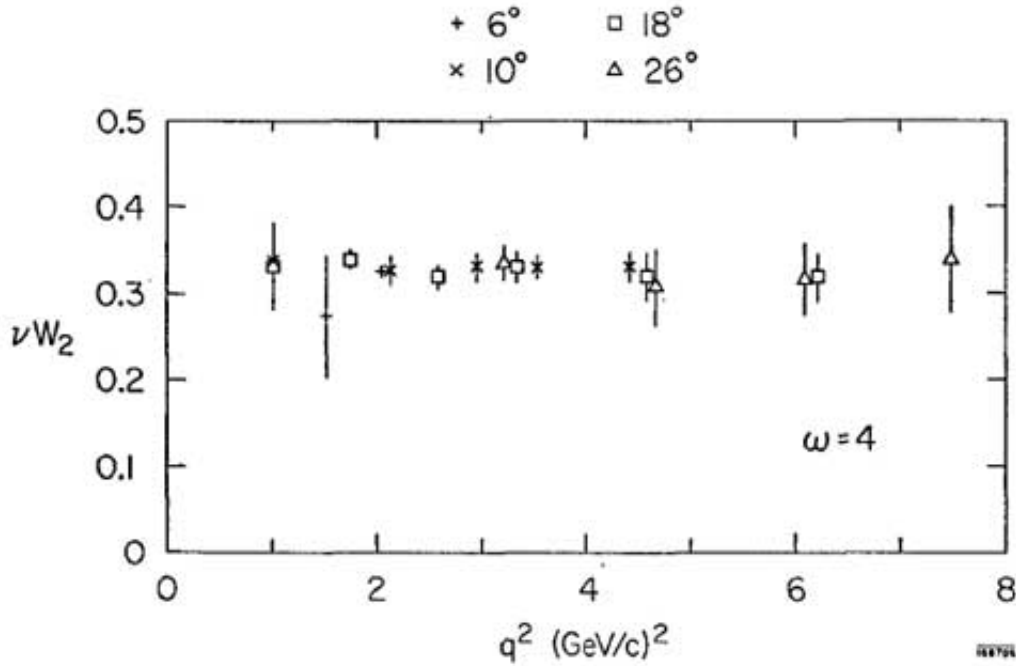


Figure 1.2: Scaling test for νW_2 as a function of Q^2 from ep scattering at the MIT-SLAC experiment[18].

section would rapidly decrease with increasing values of Q^2 . However the measured cross-section divided by the Mott cross-section for point-like scattering [14] (see figure 1.3) is 10 to 100 times higher than the expectation from elastic ep scattering. These results imply a point-like structure within the proton.

A major advance in understanding the scaling behaviour of the inelastic ep scattering results was a suggestion by Feynman [19], that the proton is composed of point-like particles that he dubbed “partons”, each carrying a fraction x , which is identified with the Bjorken scaling variable, of the total proton momentum. In the rest frame of the proton the partons are tightly bound. However, in the proton infinite momentum frame, the proton is highly Lorentz-contracted in the direction of motion, and the rate of interactions between the partons are slowed down by time dilation [20]. The lifetime of the virtual boson, by the uncertainty principle, is $\approx 1/Q$. Therefore, the partons appear to be approximately free particles on the time scale of a virtual boson with large Q^2 . The total inelastic ep cross-section is the incoherent sum of elastic scattering off the individual partons. Equation 1.8 can then be rewritten using

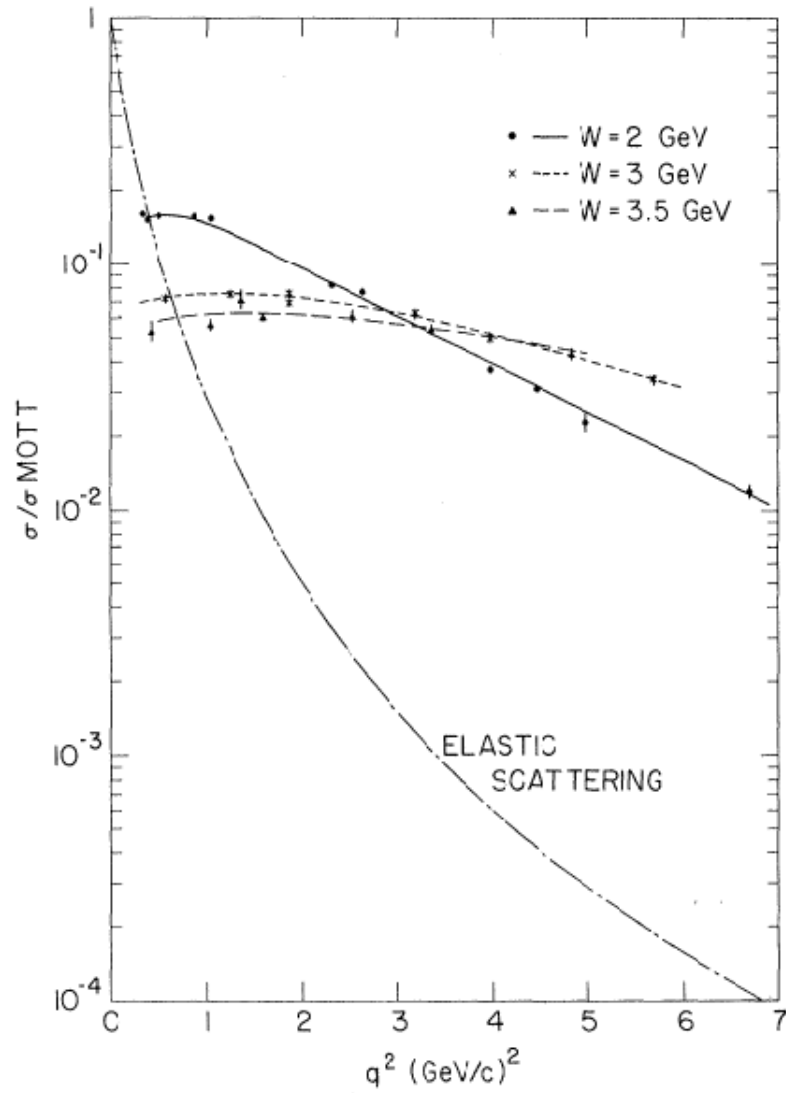


Figure 1.3: The inelastic ep divided by the Mott cross-section for fixed values of W as a function of Q^2 [14]. The elastic ep cross-section divided by the Mott cross-section is shown as the dashed-dotted line.

Lorentz-invariant variables in the Bjorken limit as:

$$\frac{d^2\sigma}{dx dQ^2} = \frac{4\pi\alpha^2}{xQ^4} [(1-y)F_2(x) + 2\frac{y^2}{2}xF_1(x)]. \quad (1.11)$$

1.4.1 Identification of the parton as a quark

In 1964 Gell-Mann and Zweig proposed the quark model as a classification scheme to explain the proliferation of particles being discovered. In the quark model hadrons are composed of spin-1/2 particles with fractional charge that give rise to their quantum numbers. At the time the quark model was proposed there was little evidence of proton substructure and the strange features, such as fractional charge, made acceptance of quarks as real particles difficult.

The discussion in section 1.4 did not identify the parton with the quark of Gell-Mann and Zweig. The NC inelastic ep cross-section can be written as the incoherent sum of elastic scatterings from the individual partons. Assuming they have spin 1/2, the cross-section takes the form:

$$\frac{d^2\sigma}{dx dQ^2} = \frac{2\pi\alpha^2}{xQ^4} [1 + (1-y)^2] \sum_q e_q^2 xq(x), \quad (1.12)$$

where e_q is the charge of the struck parton, and $q(x)$ is the density function such that $q(x)dx$ gives the probability of finding a parton with a momentum fraction between x and $x + dx$.

Helicity conservation requires two modes for e -parton scattering. For the case of the electron and parton having the same handedness, the net spin along the beam direction is zero, therefore the final state is distributed isotropically. In the other case of the electron and parton spins being aligned, the net spin of 1 requires the amplitude to be multiplied by $(1 + \cos\theta_{cm})/2 = (1 - y)$.

Comparing equation 1.11 with equation 1.12 gives:

$$F_2(x) = \sum_q e_q^2 xq(x) \quad (1.13)$$

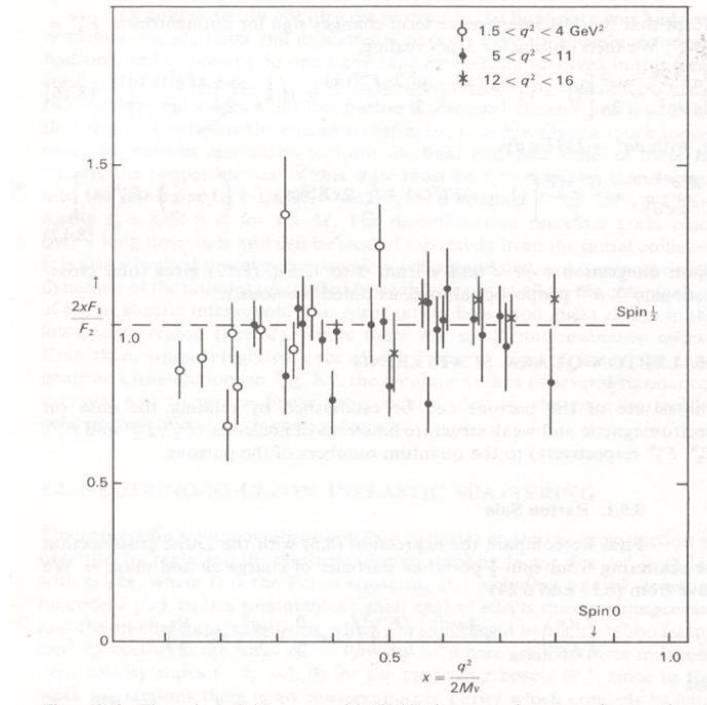


Figure 1.4: Ratio of the structure function F_1 and $2xF_2$ confirms the prediction $2xF_1(x)/F_2(x) = 1$ for spin-1/2 partons[22].

and

$$F_1(x) = \frac{1}{2x}F_2(x), \quad (1.14)$$

where equation 1.14 is called the Callan-Gross relationship [21]. The Callan-Gross relationship prediction that $2xF_1(x)/F_2(x) = 1$, confirmed by experiment [22] as shown in figure 1.4, allows the parton to be identified with the spin-1/2 quark. For instance, if the parton had spin 1 the Callan-Gross relationship would predict $2xF_1(x)/F_2(x) = 0$.

1.5 QCD and the QCD-improved quark parton model

The QPM described in section 1.4 was remarkably successful in explaining the DIS results observed by the MIT-SLAC collaboration, but there were a number of puzzles. Firstly, while the quarks are treated as free in the QPM, no free quarks have been observed. Secondly, the measured total momentum [23] of quarks was only about half

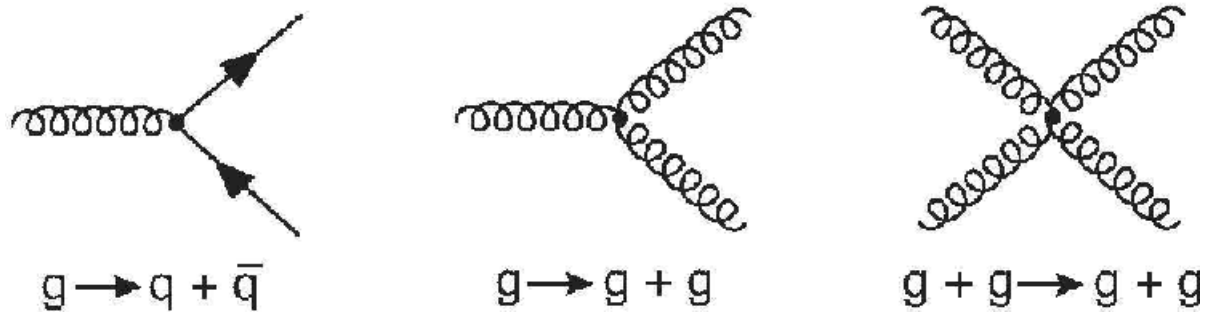


Figure 1.5: The 3 fundamental QCD vertices: gluon emission (left), three gluon vertex (middle) and four gluon vertex (right).

the proton's total momentum. Thirdly, deviations from Bjorken-scaling at both small and large x were observed. The resolution to these puzzles is given in the following sections on quantum chromodynamics (QCD) and the QCD-improved QPM.

1.5.1 Quantum chromodynamics

QCD is a non-Abelian, locally gauge-invariant and renormalizable SU(3) quantum field theory. It describes the strong interaction between quarks and the carriers of the strong force, gluons, in the SM. Both the massless gluons and the quarks carry a new degree of freedom referred to as “colour”, which comes in red (r), green (g) and blue (b). Each quark carries one colour, while the gluons carry a colour and a different anti-colour. Observable states must be “colourless”, such as baryons with three quarks (e.g., $r + g + b$) and mesons with a quark and anti-quark (e.g., $r\bar{r}$).

Due to the non-Abelian nature of QCD, the strong interaction differs from the other interactions; not only do quarks interact by the exchange of gluons, but gluons interact with each other. The fundamental vertices for QCD are shown in figure 1.5. The first experimental evidence for the existence of gluons was the observation of three-jet events [24] [25] [26] [27] at the PETRA e^+e^- collider at DESY in 1979 (see figure 1.6).

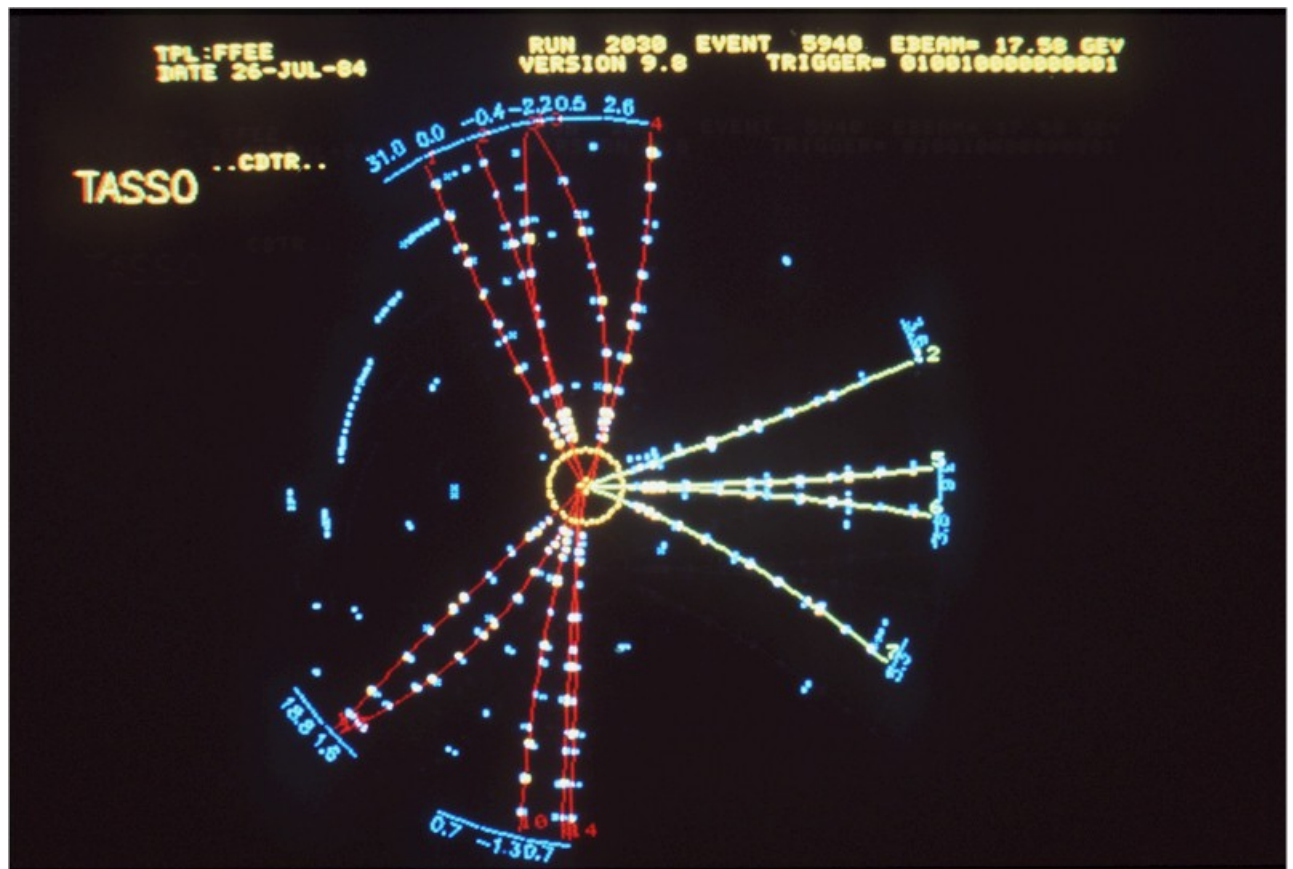


Figure 1.6: The first three jet event seen by the TASSO collaboration[24] providing support for the existence of the gluon.



Figure 1.7: Feynman diagrams of virtual quark (left) and gluon (right) loops.

1.5.2 Asymptotic freedom and confinement

The strong coupling constant, α_s , varies or “runs” with the probed energy scale, denoted as μ . In the electromagnetic case, the screening of the electric charge by electron-positron loops as seen at large distances or low energy is reduced at short distances and the coupling constant increases with μ . In the vicinity of a charge, the virtual particle of opposite charge is attracted to the charge and the virtual particle of like charge is repelled. The result of this is to partially screen the charge and reduce its field. Getting closer to the charge, the screening effect decreases and the field increases. To calculate the running coupling constant at an energy scale μ the coupling constant must be measured at a point μ_R known as the “renormalisation scale”. QCD behaves fundamentally differently from QED due to the presence of not only quark-anti-quark loops, but also gluon-loops (see figure 1.7). While the quark-anti-quark loops screen the colour charge as in QED, the gluon-loops produce an “anti-screening” effect which decreases α_s at small distances. At leading order (1-loop) α_s can be written as follows:

$$\alpha_s(\mu^2) = \frac{\alpha_s(\mu_R^2)}{1 + \alpha_s(\mu_R^2) \frac{\beta_0}{4\pi} \ln(\mu^2/\mu_R^2)}, \quad (1.15)$$

where μ_R is the renormalization scale and $\beta_0 = \frac{33-2n_f}{3}$, where n_f is the number of quark flavours with a mass less than the energy scale μ . Equation 1.15 can be redefined by introducing a scale $\Lambda = \mu e^{-2\pi/[\beta_0\alpha_s(\mu_R^2)]}$ giving the equation:

$$\alpha_s(\mu^2) = \frac{4\pi}{\beta_0 \ln(\mu^2/\Lambda^2)}. \quad (1.16)$$

Experimental measurements [28] of Λ are difficult to make precisely but it is approximately 200 MeV. Equation 1.16 is the clearest way to express that $\alpha_s(\mu^2)$ decreases logarithmically at large μ^2 (short distance scale). This property of α_s is called “asymptotic freedom” and is crucial to allow perturbative calculation of QCD (pQCD). Perturbation theory for QCD is only valid for $\mu \gg \Lambda$, as α_s is then significantly smaller

than 1. At low values of μ (large distance scale), comparable to or less than Λ , α_s becomes large, leading to the explanation of confinement of quarks in the proton.

Asymptotic freedom in QCD provides a mechanism for explaining why free quarks are not observed. In DIS the interaction between a photon with a large momentum and a quark is short-range and α_s is small. The quark is essentially free. The strong force between quarks increases as they are separated. As more work is put into separating the quarks, the amount of energy stored in the strong field becomes large enough to start producing $q\bar{q}$ pairs from the vacuum sea into reality. This lowers the potential energy of the system and effectively binds the quarks into colourless objects. Therefore, we do not see free quarks in DIS but jets of colourless hadrons along the direction of the scattered quark.

1.5.3 Factorization and DGLAP

The relative momentum of quarks and gluons emitted collinear to the struck quark is very small. Therefore, the strong interaction between them is strong and pQCD is not applicable. The “Factorization” theorem allows the DIS cross section to be written as the convolution of two terms: the pQCD calculable hard scattering cross-section and a non-perturbative parton distribution function (PDF), which absorbs the uncalculable effects. The DIS cross-section, σ , can then be written as:

$$\sigma(x, Q^2) = \sum_i \int_0^1 dx f_i(x, \mu_F^2) \hat{\sigma}_i(x, \alpha_s(\mu_R^2), \mu_F^2), \quad (1.17)$$

where μ_F is the “factorization scale”, and f_i is the PDF and $\hat{\sigma}_i$ the hard scattering cross-sections for parton i . The factorization scale separates what is included in the calculable hard scatter and the non-perturbative PDF. A parton emitted with a transverse momentum $< \mu_F$ should be considered part of the PDF, while partons emitted with a large transverse momentum contribute to the hard scatter.

The PDFs, f_i , are unique for each hadron, but are process-independent. Thus, PDFs obtained from DIS data (such as the analysis described in this thesis) can be

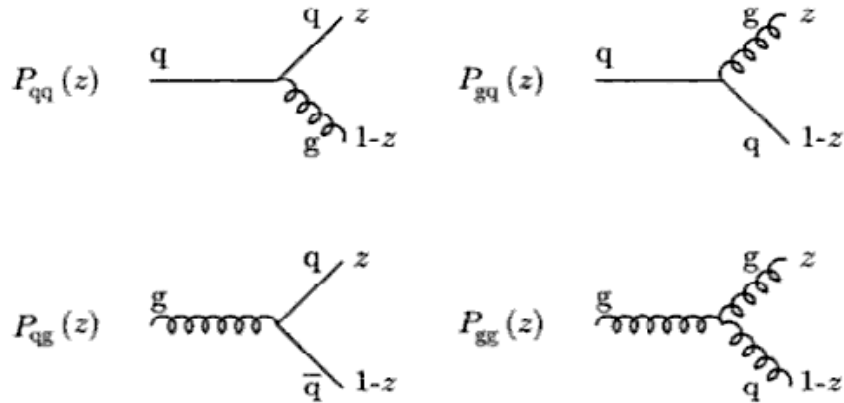


Figure 1.8: Splitting functions P_{ij} give the probability of a parton i with momentum fraction ξ , reducing its momentum to x , emitting a second parton j with momentum $z = \frac{x}{\xi}$

applied to other processes, e.g., pp collisions at the LHC.

The PDFs cannot be calculated from first principles in pQCD. However, the x dependence of the PDFs can be calculated using non-perturbative methods or by determining them experimentally at a starting scale Q_0^2 . As Q^2 increases, more partons are visible due to the QCD processes seen in figure 1.8. These processes are described by the “splitting functions”, $P_{qq}(z)$, $P_{gq}(z)$, $P_{qg}(z)$ and $P_{gg}(z)$ which give the probability of a parton with a momentum fraction ξ emitting a second parton, reducing its momentum to x , with the momentum fraction $z = \frac{x}{\xi}$. The “evolution” of the PDFs from a starting scale Q_0^2 to a higher scale Q^2 is governed by the DGLAP (DokshitzerGribovLipatovAltarelliParisi) [29] [30] [31] equations:

$$\frac{\partial q_i(x, Q^2)}{\partial \ln Q^2} = \frac{\alpha_s(Q^2)}{2\pi} \int_x^1 \frac{d\xi}{\xi} \left[\sum_j q_j(\xi, Q^2) P_{q_i q_j}\left(\frac{x}{\xi}\right) + g(\xi, Q^2) P_{q_i g}\left(\frac{x}{\xi}\right) \right] \quad (1.18)$$

$$\frac{\partial g(x, Q^2)}{\partial \ln Q^2} = \frac{\alpha_s(Q^2)}{2\pi} \int_x^1 \frac{d\xi}{\xi} \left[\sum_j q_j(\xi, Q^2) P_{g q_j}\left(\frac{x}{\xi}\right) + g(\xi, Q^2) P_{g g}\left(\frac{x}{\xi}\right) \right], \quad (1.19)$$

where q_i are the quark and anti-quark distributions and g is the gluon distribution.

The initial measurements of the proton structure functions by the MIT-SLAC collaboration showed that Bjorken scaling was observed. Further measurements observed deviations at both small and large values of x , known as “scaling violations”.

The addition of QCD processes through the DGLAP equations explain these scaling violations. F_2 is proportional to the number of quarks in the proton. As Q^2 increases the short wavelength photon resolves more QCD splittings ($g \rightarrow q\bar{q}$, $q \rightarrow qg$), typically interacting with lower- x partons. Therefore at higher Q^2 the photon interacts with relatively more low- x quarks and fewer high- x quarks, which increases F_2 at low x . At high x F_2 decreases as it is relatively unlikely for quarks from QCD splittings to have high x . This process leads to the scaling violations seen in figure 1.9.

1.5.4 Sum rules

Summing over the PDFs gives a number of rules which provide a test of the improved QPM and act as constraints in determining the PDFs from fits to data. Integrating over the valence quarks should yield:

$$\int_0^1 u_v(x) dx = 2 \quad (1.20)$$

$$\int_0^1 d_v(x) dx = 1, \quad (1.21)$$

which are the numbers of each type of valence quark in the proton. This particular result cannot be directly verified experimentally, but its consequences can be seen in the Gross-Llewellyn-Smith sum rule [32]:

$$\int_0^1 F_3^{\nu N} dx = \int_0^1 (u_v(x) + d_v(x)) dx = 3, \quad (1.22)$$

which was verified in early neutrino-nucleon scattering. Similarly the Gottfried sum rule:

$$\int_0^1 (F_2^{lp} - F_2^{ln}) \frac{dx}{x} = \frac{1}{3} \int_0^1 (u_v(x) - d_v(x)) dx = \frac{1}{3}, \quad (1.23)$$

where F_2^{lp} and F_2^{ln} are the proton and neutron F_2 structure functions, was verified in charged lepton DIS.

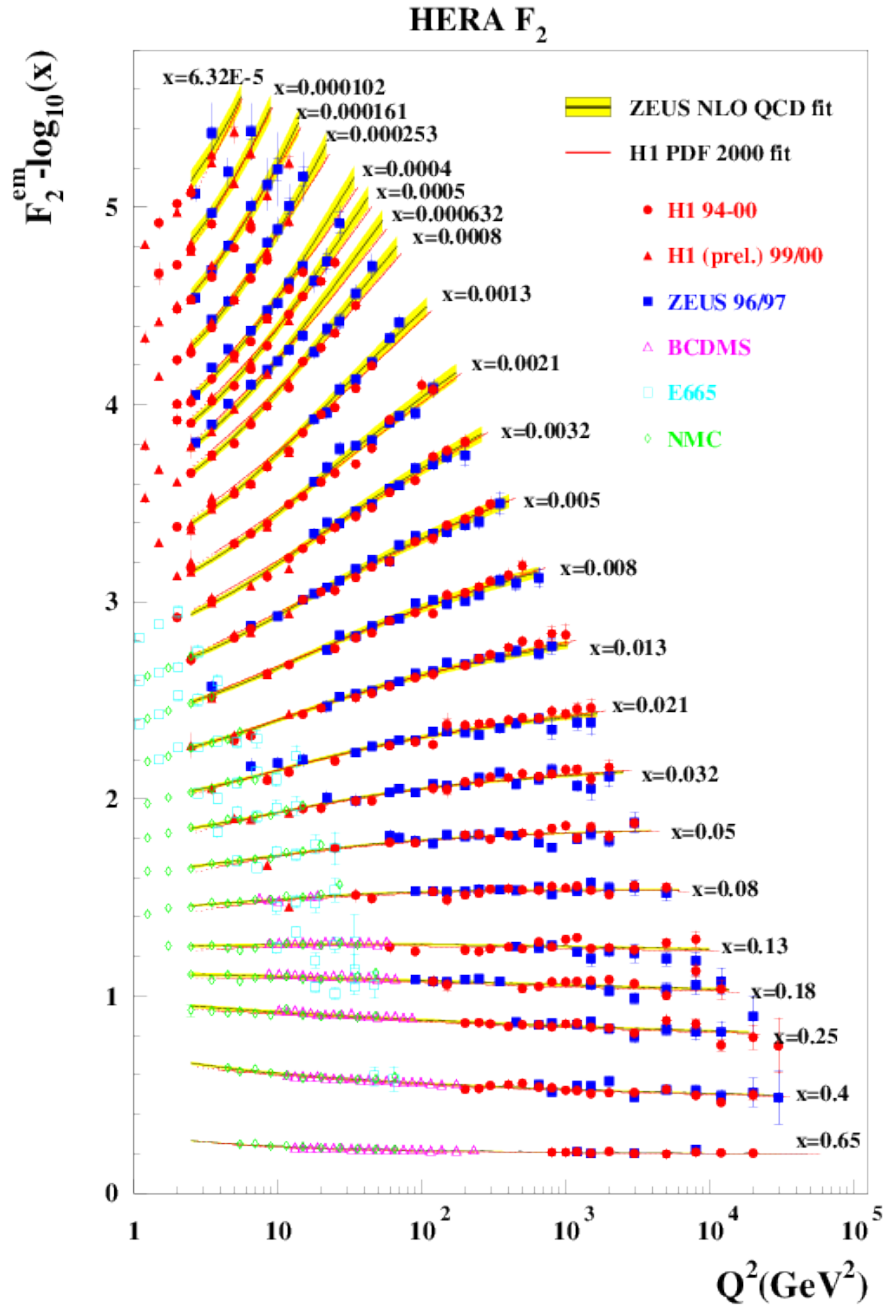


Figure 1.9: The measured F_2^γ as a function of Q^2 at fixed values of x from ZEUS (filled squares), H1 (filled circles and triangles), BCDMS (open triangles), E665 (open squares) and NMC (open diamonds). The yellow band represents the SM predictions and associated uncertainty with ZEUS NLO PDF fit, and the red curve the SM predictions from H1 PDF 2000. Scaling violation can be clearly seen at high and low x .

In the QPM the momentum sum rule can be expressed as:

$$\int_0^1 x\Sigma(x)dx = 1, \quad (1.24)$$

where $\Sigma(x)$ is the sum of all the quarks and anti-quarks in the proton, if the quarks carry all the momentum of the proton. This sum rule can be checked experimentally since $x\Sigma(x) = F_2$. Early DIS neutrino-nucleon scattering measured the momentum sum to be only:

$$\int_0^1 dx F_2 \approx 0.5. \quad (1.25)$$

This result can be explained by QCD, which indicates that the momentum deficit is carried by the gluons, and the momentum sum rule must be modified:

$$\int_0^1 x(g(x) + \Sigma(x))dx = 1, \quad (1.26)$$

where g represents the gluon distribution.

1.6 Parton distribution functions

The DGLAP formalism discussed in section 1.5.3 describes the Q^2 evolution of the PDFs, but the x dependence must be obtained by other methods. To determine the x dependence, experimental data can be fit at a starting scale Q_0^2 to obtain what is called a ‘‘PDF fit’’. The results of these fits are usually given in terms of parameterised distributions of the valence quarks (u_v, d_v) the sea quarks (quark anti-quark pairs due to $g \rightarrow q\bar{q}$) and the gluon. The parameters of the fits are constrained by several factors such as the momentum sum rules (see section 1.5.4) and a variety of experimental data.

To obtain well-constrained fits the choice of input data is important. NC measurements at low x ($x < 0.01$) give information on the total sea quark and gluon

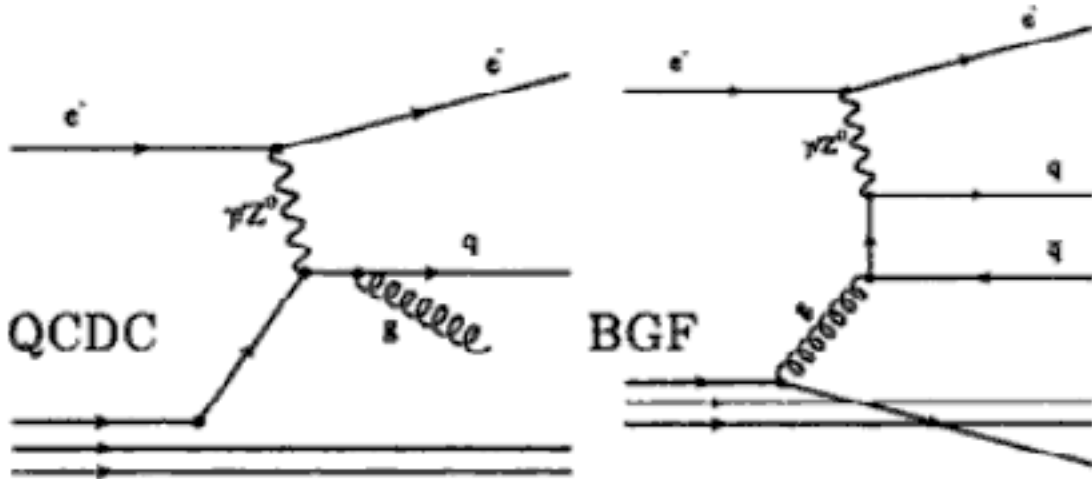


Figure 1.10: The leading order QCD contributions to the NC DIS cross-section. QCD Compton (QCDC) (left) and boson gluon fusion (BGF) (right).

distributions, while high- Q^2 NC and CC data are sensitive to the valence quark distributions. Jet production rates, charm production and the measurement of F_L (see section 1.7.2) constrain the gluon PDF, as they depend directly on the gluon PDF through Feynman diagrams such as those shown in figure 1.10.

Data from multiple experiments can be combined to decrease the statistical uncertainty and to constrain the fits across the entire range of x of the PDF fits. Examples of such PDF fits are CTEQ [33] and MRST [34], which combine both fixed target and collider data. A major drawback of this method is that some data sets are inconsistent with one another [28, p. 142]. These inconsistencies must be properly taken into account to attain meaningful results. Additionally, some data sets are collected with heavy targets such as iron. Scattering results from heavy targets must be corrected for nuclear binding effects, leading to larger uncertainties.

Some experimental collaborations, such as H1 and ZEUS at HERA, produce their own PDF fits (e.g., ZEUS-JETS and H1 PDF 2000). While this limits the statistical precision of the fits, there is generally a better understanding of the experimental systematic uncertainties since only one experiment is considered.

Recently, H1 and ZEUS have combined their datasets to produce combined fits called HERAPDFs. The HERAPDF1.5 [35] fits are used in this thesis (see chapter 8). The HERAPDF1.5 valence, sea quark and gluon distributions are parameterised at

$Q_0^2 = 1.9 \text{ GeV}^2$ using the following form:

$$xf(x) = Ax^B(1-x)^C(1 + \eta\sqrt{x} + Dx + Ex^2), \quad (1.27)$$

where $f(x)$ is the PDF and A, B, C, D, E and η are the parameters of the fit.

The PDFs as a function of x are shown for HERAPDF1.5 for $Q^2 = 10 \text{ GeV}^2$ and $Q^2 = 10000 \text{ GeV}^2$ in figure 1.11.

1.7 Electromagnetic and weak interaction

1.7.1 Electroweak theory

In 1961, Glashow proposed a unified theory of electromagnetic and weak interactions [36]. The generation of massive weak bosons through spontaneous symmetry breaking was added by Weinberg and Salam in 1968 [37], completing the theory now known as the Glashow-Weinberg-Salam model of electroweak interactions.

The weak force differs from the electromagnetic and strong interactions in that it involves only left-handed (LH) particles and right-handed (RH) anti-particles. The handedness of a particle is related to its helicity, the component of the spin of a particle projected on its direction of motion. If the spin vector is aligned with the direction of motion the particle is called RH, while if the spin is anti-aligned the particle is called LH. Thus electroweak theory groups fermions into two types, right-handed and left-handed:

$$\text{leptons} \quad \begin{pmatrix} \nu_e \\ e_L^- \end{pmatrix}, \begin{pmatrix} \nu_\mu \\ \mu_L^- \end{pmatrix}, \begin{pmatrix} \nu_\tau \\ \tau_L^- \end{pmatrix}, e_R^-, \mu_R^-, \tau_R^- \quad (1.28)$$

$$\text{quarks} \quad \begin{pmatrix} u_L \\ d_L \end{pmatrix}, \begin{pmatrix} c_L \\ s_L \end{pmatrix}, \begin{pmatrix} t_L \\ b_L \end{pmatrix}, u_R, d_R, s_R, c_R, b_R, t_R. \quad (1.29)$$

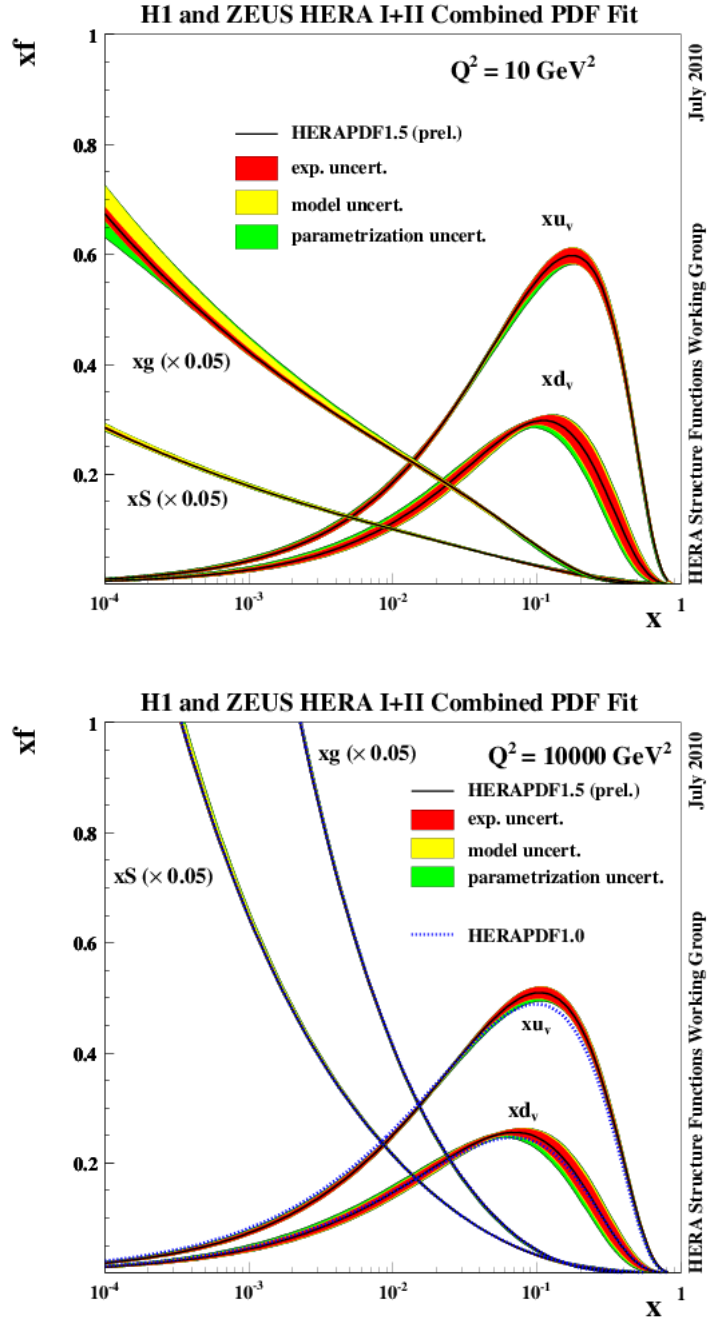


Figure 1.11: The proton valence quarks (u_v , d_v), sea quarks (S) and gluon (g) PDFs from the HERAPDF1.5 fit for $Q^2 = 10 \text{ GeV}^2$ (top) and $Q^2 = 10000 \text{ GeV}^2$ (bottom).

Fermion	T	T_3	Y	e_f
ν_e, ν_μ, ν_τ	1/2	+1/2	-1	0
e_L^-, ν_L^-, τ_L^-	1/2	-1/2	-1	-1
e_R^-, ν_R^-, τ_R^-	0	0	-2	-1
u_L, c_L, t_L	1/2	+1/2	+1/3	+2/3
d_L, s_L, b_L	1/2	-1/2	+1/3	-1/3
u_R, c_R, t_R	0	0	+4/3	+2/3
d_R, s_R, b_R	0	0	-2/3	-1/3

Table 1.4: The weak isospin T and its third component T_3 , hypercharge Y and electric charge e_f for each fermion of the SM.

The neutrino is assumed to be massless in the SM, and is only LH [15] (It is now known that neutrinos have a small mass from the discovery of neutrino oscillations). Electroweak theory introduces a new quantum number for fermions, weak isospin T , which is carried only by LH particles. A second new quantum number, hypercharge Y , is defined so that the electric charge of charged leptons is derived from the weak isospin. The electric charge of a fermion f is given by:

$$e_f = e(T_f^3 + Y_f/2), \quad (1.30)$$

where e is the unit charge, T_f^3 is the third component of the weak isospin and Y_f is the hypercharge. The values of T , T_3 and charge are summarized in table 1.4.

Electroweak theory is based on two gauge fields: an isovector triplet $\mathbf{W}_\mu = (W_\mu^1, W_\mu^2, W_\mu^3)$ and a single isoscalar B_μ . Through the introduction the Higgs field [38], spontaneous symmetry breaking results in three massive bosons W_μ^+, W_μ^-, Z_μ and one massless (the photon) A_μ . A_μ and Z_μ mediate the neutral current interaction and are mixtures of the W_μ^2 and B_μ fields governed by:

$$\begin{pmatrix} A_\mu \\ Z_\mu \end{pmatrix} = \begin{pmatrix} \cos\theta_W & \sin\theta_W \\ -\sin\theta_W & \cos\theta_W \end{pmatrix} \begin{pmatrix} B_\mu \\ W_\mu^3 \end{pmatrix}, \quad (1.31)$$

where θ_W is the weak mixing angle, which must be determined experimentally. Charged

currents are mediated by:

$$W^\pm = \frac{1}{\sqrt{2}}(W_\mu^1 \mp iW_\mu^2). \quad (1.32)$$

Weak neutral currents were first observed by the Gargamelle experiment in 1973 [39] and the W^\pm and Z^0 bosons were directly measured by UA1 and UA2 at CERN in 1983 [40] [41] [42] [43].

The electroweak interaction Lagrangian is given by:

$$L = \frac{g}{2}(J_\mu^- W_\mu^+ + J_\mu^+ W_\mu^-) + \frac{g}{\cos\theta_W}(J_\mu^3 - \sin^2\theta_W J_\mu^{em})Z_\mu + g\sin\theta_W J_\mu^{em} A_\mu, \quad (1.33)$$

where g is the coupling strength, J_μ the weak isospin current, J_μ^Y the weak hypercharge current, $J_\mu^{em} = J_\mu^Y + J_\mu^3$ is the electromagnetic current and $J_\mu^\pm = J_\mu^1 + J_\mu^2$. The first term refers to the weak charged contribution, the second to the weak neutral contribution and the third term is the electromagnetic contribution. From equation 1.33, the electromagnetic coupling e can be expressed as:

$$e = g_W \sin\theta_W. \quad (1.34)$$

The charged current contribution of equation 1.33 only selects a LH particle or RH anti-particle, while the neutral current contribution couples to both RH and LH particles. Thus we can define LH and RH coupling constants g_R and g_L :

$$g_R = -\sin^2\theta_W q \quad (1.35)$$

$$g_L = T_3 - \sin^2\theta_W q. \quad (1.36)$$

The fermion vector coupling, v , and axial-vector coupling, a , are defined as:

$$v = g_L + g_R = T_3 - 2\sin^2\theta_W q \quad (1.37)$$

$$a = g_L - g_R = T_3. \quad (1.38)$$

Fermion	v	a
ν_e, ν_μ, ν_τ	+1/2	+1/2
e^-, ν^-, τ^-	-0.038	-1/2
u, c, t	+0.192	+1/2
d, s, b	-0.346	-1/2

Table 1.5: The vector coupling v and axial coupling a for each fermion to the Z^0 boson.

They are tabulated in table 1.5.

1.7.2 The NC cross-section

The NC cross-section for scattering of a polarised charged lepton with a helicity (handedness) λ (+1 for RH and -1 for LH) by an unpolarised proton can be written in the form:

$$\frac{d^2\sigma}{dx dQ^2} = \sigma_\gamma + \sigma_{\gamma Z}^\pm(\lambda) + \sigma_Z^\pm(\lambda), \quad (1.39)$$

where the \pm indicates the charge of the lepton and σ_γ , $\sigma_{\gamma Z}^\pm(\lambda)$ and $\sigma_Z^\pm(\lambda)$ are the contributions from photon exchange, γZ interference and Z^0 boson exchange, respectively. If we consider only the σ_γ term, we obtain equation 1.12. The NC cross-section at lowest electroweak order (Born level) is given by:

$$\frac{d^2\sigma^{e^\pm p}}{dx dQ^2} = \frac{2\pi\alpha^2}{xQ^4} [Y_+ \tilde{F}_2 \mp Y_- x\tilde{F}_3 - y^2 \tilde{F}_L], \quad (1.40)$$

where $Y_\pm = 1 \pm (1-y)^2$ and \tilde{F}_2 , \tilde{F}_L , $x\tilde{F}_3$ are the generalised structure functions. As shown in section 1.4, \tilde{F}_2 is related to the total quark content of the proton. \tilde{F}_2 is also sensitive to the gluon distribution through scaling violations. The longitudinal structure \tilde{F}_L is defined as $\tilde{F}_L = \tilde{F}_2 - 2x\tilde{F}_1$. In the QPM, \tilde{F}_L is zero, as fermions cannot absorb longitudinally polarised photons without violating helicity conservation. In the QCD-improved QPM, the struck quark can radiate a gluon and acquire transverse momentum, and thus absorb a longitudinally polarised photon without helicity non-

conservation. \tilde{F}_L relates directly to the gluon density distribution of the proton. As \tilde{F}_L is multiplied by y^2 , it only contributes significantly at high y . The structure function $x\tilde{F}_3$ contains only contributions from γZ interference and Z^0 exchange. The difference between the e^-p and e^+p cross-sections is determined by $x\tilde{F}_3$. It is proportional to the difference between the quark and anti-quark distributions. Assuming that the sea quark and anti-quark distributions cancel, $x\tilde{F}_3$ is proportional to the valence quark distribution.

The generalised structure functions are given by:

$$\tilde{F}_2 = F_2^\gamma + \kappa(-v_e \pm P_e a_e)F_2^{\gamma Z} + \kappa^2(v_e^2 + a_e^2 \pm 2P_e v_e a_e)F_2^Z \quad (1.41)$$

$$x\tilde{F}_3 = \kappa(-a_e \mp P_e v_e)x F_3^{\gamma Z} + \kappa^2(2v_e a_e \pm P_e(v_e^2 + a_e^2))x F_3^Z, \quad (1.42)$$

where a_e and v_e are the axial vector and vector couplings (see section 1.7.1) of the electron to the Z^0 boson and P_e is the longitudinal polarisation of the electron beam, defined as:

$$P_e = \frac{N_R - N_L}{N_R + N_L}, \quad (1.43)$$

where N_R and N_L are the numbers of RH and LH electrons in the beam. The parameter $\kappa = \frac{1}{\sin^2 2\theta_w} \frac{Q^2}{Q^2 + M_Z^2}$ is proportional to the ratio of the Z^0 and γ propagators (propagators represent the contribution of virtual particles on the internal lines of Feynman diagrams). The structure functions can be written at leading order in terms of sums and difference of the quark and anti-quark distributions:

$$\{F_2^\gamma, F_2^{\gamma Z}, F_2^Z\} = \sum_q \{e_q^2, 2e_q v_q, v_q^2 + a_q^2\} x(q + \bar{q}) \quad (1.44)$$

$$\{xF_3^{\gamma Z}, xF_3^Z\} = \sum_q \{e_q a_q, v_q a_q\} 2x(q - \bar{q}), \quad (1.45)$$

where e_q is the electric charge of the quark.

The reduced cross-section, $\tilde{\sigma}$, is defined by dividing the cross-section by the kine-

matic factors that \tilde{F}_2 is multiplied by in equation 1.40:

$$\tilde{\sigma}^{e^\pm p} = \frac{xQ^4}{2\pi\alpha^2} \frac{1}{Y_+} \frac{d^2\sigma_{NC}^{e^\pm p}}{dx dQ^2} = \tilde{F}_2 \mp \frac{Y_-}{Y_+} x\tilde{F}_3 - \frac{y^2}{Y_+} \tilde{F}_L. \quad (1.46)$$

Parity violation due to the longitudinal polarisation of the lepton beam can be directly measured through the polarisation asymmetry, A^\pm , defined as:

$$A^\pm = \frac{2}{P_e^+ - P_e^-} \frac{\sigma^\pm(P_e^+) - \sigma^\pm(P_e^-)}{\sigma^\pm(P_e^+) + \sigma^\pm(P_e^-)}, \quad (1.47)$$

where P_e^+ and P_e^- are the average longitudinal polarisation values of the positively and negatively polarised lepton beam (see equation 1.43). The polarisation asymmetry is a direct measure of parity violation and is approximately equal to the the ratio of $F_2^{\gamma Z}$ and F_2^γ :

$$A^\pm = -\kappa a_e \frac{F_2^{\gamma Z}}{F_2^\gamma} \propto a_e v_e. \quad (1.48)$$

1.8 NC DIS Measurements

The goal of this thesis is to measure the NC cross-section described in section 1.7.2. The single differential cross-sections $d\sigma/dQ^2$, $d\sigma/dx$ and $d\sigma/dy$ and the reduced cross-section (see equation 1.46) are to be measured using both unpolarised and polarised positrons. By combining the unpolarised reduced cross-section measured in this thesis with the previously published e^-p [1] results the structure functions $x\tilde{F}_3$ and $xF_3^{\gamma Z}$ (see equation 1.45) are to be extracted, which help constrain the valence quark PDFs and the electroweak couplings and directly observe the effect of Z^0 exchange. The measurement of the polarised $d\sigma/dQ^2$ cross-sections are to be used to extract the polarisation asymmetry (see equation 1.47) to directly measure parity violation in NC DIS. The next several chapters describe the experimental environment used to collect the data and the analysis methods used to extract the measurements. The final results are presented in chapter 8. A summary follows in chapter 9.

Chapter 2

HERA and the ZEUS Detector

2.1 HERA collider

The Hadron Elektron Ring Anlage (HERA) is located in Hamburg, Germany at the Deutsches Elektronen Synchrotron DESY. HERA's main components are the proton and electron storage rings, built between 1984 and 1990 [44], that began providing beams to the experiments in the summer of 1992.

HERA has a circumference of 6.3 km and is located 15-20 m below the surface. An aerial view of the DESY laboratory and HERA can be seen in figure 2.2. The construction of the two storage rings differ considerably. The 27.5 GeV electron storage ring is built using 0.165 T conventional electromagnets. The electron beam energy is limited by synchrotron radiation, which is inversely proportional to the fourth power of the particle mass. The proton storage ring employs superconducting magnets with a field strength of 4.68 T in order to achieve a high energy of 920 GeV.

Neither beam can be accelerated to its final energy in a single step, but must have the energy increased through a number of pre-accelerators. The proton beam is produced by ionizing hydrogen, creating H^+ ions which are then accelerated to 50 MeV in a linear accelerator. Once the ions leave the linear accelerator they are stripped of their electrons by passage through a thin aluminium foil [45] leaving a proton beam.



Figure 2.1: An aerial view of DESY and the HERA collider. The dashed rings indicate the locations of the PETRA pre-accelerator and the HERA collider. The ZEUS experiment is located at the right small circle, while H1 is located at the left small circle.

This proton beam is then injected into the DESY III proton synchrotron in 11 bunches separated by 96 ns and accelerated from 50 MeV to 7.5 GeV. The 7.5 GeV proton beam from DESY III is then injected into the PETRA storage ring. This process is repeated until 70 bunches have been accumulated in PETRA, at which point the protons are accelerated to 40 GeV. The proton beam from PETRA is then injected into HERA, until up to 210 proton bunches are accumulated. The protons in HERA are then accelerated to their final energy of 920 GeV.

Electrons are obtained from a hot filament. The beam is injected into a pair of linear accelerators, LINAC I and LINAC II, which accelerate the beam to 200 MeV and 450 MeV respectively. The electrons are then injected into the electron synchrotron DESY II and accelerated up to 7 GeV. From DESY II the electrons are accumulated in 70 bunches separated by 96 ns in PETRA II and accelerated to 14 GeV. The electrons are finally injected into HERA, repeating until up to 210 bunches are filled, and accelerated to their final energy of 27.5 GeV. Positrons are produced from pair production from bremsstrahlung photons produced by the electron beam and then accelerated by the same system of pre-accelerators as the electrons.

HERA was upgraded during 2000-2002. The terms HERA-I and HERA-II are

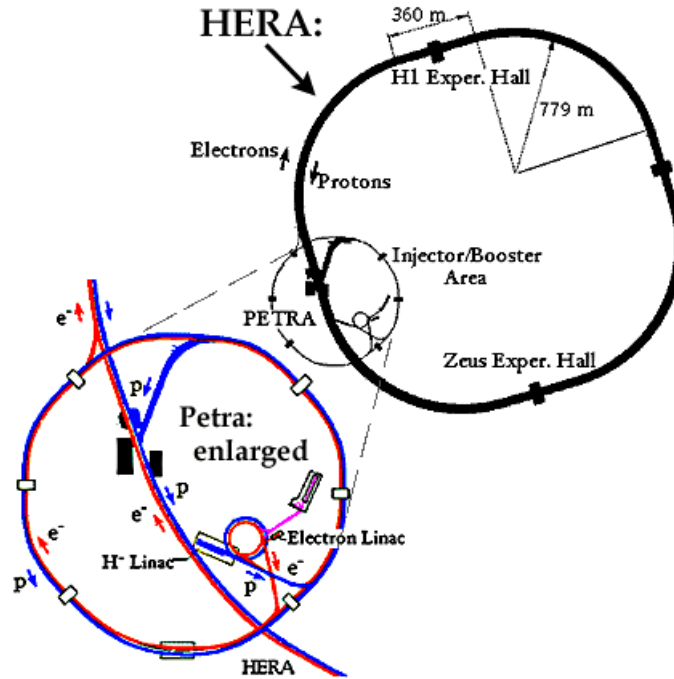


Figure 2.2: A schematic view of the HERA collider (top right) and pre-accelerator system (bottom left).

Parameter	HERA-I	HERA-II
	$e^{\pm} p$	$e^{\pm} p$
Energy (GeV)	27.5 920	27.5 920
Current (mA)	50 100	58 140
Beam size $\sigma_x \times \sigma_y$ (mm ²)	187 x 50 187 x 50	112 x 30 112 x 30
L_{inst} (cm ⁻² s ⁻¹)	1.78×10^{31}	7.57×10^{31}

Table 2.1: Electron and proton beam energies and currents for HERA-I and HERA-II.

used to distinguish between the periods before and after the upgrade. The HERA-I and HERA-II operating parameters [48] are summarized in table 2.1 (see section 2.1.3 for more information about HERA-II).

Four experiments operate at HERA. The electron and proton beams are brought into collision inside the two general purpose experiments, H1 [46] and ZEUS [47], located in the north and south halls respectively. Two experiments, HERMES (east hall) and HERA-B (west hall), use only the electron and proton beams, respectively.

The HERA collider ceased operation in the summer of 2007.

2.1.1 The bunch structure

Due to the radio-frequency (RF) used in the cavities to accelerate the beams, most particle accelerators (and by extension particle colliders) do not have continuous beams, but have a “bucket” structure. Filled buckets are referred to as “bunches”. At HERA not all the RF buckets are filled. For those buckets that are filled, there arise four distinct situations:

1. Colliding bunch: an electron bunch is paired with a proton bunch. These bunches are brought into collision inside the H1 and ZEUS detectors.
2. Electron pilot bunch: an electron bunch without a corresponding proton bunch.
3. Proton pilot bunch: a proton bunch without a corresponding electron bunch.
4. Empty bunch: the electron and the protons buckets are both empty.

Figure 2.3 illustrates a typical bunch structure at HERA. Time $t = t_0$ has an empty bunch, $t = t_1$ a proton pilot bunch and $t = t_2$ an electron pilot bunch. The remaining bunches are colliding bunches. Events that occur during colliding bunches are used for physics analysis. Pilot and empty bunches are used for background studies, allowing an estimation of the interaction of each beam with residual gas in the beampipe (beam-gas events).

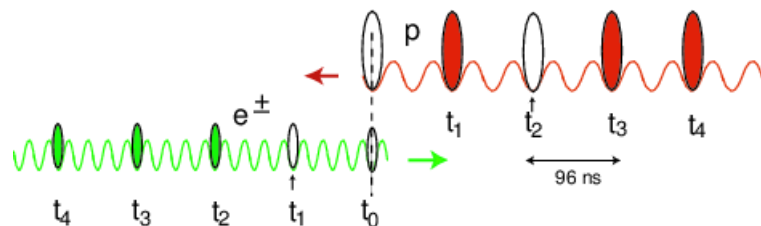


Figure 2.3: A schematic diagram of a typical HERA bunch structure.

2.1.2 Luminosity

One of the key parameters of a colliding beam machine is the collision rate at the interaction region. The reaction rate, R , is given by:

$$R = \sigma L, \quad (2.1)$$

where σ is the cross section of the reaction, and L is the instantaneous luminosity. The instantaneous luminosity can be expressed as as:

$$L = f \frac{n_1 n_2}{A}, \quad (2.2)$$

where f is the bunch crossing rate, n_1 and n_2 are the number of particles in each bunch and A is the effective cross sectional area of the beam overlap. This area can be expressed as:

$$A = 4\pi\sigma_x\sigma_y, \quad (2.3)$$

where σ_x and σ_y are the Gaussian transverse widths of the beams.

To relate the instantaneous luminosity L to the number of events, N , of a process with a cross section, σ , the integrated luminosity

$$\mathcal{L} = \int L dt = \frac{N}{\sigma} \quad (2.4)$$

is defined. \mathcal{L} is expressed in units of inverse picobarns (pb^{-1}) at HERA, where a barn is 10^{-24} cm^2 . The integrated luminosity is a measure of the amount of data taken and is summarized for both HERA-I and HERA-II in table 2.2.

2.1.3 HERA-II upgrade

During a long shutdown from 2000 to 2002 HERA was upgraded [49] to achieve a higher instantaneous luminosity, as shown in table 2.1, and to provide longitudinally

Period	94-97	98-99	99-00	03-04	04-06	06-07	07 LER	07 MER
lepton beam	e^+	e^-	e^+	e^+	e^-	e^+	e^+	e^+
E_p (GeV)	820	920	920	920	920	920	460	575
E_e (GeV)	27.5	27.5	27.5	27.5	27.5	27.5	27.5	27.5
\mathcal{L} (pb^{-1}) HERA	70.9	25.2	95.0	84.5	290.9	180.5	15.69	9.36
\mathcal{L} (pb^{-1}) ZEUS	48.3	16.7	65.9	40.6	213.5	145.9	13.18	7.77

Table 2.2: Instantaneous and integrated luminosity values for various running periods at HERA and ZEUS. LER and MER refer to low and medium proton energy runs, respectively, in order to measure the structure function F_L .

polarised electron beams for H1 and ZEUS.

The higher luminosity for HERA-II was primarily achieved by reducing the cross sectional area of the bunches (see table 2.1) and a modest increase in the beam currents. To reduce the size of the bunches at the interaction point, new superconducting magnets GO and GG were installed on either side of the detector (see figure 2.5 to see the location of the GO and GG magnets). It should be noted in table 2.2 that the amount of electron data collected at HERA-II is over 10 times that of HERA-I. This allows for a much more precise extraction of $x\tilde{F}_3$ and $xF_3^{\gamma Z}$ at HERA-II, as discussed in section 8.1.3.

The electron spin can become transversely polarised in high energy storage rings through a phenomenon known as the Sokolov-Ternov effect [50]. An electron can have its spin aligned parallel or anti-parallel with respect to the magnetic field of the storage rings bending magnets. The spin of the electron can flip when the electron emits synchrotron radiation. The rate of transition from parallel to anti-parallel, $\omega_{\uparrow\downarrow}$ and anti-parallel to parallel, $\omega_{\downarrow\uparrow}$, is given by [51]:

$$\omega_{\uparrow\downarrow} = \frac{f\sqrt{3}}{16} \left(1 + \frac{8}{5\sqrt{3}}\right) \frac{c\lambda_C r_0 \gamma^5}{\rho^3} \quad (2.5)$$

$$\omega_{\downarrow\uparrow} = \frac{f\sqrt{3}}{16} \left(1 - \frac{8}{5\sqrt{3}}\right) \frac{c\lambda_C r_0 \gamma^5}{\rho^3}, \quad (2.6)$$

where $\gamma = E_e/m_e$ is the Lorentz factor, ρ is the bending radius of the beam in the magnetic field, λ_C is the reduced Compton wavelength and r_0 is the classical electron radius. The Sokolov-Ternov effect occurs due to the asymmetry in the rate

of transition (see equation 2.6) from parallel to anti-parallel and from anti-parallel to parallel. This asymmetry enhances the anti-parallel state due to the anti-parallel state being the lower energy state (for a positron beam the asymmetry enhances the parallel state). Thus, an initially unpolarised electron beam circulating in a storage ring becomes transversely polarised with time according to [52]:

$$P(t) = P_{max}(1 - e^{-t/\tau}), \quad (2.7)$$

where $P_{max} = \frac{\omega_{\uparrow\downarrow} - \omega_{\downarrow\uparrow}}{\omega_{\uparrow\downarrow} + \omega_{\downarrow\uparrow}} \frac{8}{5\sqrt{3}} \approx 0.924$ is the theoretical maximum polarisation and τ the polarisation build-up time. P_{max} is less than one due to the small probability of an electron transitioning from the anti-parallel state to the parallel state. The polarisation build-up time, τ is a characteristic of the storage ring given by [51] [53]:

$$\tau = \frac{1}{\omega_{\uparrow\downarrow} + \omega_{\downarrow\uparrow}} = \frac{8\rho^3}{5\sqrt{3}c\lambda_C r_0 \gamma^5}. \quad (2.8)$$

The bending radius at HERA is not constant but consists of 4 circle arcs connected by straight sections, and ρ^3 must be replaced by:

$$\frac{1}{\rho^3} \rightarrow \oint \frac{1}{|\rho(\theta)|^3} \frac{d\theta}{2\pi} = \frac{1}{2\pi R} \oint \frac{1}{|\rho(s)|^3} ds, \quad (2.9)$$

where $\rho(\theta)$ is the bending radius at the azimuthal angle θ around the storage ring, R is the average radius of the ring and s is the position around the circumference of the ring corresponding to θ . At HERA the value of τ is approximately 40 minutes.

At ZEUS longitudinally polarised beams are of interest rather than transversely polarised beams, as the projection of the spin of a particle in the direction of its motion defines its helicity. Spin rotators consisting of a series of horizontal and vertical dipole magnets were installed upstream and downstream of H1 and ZEUS (see figure 2.4) to obtain a longitudinally polarised electron beam at the interaction point.

The longitudinal polarisation of the electron beam is typically 40-50% of the theoretical maximum, with an average polarisation of approximately 35%. This is due

to a number of depolarisation effects in a real-world storage ring [54] [55].

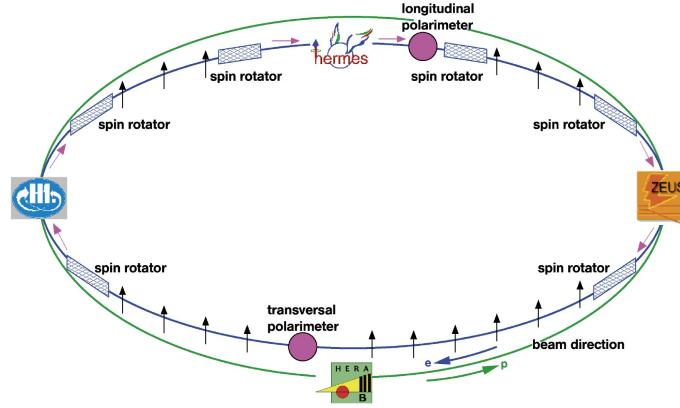


Figure 2.4: A schematic view of HERA showing the location of the spin rotators, polarimeters and experiments. The black arrows indicate whether the electron polarisation is transverse or longitudinal to the direction of motion.

2.1.4 Polarisation measurement

The polarisation of the electron beam is measured by two independent polarimeters: the transverse polarimeter (TPO) [56] and the longitudinal polarimeter (LPOL) [57].

Both polarimeters utilise the polarisation dependent Compton scattering cross-section. They also both use a laser beam to provide the incident photons. The Compton scattering cross-section is sensitive to the transverse, P_y , and longitudinal, P_z , components of the lepton beam polarisation and is given by [58]:

$$\frac{d^2\sigma}{dEd\phi} = \Sigma_0(E) + S_1\Sigma_1(E)\cos 2\phi + S_3P_y\Sigma_{2y}(E)\sin\phi + S_3P_z\Sigma_{2z}(E), \quad (2.10)$$

where S_1 and S_3 are the linear and circular components of the laser beam polarisation. The $\Sigma_{0/1/2y/2z}$ terms are functions of the energy of the scattered photon only. Both TPO and LPOL measure the electron beam polarisation by measuring the difference of the Compton scattering cross-section when switching the laser beam polarisation between left and right, i.e., $S_1 = 0$ and $S_3^\pm = \pm 1$:

$$\frac{d^2\sigma}{dEd\phi}(S_3^+) - \frac{d^2\sigma}{dEd\phi}(S_3^-) = (S_3^+ - S_3^-)[P_y\Sigma_{2y}(E)\sin\phi - P_z\Sigma_{2z}(E)]. \quad (2.11)$$

Equation 2.11 indicates that to measure P_y both the energy and the position (to determine the scattering angle ϕ) of the scattered photon must be known, while knowing the energy of the scattered photon is sufficient to measure P_z .

The TPOL utilizes a green argon-ion (2.4 eV photons) laser with a 10 W continuous beam, made circularly polarised by a Pockels cell, switching polarisation with a frequency of 84 Hz. The laser beam is then transported over 200 m into the HERA tunnel to collide with the transversely polarised electron beam. The TPOL is operated in the so-called “single-photon” mode, where the intensity of the beam was chosen so that there is a less than 1% chance of multiple Compton photons per bunch crossing. The backscattered Compton photons are detected in a tungsten-scintillator sampling calorimeter. The calorimeter is divided into two independent upper and lower halves. This allows the energy of the Compton photon to be measured using $E_\gamma = E_u + E_d$, where E_u and E_d are the energies measured in each half of the calorimeter. To obtain information on the position of the photon the energy asymmetry $\eta(y) = (E_u - E_d)/(E_\gamma)$ between the upper and lower halves is used. The function $\eta(y)$ is then translated into a vertical position y through an $\eta - y$ transformation determined from test beam measurements. The polarisation is then measured by the difference in the mean $\eta(y)$ distributions for left and right circularly polarised light.

The LPOL measures the longitudinal polarisation using the large asymmetry in the energy distributions of the backscattered Compton photons when circularly polarised photons scatter from a longitudinally polarised electron beam. In contrast to the TPOL, the LPOL operates in the “multi-photon” mode, where ≈ 1000 Compton photons are backscattered per bunch crossing. The multi-photon mode was chosen due to large bremsstrahlung background at the measurement point. This is achieved by the use of a high-powered pulsed Nd:YAG laser, pulsed at 100 Hz with a fixed pulse energy of 100 mJ with a length of 3 ns. Circularly polarised light is obtained by means of a Pockels cell, flipping the helicity for every pulse.

The laser beam is guided 72 m into the HERA tunnel to collide with the longitudinally polarised electron beam. The Compton photons are detected 54 m from the

interaction point in a Cerenkov calorimeter, constructed of $\text{NaBi}(\text{WO}_4)$ crystals. The polarisation is then measured using the asymmetry in the total energy deposited for the left and right circularly polarised laser pulses.

2.2 The ZEUS detector

The ZEUS detector is a general purpose detector situated in the HERA south hall designed to detect as many particles produced in ep collisions as possible. ZEUS has the typical onion structure of modern collider experiments. An inner tracking region is surrounded by a thin solenoid producing a uniform magnetic field. Surrounding the tracking region is a high resolution calorimeter. This is further surrounded by an iron sampling calorimeter instrumented with muon chambers. The ZEUS detector differs from most collider detectors in that it is asymmetric due to the large imbalance of the beam energies. Schematic views of the ZEUS detector are shown in figure 2.5 and 2.6.

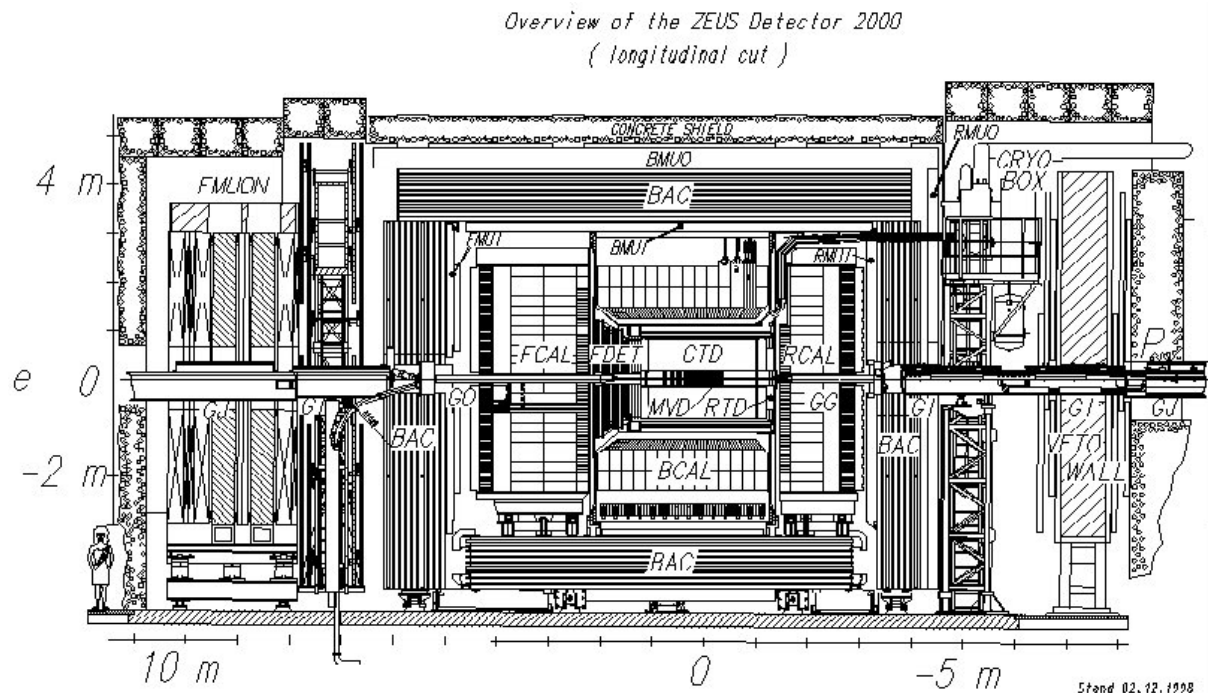


Figure 2.5: Schematic view of ZEUS detector along the beam.

The ZEUS coordinate system (see figure 2.7) is described by a right-handed coordinate system with its origin at the nominal interaction point. The proton beam

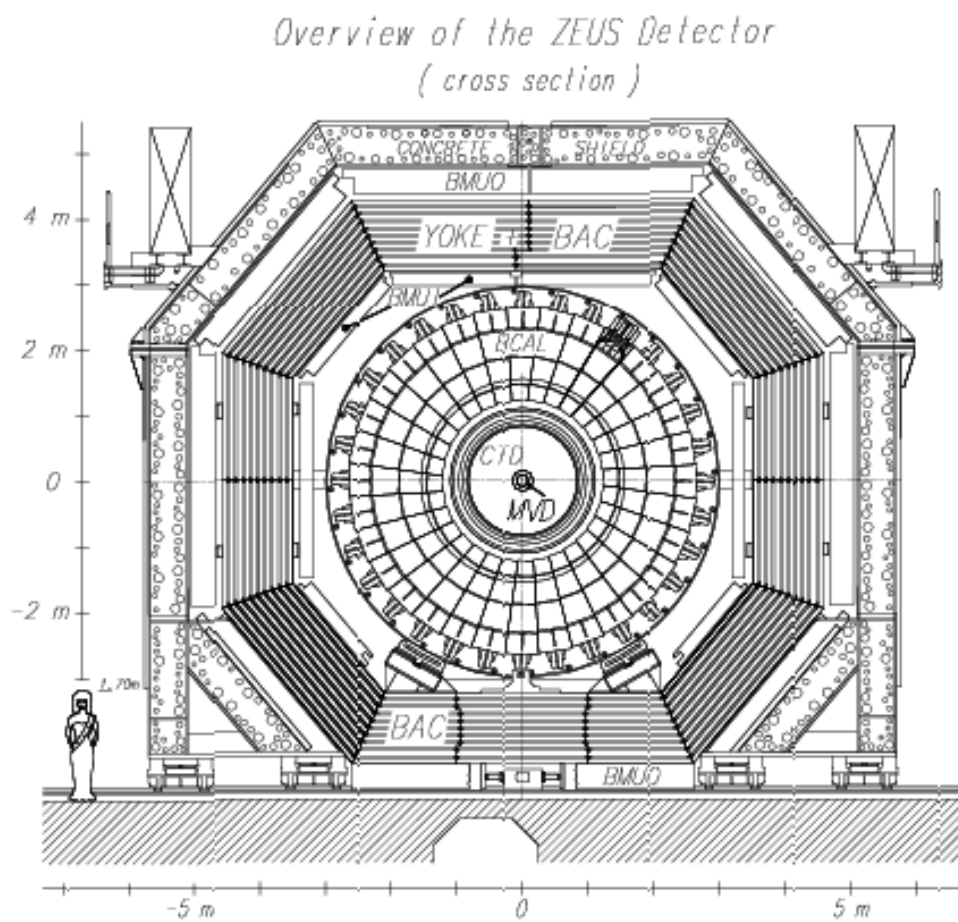


Figure 2.6: Schematic $x - y$ view of ZEUS detector.

direction is defined as $+z$. The $+x$ axis points horizontally towards the centre of HERA and the $+y$ axis points upwards. The polar angle θ is measured with respect to the z axis, while the azimuthal angle is measured in the $x - y$ plane. The $+z$ direction is referred to as the forward direction, while the $-z$ direction is referred to as the rear direction.

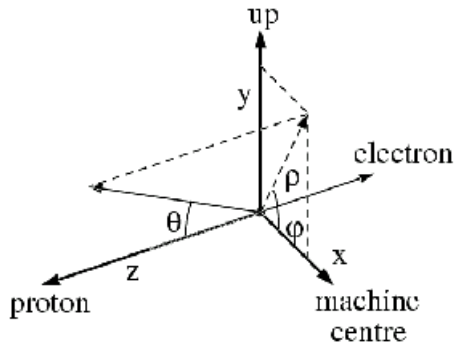


Figure 2.7: The ZEUS coordinate system.

At the core of the ZEUS detector, immediately surrounding the interaction point, are the tracking detectors. The silicon strip microvertex detector (MVD) sits closest to the interaction point. The MVD is surrounded by a cylindrical drift chamber called the central tracking detector (CTD). Surrounding the CTD and MVD is a thin superconducting solenoid (SOLENOID) which produces a uniform magnetic field of 1.8 T along the $+z$ direction. Forward of the CTD is the forward detector (FDET) consisting of the straw-tube tracker (STT) and planer drift chambers (FTD). These tracking detectors allow the direction, charge and momentum of charged particles leaving the interaction point to be measured.

The energy of both charged and neutral particles is measured in a uranium-scintillator sampling calorimeter (CAL) which surrounds the inner tracking detectors. The CAL is divided into three sections: the FCAL in the forward direction, the BCAL surrounding the central “barrel” region of the detector and the RCAL in the rear direction. Due to the asymmetry in the beam energy the FCAL is much thicker than the RCAL. In front of the BCAL and RCAL is the presampler (PRES), which is used to correct for energy loss. The hadron electron separator (HES) is placed at the electromagnetic shower maximum in the FCAL and RCAL to aid in identifying

electrons in dense hadronic showers.

Surrounding the CAL is an iron-scintillator sampling backing calorimeter (BAC) which is instrumented to measure energy leakage from the CAL. The iron in the BAC, called the yoke, is magnetized through the use of copper coils to serve as a return path for the magnetic field of the solenoid. Muon chambers (FMUON, BMUON and RMUON) are placed on the inside and outside of the iron yoke.

The veto wall (VETO) is located -7.5 m from the interaction point. It consists of an iron wall 87 cm thick and is instrumented with scintillators on both sides. The VETO protects the detector from particles produced in proton beam-gas events or from the proton beam halo interacting with beam-line material. The C5 detector consists of two layers of scintillator interleaved with tungsten and placed at -1.2 m and centred around the beampipe. The shape of the C5 detector face is 20×20 cm² with the corners removed (isosceles triangles with side lengths of 5 cm x 5 cm x 7 cm). It is used to detect beam-gas events. Events flagged by the VETO and/or C5 at the correct time for background events are removed, reducing background contamination in the analysis (see section 6.2).

The construction and design of the ZEUS detector is described elsewhere [47]. In the following sections, the detector components most relevant to this analysis are described in detail.

2.2.1 The microvertex detector

The MVD [59] was installed during the 2000-2002 HERA-II upgrade. Its major purpose is to improve track reconstruction and the determination of the primary and secondary vertices (see section 4.3.3). The MVD reconstructs tracks by means of 712 single-sided silicon strip detectors, sub-divided into two sections: the forward MVD (FMVD) and the barrel MVD (BMVD). A schematic overview of the MVD is shown in figure 2.8.

Figure 2.9 (left) shows the layout of the BMVD. The BMVD consists of 30 “ladders”, which support the silicon sensors along the 622 mm length of the MVD, ar-

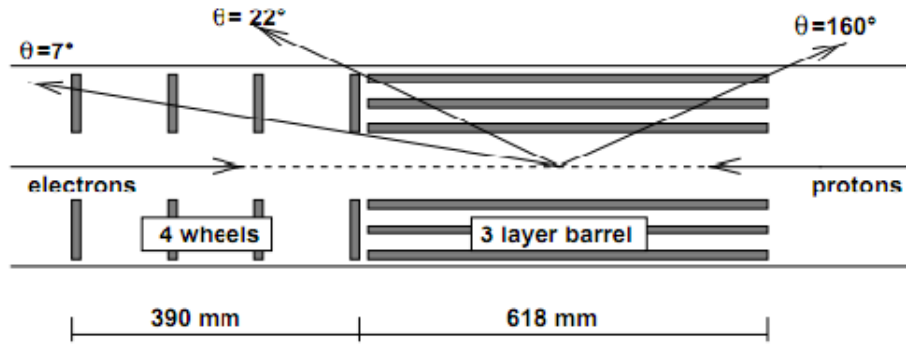


Figure 2.8: Schematic view of the MVD in the $y - z$ plane.

ranged in three concentric layers around the beampipe. The azimuthal coverage by three layers of silicon sensors is 75% with the remaining 25% being covered by two layers. This is due to a lack of space around the elliptical beampipe. Each ladder is constructed from five modules, which are composed of two half-modules. Each half-module is composed of two sensors, one providing $r - \phi$ and the other $z - \phi$ information. The half-modules are coupled together, as shown in figure 2.10, so that a track passing through a module may leave hits in both $r - \phi$ and $z - \phi$ sensors. The BMVD is centered on the nominal vertex position.

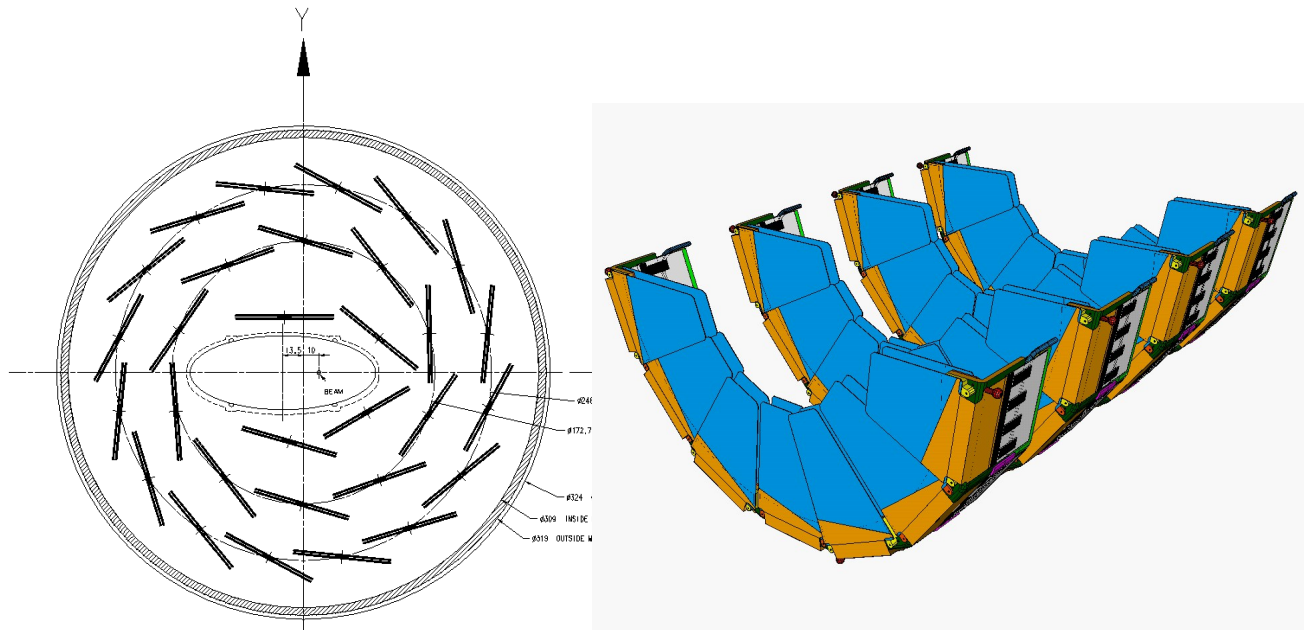


Figure 2.9: Left: cross-sectional ($x - y$) view of the BMVD. Right: isometric view of the FMVD.

The FMVD modules differ only in their geometry. The wedge-shaped modules

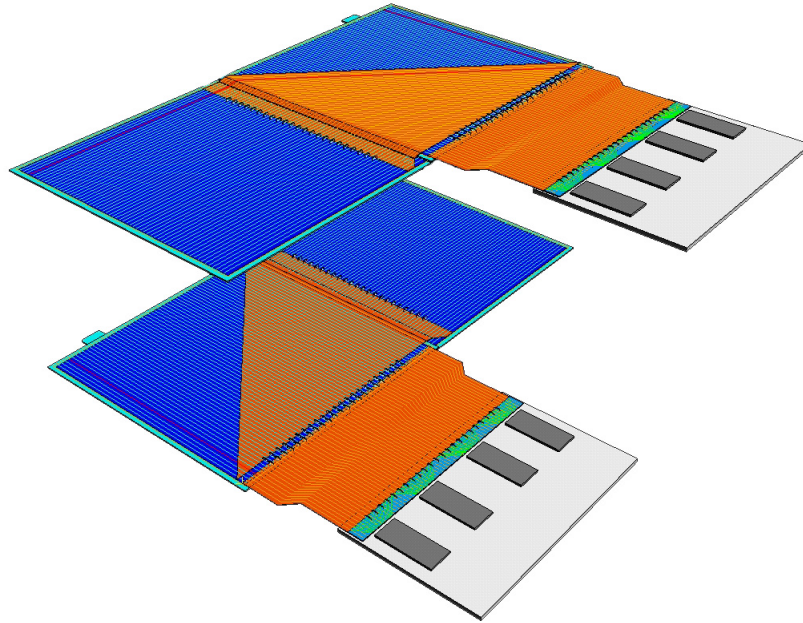


Figure 2.10: Two BMVD half-modules showing their orientation to construct a MVD module.

are arranged in four wheels, mounted perpendicular to the beampipe as shown in figure 2.9 (right).

The MVD has a polar angle coverage from 7° to 160° . Test beam measurements demonstrate that the barrel half-modules have a spatial resolution of $\approx 13 \mu\text{m}$. After the final alignment of the MVD with respect to the rest of the ZEUS detector the impact parameter (perpendicular distance from the track to the event vertex) resolution was determined to be $\approx 100 \mu\text{m}$.

2.2.2 The central tracking detector

The CTD [60] [61] is a cylindrical multicell drift chamber. The chamber operates in a 1.43 T magnetic field, created by the thin superconducting solenoid. The magnetic field allows the momenta of charged particles passing through the CTD to be measured. The polar angle coverage of the CTD ranges from 11.3° to 168.2° (see section 5.5 for further discussion of this angular region), and the azimuthal coverage is 100%. The CTD has a length of 204 cm and is placed almost symmetrically about the nominal interaction point ($z = 0.0$), extending from $z = -100$ cm to $z = 104$ cm. It has an inner radius of 18.2 cm and an outer radius of 79.4 cm. The CTD volume is

filled with a Ar/CO₂/C₂H₆ gas mixture, in the proportions 83/3/14, at 3 mbar above atmospheric pressure. The gas mixture is bubbled through ethanol and water (leaving trace amounts of both in the gas mixture) to prevent aging by whisker growth [62].

The CTD has nine “superlayers” and eight octants (see figure 2.11). Each superlayer is divided into “drift cells”, as shown in figure 2.12 each containing 8 tungsten sense wires of 30 μm diameter and 34 field shaping wires. Charged particles passing through the CTD ionize the gas mixture. The electrons drift to the sense wires, while the ions drift to the field wires. Close to the signal wires the number of electrons is amplified by avalanche multiplication. The large magnetic field inside the CTD changes the drift direction of electrons by the Lorentz angle, which is a function of the magnetic and electric fields and the gas composition. It is 45° for the CTD. The cells are tilted 45° with respect to the radial direction and the electric field is shaped so that the drift direction is perpendicular to the radial direction. This decreases the charge collection time to a maximum of 500 ns. The five odd numbered superlayers have their wires parallel to the z -axis while the wires of the even numbered superlayers are rotated by $\pm 5^\circ$ (called “stereo” wires). These stereo wires give information on the z position of particles passing through the CTD and thus their polar angle. Additional z position information can be obtained by measuring the time difference between the arrival of the signal at each end of the sense wires in superlayers 1, 3 and 5. This is referred to as the “ z -by-timing” system [63]. The z -by-timing system is fast enough to be used in the first level trigger as a method of reducing background (see section 2.2.8).

The CTD has a $x - y$ resolution of 200 μm on a single hit measurement based on measuring the drift time of the ionization electrons to the sense wire, and a z resolution of 2 mm (the z -by-timing measurement is much less precise at 3 cm). Once the event has been fully reconstructed (see sections 3.2.3 and 4.3.3), a fit to all tracks can be used to measure the primary vertex with a resolution of 0.1 cm in $x - y$ and 0.4 cm in z . The transverse momentum resolution for tracks passing through all nine

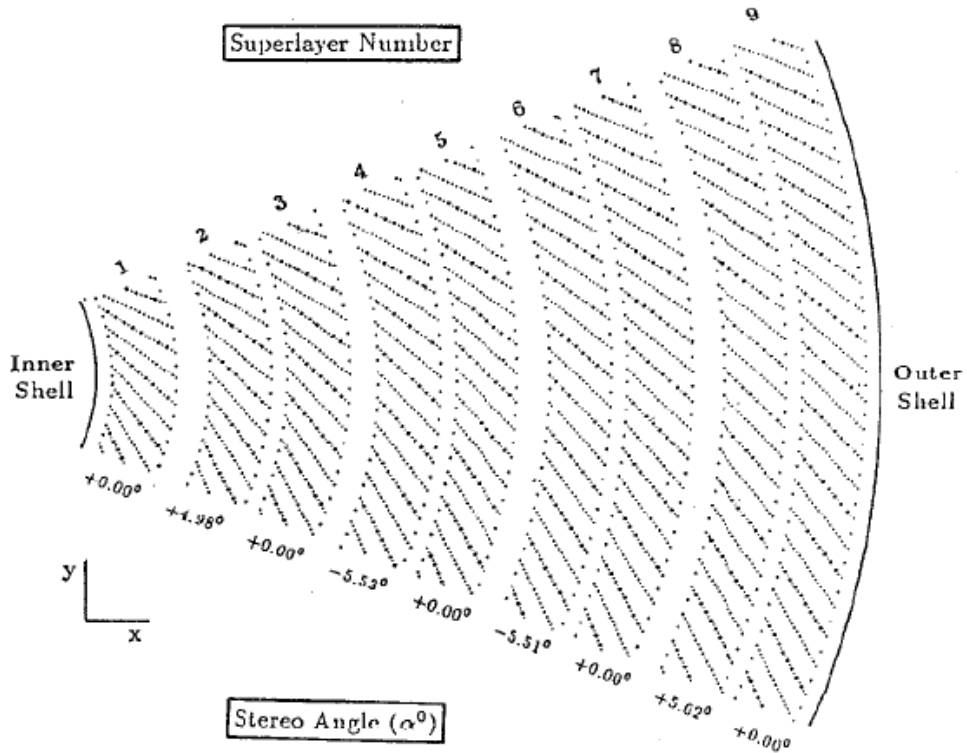


Figure 2.11: CTD octant with 9 superlayers.

superlayers is given by [64]:

$$\frac{\sigma_{P_T}}{P_T} = 0.0058P_T \oplus 0.0065 \oplus \frac{0.0014}{P_T} \quad (2.12)$$

in the interval $0.150 \text{ GeV}/c < P_T < 5 \text{ GeV}/c$, where P_T is expressed in GeV/c and \oplus indicates a quadratic sum. The first term comes from the single hit resolution, the second from scattering in the beampipe and inner wall of the CTD and the third term multiple scattering in the CTD.

2.2.3 The forward/rear tracking detector

The forward tracking detector (FDET) consists of the forward tracking detector (FTD) [65] and the straw-tube tracker (STT) [66]. The FDET is intended to complement the angular coverage of the CTD, allowing the reconstruction of tracks close to the beampipe that exit the CTD before crossing more than a couple of superlayers. The position of the FDET in relation to the other tracking detectors is shown in

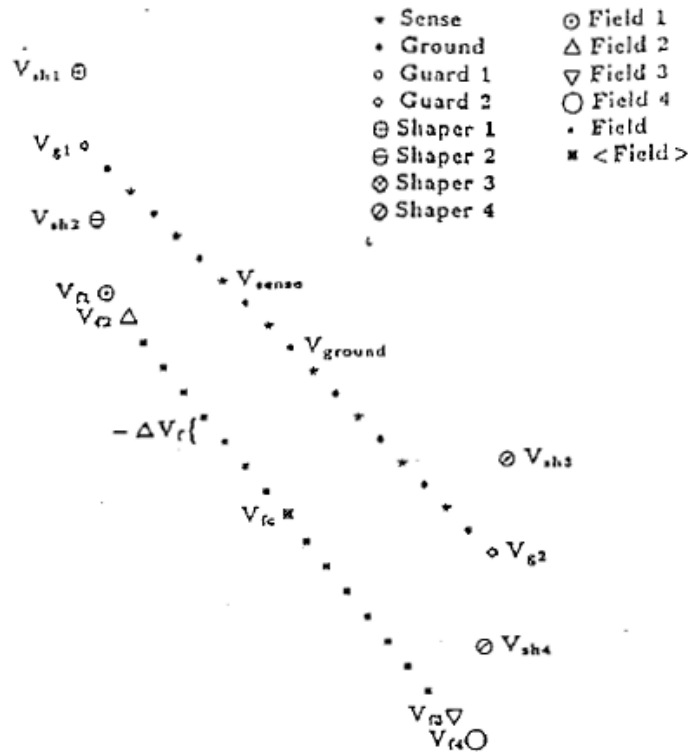


Figure 2.12: A close-up view of a single CTD cell showing the relative location of sense and field shaping wires.

figure 2.13.

The FTD consists of three planar drift chambers. The construction of each chamber (labelled FTD1, FTD2 and FTD3) is identical, circular with a hole in the center for the beampipe, except for the chamber radius which increases with z . Each drift chamber is divided into three readout planes, whose sense wires are rotated by 120° to each adjacent plane. The orientation of the readout planes is shown in figure 2.14. The gas used in the drift chambers consists of an Ar/C₂H₆ mixture. A single hit resolution of $\approx 250 \mu\text{m}$ is achieved.

The rear tracking detector (RTD) is located at the opposite end of the CTD. It consists of single planar drift chamber, constructed identically to the FTD chambers.

The STT was installed during the 2000-2002 HERA-II upgrade. It consists of two straw-tube drift chamber modules, situated between the FTD modules. The STT replaces the transition radiation detector (TRD), which was installed during HERA-I, in order to cope with the higher luminosity of HERA-II. The layout is shown in figure 2.15. Each STT module is composed of 24 sectors, grouped into four superlayers

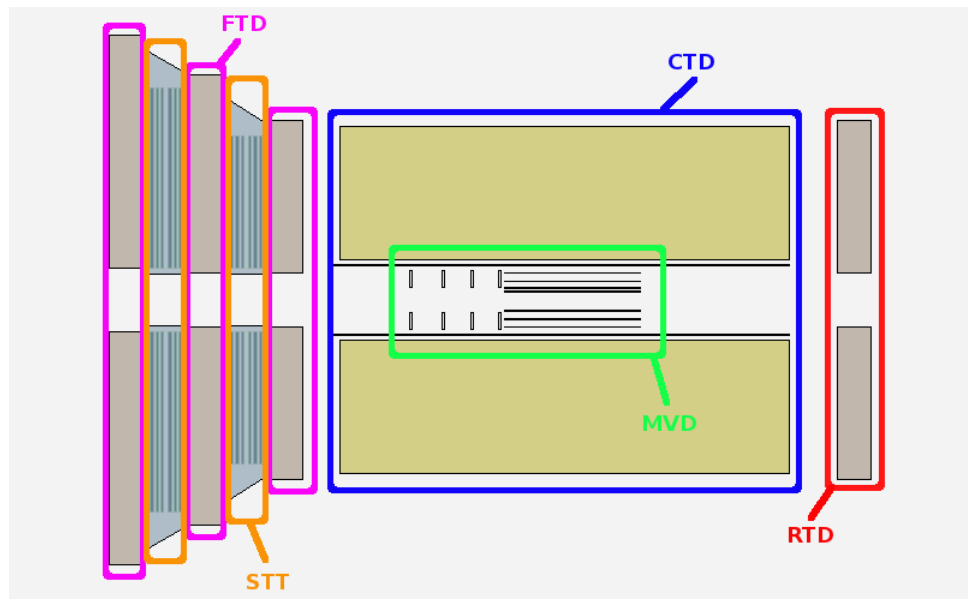


Figure 2.13: Schematic view of the tracking chambers showing the positions of the MVD (green), CTD (blue), FTD (purple), STT (orange) and RTD (red).

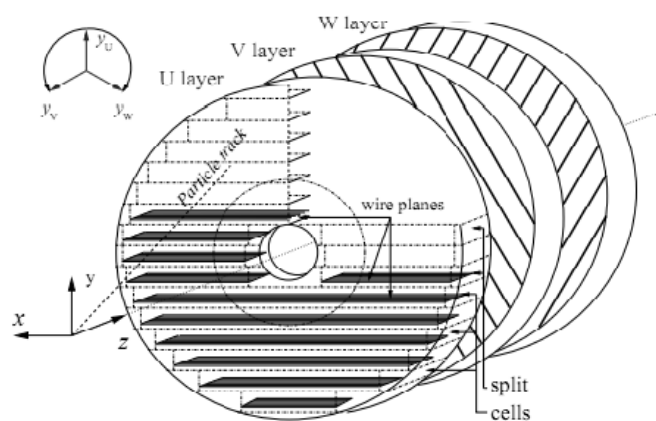


Figure 2.14: A schematic view of a FTD/RTD drift chamber showing the orientation of the sense wires in each plane.

containing six sectors each. Three sectors are installed at the same z location forming a layer. To create a superlayer, a second layer of 3 sectors rotated by 60° is combined with the first layer. The four superlayers are then installed, rotated again with respect to each other. The angular difference between superlayers 1 and 2 as well as 3 and 4 is 30° , while the angle between superlayers 2 and 3 is only 15° . Each sector consisted of three layers of “straws” with a diameter of 7.5 mm. Each straw acts as an independent drift chamber, constructed of a double layer of Kapton foil coated with thin layers of aluminum, carbon and polyethylene which acts as a cathode. A $50 \mu\text{m}$ Cu/Be wire strung down the middle of the straw serves as the anode. The straws are filled with an Ar/CO₂ gas mixture. STT hits, which have a resolution of $350 \mu\text{m}$ [67], are matched with hits from the FDT, CTD and the MVD to form a track.

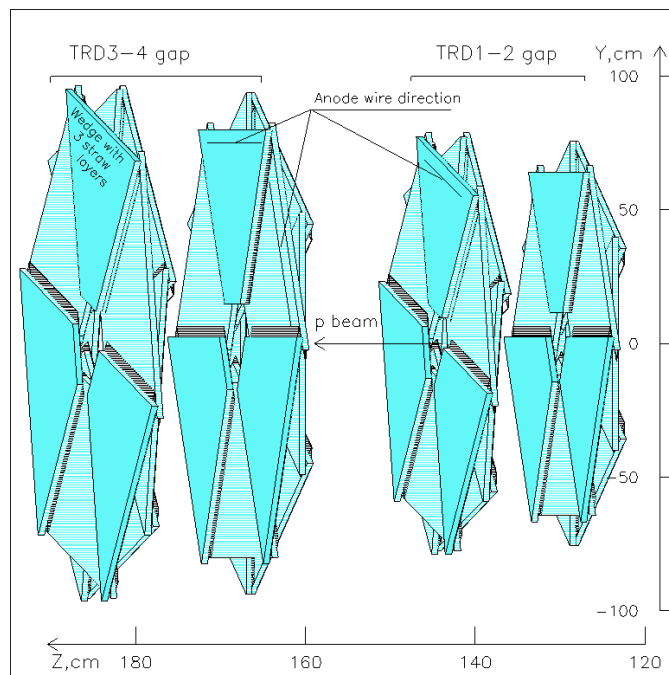


Figure 2.15: The 2 STT modules. Each module consisting of 4 superlayers.

2.2.4 The uranium-scintillator calorimeter

The ZEUS CAL is a high-resolution uranium-scintillator sampling calorimeter [68] [69]. The CAL is nearly hermetic, with a solid angle coverage of 99.7% of 4π . The calorimeter is composed of 3.3 mm depleted uranium (98.3% depleted U, 1.7% Nb) absorber

plates, clad in 0.2 mm of stainless steel, interleaved with 2.6 mm of plastic scintillator (SCSN-38).

When a high energy electron or photon enters the calorimeter it loses energy through the creation of secondary electrons, positrons and photons, which in turn create particles with lower energy. The processes that play a major role in the development of electromagnetic showers are:

- **bremsstrahlung:** An electron passing through the electric field of a nucleus in the absorber will lose energy by emitting photons. The energy loss is proportional to Z^2 , where Z is the atomic number (number of protons in the nucleus) of the nucleus.
- **Pair production:** Photons with an energy greater than twice the rest mass of the electron can create an electron-positron pair. The pair production cross-section is proportional to Z^2 .
- **Ionization:** A charged particle travelling through a medium will lose energy via ionization. The energy loss is proportional to Z .
- **Compton scattering:** Photons travelling through matter can lose energy by inelastically scattering from atomic electrons. The Compton scattering cross-section is proportional to Z .
- **Photoelectric effect:** An atomic electron completely absorbs the energy of the incoming photon and the atom becomes ionized. The cross-section is proportional to Z^4 - Z^5 .

The high-energy portion of the shower is dominated by pair production and bremsstrahlung, with interactions spaced roughly by the radiation length, X_0 , the mean distance over which the energy of a high-energy electron is reduced by a factor $1/e$ by bremsstrahlung. For uranium, $X_0 = 3.2$ mm. The energy in the CAL is sampled after absorber plates of $1X_0$ thickness in order to have frequent enough sampling for good electromagnetic energy resolution.

Hadronic showers are more complex than electromagnetic showers due to the wide variety of strong interaction processes, governed by a hadronic interaction length, λ , the mean distance that a hadron travels before an nuclear interaction occurs. For uranium, $\lambda = 105$ mm, which is much longer than the radiation length. A large number of physical processes and particles contribute to a hadronic shower:

- Charged particles such as π^\pm which lose their energy through ionization.
- Neutral particles such as π^0 which decay into photons. Additionally, excited nuclei lose their energy by emitting photons. These photons lose energy through purely electromagnetic processes.
- Neutrinos and low energy fragments of nuclei.
- Spallation and fission neutrons (which carry away some of the nuclear binding energy).

The hadronic shower can be divided into 3 categories: a hadronic part, an electromagnetic part and a part that escapes detection. The part of the hadronic shower that escapes the detector lowers the calorimeter energy response to hadronic showers.

The ratio of the calorimeter response to electromagnetic and hadronic showers, e/h , is in general greater than 1. A “compensating” calorimeter has an equal response to both electromagnetic and hadronic showers ($e/h = 1$). The choice of depleted uranium absorber plates and plastic scintillator allow part of this missing energy to be measured. The choice of the high- Z uranium gives a large neutron yield which is correlated with the amount of “lost” binding energy. Plastic scintillator is used due to the large number of hydrogen (protons) in its chemical makeup. The neutrons transfer their energy to the protons in the plastic scintillator through elastic scattering. The resulting scattered protons deposit their energy through ionization in the scintillator, boosting the response to the hadronic shower. The use of the high- Z uranium plates also reduces the electromagnetic component of the shower as low energy photons are converted preferentially in the absorber material (photoelectric effect). Tuning

the ratio of the thickness of the uranium and plastic scintillator plates allows the enhanced hadronic response and the reduced electromagnetic response result in an almost perfectly compensating calorimeter. Each layer of scintillator in the ZEUS CAL is 2.6 mm thick, giving $e/h = 1.0 \pm 0.03$ [70].

Fig. 2.16 shows a simplified view of the CAL and its relation to the solenoid and tracking detectors. Each calorimeter section (FCAL, BCAL and CAL) is divided longitudinally into electromagnetic (EMC) and hadronic (HAC) sections. In the FCAL and BCAL the HAC section is divided into two further sections, HAC1 and HAC2. The FCAL and BCAL are built in 23 vertically aligned modules. An isometric view of an FCAL module is shown in figure 2.17. Each module is divided into 20×20 cm² towers. The EMC section of each tower in the FCAL (RCAL) is composed of four (two) EMC sub-towers (see figure 2.17). The BCAL is constructed from 32 wedge shaped modules oriented along the z axis. The BCAL modules extend from an inner radius of 1232 mm to an outer radius of 2296 mm. The EMC section of each BCAL module is divided into 53 towers with a dimension of 49×233 mm² at the inner CAL face. The HAC section of each module in the BCAL is composed of 14 towers whose first layer measures 244×271 mm². The depths of the EMC sections of the FCAL, BCAL and RCAL correspond to 25.9, 22.7 and 25.9 radiation lengths, respectively, or approximately 1 interaction length for hadronic interactions. The total depths of the FCAL, BCAL and RCAL are 7.14λ , 5.1λ and 3.99λ , respectively.

Each scintillator layer in each tower or sub-tower (referred to as a cell, the smallest readout unit in the CAL) is read out on two sides of the module edge via wavelength shifters (WLS) which transport the shifted (blue to green) light to the photomultiplier tubes (PMT). The energy deposited in each cell is measured by the sum of both PMT signals. The imbalance between the PMT signals on each side is used to obtain a spatial resolution on the incident particle position of ≈ 3.4 cm/ \sqrt{E} for electrons and ≈ 6.6 cm/ \sqrt{E} for hadrons, as measured in a test beam. A large imbalance can also be used to detect a faulty PMT, which is described in more detail in section 4.3.1. The time difference (timing) between the nominal bunch crossing and the signal in

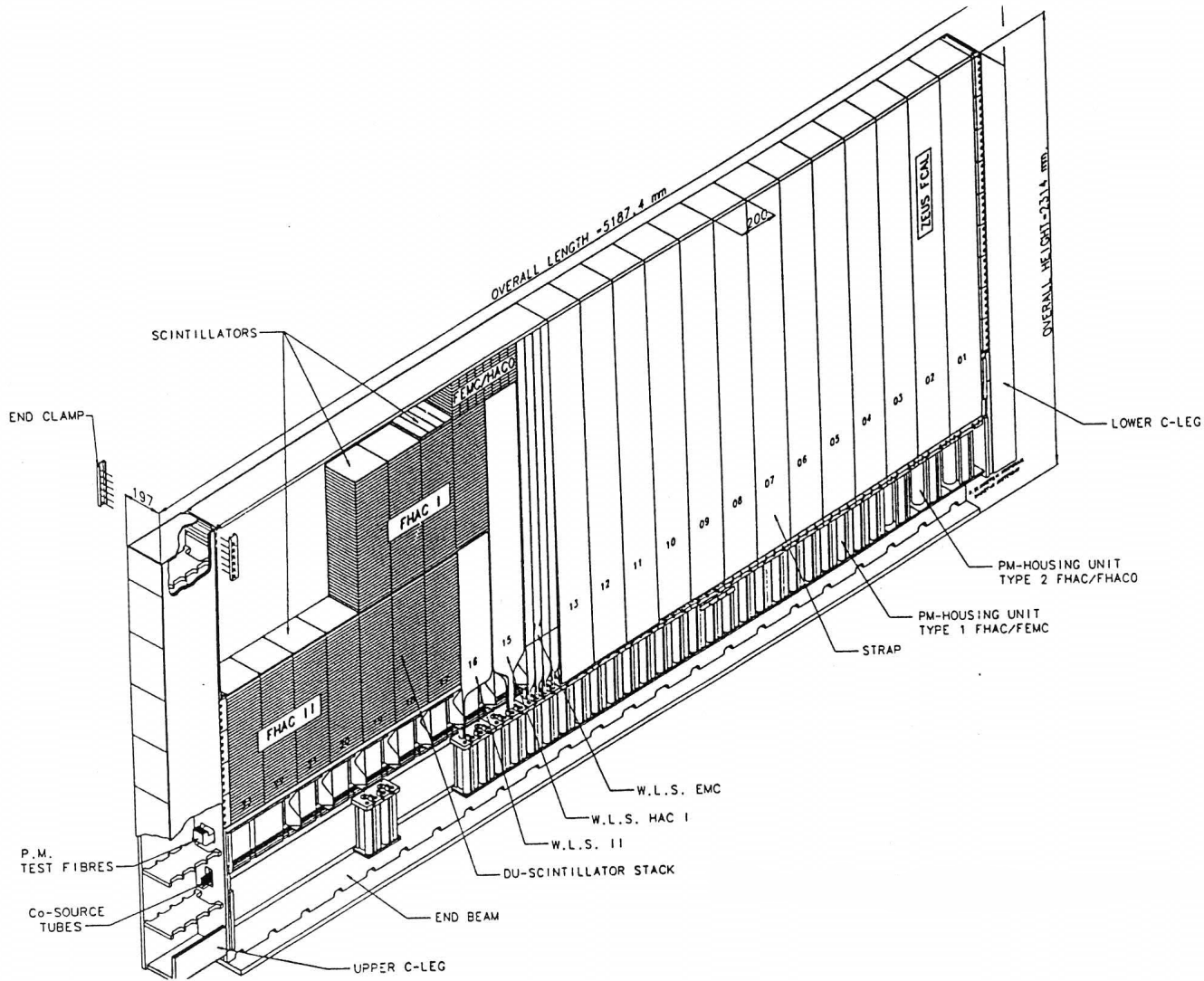


Figure 2.17: An isometric view of a FCAL module showing the towers and cells. The wavelength shifters and light-guides that transmit the light signal from each cell to the photomultipliers run parallel to the module sides.

without needing to disassemble the CAL, the diodes are grouped onto a “ski”, which is inserted into a gap from the top of each module. The RCAL HES is built in a similar manner to the FCAL HES, but consists of a single layer at a depth of $3 X_0$.

Due to the small size of the HES diodes, the HES provides a fine spacial resolution of ≈ 5 mm [72] for an electron with an energy greater than 5 GeV. Thus, when possible, the electron position is determined by the HES.

2.2.6 The presampler

Particles produced in beam collisions must travel through inactive material to reach the CAL. This leads to a decrease in the measured energy. To compensate for the energy loss, a presampler (PRES) [73] is installed on the CAL face. The PRES consists of a single layer of scintillating tiles, 5 mm thick with a dimension of 20 x 20 cm², which are read out by PMTs via wave-length shifting fibers embedded in the scintillator. The light output is proportional to the particle multiplicity. The correction is parameterised as a linear function of the energy deposited in the PRES, which was obtained using test-beam results. Test-beam results using electrons with an energy between 5 – 30 GeV with 0 – 4 X_0 of aluminium absorber positioned in front of the CAL give a precision of 2% on the electron energy measurement.

2.2.7 Luminosity measurement

The measurement of the luminosity is critical for the measurement of cross sections. At accelerators this is typically done using a well understood physics process. At ZEUS, the measurement relies on the detection of photons produced by bremsstrahlung, the “Bethe-Heitler” process $ep \rightarrow ep\gamma$ [74], since this cross-section is known to 0.5%.

The momentum transfer to the proton is negligible, thus the bremsstrahlung photon emerges at a very small angle with respect to the electron beam and the sum of the energies of the final state electron and photon are equal to the initial electron beam energy. The instantaneous luminosity is therefore obtained by counting photons in the luminosity detector (LUMI) using the equation:

$$L = R^{ep\gamma} / \sigma_{B-H}^{th}, \quad (2.13)$$

where $R^{ep\gamma}$ is the observed rate of Bethe-Heitler events and σ_{B-H}^{th} is the theoretical cross-section corrected for the detector acceptance. The chief background is bremsstrahlung photons from electron beam-gas interactions. To obtain $R^{ep\gamma}$ from

the total measured rate R^{total} , electron pilot bunches (see section 2.1.1) are used to estimate the background rate R^{bkg} . Thus, the observed rate is measured using the formula:

$$R^{e\gamma} = R^{total} - kR^{bkg}, \quad (2.14)$$

where k is the ratio of the electron current for colliding bunches to the current for electron pilot bunches.

There are two LUMI systems at ZEUS: the photon calorimeter (PCAL) [75] and the luminosity spectrometer (SPEC) [76]. The layout of the two LUMI systems is shown in figure 2.18. The photons and electrons follow the same path until the beam is

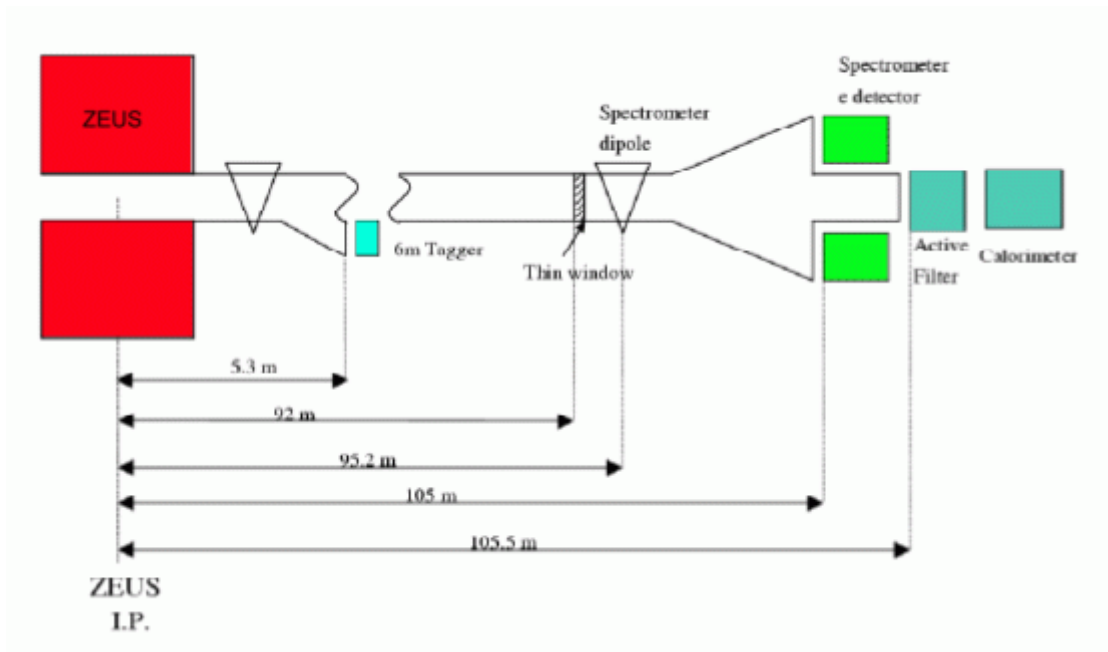


Figure 2.18: A schematic view of the ZEUS luminosity system. The bright green rectangles represent the location of the SPEC detector, while the turquoise rectangles represent the location of the PCAL detector.

deflected by a bending magnet. The photons then pass through a thin window where $\approx 9\%$ of them are converted into e^-e^+ pairs which are bent using a dipole magnet into the SPEC detector (located at $z = -105$ m). The photons which do not convert in the window are detected in the PCAL, a lead-scintillator calorimeter.

The PCAL operated continuously during the data taking period used in this anal-

ysis, while the SPEC was offline occasionally. The PCAL luminosity measurement is more precise than the SPEC measurement on a run-by-run basis, thus the PCAL luminosity is used. The systematic uncertainty for the SPEC luminosity is smaller than for the PCAL, resulting in a precision of 1.8% on the luminosity measurement. The PCAL luminosity is scaled by the average factor $\frac{\mathcal{L}_{SPEC}}{\mathcal{L}_{PCAL}} = 1.01$ to reflect the more precise total luminosity measurement from the SPEC.

2.2.8 The trigger

The ZEUS trigger system [77] is designed to reduce an input event rate of 10.42 MHz (due to the 96 ns spacing between bunches) to an output rate of physics events of 10 Hz (limited by processing speeds and storage). The total number of interactions is dominated not by ep events but by background sources such as beam-gas and cosmic muons. In order to select interesting ep physics events and reject background efficiently, a very fast and sophisticated trigger system is needed.

The trigger system adopted by ZEUS is divided into three levels, shown in a simplified diagram in figure 2.19. The design of the trigger allows more time for more complex reconstruction algorithms at upper levels, while keeping dead time (dead time is the time where the detector is unable to observe a bunch crossing) low.

First level trigger

The main aim of the first level trigger (FLT) is to reduce the event rate from ≈ 10 MHz to less than ≈ 1 kHz (which is the maximum input rate of the second level trigger (SLT)). It would be difficult, if not impossible, to design a trigger that could make a decision to accept or reject an event during the short, 96 ns, spacing between bunch crossings. To overcome this, the FLT is implemented in hardware, utilizing a pipeline system. Each step in the pipeline must be completed in 96 ns in order to accept the next event.

The FLT is divided into two systems: component FLTs and the global FLT (GFLT). Each detector component processes its own data in a pipeline with a max-

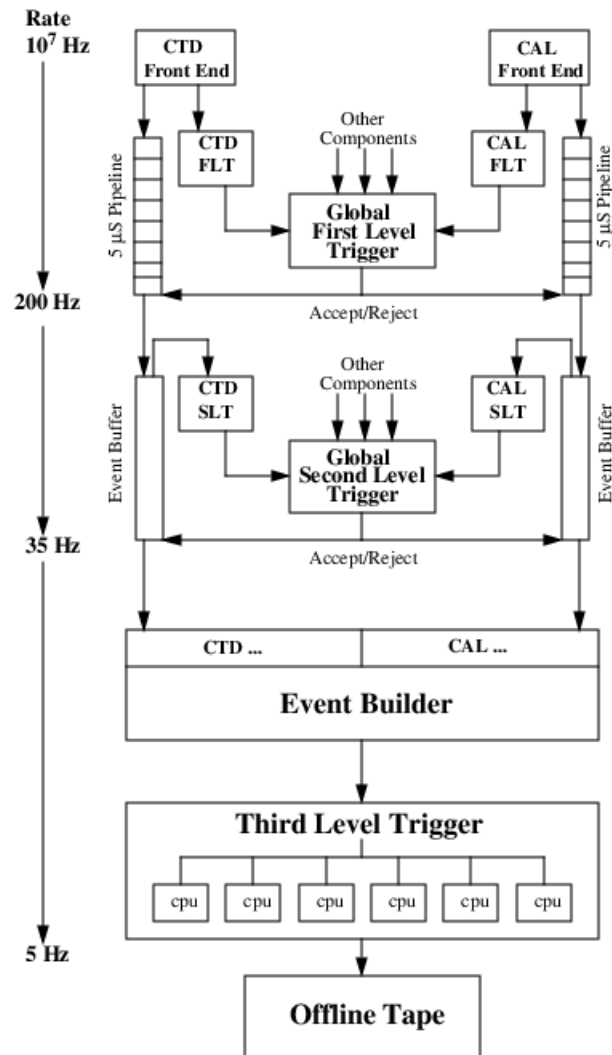


Figure 2.19: A schematic view of the ZEUS trigger system. The rates shown on the left hand side represent typical events rates for each trigger level.

imum depth of 26 bunch crossings ($2.5 \mu\text{s}$). The results of each component FLT are then sent to the GFLT which combines information from the component FLTs and makes a decision in 20 bunch crossings ($1.92 \mu\text{s}$). The information passed to the GFLT from the various component FLTs is typically very general and less precise than in the final reconstructed event. For instance, the calorimeter FLT (CFLT) provides total and regional energy sums, the CTD provides the number of tracks and the primary vertex (see section 4.3.3) obtained from the less precise z -by-timing method (see section 2.2.2). The component FLTs are fixed, whereas the GFLT is reprogrammable. This allows the FLT to be adapted to changing experimental conditions during the lifetime of the experiment. The event is taken by the GFLT if any of the 64 output bits, “slots”, are fired. If the GFLT accepts an event, the data is read from the stopped pipelines and is written to buffers. If the data is analogue, it is digitized first. During this time the ZEUS detector is dead for approximately $10 \mu\text{s}$. At the maximum GFLT rate, 1 kHz, the dead time is no larger than $1 \text{ kHz} \cdot 10 \mu\text{s} = 1\%$. The effect of the dead time on the luminosity measurement is automatically taken into account by disabling the luminosity system when the ZEUS detector trigger system is dead.

Second level trigger

The SLT is designed to reduce the 1 kHz input rate to a 100 Hz output rate. The design of the SLT is similar to the FLT, with component SLTs which feed into the global SLT (GSLT). The SLT is implemented using a transputer network, which allows fast and efficient parallel processing and easy re-programming.

The lower input rate compared to the FLT allows more time ($\approx 10 \text{ ms}$) to be spent reconstructing the event. At the SLT there is sufficient time to reconstruct tracks, obtain a better estimate of the primary vertex and reconstruct calorimeter clusters. Additionally, calorimeter timing information can now be used to reject background events. Once the GSLT receives the reconstructed values from each component SLT, the information is categorized by physics filters designed to accept certain physics

processes, such as high- Q^2 CC and NC DIS or photoproduction. If the event passes at least one of the physics filters, the information from each detector component is sent to another transputer network called the event builder (EVB). The EVB combines the information from all the detector components and sends the complete event to the third level trigger (TLT).

Third level trigger

The TLT consists of a computer farm, which runs slightly simplified versions of the offline reconstruction code on the events passed to it from the EVB. This allows sophisticated algorithms, such as electron finders and muon finders, to be used, and the kinematic variables Q^2 , x and y can be calculated. As the TLT runs on computers, its physics filters are software based and fully reconfigurable to meet the demands of the ZEUS physics groups or reduce rates when background conditions are high. Events accepted by the TLT, are written to magnetic tape at a rate of ≈ 10 Hz. These events can then be processed offline by the most up-to-date reconstruction and calibration software.

Chapter 3

Data, Monte Carlo and Analysis Environment

3.1 Data sample

The ZEUS e^+p data used in this analysis was taken in 2006/2007 at a proton beam energy of 920 GeV and positron beam energy of 27.56 GeV. This is the last HERA data period taken at $\sqrt{s} = 318$ GeV. The data were taken with both right (RH) and left-handed (LH) beams of polarised positrons. The average polarisation of the positron beam, P_e , was determined using the LPOL and TPOL. The runs considered for the luminosity and polarisation calculations must pass data quality cuts described in section 6.4. The total data set has a luminosity of 135.5 pb^{-1} , 78.8 pb^{-1} taken with right-handed polarisation and 56.7 pb^{-1} taken with left-handed polarisation. The LH run period has been further sub-divided into a LH1 and LH2 run period for reasons described in section 5.2.1. A summary of the luminosity and luminosity-weighted polarisation¹ for each sub-period is shown in table 3.1.

¹The luminosity-weighted polarisation is calculated as follows: $P_e = \frac{\sum P_i \times \mathcal{L}_i}{\sum \mathcal{L}_i}$ where P_i and \mathcal{L}_i are the polarisation and luminosity for run i , where i denotes the ZEUS run number.

Period	$\mathcal{L}(pb^{-1})$	P_e
ALL	135.5	+3.50
RH	78.80	+31.8
LH	56.68	-35.9
LH1	33.18	-35.5
LH2	23.52	-36.5

Table 3.1: Summary of the luminosity and polarisation for each run period.

3.2 Monte Carlo and simulation

The modern high-energy physics experiment is both large and complex. This complexity is also seen in the physics events themselves, where many possible final states may be produced. These factors make analytic calculation of the detector acceptance and resolution unfeasible. Thus, Monte Carlo (MC) techniques are used to simulate both the physics processes and the detector response.

Physics processes are simulated by computer programs called MC generators. These programs implement theoretical models of the physical interactions. Approximations are often employed to minimize processing time, which can be considerable. Additionally, the theoretical calculations cannot be done to all orders of perturbation theory. For each event, the output of the MC generator consists of a list of final-state particles and their four-momenta. Another program then simulates the interaction of these particles with the detector and inactive material, in order to study the detector acceptance and resolution.

3.2.1 NC MC sample

The NC DIS events are generated using the DJANGO 1.6 [80] program, which provides an interface between the HERACLES 4.6.1 [81] program and the ARIADNE 4.10 [83] or LEPTO 6.5 [84] program. Final hadronisation is done using the Lund string model implemented in JETSET 7.4 [85]. HERACLES simulates the first order electroweak corrections. ARIADNE or LEPTO is used to simulate the QCD cascade. Each of these programs provides a different element needed for a complete description

of NC DIS.

To simulate the NC DIS events the first step is to determine the leading-order process shown in figure 3.1, $V^*q \rightarrow q'$, where V^* is a virtual gauge boson, q is the struck quark in the proton and q' is the scattered quark. The momentum and flavour of the quark q is extracted using the CTEQ5D PDF sets. Figure 3.1 (b – d) show the Feynman diagrams that correspond to corrections at order α_s .

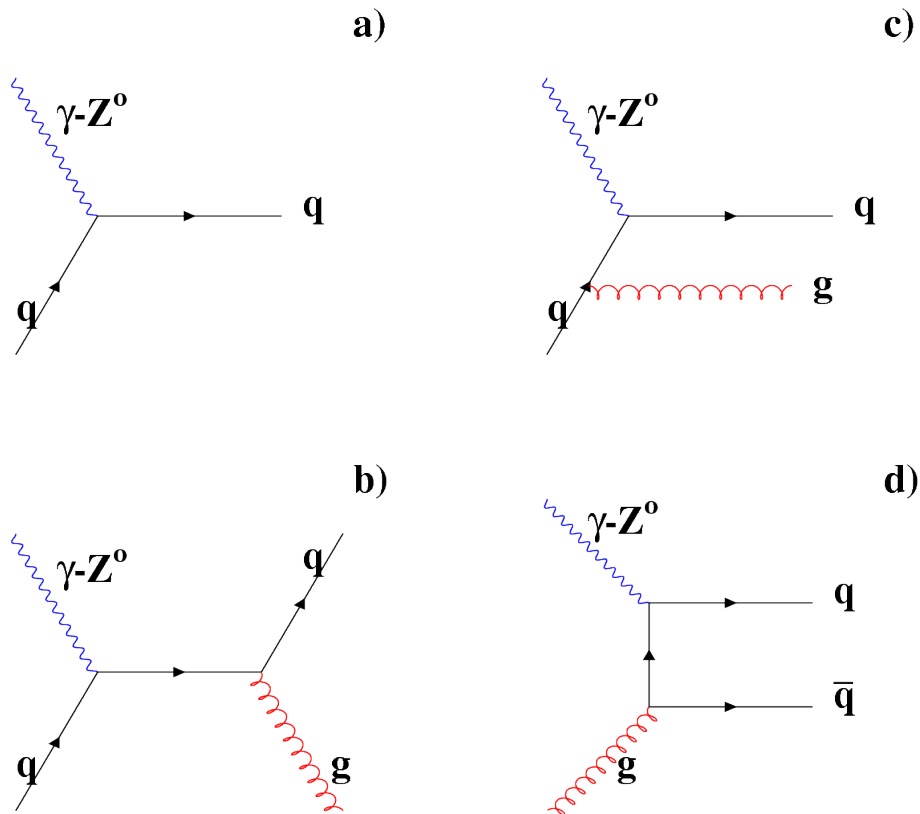


Figure 3.1: Feynman diagrams for a) the leading order process b) and c) gluon emission d) the boson gluon fusion (BGF) process.

Once the struck quark has been determined, the second step is to simulate the QCD cascade with ARIADNE or LEPTO. The interacting quarks cannot be treated as free, as they are connected by the colour field to the rest of the proton. LEPTO implements the Matrix Element and Parton Shower (MEPS) approach to the QCD cascade. The first-order QCD processes $V^*q \rightarrow gq'$ (QEDC) and $V^*g \rightarrow q\bar{q}$ are incorporated into the matrix element. The higher order QCD processes $q \rightarrow qg$,

$g \rightarrow q\bar{q}$ and $g \rightarrow gg$ are taken into account using the DGLAP equations. ARIADNE takes another approach, the Colour-Dipole Model (CDM), in which $q\bar{q}$ pairs are seen as colour dipoles. The emission of a gluon by one of the quarks is treated as radiation emitted from the colour dipole. As the emitted gluon itself has colour the resulting $qg\bar{q}$ combination can be treated as two separate dipoles: qg and $g\bar{q}$. The emission of a second gluon is treated as radiation emitted from the qg and $g\bar{q}$ dipoles. The BGF process is not described in the CDM and is simulated by having the struck quark dipole emit its anti-partner according to the BGF matrix element.

The output of either LEPTO or ARIADNE is the same, a set of coloured quarks and gluons. One final step is needed, known as fragmentation, to transform the set of coloured quarks and gluons into colourless hadrons that are detected in the experiment. This is done by JETSET 7.410, which implements the Lund string model. In this model the partons are connected by strings which approximate the colour force field. As the partons move apart, the potential energy of the string increases until enough energy exists to break the string, forming a new $q\bar{q}$ pair. This process stops once all the available energy is contained in the mass and energy of hadrons.

ARIADNE has been used to simulate the QCD cascade as it has been found to show good agreement with the data. MC events generated with LEPTO is used as a systematic check on the QCD cascade (see section 7.3).

The corrections to the lepton vertex, $eV^* \rightarrow e'$, where e is the incoming electron and e' is the scattered electron, are done with the HERACLES program. The leading-order electroweak corrections included are initial and final-state radiation (ISR and FSR), self-energy corrections and propagator corrections. These processes are shown in figure 3.2. ISR photons are emitted collinearly with the incoming electron beam and are lost down the beampipe, which effectively reduces the centre-of-mass energy. FSR photons can lower the energy of the detected electron, but these photons are often included in the electron calorimeter cluster and their energy is effectively added to the electron energy.

In addition to the NC DIS MC described above there are two other event types

that must be included for a complete description of NC DIS: Diffractive NC, and QED Compton (QEDC).

Diffractive NC events are characterised by having no activity between the jet and the proton remnant. The difference between NC DIS and Diffractive NC can be most readily seen in the maximum pseudorapidity distribution, η_{max} , given by:

$$\eta_{max} = -\ln\left(\tan\frac{\theta_c}{2}\right), \quad (3.1)$$

where θ_c is the most forward energy cluster with an energy over 400 MeV. Diffractive events typically have a lower value of η_{max} (see figure 3.3) compared to NC DIS events. RAPGAP 2.08/06 [86] is used to generate diffractive NC MC instead of DJANGO. The fraction of diffractive events was found by scaling the Diffractive MC η_{max} distribution to best describe the data.

The QEDC process is very similar to the ISR and FSR diagrams (see figure 3.4), the major difference being the off-shell intermediate electron between the two photon vertices. The QEDC process itself can be divided into elastic and inelastic QEDC, where the proton remains intact in elastic QEDC. Kinematic reconstruction of QEDC events is challenging; the emitted photon is not collinear with either the initial or final-state electron and is considered part of the hadronic final state. This can cause migration of the measured kinematic variables. Inelastic QEDC is correctly modelled in the MC, and these migrations are not a problem [78]. Elastic QEDC events are not included in the MC and must be removed by the event selection in section 6.5.4.

Multiple NC DIS MC samples are used in this analysis, each generated at a different lower Q^2 limit. This was done to decrease the size of the MC samples that must be generated, while ensuring high statistics in the high- Q^2 regions. These samples are described in table 3.2. Note that the luminosity of even the lowest Q^2 sample is over seven times larger than the data sample, thus uncertainty due to MC statistics can be neglected.

These samples are luminosity-weighted to allow direct comparison with data. If

Q_{min}^2	Nr. events	$\sigma(pb)$	$\mathcal{L}(pb^{-1})$
100	7999056	8111.06	986.191
400	1999958	1168.43	1711.663
1250	999993	198.12	5047.4
2500	500000	59.2041	8445.36
5000	500000	14.9364	33475.3
10000	260000	2.82644	91988.5
20000	99995	0.317446	304363
30000	60000	0.056556	060895
40000	20000	0.011496	1739735
50000	20000	0.0022865	8746993

Table 3.2: Summary of the NC DIS MC.

only one NC DIS MC sample were used, then the weight factor for each event, w , would be given by $w = \frac{\mathcal{L}_{data}}{\mathcal{L}_{MC}}$ where $\mathcal{L}_{MC} = \frac{N_{event}}{\sigma_{sample}}$. Due to the MC being generated at multiple minimum Q^2 limits, so that the samples partially overlap in Q^2 , the expression used to calculate the weight, w_i , for an event $Q_{event}^2 > Q_i^2$ is as follows:

$$w_i = \frac{\mathcal{L}_{data}}{\sum_{j \leq i} \mathcal{L}_{MC,j}} \quad (3.2)$$

where i denotes the sample with the highest minimum Q^2 such that $Q_i^2 < Q_{event}^2$.

3.2.2 Background Monte Carlo

The chief source of background in this high- Q^2 NC DIS analysis is that of misidentified photoproduction (PHP) events, shown in figure 3.5. Photoproduction events are characterised by a quasi-real photon ($Q^2 \approx 0$) being exchanged between the electron and the proton. In this case the electron undergoes very little momentum change and is therefore practically undeflected and is lost down the rear beamhole. PHP can be misidentified as NC DIS if part of the hadronic final state is interpreted as an electron. PHP background must be rejected by offline selection cuts described in section 6.5.

The PHP MC was generated as both “direct” and “resolved” samples. In the former process the photon interacts directly with the proton, while in the latter it is “resolved” into a $q\bar{q}$ pair which interacts with the proton. Both of these processes are

	Q_{max}^2	Nr. events	$\sigma(pb)$	$\mathcal{L}(pb^{-1}) \cdot 1.56$
direct	4	530000	2830	187.28
resolved	4	630000	11900	52.94

Table 3.3: Summary of the PHP MC.

simulated using HERWIG 5.9 [87] with kinematic cuts of $E_T > 30$ GeV or $P_T > 6$ GeV, where E_T and P_T are the transverse energy and momentum respectively. These restrictions are to avoid the need to produce large samples due to the large PHP cross-section.

The samples are summarized in table 3.3. The integrated luminosities shown are scaled further by a factor of 1.56, which was determined by a previous study [111]. The scaling factor was determined by selecting a PHP enriched sample from the 2006/2007 e^+p data and scaling the PHP MC so that it agrees with the PHP enriched sample.

3.2.3 Event reconstruction and software environment

The data and MC events follow the analysis framework shown in figure 3.6. The data events come from the tapes recorded by the TLT. The MC events are generated by AMADEUS, which provides an interface between the individual MC event generators and the ZEUS analysis framework, and simulated in the detector by MOZART [88] which is based on the GEANT 3.21 package [89]. The output of MOZART is passed to the CZAR program (also called ZGANA) which simulates the trigger logic used for the data.

The events passed by the TLT for both data and MC are processed by the ZEPHYR program, which first does calibration and applies corrections (such as dead cells, see section 4.3.1) and then performs full event reconstruction. The reconstructed events are categorised by a series of physics filters and written to data summary tapes (DST). Each of these physics filters corresponds to a DST-bit and these are used to select a subset of the total dataset for analysis.

The offline analysis of data and MC is done with a common set of tools incorporated in ORANGE (overlying routine for analysis of ntuple generation) [90]. OR-

ANGE is underpinned by a set of routines called EAZE (“effortless” analysis of ZEUS results), which aid in the retrieval of data and reconstruction of physical objects such as electrons and muons. The output of ORANGE is a ntuple which is analysed using ROOT (The ntuples may also be analysed using a number of other programs and computer languages) [91]. The ORANGE ntuples used in this analysis were part of the “common ntuple project” and are referred to as “common ntuples”. The aim of this project is to create a set of ORANGE ntuples with the broadest possible scope, suitable for use in a wide range of physics analyses, and for data preservation.

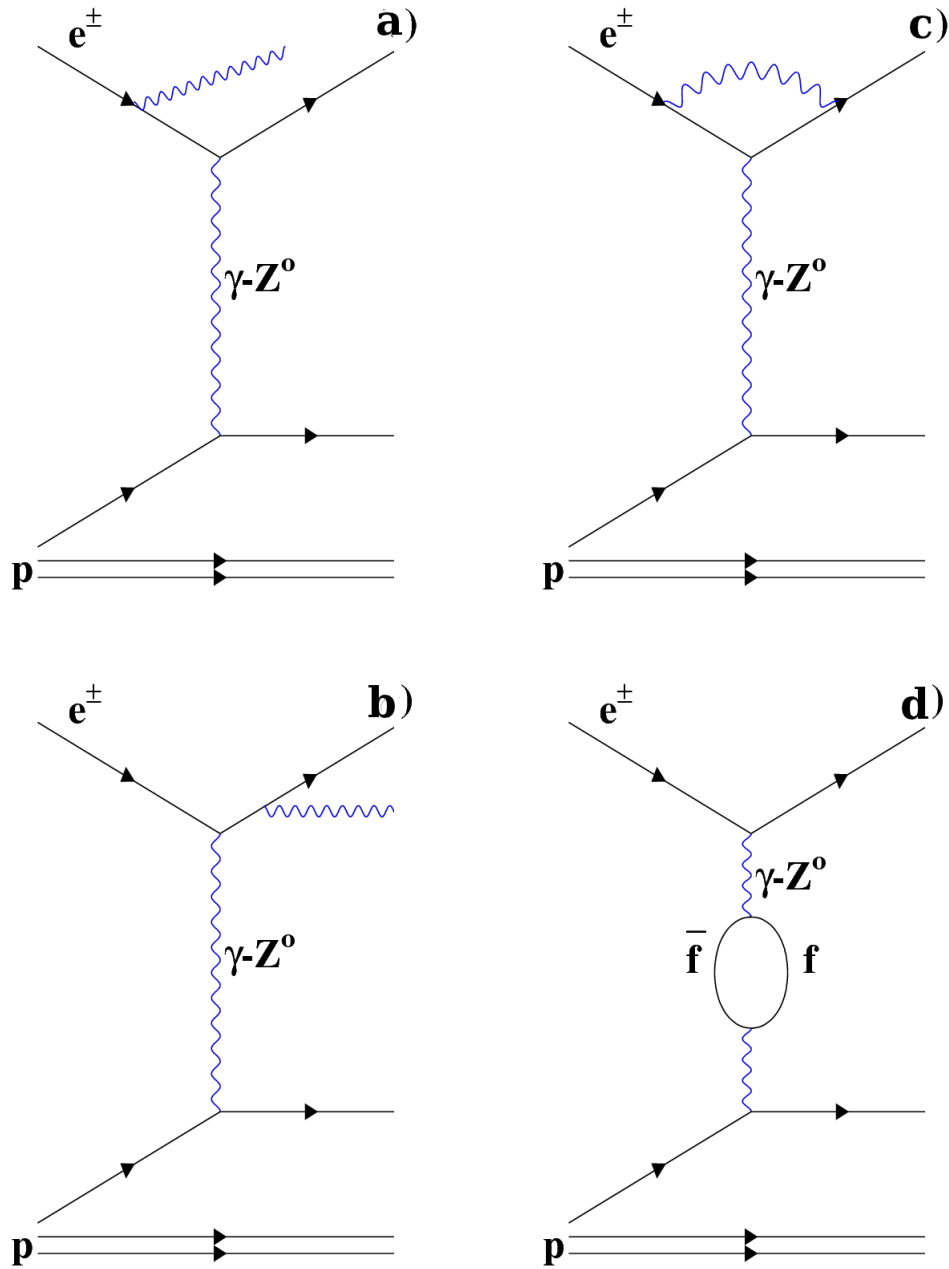


Figure 3.2: Feynman diagrams for a) ISR b) FSR c) vertex correction d) self-energy.

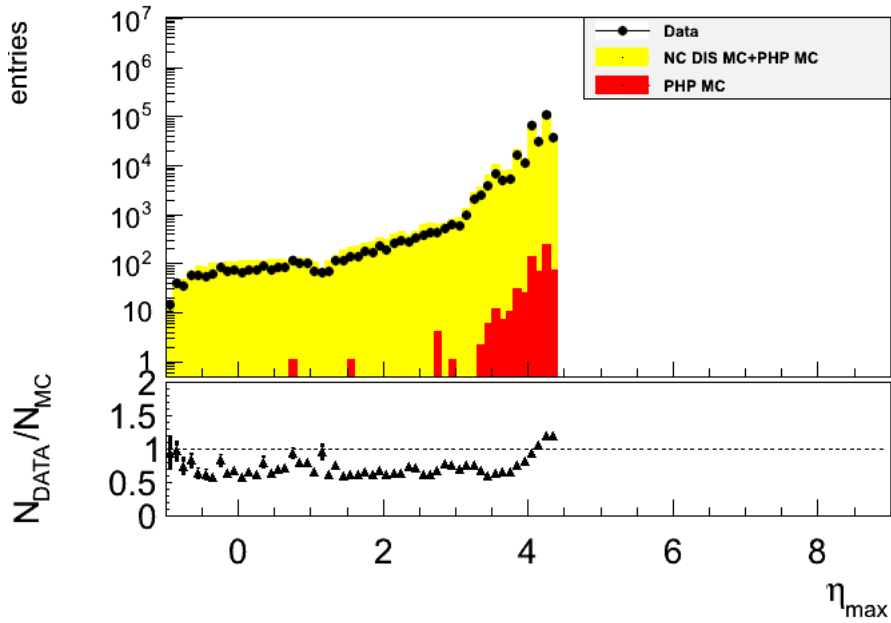


Figure 3.3: The η_{max} distribution found in data and MC. The long tail at low values of η_{max} is due to diffractive events.

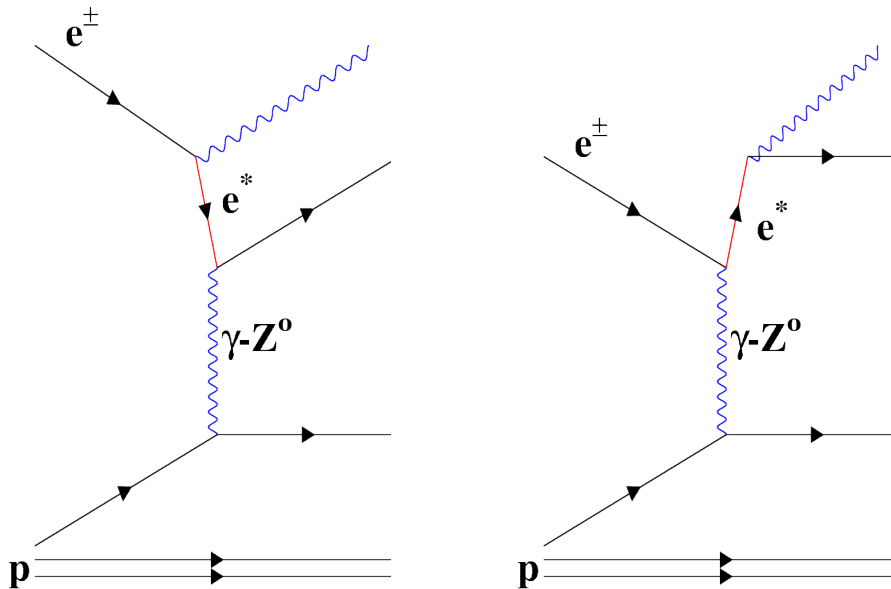


Figure 3.4: Feynman diagrams for the QEDC Compton process.

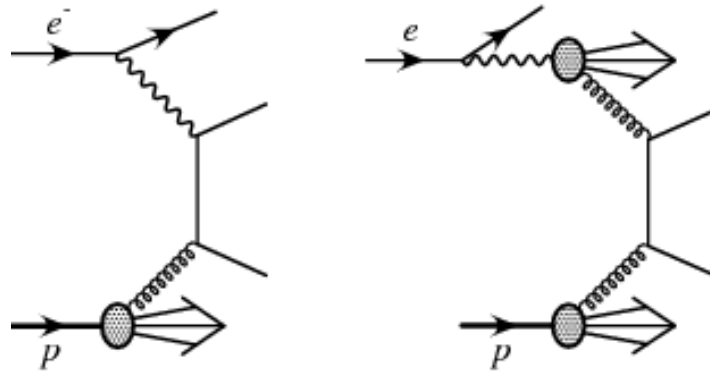


Figure 3.5: Feynman diagrams representing direct (left) and resolved (right) photo-production.

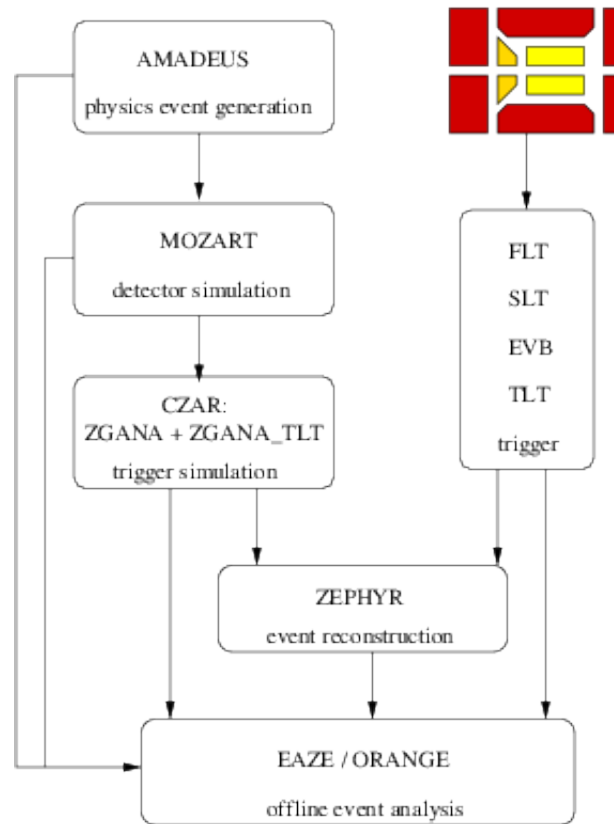


Figure 3.6: The ZEUS software framework.

Chapter 4

Event Reconstruction

4.1 Event characteristics

4.1.1 Event topology

The most significant signature of ep NC DIS events is a high energy and isolated scattered electron in the detector. The transverse momentum of this electron is balanced by the hadronic system that is produced from the colour flow between the struck quark and the proton remnant. These features can be seen in figure 6.1 in section 6.1, which shows a typical NC event. A more detailed discussion of the event topology as x and Q^2 vary is presented below. At low Q^2 the electron undergoes very little momentum change and is deflected relatively little. This results in an electron with an energy close to the incoming electron beam located in the RCAL. With increasing values of Q^2 the scattering angle increases, with the electron frequently being detected in the BCAL and FCAL. At high Q^2 and high x the scattered electron energy is large, and the hadronic system is produced in the forward direction with high energy due to the struck quark carrying a large fraction of the incoming proton momentum. At low x the struck quark is scattered by a large angle and is found in the rear direction with a small energy. This is described graphically in figure 4.1. The proton remnant carries a $(1 - x)$ fraction of the original proton momentum, but this is lost down the forward beampipe, since the proton remnant carries very small transverse momentum.

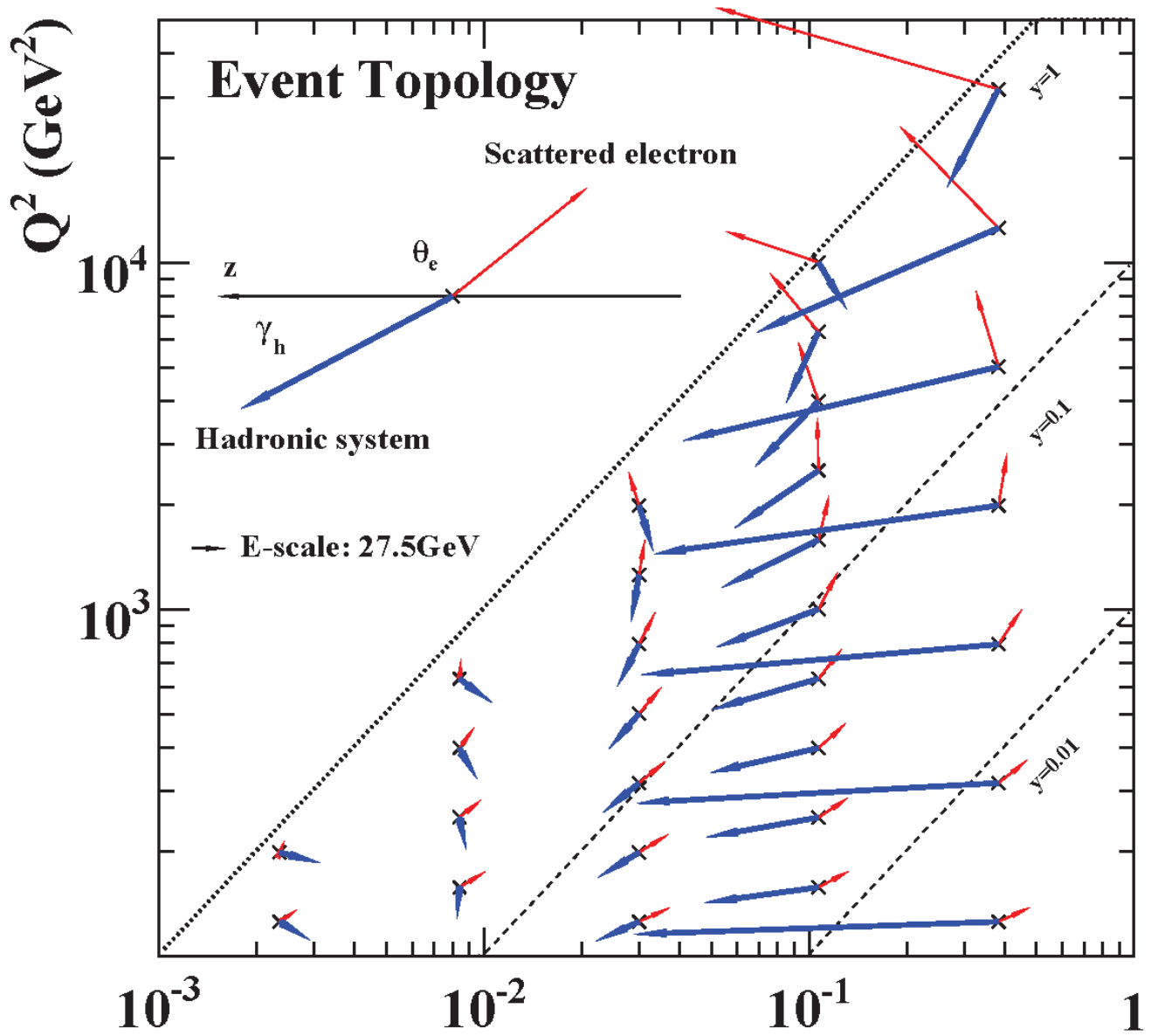


Figure 4.1: Event topology of NC DIS events for different Q^2 and x values. The thin red arrows point in the direction of the scattered electron and the thick blue arrow corresponds to the angle of the scattered quark. The arrow length is proportional to the energy.

4.1.2 Event observables

The ZEUS detector is nearly hermetic with good resolution, and thus both the scattered electron and hadronic final state can be measured over a wide kinematic range. The energy of the scattered electron, E'_e , is measured in the CAL and its angle, θ_e , is determined from the position of the electron energy deposit and the interaction vertex. All other energy deposits are assigned to the hadronic system, which includes one or more jets and the proton remnant. In order to reconstruct the energy, E_h , and the angle, γ_h , of the hadronic system, the influence of the fragmentation process and the loss of particles down the beam hole must be minimised. This can be done by using the hadronic transverse momentum, $p_{t,h}$, and the difference between the energy and the longitudinal momentum of the hadronic final state, δ_h , which are defined as:

$$p_{t,h}^2 = p_{x,h}^2 + p_{y,h}^2 = \left(\sum_i E_i \sin\theta_i \cos\phi_i \right)^2 + \left(\sum_i E_i \sin\theta_i \sin\phi_i \right)^2 \quad (4.1)$$

$$\delta_h = (E - p_z)_h = \sum_i (E_i - p_{z,i}), \quad (4.2)$$

where the sum runs over all CAL deposits except those of the scattered electron. These quantities are insensitive to the composition of the final state, only depending on the energy and angles of the CAL deposits, and to the loss of particles down the beampipe because these particles have small transverse momentum and their δ_h is almost zero.

In the QPM the quantities γ_h and E_h correspond to the scattering angle and the energy of the struck quark and are given by:

$$\cos\gamma_h = \frac{p_{t,h}^2 - \delta_h^2}{p_{t,h}^2 + \delta_h^2} \quad (4.3)$$

$$E_h = \frac{p_{t,h}}{\sin\gamma_h}. \quad (4.4)$$

It should be noted that at very low y the hadronic system is very forward, therefore the measurements of $p_{t,h}$ and δ_h , and hence γ_h become imprecise.

4.2 Reconstruction of kinematic variables

In section 1.3.2 the Lorentz-invariant variables Q^2 , x and y are shown to be related by $Q^2 = sxy$; thus the reconstruction of Q^2 , x and y require only two variables. The previous section described four measurable quantities E'_e , θ_e , E_h and γ_h ; therefore, the measurement of the kinematic variables are over-constrained and several reconstruction methods are possible.

In the ZEUS reference frame, ignoring particle masses, the four momenta of the incoming and outgoing electron, k and k' , and the hadronic system, p and p' can be written as:

$$k = \begin{pmatrix} E_e \\ 0 \\ 0 \\ -E_e \end{pmatrix}, k' = \begin{pmatrix} E'_e \\ E'_e \sin \theta_e \cos \phi_e \\ E'_e \sin \theta_e \sin \phi_e \\ E'_e \cos \theta_e \end{pmatrix}, p = \begin{pmatrix} E_p \\ 0 \\ 0 \\ E_p \end{pmatrix}, p' = \begin{pmatrix} E_h \\ E_h \sin \gamma_h \cos \phi_h \\ E_h \sin \gamma_h \sin \phi_h \\ E_h \cos \gamma_h \end{pmatrix} = \begin{pmatrix} E_h \\ p_{x,h} \\ p_{y,h} \\ p_{z,h} \end{pmatrix}, \quad (4.5)$$

where E_e and E_p are the initial energies of the incoming electron and proton respectively. E'_e , θ_e and ϕ_e are the energy, polar and azimuthal angles of the scattered electron, and E_h , γ_h and ϕ_h are the those of the struck quark.

Using the equations 4.5 along with energy, longitudinal momentum and transverse momentum conservation, the kinematic variables Q^2 , x , y can be reconstructed using any two of the variables E'_e , θ_e , E_h and γ_h .

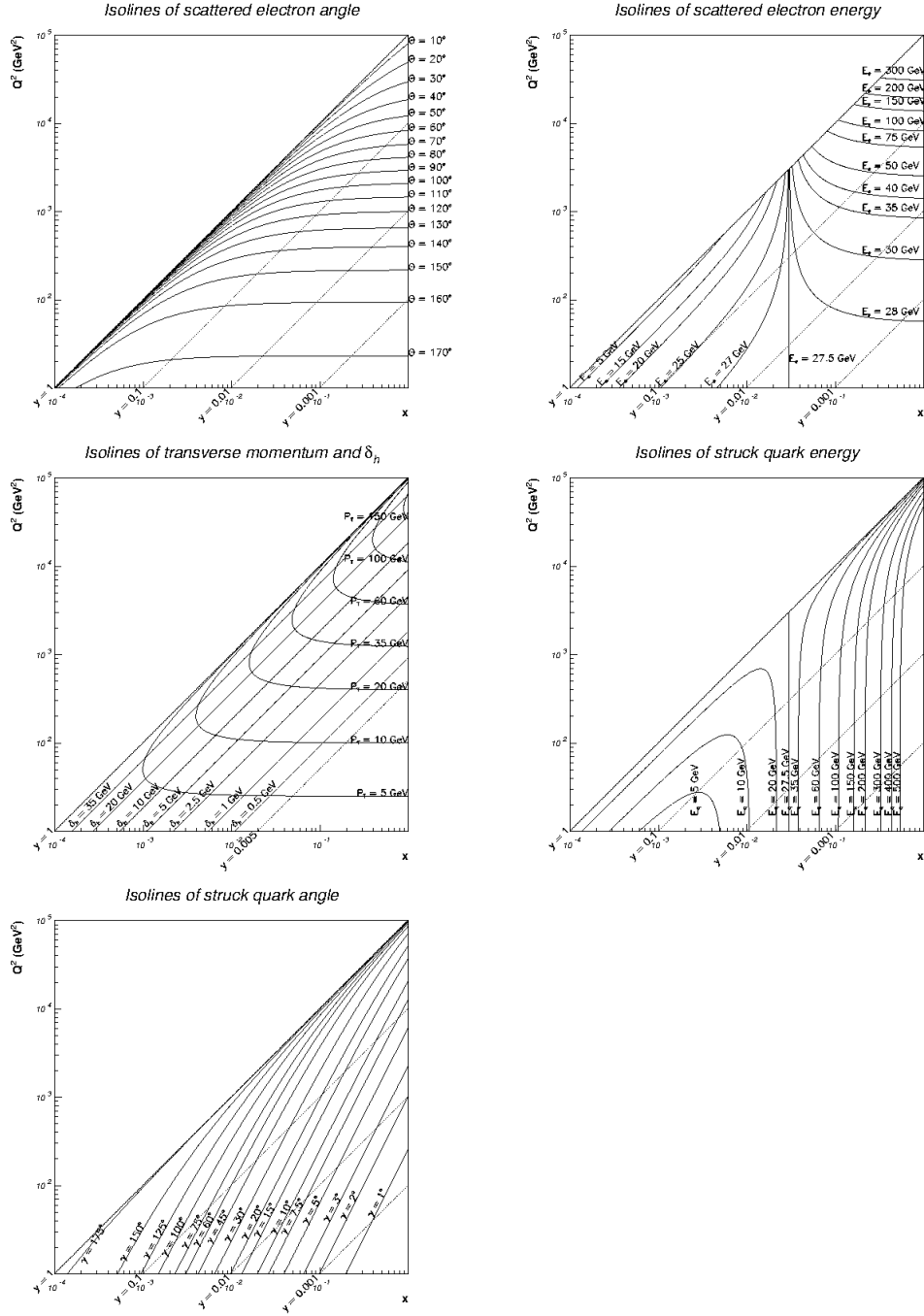


Figure 4.2: Isolines of observable quantities in the $x - Q^2$ plane: θ_e (top left), E'_e (top right), $p_{t,h}$ and δ_h (middle left), E_h (middle right) and γ_h (bottom left).

Figure 4.2 shows isolines of observable quantities, E'_e , θ_e , E_h , $p_{t,h}$, δ_h and γ_h , in the kinematic plane. In areas where the isolines are closer together the kinematics can be determined more precisely.

4.2.1 Electron method (EL)

This method uses only the scattered electron variables, E'_e and θ_e . The kinematic variables are given by:

$$Q_{EL}^2 = 2E_e E'_e (1 + \cos\theta_e) \quad (4.6)$$

$$y_{EL} = 1 - \frac{E'_e}{2E_e} (1 - \cos\theta_e) \quad (4.7)$$

$$x_{EL} = \frac{Q_{EL}^2}{s y_{EL}}, \quad (4.8)$$

where s is the centre-of-mass energy squared.

The EL method accurately reconstructs the kinematics at high y due to the close spacing of isolines for both the E'_e and θ_e , as seen in figure 4.2 (top right and left). At low y and Q^2 the EL method reconstructs the kinematics poorly as the isolines for E'_e become sparse.

4.2.2 Jacquet-Blondel method (JB)

The Jacquet-Blondel method uses the variables $p_{t,h}$ and δ_h which are calculated using only the hadronic final state. The kinematic variables are calculated as:

$$y_{JB} = \frac{\delta_h}{2E_e} \quad (4.9)$$

$$Q_{JB}^2 = \frac{p_{t,h}^2}{1 - y_{JB}} \quad (4.10)$$

$$x_{JB} = \frac{Q_{JB}^2}{s y_{JB}}. \quad (4.11)$$

Figure 4.2 (middle) shows the lines of constant $p_{t,h}$, δ_h , and E_h . The accuracy of the measurement of the hadronic final state is poor due to dead material and backscattering/backsplash in the calorimeter. The inaccurate reconstruction of $p_{t,h}$ leads to a large uncertainty in Q^2 due to the sparsity of isolines. The JB method does provide a good estimate y in the low- y region, where E'_e and θ_e carry little information.

4.2.3 Double-Angle method (DA)

The double-angle method uses the angles θ_e , from the scattered electron, and γ_h , from the hadronic system, to reconstruct the kinematic variables of the event. The advantage of the DA method is that it is independent of the overall energy scale [92]. The kinematic variables are given by:

$$Q_{DA}^2 = 4E_e^2 \frac{\sin\gamma_h(1 + \cos\theta_e)}{\sin\gamma_h + \sin\theta_e - \sin(\gamma_h + \theta_e)} \quad (4.12)$$

$$y_{DA} = \frac{\sin\theta_e(1 - \cos\gamma_h)}{\sin\gamma_h + \sin\theta_e - \sin(\gamma_h + \theta_e)} \quad (4.13)$$

$$x_{DA} = \frac{E_e \sin\gamma_h + \sin\theta_e + \sin(\gamma_h + \theta_e)}{E_p \sin\gamma_h + \sin\theta_e - \sin(\gamma_h + \theta_e)}. \quad (4.14)$$

The DA method is better suited than the other available methods to reconstructing the kinematics over most of the kinematic plane. An exception to this is at high- y , where the isolines of θ_e and γ_h become parallel, and the EL method becomes more accurate.

A useful feature of the DA method is that E_e' can be predicted from the two angles θ_e and γ_h using energy and momentum conservation. The expression for the DA predicted electron energy, E_{DA} is given by:

$$E_{DA} = 2E_e \frac{\sin\gamma_h}{\sin\gamma_h + \sin\theta_e - \sin(\gamma_h + \theta_e)}. \quad (4.15)$$

This allows an estimate of variables such as $p_{t,e}$ and $p_{t,h}$ that are independent of the measured energies.

4.2.4 Resolution and comparison of reconstruction methods

Figures 4.3, 4.4 and 4.5 show the relative difference, or bias, in the measurement of Q^2 , x and y using the three reconstruction methods described in the previous section

and the “true” generated value. The bias is calculated as follows:

$$\frac{Q_{gen}^2 - Q_{reco}^2}{Q_{gen}^2}, \frac{x_{gen} - x_{reco}}{x_{gen}}, \frac{y_{gen} - y_{reco}}{y_{gen}}, \quad (4.16)$$

where the subscripts “gen” and “reco” indicate “generated” and “reconstructed”, respectively. The events used in the figures passed all offline selection cuts, described in chapter 6, except for kinematic cuts. The bias is plotted in bins of x and Q^2 displayed in the approximate positions on the kinematic plane. Each event is assigned to a bin according to its generated kinematic values.

The EL method, as discussed in the previous section, reconstructs the kinematics well at high y , comparable to the DA method (in a number of bins better). At high x and low Q^2 the EL method performs poorly with worse resolution and bias compared to the DA and JB methods. The JB method provides a reasonable estimation of x and y , but with a resolution that is worse than the DA or EL methods. The estimation of Q^2 is particularly poor across the entire kinematic plane using the JB method. In general, but specifically in the high- Q^2 and high- x region that is important to this analysis, the DA method provides the best overall bias and resolution; therefore the DA method is used as the primary method of kinematic reconstruction in this analysis.

4.3 Offline event reconstruction

Once an event survives the trigger preselection (see section 6.3) and data quality selection (see section 6.4), results from the individual detector components must be combined into the final event information. This is done offline to make use of the most precise reconstruction methods in order to obtain the best possible resolution from the ZEUS detector. Tracks must be reconstructed, from which the primary and secondary vertices can be determined. The calorimeter energy scale can be determined from the large physics samples available at ZEUS, which are used to obtain correction factors. Once these procedures have been completed the electron and hadronic final state can

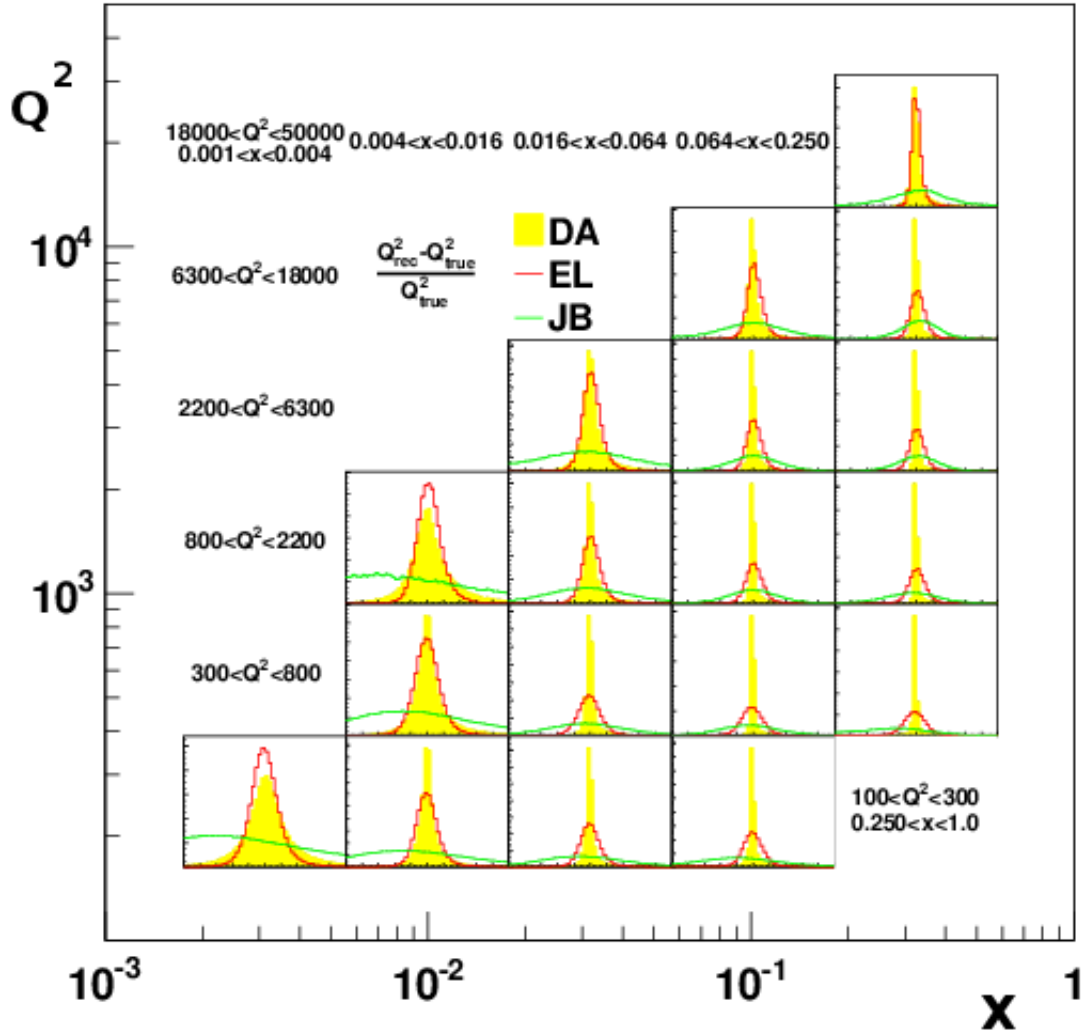


Figure 4.3: Bias of Q^2 : $\frac{Q_{gen}^2 - Q_{reco}^2}{Q_{gen}^2}$ for each reconstruction method in bins of Q^2 and x . The red filled circles are EL, the blue open circles are JB and the yellow histogram is DA.

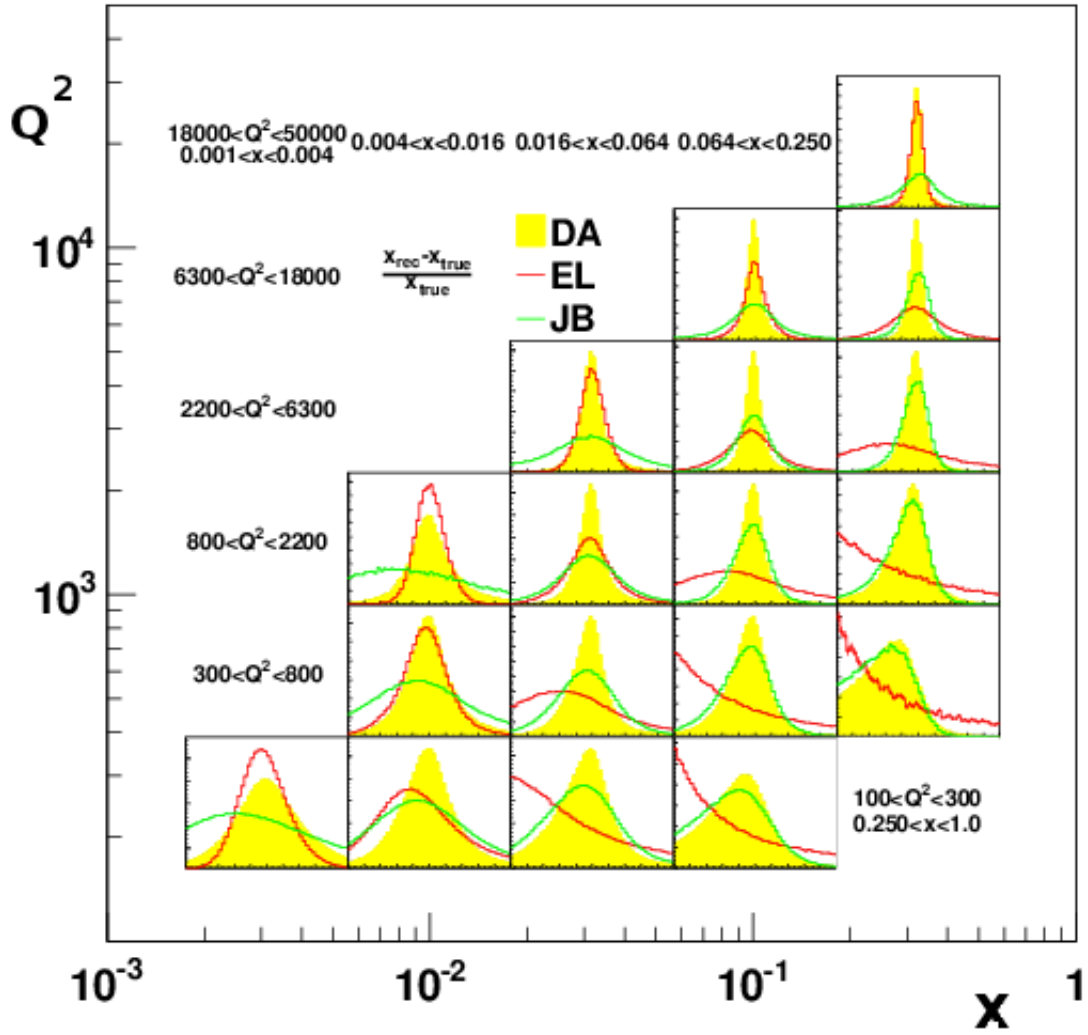


Figure 4.4: Bias of x : $\frac{x_{gen} - x_{reco}}{x_{gen}}$ for each reconstruction method in bins of Q^2 and x . The red filled circles are EL, the blue open circles are JB and the yellow histogram is DA.

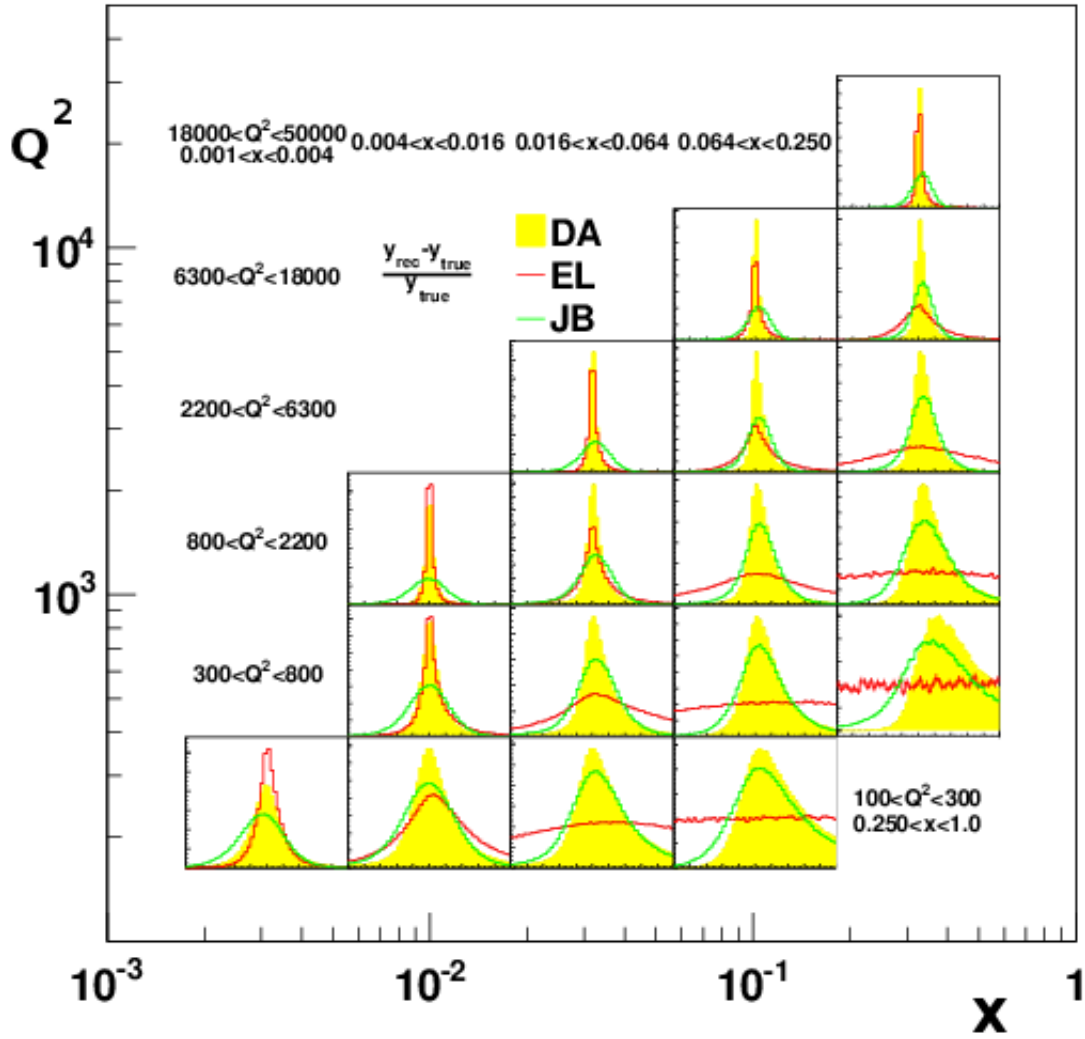


Figure 4.5: Bias of y : $\frac{y_{\text{gen}} - y_{\text{reco}}}{y_{\text{gen}}}$ for each reconstruction method in bins of Q^2 and x . The red filled circles are EL, the blue open circles are JB and the yellow histogram is DA.

be measured.

4.3.1 Calorimeter pre-corrections

False signals in the calorimeter that are not due to energy deposited by the final-state particles of the ep collision can affect the measurement of the kinematic variables, especially if the analysis relies heavily on calorimeter measurements. These false signals can come from a variety of sources: radiation noise, PMT sparks, hot cells and bad cells.

The ZEUS calorimeter uses depleted uranium as an absorber and the natural radioactivity gives rise to a source of calorimeter “noise”. To suppress this noise, a minimum energy requirement is imposed on each cell of 60 MeV and 110 MeV for EMC and HAC cells respectively. For cells that are isolated, surrounded by cells with no energy, the cuts are raised to 80 MeV and 140 MeV for EMC and HAC cells. Cells with energies less than these cuts are removed from the event.

PMT sparks generate spurious large energy deposits and are due to the relatively rare spontaneous discharge of the photomultiplier tubes. These spontaneous discharges occur most often between the photocathode and shielding of the PMT, or in broken PMT bases. In this case one of the PMTs seems to measure a large energy deposit, while the PMT on the other side of the cell does not. This creates an imbalance in the energy reported by each PMT and can be used to reject PMT sparks. PMT sparks are rejected by requiring the following:

$$\|Imb\| < 0.49E_{cell} + 0.03 \text{ GeV and } E_{cell} > 1 \text{ GeV}, \quad (4.17)$$

where E_{cell} and Imb are the sum and difference of the cell PMTs, respectively.

In addition to radiation noise and PMT sparks, long-term analysis of the behaviour of calorimeter cells reveals that some cells fire more frequently and have higher average energy. These cells are labelled as “hot”. Hot cells are detected on a run-by-run basis using a random trigger. Cells that show markedly different behaviour are marked as

hot, and used in the noise suppression algorithm.

Cells that have only one non-functioning PMT are labelled “bad” and may still be used for analysis, with twice the energy of the working PMT being assigned to the cell. In the case of a cell with two non-functioning PMTs no information can be recovered from the cell and it is called a “hole”. Having too many holes can significantly alter the measured energy in the calorimeter and the number must be kept to a minimum. Both bad cells and holes are closely monitored (typically 1-2 times/week) and, in general, were a very small fraction of the total number of cells (typically less than 300 bad cells and less than 3 holes). The PMTs and bases in bad cells and holes were repaired during HERA shutdowns.

4.3.2 Calorimeter alignment

The CTD is used as a frame of reference for all other components of the ZEUS detector. To reconstruct a NC event well, the position of the calorimeter with respect to the CTD must be known precisely. In this analysis the matching of a track in the CTD to a calorimeter cluster is extremely important, so any misalignment can lead to misidentification and a drop in the electron finding efficiency.

The alignment constants were measured by an optical survey while the detector was open during shutdowns. The alignment was further checked using NC DIS events. This method uses the position of the electron track extrapolated to the calorimeter surface and compares to the position measured using the calorimeter alone [93]. Following the application of the results of these studies the precision of the alignment is better than 1 mm for RCAL, 1 mrad in θ for the BCAL and 2 mm for the FCAL.

4.3.3 Tracking and event vertex reconstruction

Track reconstruction

The tracks of charged particles passing through the ZEUS detector are reconstructed using the ZEUS inner tracking detectors: the CTD, MVD and STT. One of the major

achievements of the HERA-II running period is the “global tracking” which combines information from all three tracking detectors into a single set of tracks.

Track reconstruction begins with a pattern recognition program called VCTRACK [94]. VCTRACK starts from the outermost layer of the CTD or the STT and groups together hits to form a “seed”: 3 hits are required in the CTD and 8 hits are required in the STT. The seed gives an approximate estimation of the momentum and charge of the track which is used by VCTRACK to proceed inwards in the $x - y$ plane towards the interaction point. As the pattern recognition proceeds inwards the potential track picks up hits and forms a “road” from the CTD or STT through the MVD. The output of the pattern recognition (the roads) are then input into the Rigorous Track Fit (RTFIT) [95]. RTFIT is based on a Kalman filter algorithm [96]. It improves the accuracy of the track fit by removing outliers, taking into account the inhomogeneous magnetic field, multiple scattering and ionization loss. The output of RTFIT is a set of tracks with their final track helix parameters.

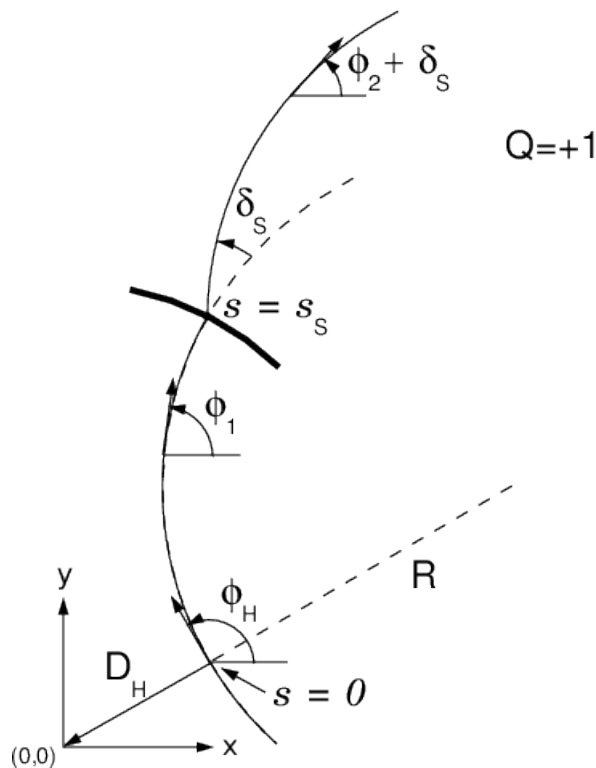


Figure 4.6: Track helix in the $x - y$ plane for a positively charged track.

The track helix parametrization is based on the “distance of closest approach”

D_H , i.e., the distance from the point on the helix closest to a chosen reference point $(x_{ref}, y_{ref})=(0, 0)$, as shown in figure 4.6. This parametrization is designed to describe the track of particles in the solenoidal magnetic field of the ZEUS detector. The parametrization is described using the following five parameters:

- ϕ_H : the azimuthal angle of the direction vector of the helix at the point of closest approach.
- Q/R : ratio of the charge Q to the radius of curvature.
- QD_H : the distance of closest approach to the reference point multiplied by the charge.
- Z_H : the z position of the point of closest approach.
- $\cos\theta$: the polar angle of the track with respect to the $x - y$ plane.

Vertex reconstruction

The primary vertex finding is done using the same program, VCTRACK, used to reconstruct the tracks of charged particles. A constraint is applied on the vertex position: the primary vertex position is assumed to lie along the axis of the proton beam direction. A set of tracks compatible with this constraint and with a common vertex are found. The vertex is initially found by calculating the weighted centre-of-gravity of those tracks and minimising the χ^2 of the fit. In this procedure tracks are discarded that lead to a χ^2 greater than a certain χ_{cut}^2 . After the primary vertex and the associated tracks have been found a “deterministic annealing Filter” (DAF) [97] [98] is applied to improve the reconstruction of the vertex position. This method uses a “thermodynamical approach” replacing the χ^2 cut with a smooth temperature dependent weight function:

$$w(\chi^2, T) = \frac{1}{1 + \exp(\frac{\chi^2 - \chi_{cut}^2}{2T})}, \quad (4.18)$$

where T is the temperature and χ^2 is the contribution of the track to the total χ^2 of the vertex fit. Each track is assigned a weight according to equation 4.18 starting at a high temperature. Then the vertex is re-fit with a weight assigned to each track. The temperature is then reduced and the procedure repeated. As this procedure is iterated, outlier tracks are effectively removed as their weights become negligible. This procedure is repeated until it converges or a minimum temperature is reached. The primary vertex position is further constrained by the beam-spot. The beam spot is a 3D distribution of the ep collision volume defined by the sizes of the proton and electron bunches. It has a cross-sectional area of $80 \times 20 \mu\text{m}^2$ in x , y and 8 cm in z . The position at which the ep beams are brought into collision within the ZEUS detector changes with time; therefore the beamspot is determined every 2000 events by fitting the x , y and z distributions of the initial primary vertex. DAF vertexing with the beamspot constraint significantly improves the vertex finding efficiency and resolution [99].

Secondary vertices from the decays of unstable particles can also be determined but are not used in this analysis.

4.3.4 Electron identification

The identification of a scattered electron is crucial in selecting NC DIS events and distinguishes the event from various background sources such as charged current and photoproduction events. Additionally, precise determination of the scattered electron energy and angle are required to determine the kinematic variables Q^2 , x , and y accurately. Electron candidates are characterised by an isolated energy deposit in the electromagnetic calorimeter with little to no energy leakage into the hadronic calorimeter, and an associated track.

There are two main electron finders used in analyses at ZEUS: Sinistra [110] and EM [101]. Sinistra was optimised chiefly for low- Q^2 events where the electron is found in the RCAL. EM on the other hand was optimised for high- Q^2 events where the electron is often scattered into the BCAL or even the FCAL, and was therefore

used in this analysis. Additionally EM was found to have better PHP rejection [100]. Sinistra has been used as a systematic check as described in section 7.3.

Clustering

The scattered electron typically leaves energy deposits in several calorimeter cells due to showering in dead material between the interaction vertex and the calorimeter. To identify the scattered electron in the detector the energy deposits belonging to the electron must be grouped together. The process is called the “cell-island algorithm” [102]. The basic structure of a cell-island is a local maximum of energy surrounded by lower energy deposits. To build a cell-island the energy of each cell is compared to its neighbouring cells, both those that share a side and diagonally adjacent cells. If the energy deposits of the surrounding cells are lower than a given cell, then it is defined as a “local maximum”. If a higher energy neighbour is found then a link is formed to that neighbour and the cell is included in the cell-island. This process repeats until all cells are included. Figure 4.7 shows this process schematically in 2D. The cell-island method allows clusters of cells to be formed that have only one, well-defined, point of maximum energy. Additionally the algorithm allows cell-islands to contain cells from different parts of the calorimeter (such as the RCAL and the BCAL at their boundary).

The position of each cell-island is calculated as a weighted average of the centres of each cell in the cell-island, where the weights depend logarithmically on the cell energy [103]:

$$\vec{r}_{isl} = \frac{\sum_i w_i \vec{r}_i}{\sum_i w_i} \quad (4.19)$$

$$w_i = \max(0, W_0 + \ln \frac{E_i}{\sum_j E_j}), \quad (4.20)$$

where \vec{r}_{isl} is the position assigned to the cell-island, \vec{r}_i the position of the i th cell, w_i the weight assigned to the cell and E_i the energy assigned to the cell. The sums run over all cells in the cell-island. W_0 is a tunable parameter that sets the minimum

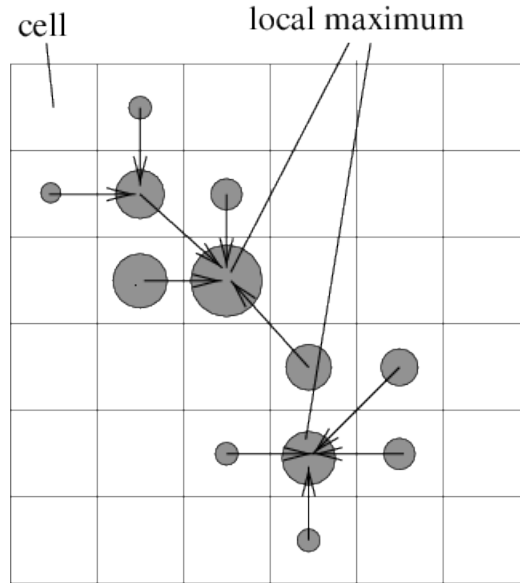


Figure 4.7: A schematic diagram of the cell-island algorithm in two dimensions. The size of a circle corresponds to the energy deposit in the cell.

fraction of the shower energy of the cells that contribute to the cell-island position. Values of $W_0 = 4$ and $W_0 = 2$ were used for EMC and HAC cells respectively [102]. In the RCAL, if the matched HES cluster is found within 10 cm of the electron position, then the HES position is used instead of the calorimeter position. The logarithmic weights take into account the exponential lateral falloff of the shower energy.

EM electron finder

The EM electron finder is based on detailed parameterizations of the detector response for electrons, using both tracking and calorimeter information, to assign a probability that a calorimeter energy deposit is from an electron. EM uses the term “Grand Probability” P_{grand} discussed further below. The probability that a calorimeter cluster is an electron is calculated using several sub-probabilities based on properties of the energy deposit and tracking information. These sub-probabilities are calculated using the following seven variables:

- f_{HAC} : the fraction of the calorimeter cluster energy in the HAC layers.
- f_{CLeak} : the fraction of EMC energy outside the highest energy cell strip pair. A cell strip is a set of EMC cells which have the same tower number, cell type and

are in the same calorimeter (F/B/RCAL). If t is the tower number and k the cell type, where $1 \leq k \leq 4$ for EMC cells, then the strip number can be defined as $s = 4(t - 1) + k$. $f_C(s)$ is then the fraction of a cluster's EMC energy in the strip s and s_{max} the highest energy strip, so that:

$$f_{CLeak} = 1 - [f_C(s_{max}) + \max(f_C(s_{max} - 1), f_C(s_{max} + 1))]. \quad (4.21)$$

- f_{MLEak} : the fraction of energy in the highest energy module pair can be defined in terms of $f_M(m)$, the fraction of energy in module m with m_{max} being the highest energy module. The variable f_{MLEak} can therefore be defined as:

$$f_{MLEak} = 1 - [f_M(m_{max}) + \max(f_M(m_{max} - 1), f_M(m_{max} + 1))]. \quad (4.22)$$

- E_{cone} : the energy in a $\eta - \phi$ cone of $R < 0.8$ around the calorimeter cluster not belonging to the energy assigned to the electron.
- $\delta\theta = |\theta_{trk} - \theta_{CAL}|$: the difference between the polar angles of the track and the calorimeter cluster.
- $\delta\phi = |\phi_{trk} - \phi_{CAL}|$: the difference between the azimuthal angles of the track and the calorimeter cluster.
- $\delta_{1/P} = |1/E - 1/P_{trk}|$: quantifies the difference between the calorimeter cluster's energy and the track momentum.

The parametrizations of these seven variables are determined for the F/B/RCAL separately. The RCAL and BCAL distributions are derived from ZEUS data. Due to the small number of events in the FCAL for data, NC DIS MC is used to determine the FCAL parametrizations.

Each of the variables is transformed into a sub-probability: $P(f_{HAC})$, $P(f_{CLeak})$, $P(f_{MLEak})$, $P(E_{cone})$, $P(\delta\theta)$, $P(\delta\phi)$, $P(\delta_{1/P})$. If the variable x is in the range $0 < x < x_{max}$ and has a sub-probability density $f(x)$ the corresponding probability $P(x)$

is given by:

$$P(x) = \int_x^{x_{max}} f(x') dx'. \quad (4.23)$$

As $\int f(x) dx = 1$, the sub-probability $P(x)$ is uniformly distributed between 0 and 1 for real electrons. A high value of $P(x)$ corresponds to a low value of x and therefore a better electron, as fake electrons tend to have larger values for each of the variables.

Electron candidate reconstruction

The process of finding an electron using EM begins by grouping calorimeter cells into cell-islands. For a cell-island to be considered by the EM electron finder it must have an energy of at least 4 GeV and have no more than 30% (50%) of its energy deposited in the HAC section of the FCAL (BCAL).

The next step searches for a track that can be matched to the cell-island. The following criteria are required for a track to be matched to a cell-island:

- The transverse momentum of the track must be greater than 0.1 GeV/c.
- The distance of closest approach of the track to the beamline must be less than 2 cm.
- The polar and azimuthal angles between the track and the cell-island must be less than 45° , where the angle of the cell-island is calculated with respect to the z axis.
- The distance of closest approach between the cell-island and the track end-point extrapolated to the face of the calorimeter must be less than 50 cm.

The track with the highest probability P_{trk} , which is the product of the sub-probabilities $P(\delta\theta)$, $P(\delta\phi)$ and $P(\delta_{1/P})$, is assigned to the electron candidate. If no track is assigned to the electron candidate it is treated as trackless.

EM then attempts to merge the electron candidate with nearby clusters that may be due to FSR. If a cell-island is within a $\eta - \phi$ cone of $R < 0.8$ around the electron

candidate then it is merged with the electron candidate and the grand probability is then re-calculated. If the grand probability of the merged electron candidate becomes worse, the original electron candidate is used. If multiple cell-islands are within the $\eta - \phi$ cone, then the merged candidate which gives the best grand probability is taken.

Grand probability and candidate ordering

Calculation of the grand probability uses the assumption that the sub-probabilities, p_i , are uniformly distributed between 0 and 1 and are uncorrelated. The product of the sub-probabilities, $P = \prod_{i=1}^N p_i$, can be transformed into the grand probability P_{grand} [101]:

$$P_{grand} = P \sum_{k=0}^{N-1} \frac{(-\log P)^k}{k!}, \quad (4.24)$$

where P_{Grand} is uniformly distributed between 0 and 1. If the electron candidate is found in the CTD acceptance region ($0.3 < \theta_e < 2.85$) the summation in equation 4.24 runs over all 7 sub-probabilities; outside it runs over only the 4 sub-probabilities based on calorimeter information. In the case of an electron inside the CTD acceptance but with no matched track, P_{grand} is calculated only using the calorimeter variable sub-probabilities, but scaled by the suppression factor ϵ_{trk} .

The electron candidates found by EM are ordered according to P_{sel} , the probability that the candidate is the scattered electron and not just an electron. It is calculated as follows:

$$P_{sel} = P_{Grand} \frac{1}{Q_{EL}^4} P_{pt}, \quad (4.25)$$

where P_{pt} is the probability that the candidate is misidentified as an electron¹, and

¹ P_{pt} is defined by three cases:

1. $P_{pt} = 1$ if there is only 1 candidate.
2. If the electron candidate has the highest p_t (now called p_t^{true}) the candidate with the second highest p_t is labelled p_t^{fake} .
3. If the electron candidate does not have the highest p_t (now called p_t^{true}) the candidate with

that a second electron candidate with a higher p_t is the correct one. The Q_{EL}^4 factor comes from the Q^2 dependence of the NC DIS cross-section, and suppresses high Q^2 candidates as they happen less often. P_{sel} is therefore used to select the best electron candidate in an event, but P_{grand} is used to select or reject the electron.

Electron track measurement

The accuracy of the electron angle measurement is important due to the use of the DA method for reconstruction of the kinematic variables. Q^2 is particularly sensitive to θ_e (see figure 4.2).

The angle of the scattered electron can be obtained using two methods: from the measured position in the calorimeter and the interaction vertex and directly from the angle of the matched track. The measurement of the scattering angle using the calorimeter position is affected by the calorimeter structure (supercracks, module edges, etc). The angle measurement based on the matched track is more accurate. The bias, $\theta_e - \theta_{e,true}$, for events reconstructed using only calorimeter information and, when possible, the angle from the matched track is shown in figure 4.8. Thus, the angle from the matched track is used whenever possible (see details in section 5.5).

4.3.5 Hadronic final state reconstruction

The hadrons produced from the struck quark and the proton remnant leave energy deposits in the calorimeter. Due to the use of the DA method (see section 4.2.3) the reconstruction of the kinematic variables does not depend heavily on the energy of the hadronic system, but does depend on γ_h (see section 4.1.2). The following sections describe the reconstruction of the hadronic final state, the corrections applied to the

the highest p_t is labelled p_t^{fake} .

In the second and third cases the value of P_{p_t} is calculated using a formula of the form:

$$P_{p_t} = Ae^{(-B(r(p_t^{fake}, p_t^{true})) + C)^D} \quad (4.26)$$

$$r(p_t^{fake}, p_t^{true}) = \log\left(\frac{p_t^{fake}}{\sqrt{((p_t^{true})^2 + 1)}}\right) \quad (4.27)$$

where the parameters A, B, C and D are determined from MC in bins of p_t^{true} .

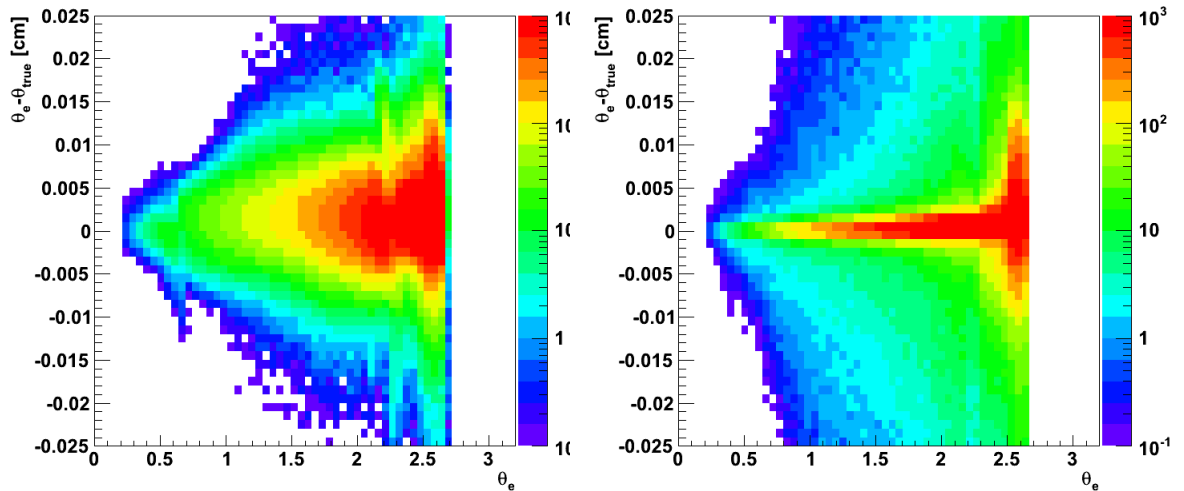


Figure 4.8: The difference between the reconstructed and generated polar angle of the scattered electron using only calorimeter information (left) and using calorimeter and tracking information (right). The plots are made with NC DIS MC events passing the event selection.

hadronic system and the uncertainty on the hadronic energy scale.

Clustering

The calorimeter cells assigned to the hadronic final state are clustered using the same algorithm used to cluster the cells of the scattered electron (see section 4.3.4). Unlike the case of the electron cells, cell-islands are formed in the EMC, HAC1 and HAC2 sections of the calorimeter separately. The cell-islands of each calorimeter section are then combined into a three-dimensional object called a cone-island [102].

Backsplash correction

The cone-islands are used to calculate the variables $P_{t,h}$ and δ_h using the equations 4.1 and 4.2, where i runs over all cone-islands. The variable γ_h is then calculated from these variables according to equation 4.3. The γ_h distribution for both data and MC is shown in figure 4.9 (left). There is a significant difference between data and MC at low values of γ_h , which has been identified with “backsplash”, the process in which where particles deposit some of their energy in a location different from

where their initial direction would have suggested. The sources of backplash are: backscattering from the CAL due to the albedo effect and scattering or showering of particles in material before they reach the calorimeter. A previous study [104] showed that backplash is indeed observed in MC. Demonstrating that backplash occurs in data is more difficult as no “true” information of particles passing through the detector is available. Generally, backplash energy deposits have an energy less than 3 GeV, but as they are located in the rear region of the detector they have a large effect on δ_h and consequently contribute to a large bias of γ_h .

The correction for the effect of backplash in the reconstruction of the hadronic final state introduces a variable γ_{max} to remove cone-islands that are likely due to backplash. The value of γ_{max} is determined from MC and is parametrized as a function of γ_h [104] shown in figure 4.10. To determine γ_{max} cone-islands are created for each particle in the MC separately. Two samples are defined based on the variable d , the distance from where a particle entered the calorimeter and deposited its energy. A control sample is defined with $d < 40$ cm and a backplash sample with $d > 110$ cm. γ_{max} is chosen such that less than 1% of cone-islands in the control sample are rejected. A perfect understanding of backplash in the ZEUS detector is difficult due to the difficulties of simulating low energy hadronic interactions and obtaining a precise understanding of dead material in the detector.

Cone-islands that satisfy the following criteria are rejected:

$$\theta_{isl} > \gamma_{max} \text{ and } E_{isl} < 3 \text{ GeV}, \quad (4.28)$$

where θ_{isl} and E_{isl} are the polar angle and energy of the cone-island. The backplash corrected γ_h is calculated iteratively for each event using the following prescription:

1. Calculate γ_h using all cone-islands.
2. Calculate γ_{max} and reject cone-islands satisfying equation 4.28.
3. Calculate γ_h using the remaining cone-islands.

4. Repeat steps 1-3 until the difference between successive calculations agrees to within 1% or to a maximum of three iterations.

Figure 4.9 (bottom) shows the good agreement between data and MC after applying the backplash correction.

Dead material and supercrack corrections

The particles that make up the cone-islands lose energy due to interactions with dead material and in the boundaries of the BCAL and F/RCAL (these regions are called “supercracks”). These energy losses are studied using the reconstructed and true MC hadronic energy [104]. The effect of dead material is corrected using a fit of energy loss as a function of the dead material. The energy loss in the supercrack region is treated by parameterizing the energy loss as a function of the cone-island’s polar angle.

Overestimation of the energy of hadrons at low energy

As hadrons and electromagnetic particles shower differently, cone-islands are divided into two categories according to the fraction of energy measured in the EMC section of the calorimeter, $f_{EMC} = E_{isl,EMC}/E_{isl}$: “electromagnetic-like” ($f_{EMC} = 1$) and “hadronic-like” ($f_{EMC} < 1$). An overestimation of the energy of hadron-like cone-islands is observed for $E_{isl} < 7$ GeV. Both the hadron-like and electromagnetic-like cone-islands behave similarly for $E_{isl} > 7$ GeV [104]. The energy overestimation at low energy is likely due to the increase in the probability of hadrons to deposit their energy due to ionization loss instead of showering as the energy decreases. The energy deposition due to ionization loss is 60% higher than from showering. This effect has been observed in test beam measurements [105] of the ZEUS calorimeter modules. Additionally, the differing noise suppression cuts for EMC and HAC cells (see section 4.3.1) can have an influence at low E_{isl} . To correct for this effect, a correction as a function of f_{EMC} is applied [104].

Hadronic energy scale

The hadronic energy scale was investigated by comparing the hadronic transverse momentum $P_{t,h}$ with the value predicted using the DA method $P_{t,DA}$. Figure 4.11 shows the ratio of $P_{t,h}/P_{t,DA}$ for both data and MC, which generally agree within a percent. Thus a 1% uncertainty is assigned to the hadronic energy scale (see section 7.3). The ratio $P_{t,h}/P_{t,DA}$ does exhibit some fluctuations of up to 3%, especially at low γ_h . The calculation of γ_h has no dependence on the hadronic energy scale since the scales cancel. The DA method is used to calculate the cross sections, which are sensitive to changes in γ_h and not $P_{t,h}$ and δ_h separately, and no correction is applied.

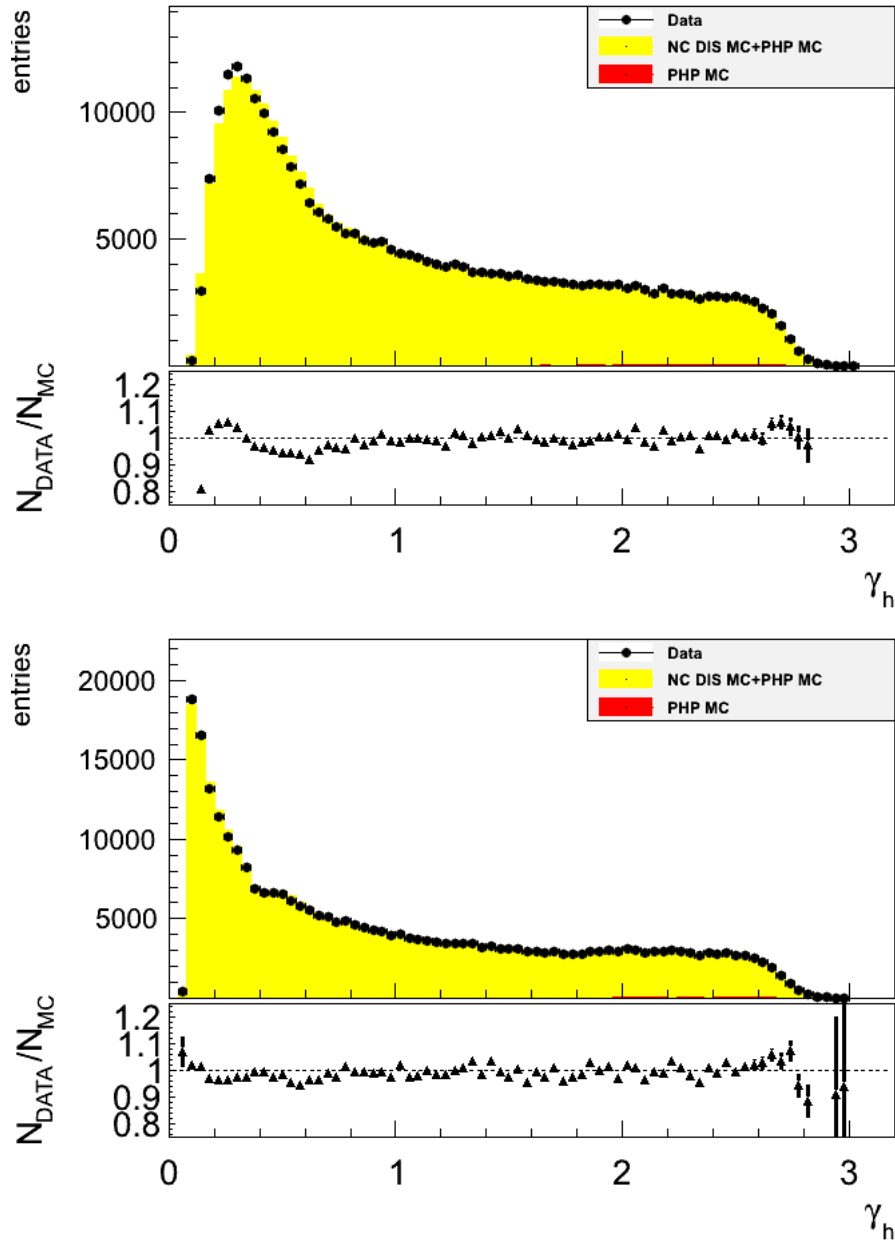


Figure 4.9: The γ_h distribution before (top) and after (after) applying the backslash correction. The points are data and the yellow histogram is NC DIS MC and PHP MC.

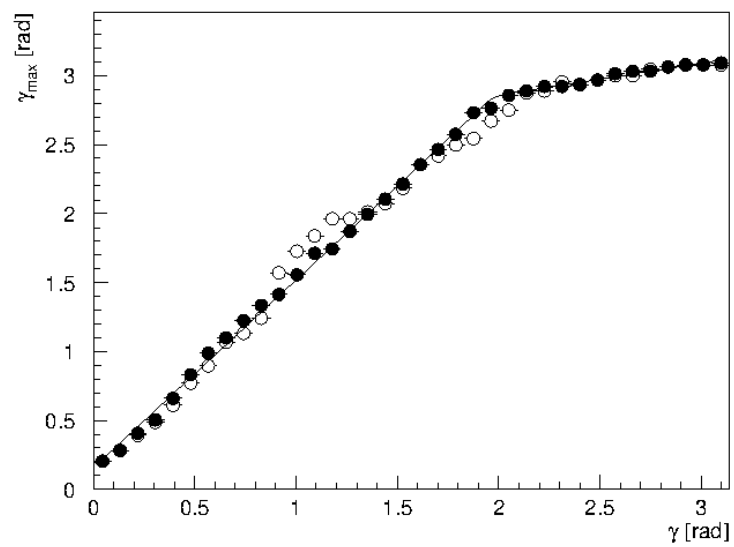


Figure 4.10: γ_{max} as a function of γ_h . The closed black circles correspond to MC for 1997-1998 and the open black circles correspond to 1995-1996 MC.

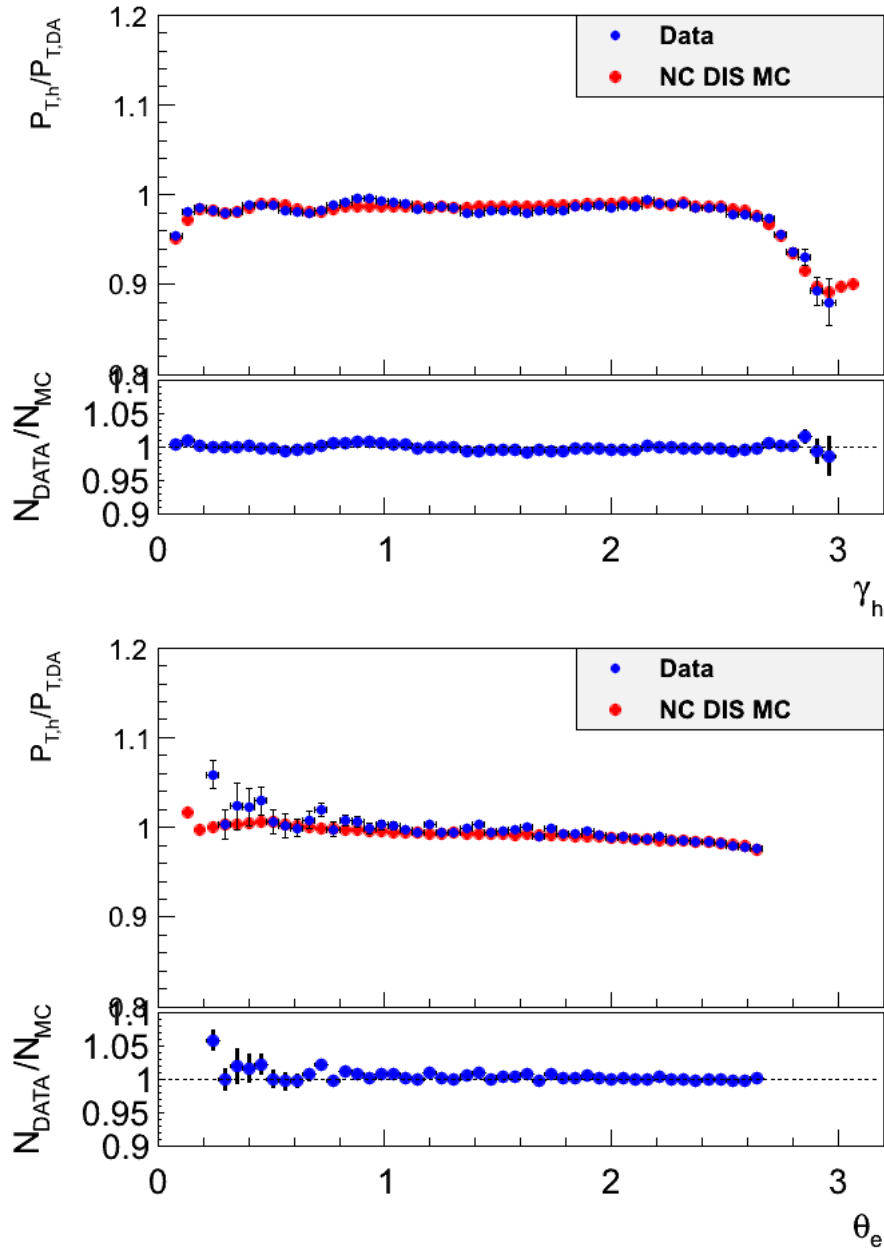


Figure 4.11: The hadronic energy scale determined from $P_{t,h}/P_{t,DA}$ versus γ_h (top) and θ_e (bottom). The data and MC are shown as blue and red dots, respectively. The data and MC ratios are shown below each plot.

Chapter 5

Corrections to DATA and MC samples

In chapter 3 the data and MC samples used in this analysis are introduced. A comparison between the data and MC show that the event kinematics are well reconstructed and that the MC reasonably describes the data, but the percentage difference or “normalisation” between data and MC (see table 5.1) is larger than the luminosity uncertainty. As this high- Q^2 analysis is a high statistics, high-precision measurement, any difference between the data and the MC description must be understood. The cross-section measurement, which depends on the detector acceptance correction, requires that the MC describe the data as well as possible. Therefore several studies were done and corrections developed to improve the MC description of the data.

There are two main corrections which must be made to the MC to account for the effects of the F_L structure function and the lepton beam polarisation P_e . These

	Nr. DATA	Nr. MC	Nr. PHP	Norm. (%)
ALL	302073	309347	656	2.6
RH	178644	179910	375	0.92
LH	123429	129398.8	280	5.1
LH1	73247	75751.8	166	3.6
LH2	50182	53685.7	115	7.2

Table 5.1: Normalisation between data and MC before the application of the corrections outlined in chapter 5.

are described in sections 5.1 and 5.2. Further corrections are described in sections 5.3 to 5.7.

5.1 F_L correction

The NC DIS cross-section, described in section 1.7.2, depends on the longitudinal structure function F_L . For much of the kinematic region that is covered by this analysis, the contribution from F_L is small compared to that from F_2 and xF_3 . An examination of equation 1.40 shows that F_L will contribute to the NC cross-section at high values of y . Analyses show [106] that F_L may contribute over 10% at high values of y and small x .

The MC used in this analysis has been generated with $F_L = 0$. This is done so that the predictions from the HECTOR program, where F_L is set to 0, can be used for unfolding the cross sections. To unfold the cross-sections the MC must also have $F_L = 0$ (described in more detail in section 7.2). To include F_L in the MC simulation, events were reweighted, in bins of the true Q^2 and x , by the ratio of the NC cross-section with F_L , σ_{F_L} , and without F_L , $\sigma_{w/o F_L}$, as follows:

$$w_{F_L} = \frac{\sigma_{F_L}}{\sigma_{w/o F_L}}. \quad (5.1)$$

Both cross-section predictions were done using CTEQ5D, which uses the same PDFs used to generate the MC events. The effect of applying this reweighting factor can be clearly seen in MC description of y_{DA} in figure 5.1 where the inclusion of F_L gives a much better description of the data than without F_L . The overall effect of the correction is typically 1%, but increases to 8% in the highest y bins.

5.2 Polarisation

The NC MC used in this analysis were generated with $P_e = 0$ and thus does not take into account the polarised lepton beams that were available for HERA-II. This

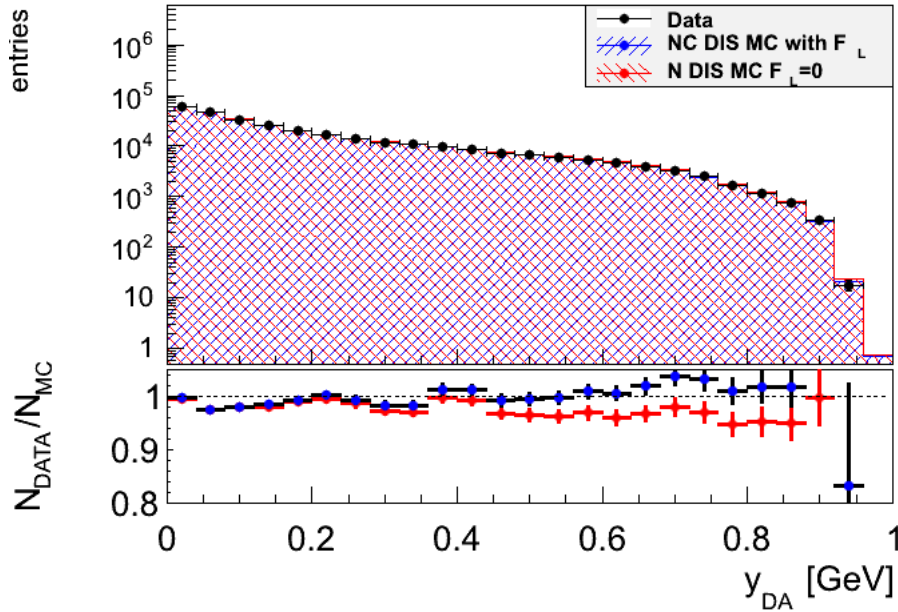


Figure 5.1: The y_{DA} distribution. The points are data, the blue hashed histogram is NC DIS MC with F_L included and the red hashed histogram is NC DIS MC without F_L . The ratio of data and MC is shown below, with the blue points with F_L and the red points without F_L .

was done to limit the number of MC samples that must be generated, since P_e would differ for each analysis depending on which physics runs were used. To take the lepton beam polarisation into account, predictions for the integrated cross-sections for both the unpolarised, $\sigma_{P_e=0}$, and the average polarisation of each data period, σ_{POL} , cases are utilized. These predictions were done using the HECTOR program with the CTEQ5D PDFs. The MC was reweighted by the factor w_{POL} , in bins of true Q^2 , by the ratio of the polarised and the unpolarised cross-section as follows:

$$w_{POL} = \frac{\sigma_{POL}}{\sigma_{P_e=0}}. \quad (5.2)$$

The influence on the normalisation of the MC to the data is 1% upwards for the RH data, and 1% downwards for the LH data. The direction of the correction, upwards or downwards, is as expected from equations 1.41 and 1.42. The magnitude of the correction varies greatly with Q^2 , from on the order of half a percent at low- Q^2 to 10% for the highest Q^2 bins.

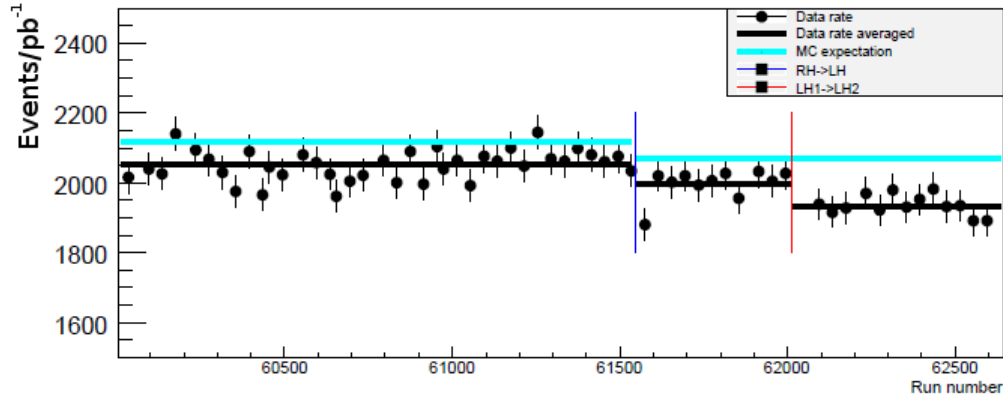


Figure 5.2: The event rate (the number of events per pb^{-1}) as a function of run number. The black points are the data, the black line is the average rate, the light blue line is the rate predicted from MC (with F_L and polarisation corrections only). The dark blue vertical line indicates the switch from RH to LH and the red vertical line indicates the shutdown in 2007 separating the LH1 and LH2 run periods.

5.2.1 Running Periods

It has already been mentioned that the data sample is divided into both a RH and LH sample, and the LH sample further divided into LH1 and LH2 samples. The reason for the division of the LH period was due to an observed difference in the events per integrated luminosity, or the “rate”. Figure 5.2 shows the rate as a function of the run number for data, and the expected MC rate (corrected for F_L and positron beam polarisation). Due to the polarisation change between the RH and LH periods, a drop in the observed rate is expected. An examination of the LH period shows a second rate drop which we use to define the LH1 and LH2 periods. The rate drop corresponds to a shutdown in early 2007. Unlike the rate drop between the RH and LH periods, the rate drop between the LH1 and LH2 periods has no obvious explanation. In all run periods the rate observed in data is lower than that expected from the MC. Several reasons were investigated to account for the rate drop between data and MC:

- Trigger inefficiencies
- Track veto efficiency
- Track matching efficiency

- The Z_{vtx} distribution
- The electron energy measurement
- Problems with the luminosity measurement

These investigations were found to account for the rate drop reasonably well, and are described more completely in the following sections.

5.3 Trigger Rates

The trigger system, as described in section 2.2.8, is used to select specific types of events to be used in this analysis. There are many specific triggers, each associated with a trigger bit (=1 if passed, 0 if failed), running at all 3 levels of the trigger system. It is crucial that each trigger used in this analysis be working in the expected manner. To check this, the number of events per pb^{-1} for each FLT, SLT and TLT trigger bit is plotted as a function of the run number. Any significant variation in the number of events taken by a trigger bit may be a sign of a problem with the trigger. Most trigger bits show no large variations, such as FLT 40 shown in figure 5.3. Two bits, FLT 30 and FLT 36 (FLT 30 shown in figure 5.3), show a rate drop for a number of runs during the RH running period. This is visible as a double-line (see figure 5.4) with some runs having an average of 1600 events per pb^{-1} and others with an average of 1000 events per pb^{-1} . The reason for this has already been noted in [107] and is described in the next section.

5.3.1 RISOE Correction

FLT 30 and FLT 36 look for an isolated electron in the RCAL and are labelled RISOE triggers. The reason for the rate drop was found to be a bug with a specific trigger configuration used between the period lasting from run 60226 until 60778 where the threshold of RCAL_EMG (a variable used for RCAL electrons) was set to infinity. The logic for these bits included RCAL_EMG OR RCAL_EMG.TH; no events could

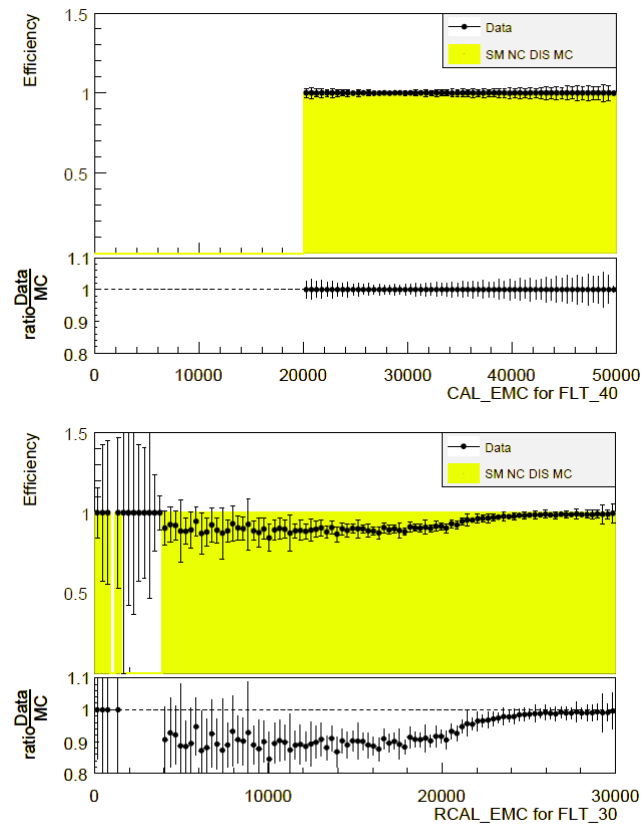


Figure 5.3: The efficiency of the CAL EMC variable for FLT 40 (top) and RCAL EMC (bottom) for FLT 30. The black points are data and the yellow histogram is MC. The ratio of data to MC is shown below. The drop in efficiency for the data FLT 30 is due to the RISOE bug.

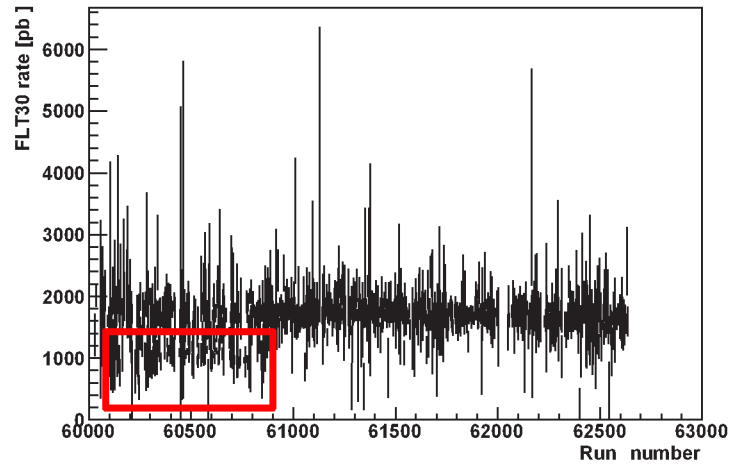


Figure 5.4: The rate for FLT 30 for NC DIS events as a function of run number. The double line structure (red box) is due to the RISOE bug.

pass the RCAL_EMG threshold but still passed the trigger slot due to passing the RCAL_EMG_TH threshold. The bug was not discovered immediately as the rate for the affected triggers did not drop to 0. As not all runs were taken with bug-affected trigger configurations, this explains the double-line structure seen in figure 5.4. In all 15 pb^{-1} are affected by the RISOE bug.

The influence of the bug is small, affecting only events exclusively triggered by FLT 30 or FLT 36, biasing about 10% of the data sample. A correction routine was developed to compensate for the events lost by the RISOE bug. This routine operates on events of the same kind as the affected events and assigns a weight greater than 1 to compensate for the events lost. As the bug affects only the RH running period there is only a 0.15% increase in the total number of data events (0.25% for RH, and 0% for the LH period as it is unaffected).

5.4 Track Veto Efficiency

At the FLT level most trigger bits have a “track veto”. A track veto rejects a trigger bit, regardless of other information, based on the specific track topology. Track vetos are based on track classes, seen in figure 5.5, which are a function of two variables:

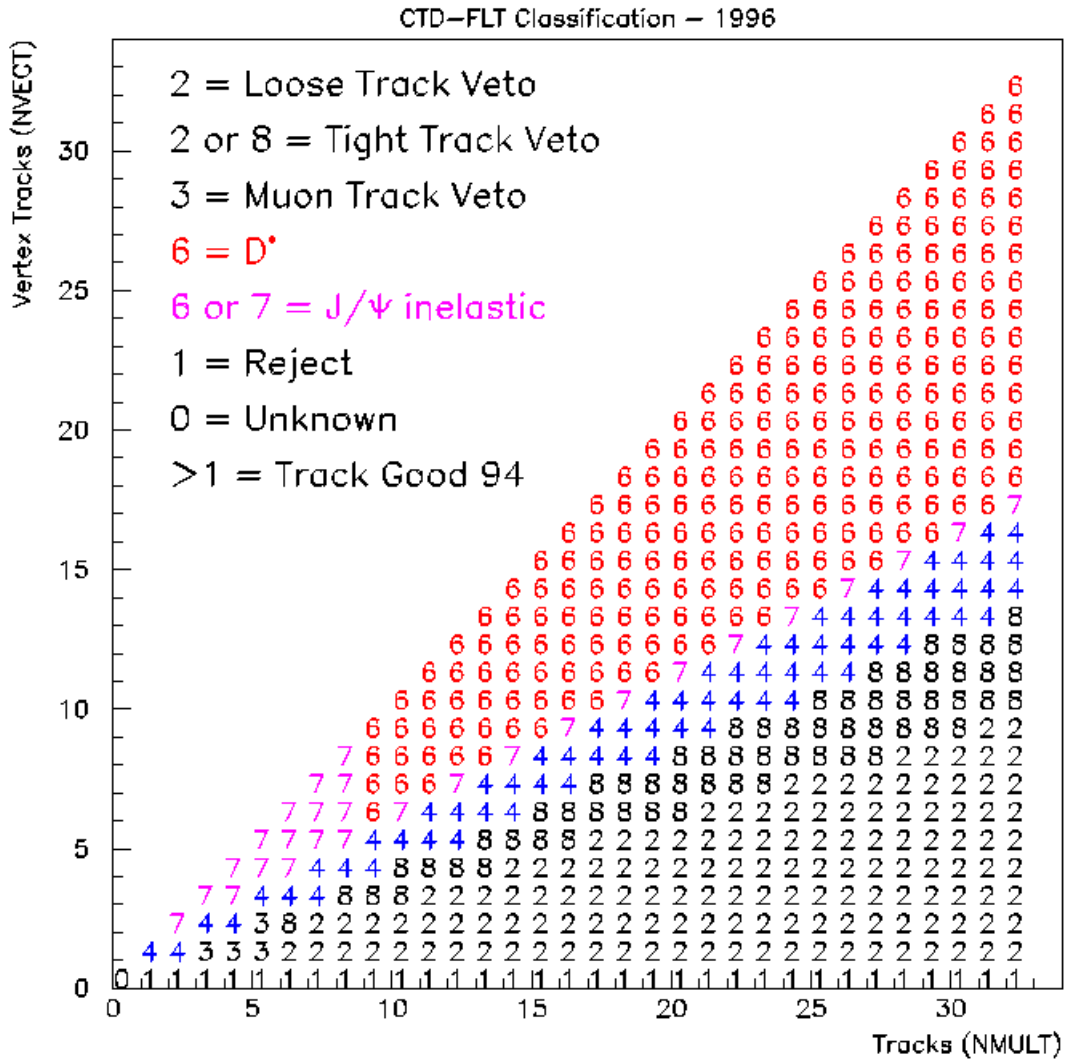


Figure 5.5: Definition of track classes.

the total number of tracks and the number of vertex fitted tracks. Not all FLT bits utilise the same track vetos, and are listed for each FLT bit below:

1. FLT bits 38, 41 and 47 - track class 2
2. FLT bits 39, 43 and 46 - tracks classes 0, 1, 2
3. FLT bit 44 - track classes 0, 1, 2, 8
4. FLT bits 28 and 40 (if an isolated electron is found in FCAL) - track class 2 is always rejected; track class 8 if the number of tracks is greater than or equal to 26.

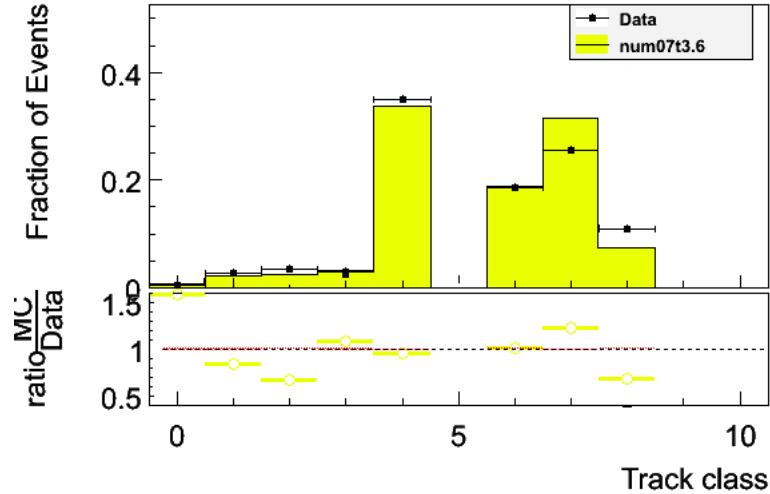


Figure 5.6: Track classes in data and MC (fraction of events). The points are data and the yellow histogram NC DIS MC. The ratio of MC to data is shown below.

5. FLT bit 28 (if an isolated electron is found in BCAL) - track classes 0, 1 and 2 is always rejected; track class 8 if the number of tracks is greater than or equal to 26.
6. FLT bit 30 - No track veto.

Figure 5.6 shows that track classes 0 and 1 play a very small role in this analysis. Track class 0 corresponds to events with no tracks and no vertex tracks. Track class 1 corresponds to events with no vertex tracks. These track classes are rejected by the good track requirement described in section 6.5. This means that we can ignore the effect of track classes 0 and 1; therefore track veto types 1 and 2 can be treated together and are called “loose track veto”. Additionally, track veto types 4 and 5 can also be treated together and are called “semi-loose track veto”. Track veto type 3 is called “tight track veto”.

The track class distribution is not well described by the MC as is shown in figure 5.6. This leads to events being accepted by the trigger at a different rate in data than MC. A correction is implemented using the only FLT trigger bit used in the selection that does not have a track veto, FLT 30. Each track veto type: loose,

	p_0	p_1	p_2	p_3	p_4
ALL	0.990406	-0.0162219	0.0195796	-0.0143367	0.00279945
RH	0.98102	0.0144755	-0.00345285	-0.00461526	0.00280495
LH	0.968389	0.0141884	0.00176994	0.00637733	-0.00537189
LH1	0.967661	0.0224066	0.00356801	-0.00576068	-0.00113368
LH2	0.969161	0.00287554	-0.00078312	0.0230519	-0.0109313

Table 5.2: The parameters of the fourth degree polynomial fit to the loose track veto efficiency correction as a function γ_h for each running period.

	p_0	p_1	p_2	p_3	p_4
ALL	0.990406	-0.0162219	0.0195796	-0.0143367	0.00279945
RH	0.98102	0.0144755	-0.00345285	-0.00461526	0.00280495
LH	0.968389	0.0141884	0.00176994	0.00637733	-0.00537189
LH1	0.967661	0.0224066	0.00356801	-0.00576068	-0.00113368
LH2	0.969161	0.00287554	-0.00078312	0.0230519	-0.0109313

Table 5.3: The parameters of the fourth degree polynomial fit to the semi-loose track veto efficiency correction as a function γ_h for each running period.

semi-loose and tight track vetos were studied separately. An efficiency is defined:

$$\text{TVE} = \frac{N_{FLT30} \ \& \ \text{Track Veto}}{N_{FLT30}}, \quad (5.3)$$

where N_{FLT30} is the number of events of the NC selection with FLT 30, and $N_{FLT30} \ \& \ \text{Track Veto}$ is the number of NC events with FLT 30 and the track veto under study. For each track veto the efficiencies are plotted as a function of different variables (both detector and kinematic related). The γ_h distribution shows the clearest difference between data and MC (This is expected as it is highly correlated with the number of tracks). To determine a weight, w_{TVE} , for each MC event a fourth-degree polynomial is fit to the ratio of $\frac{\text{TVE}_{\text{DATA}}}{\text{TVE}_{\text{MC}}}$ for all 3 track vetos for each running period:

$$w_{\text{TVE}} = p_0 + p_1 * \gamma_h + p_2 * \gamma_h^2 + p_3 * \gamma_h^3 + p_4 * \gamma_h^4, \quad (5.4)$$

where $p_1 \dots p_4$ are the parameters of each fit to $\frac{\text{Eff}_{\text{DATA}}}{\text{Eff}_{\text{MC}}}$ (see figure 5.7) and γ_h is the hadronic angle. The parameters for each track veto and running period are summarized in tables 5.2, 5.3 and 5.4.

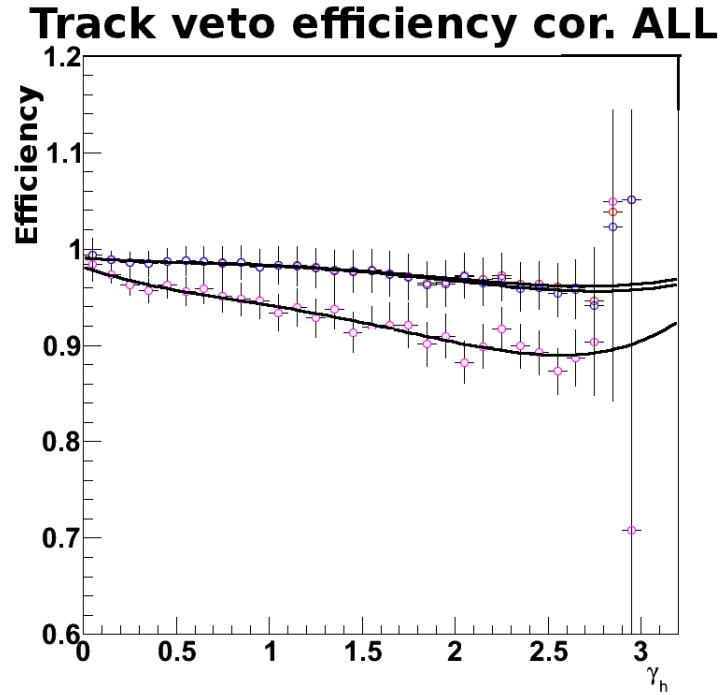


Figure 5.7: The track veto efficiency correction ($\frac{TVE_{DATA}}{TVE_{MC}}$) as a function of γ_h for the ALL running period. The loose track veto is shown as the open red points, the semi-loose track veto open blue points and the tight track veto open purple points.

	p_0	p_1	p_2	p_3	p_4
ALL	0.990406	-0.0162219	0.0195796	-0.0143367	0.00279945
RH	0.98102	0.0144755	-0.00345285	-0.00461526	0.00280495
LH	0.968389	0.0141884	0.00176994	0.00637733	-0.00537189
LH1	0.967661	0.0224066	0.00356801	-0.00576068	-0.00113368
LH2	0.969161	0.00287554	-0.00078312	0.0230519	-0.0109313

Table 5.4: The parameters of the fourth degree polynomial fit to the tight track veto efficiency correction as a function γ_h for each running period.

As more than one FLT bit is often triggered for each event, care must be taken to determine whether to apply the loose, semi-loose or tight track veto correction to an event. The method used to select which weight to apply to an event is detailed in the following:

- If FLT 30 is triggered then $w_{\text{TVE}} = 1$ as FLT 30 uses no track veto.
- If the event is not triggered by FLT 30 but is triggered by FLT bits with the loose track veto only (FLT bits 38, 39, 41, 43, 47 and 46) then the loose track veto correction is applied.
- If the event is not triggered by FLT 30 but is triggered by a semi-loose track veto but not loose track veto (bits 28 and 40) then the semi-loose track veto is applied.
- If the event is not triggered by FLT 30 but is triggered by a tight track veto but not (semi-)loose track veto (bit 44) then the tight track veto is applied.

The overall effect of the TVE correction on the normalisation is 0.4% and 0.7% for the RH and LH data sets respectively.

5.5 Track matching efficiency

The NC event selection (see section 6.5) imposes a number of criteria on the track matched to the calorimeter cluster of the electron candidate. Thus the analysis relies heavily on an accurate MC description of the tracking and the track matching efficiency² (TME) of the data. The study of the track veto efficiency demonstrates (section 5.4) that the MC description of the tracks does not agree perfectly with the data. It is thus prudent to investigate how well the MC describes the track matching efficiency of the data.

²The TME describes how often a track is matched to the calorimeter cluster of an electron candidate.

To investigate the track matching efficiency in both data and MC, two samples are defined: the normal NC event selection and the normal NC selection excluding all track related cuts. The track related cuts to be excluded are the following:

- Require a matched track to the calorimeter cluster if in the CTD acceptance region.
- The track momentum must be greater than 3 GeV.
- The distance of closest approach between the track and cluster must be less than 10 cm.
- The distance of the cluster to module edge must be greater than 1.5 cm.
- At least one good track required.

All tracking cuts except for the good track requirement demand that the electron be within the CTD acceptance region. Historically this region has been defined as $0.3 < \theta_e < 2.85$. This is the definition used to study the TME. The TME is then defined as:

$$\text{TME} = \frac{N_{\text{all cuts}}}{N_{\text{w/o trk req.}}}, \quad (5.5)$$

where $N_{\text{all cuts}}$ is the number of events satisfying all the selection cuts and $N_{\text{w/o trk req.}}$ is the number of events satisfying all the selection cuts without requiring the tracking cuts. The TME³ is then determined as a function of a number of variables, as shown in figure 5.8 for the electron energy and θ_e . Both plots clearly show that the TME is higher in MC than data for electron energy less than 30 GeV and $\theta > 2.5$. To eliminate this TME disagreement between data and MC the CTD acceptance region is re-defined as $0.3 < \theta_e < 2.5$.

³PHP MC is used to estimate the background contamination and is subtracted from the data before comparing to NC DIS MC.

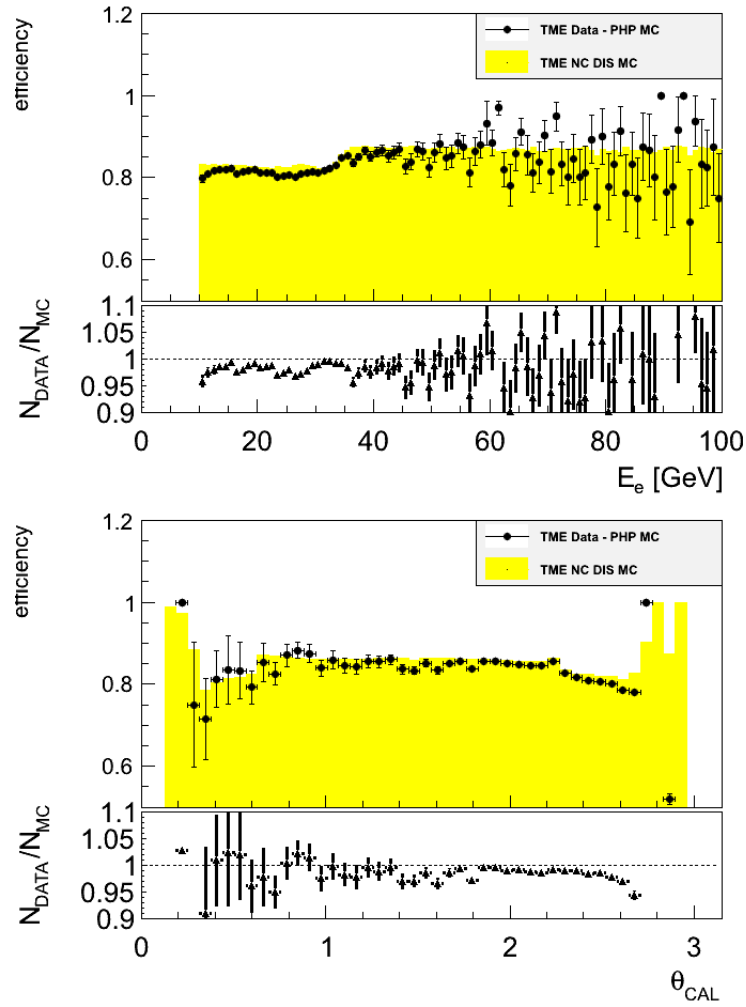


Figure 5.8: The TME as a function of E_e (top) and θ_e (bottom). The points are data and the yellow histogram is MC. The ratio of data and MC is shown below.

5.6 Electron energy measurement

As this analysis uses the DA method (see section 4.2.3) the electron energy does not enter directly into the calculation of the kinematic variables. The electron energy does enter into the event selection through a cut on the electron energy (see section 6.5). The electron energy measurement is biased by a number of detector effects: dead material between the interaction point and the calorimeter and inhomogeneity in the calorimeter so that the measured energy depends on position and shortcomings in the MC description of the detector.

5.6.1 Electromagnetic energy scale pre-correction

Before any other corrections are applied to the energy of the scattered electron, energy scale corrections to the F/B/RCAL are performed at the EAZE/ORANGE reconstruction level (see section 3.2.3). Due to limited statistics in the FCAL and BCAL the electromagnetic and hadronic energy scales are scaled by a global factor, determined by taking the ratio of the transverse energy of a jet, E_T , to the transverse momentum predicted from the DA method. The RCAL is treated differently due to the large number of events found there. The HAC cells of the RCAL are treated identically to the F/BCAL cells and are scaled by a global factor [108]. The scaling factors for the EMC section of the RCAL are obtained using two methods: using E_{DA} (see equation 4.15) to compare to measured energy, and using kinematic peak events⁴, where the energy of the scattered electron is known to be 27.56 GeV. The RCAL EMC cells scaling factors are extracted individually when possible. For cells that have limited statistics, the scaling factors are extracted as a function of the RCAL radius.

⁴Kinematic peak events are a special type of event where $x = E_e/E_p$, and $E'_e \approx E_e = 27.56$ GeV. Figure 4.2 shows that there is a large region of phase-space in which E'_e is approximately constant. Events from this region of phase-space are often used for detector studies as the energy of the scattered electron is known.

5.6.2 Dead material and non-uniformity corrections

Dead material correction

The measured energy of the scattered electron is lower than the true energy due to energy losses as the electron traverses inactive (or dead) material, such as the beampipe, tracking detectors, cables and the solenoid between the interaction point and the calorimeter. The dead material map is obtained from the detector simulation, allowing the number of radiation lengths (X_0) that the electron passes through to be calculated as a function of the Z_{vtx} and the polar and azimuthal angles. The corrected electron energy, E_{cor} , is calculated using the following formula:

$$E_{cor} = 2E_{meas} \left(1 + \frac{A(X_0)}{E_{meas}^{B(X_0)}} \right) \quad (5.6)$$

where E_{meas} is the measured electron energy in the calorimeter and $A(X_0)$ and $B(X_0)$ are based on a parameterisation derived from test beam results [109].

Non-uniformity correction

The measured energy of the scattered electron may be over or under-estimated depending on the position of the electron in the calorimeter due to non-uniformities. These non-uniformities are due to gaps and structures in the construction of the calorimeter. For both the RCAL and the BCAL the non-uniformities are parametrised by comparing the measured energy of the electron to that predicted by the double angle method for both data and MC separately. In the RCAL this is done as a function of the x and y position of the electron, while in the BCAL it is done as a function of the electron angles and the distance to the cell and module edges.

In the RCAL energy loss due to the non-uniformities is more pronounced in cells near the beampipe. In these cells, the scattered electron enters the calorimeter almost parallel to the cell gaps, therefore losing a larger fraction of its energy in dead material within the calorimeter. As with the RCAL, energy losses occur in dead material between the cell gaps of the BCAL. In the gaps between modules the electron energy

is overestimated, because the electron enters the module cracks perpendicular to the CAL face and the shower develops parallel to the wavelength shifters. To take the non-uniformity of the RCAL and BCAL into account, existing routines are used.

5.6.3 Energy scale and resolution

After the dead material and non-uniformity corrections have been applied there is still a significant discrepancy between the data and MC. This is especially visible in the δ_{tot} and E_e distributions (see figure 5.9). Previous NC analyses [1] have shown that these discrepancies are due to the electron energy scale and resolution in the MC differing from that of the data. The electron energy scale and resolution in data and MC are studied by taking the ratio of E_e^{cor}/E_{DA} in bins of E_{DA} (figure 5.10) for the RCAL and BCAL separately⁵, where E_e^{cor} is the electron energy after all corrections have been applied. The E_e^{cor}/E_{DA} distribution for each E_{DA} bin is fitted with a Gaussian function, the mean and sigma of the fit becoming the energy scale and resolution respectively. A constant is fitted to the ratio of the energy scales for MC and data (MC/data) for both the RCAL and BCAL. The difference between the data and MC energy scales is found to be within 1%, as summarized in table 5.5. The MC is then scaled by these factors.

In figure 5.11 the electron energy resolutions in the RCAL and BCAL are shown for data and MC. To determine the energy dependence of the resolution in the RCAL and BCAL, the data and MC are fitted with the formula:

$$\frac{\sigma(E)}{E} = \frac{a}{\sqrt{E_{DA}}} + b + \frac{c}{E_{DA}}, \quad (5.7)$$

where a , b and c are the parameters of the fit. The electron energy resolution in the MC is found to be better than data. To obtain a correction factor, the quadratic difference, $\sqrt{\sigma_{data}^2 - \sigma_{MC}^2}$, is calculated and fitted with a 0th order polynomial. The result of the fit is a smearing factor, summarised in table 5.5, which is applied to the

⁵The scale and resolution in the FCAL is not studied due to limited statistics.

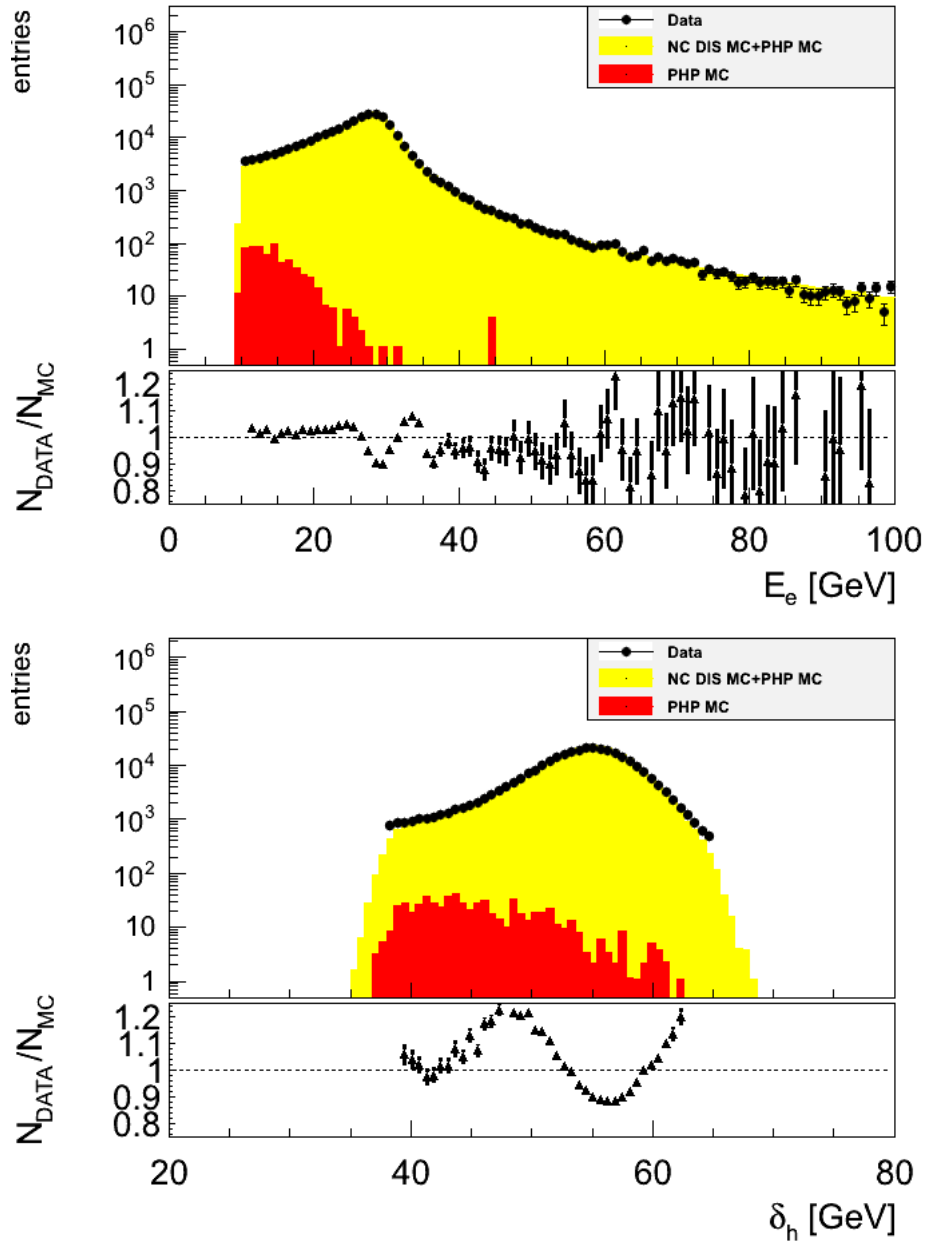


Figure 5.9: The E_e (top) and δ_{tot} (bottom) distributions before applying electron energy scale and resolution corrections. The black points are data, the yellow histogram is NC DIS MC plus PHP MC and the red histogram is PHP MC. The ratio of data to MC is shown below.

	RCAL	BCAL
Shift	-0.7%	-1.1%
Smear	3.22%	2.93%

Table 5.5: Summary of the factors used to scale and smear the MC for the RCAL and BCAL.

MC according to:

$$E_e^{cor} = (1 + SG)E_e, \quad (5.8)$$

where E_e^{cor} is the corrected electron energy, E_e is the unsmeared electron energy, S is the smearing factor, and G is a random variable generated according to a Gaussian distribution of zero mean and unit variance.

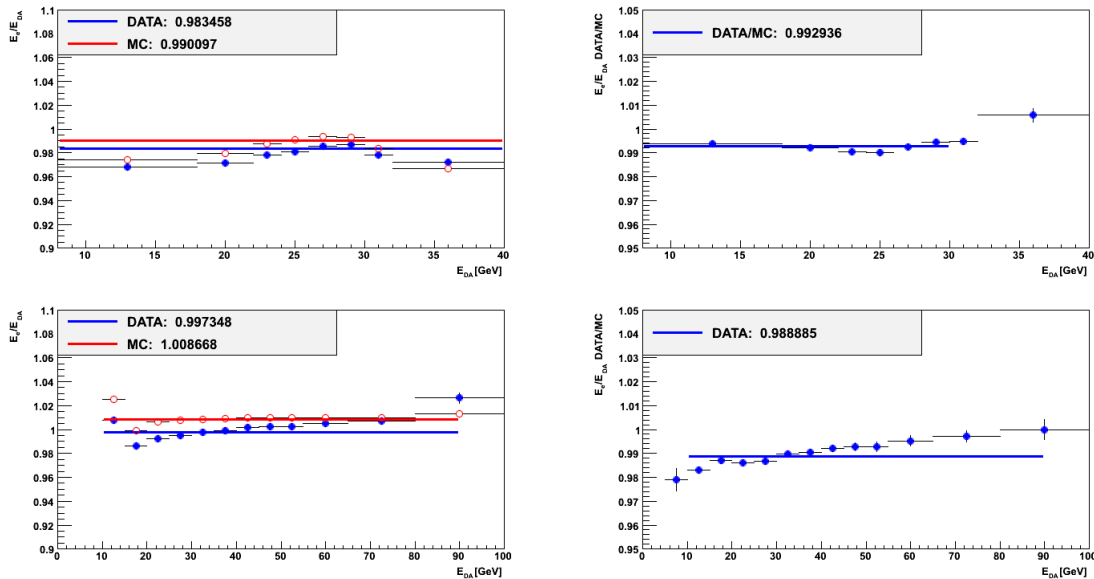


Figure 5.10: E_e/E_{DA} distributions for the RCAL (top left) and BCAL (bottom left). The blue points are data and the red points are NC DIS MC. The ratios of data and MC for the RCAL and BCAL are shown on the top right and bottom right for the RCAL and BCAL, respectively.

The effect of applying the electron energy scale and resolution corrections to the MC is seen in figure 5.12, where the description of the data by the MC is improved. The uncertainty of the fits to the electron energy scale and resolution is large, and the systematic effects of varying the factors are discussed in section 7.3.

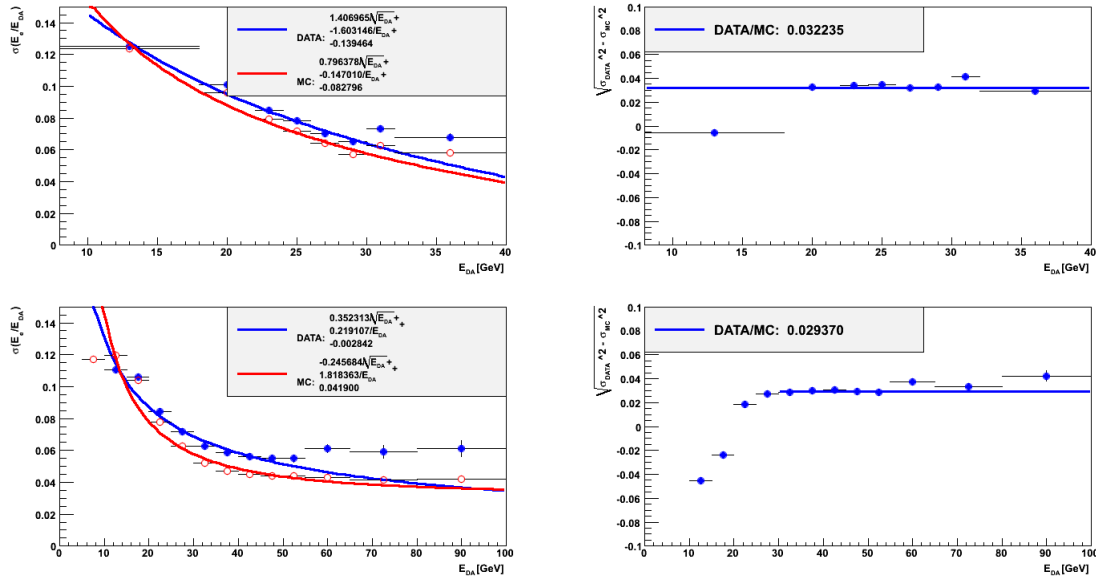


Figure 5.11: The resolution distributions for the RCAL (top left) and BCAL (bottom left). The blue points are data, and the red points are NC DIS MC. $\sqrt{\sigma_{data}^2 - \sigma_{MC}^2}$ is shown for the RCAL (top right) and BCAL (bottom right).

5.7 Z_{vtx} re-weighting

5.7.1 Introduction

The determination of the primary vertex (see section 4.3.3), especially the z -coordinate, Z_{vtx} , is crucial to the reconstruction of a NC event. Due to the use of the double angle method for the measurement of the kinematic variables, the reconstruction of the polar and azimuthal angles requires the input of the Z_{vtx} . The trigger and detector acceptances also depend on the Z_{vtx} . It is important that the Z_{vtx} distribution accurately describes the “true” Z_{vtx} ⁶ distribution of the data. The aim of Z_{vtx} re-weighting is to re-weight the MC to account for any discrepancy.

5.7.2 The Z_{vtx} distribution

Although most events originate near the nominal $Z_{vtx} = 0$ cm position there are a number of effects due to the bunch structure of the electron and proton beams, discussed in section 2.1.1, that make the tails of the Z_{vtx} distribution large. The

⁶The “true” Z_{vtx} distribution is the underlying Z_{vtx} distribution, without the biasing effects of the reconstruction, due to the bunch structure of the electron and proton beams (see section 5.7.1).

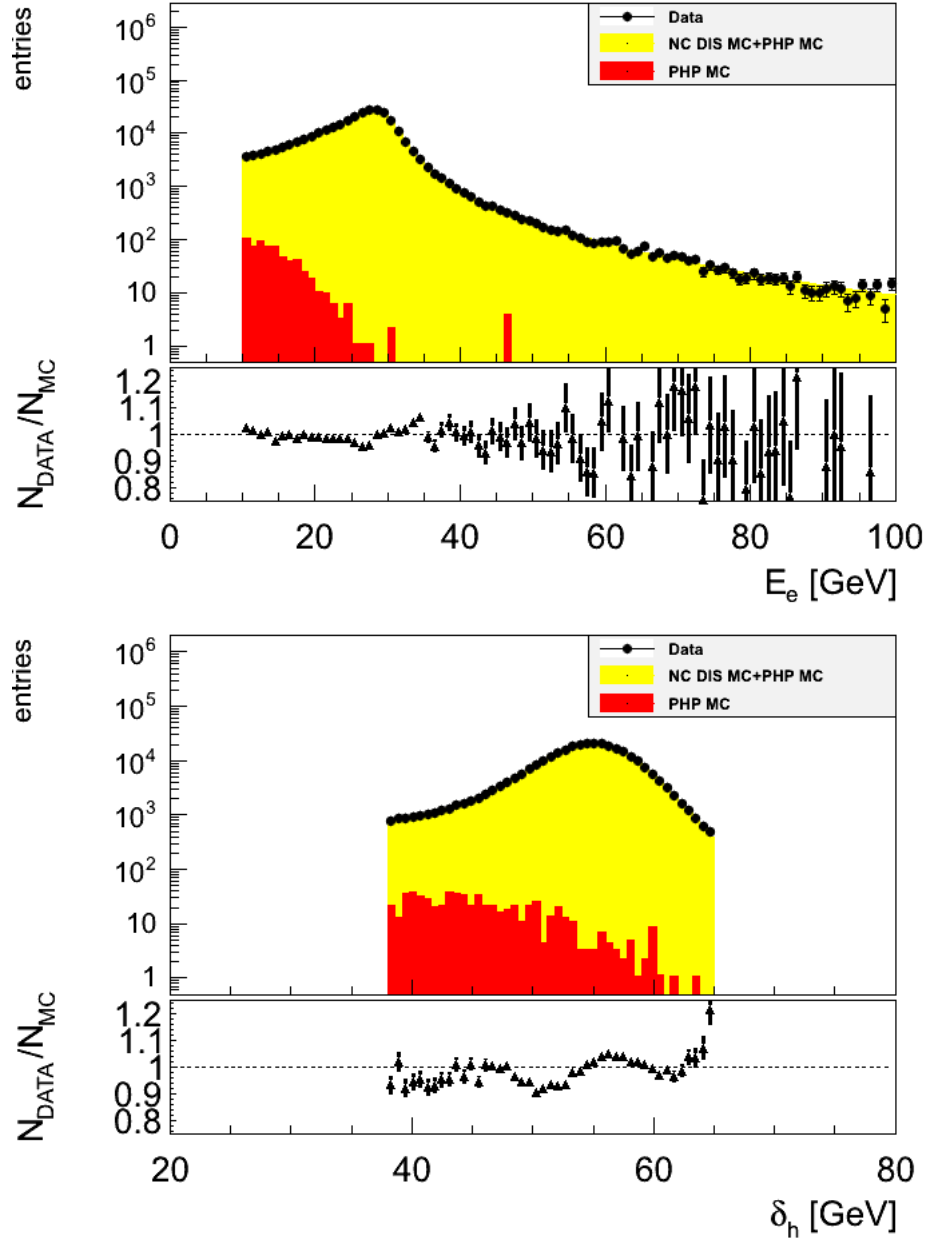


Figure 5.12: The E_e (top) and δ_{tot} (bottom) distributions after applying electron energy scale and resolution corrections. The black points are data, the yellow histogram is NC DIS MC plus PHP MC and the red histogram is PHP MC. The ratio of data to MC is shown below.

electron and proton bunches have a length of 0.83 cm and 8.5 cm respectively. The Z_{vtx} distribution is thus dominated by the proton bunch length. This gives rise to a large central peak in the Z_{vtx} distribution between ± 10 cm. Due to the bunch structure of the beam and limitations of the accelerator system when injecting beams into HERA, the nominally empty bunches surrounding the colliding bunches may be partially filled and are called “satellite bunches”. Two situations can occur:

1. The nominal proton bunch interacts with an electron satellite bunch (electron satellite peak) (± 30 cm).
2. The nominal electron bunch interacts with a proton satellite bunch (proton satellite peak) (± 70 cm).

These two situations produce “satellite peaks”. Satellite bunches may interact with one another. The Z_{vtx} distribution consists of a central peak, two electron satellite peaks, two proton satellite peaks and small effects that arise from collisions between satellite bunches.

5.7.3 NC event selection

The NC event selection, described in section 6.5, biases the measurement of the Z_{vtx} . The tracking selection, for instance, preferentially selects events that have a well reconstructed vertex near the nominal interaction point due to the detector geometry. To determine the true Z_{vtx} distribution, an event selection which minimises the bias introduced by the normal NC event selection is used:

- Trigger selection: Identical to that described in section 6.3.
- Electron selection:
 - $P_{grand} > 10^{-3}$
 - $E_e > 15$ GeV
 - $E_{iso} < 5$ GeV

- $10^\circ < \theta_e < 140^\circ$
- Kinematic:
 - $Q_{DA}^2 > 185 \text{ GeV}^2$
 - $y_{el} < 0.95$
- Background rejection:
 - $38 < \delta_{tot} < 65 \text{ GeV}$
 - $\frac{P_T}{\sqrt{E_T}} < 4 \sqrt{\text{GeV}}$
 - $\frac{P_T}{E_T} < 0.7$
 - $y_{JB}(1 - x_{DA})^2 > 0.004$
- Detector Geometry:
 - Supercrack cut
 - RCAL chimney cut
 - Electron radius in RCAL

The cuts listed above are described in further detail in section 6.5. The cut on the electron energy is raised from 10 GeV to 15 GeV to reject contamination from background sources due to the removal of tracking requirements from the electron selection.

5.7.4 Efficiencies

The main tool used in this analysis to ensure an unbiased vertex selection is the efficiency:

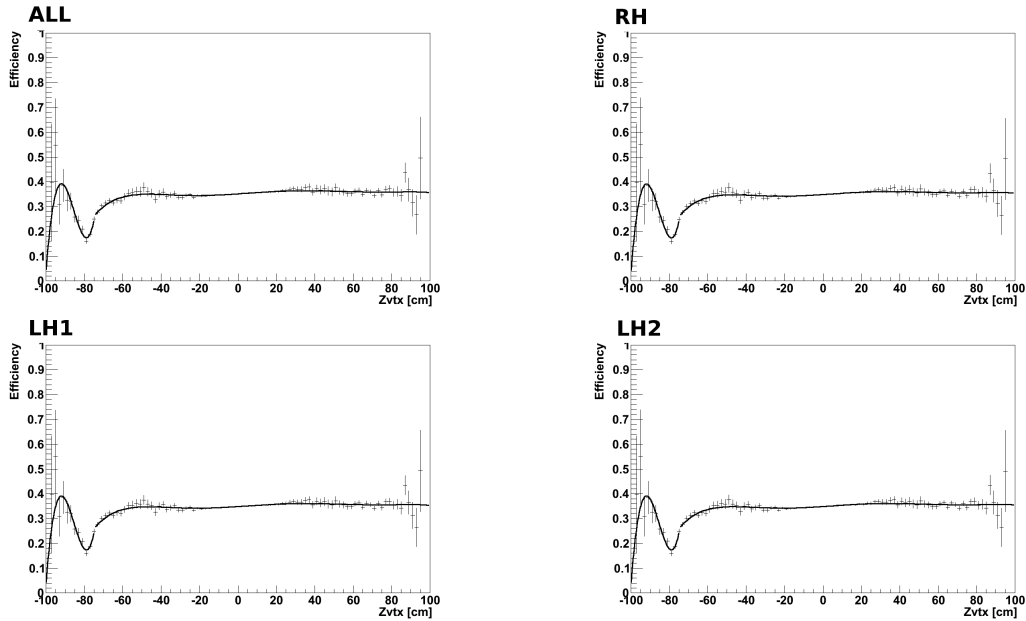
$$Efficiency = \frac{\text{Number of reconstructed events passing all selection cuts (see section 5.7.3)}}{\text{Number of generated events}} \quad (5.9)$$

	$-100 \text{ cm} < Z_{vtx} < -75 \text{ cm}$			
ALL	99.1	3.51	0.0414	$1.61 \cdot 10^{-4}$
RH	76.6	2.65	0.0303	$1.15 \cdot 10^{-4}$
LH1	84.5	2.93	0.0337	$1.28 \cdot 10^{-4}$
LH2	84.7	2.94	0.0338	$1.28 \cdot 10^{-4}$

	$-100 \text{ cm} < Z_{vtx} < 100 \text{ cm}$						
ALL	0.355	$6.73 \cdot 10^{-4}$	$1.99 \cdot 10^{-6}$	$-4.63 \cdot 10^{-7}$	$2.17 \cdot 10^{-9}$	$9.10 \cdot 10^{-11}$	$-8.00 \cdot 10^{-13}$
RH	0.379	$6.61 \cdot 10^{-4}$	$1.12 \cdot 10^{-5}$	$-3.42 \cdot 10^{-7}$	$-2.55 \cdot 10^{-9}$	$6.33 \cdot 10^{-11}$	$-1.26 \cdot 10^{-13}$
LH1	0.349	$5.32 \cdot 10^{-4}$	$1.23 \cdot 10^{-5}$	$-3.30 \cdot 10^{-7}$	$-2.65 \cdot 10^{-9}$	$6.21 \cdot 10^{-11}$	$-9.96 \cdot 10^{-14}$
LH2	0.349	$5.30 \cdot 10^{-4}$	$1.23 \cdot 10^{-5}$	$-3.31 \cdot 10^{-7}$	$-2.66 \cdot 10^{-9}$	$6.23 \cdot 10^{-11}$	$-9.84 \cdot 10^{-14}$

Table 5.6: Parameters for the fit to the Z_{vtx} efficiency for each running period.

using the 2006-2007 e^+p inclusive MC described in section 3.2.1. The efficiencies are determined for each running period, as show in figure 5.13. The efficiency is flat across most of the region of $-100 \text{ cm} < Z_{vtx} < 100 \text{ cm}$ with a dip in the efficiency at $\approx -75 \text{ cm}$ whose cause is unknown. To parametrize the efficiency a 6th order polynomial is fitted in the range $-75 \text{ cm} < Z_{vtx} < 100 \text{ cm}$ and a 3rd order polynomial to the $-100 \text{ cm} < Z_{vtx} < -75 \text{ cm}$. The parameters of the fits to the efficiencies are shown in table 5.6.

Figure 5.13: Z_{vtx} efficiencies for ALL (top left), RH (top right), LH1 (bottom right) and LH2 (bottom left) running periods. The black line is the fit to efficiency.

The efficiencies determined from the MC are then used to obtain the true Z_{vtx} distribution from the reconstructed Z_{vtx} distribution in data. This is achieved by

scaling each bin of the the reconstructed Z_{vtx} distribution by the reciprocal of the efficiency evaluated at the bin centre. Once scaled the Z_{vtx} distribution in data can be directly compared to the generated MC Z_{vtx} distribution.

5.7.5 Fitting

In section 5.7.2 the general shape of the Z_{vtx} distribution is outlined, and is used to determine a plausible function to fit to the true Z_{vtx} distribution. The sum of seven Gaussians, consisting of a central Gaussian peak, two proton satellite Gaussian peaks, two electron satellite peaks and two additional Gaussians to account for collisions between satellite bunches, is used to fit the true Z_{vtx} distribution in data. To constrain the fit, the proton satellites are assumed to have identical width and mean. The same assumption is made in the case of the electron satellite peaks and the two peaks corresponding to collisions between satellite peaks. The function fit to the true data Z_{vtx} distribution is given as:

$$A_1 e^{-\frac{(x-a)^2}{2\sigma_1^2}} \quad (5.10)$$

$$+ B_1 e^{-\frac{(x-(30+b))^2}{2\sigma_2^2}} + B_2 e^{-\frac{(-x-(30+b))^2}{2\sigma_2^2}} \quad (5.11)$$

$$+ C_1 e^{-\frac{(x-(60+b))^2}{2\sigma_2^2}} + C_2 e^{-\frac{(-x-(60+b))^2}{2\sigma_2^2}} \quad (5.12)$$

$$+ D_1 e^{-\frac{(x-(72+c))^2}{2\sigma_3^2}} + D_2 e^{-\frac{(-x-(72+c))^2}{2\sigma_3^2}}. \quad (5.13)$$

The resulting fits for each running period are shown in figure 5.14 and the associated parameters are tabulated in table 5.7.

5.7.6 Reweighting

The resulting fits to the true Z_{vtx} distribution in data, described in section 5.7.5, are divided by the generated Z_{vtx} distribution of the MC. This ratio is then used to re-weight the reconstructed Z_{vtx} in MC. The Z_{vtx} re-weighting values show that true Z_{vtx} distribution in data has changed through the different running periods periods

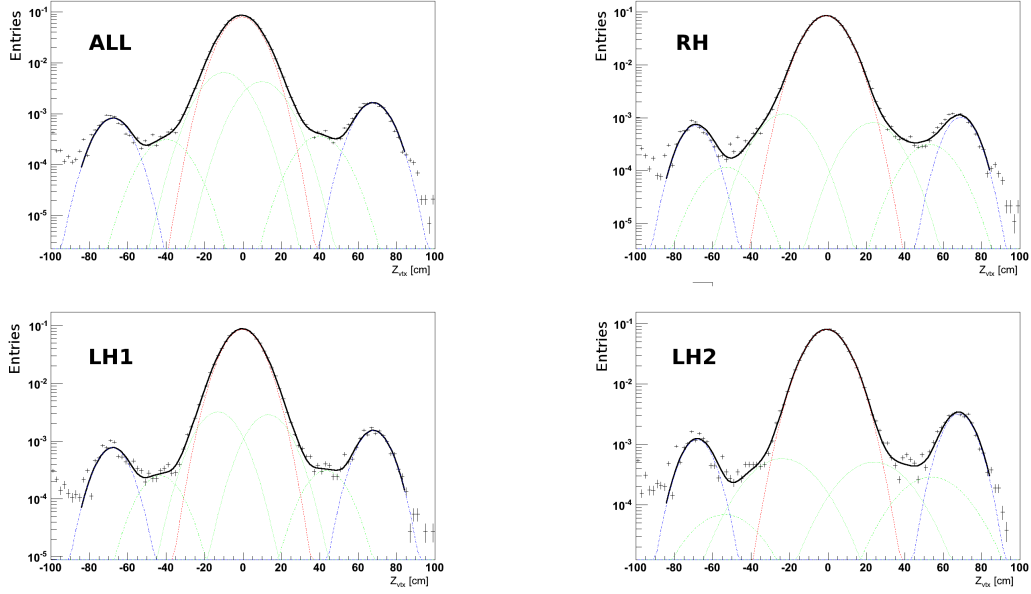


Figure 5.14: Fits to the Z_{vtx} distribution in data after the efficiency from MC has been applied for ALL (top left), RH (top right), LH1 (bottom right) and LH2 (bottom left) running periods. The black line is the fit to the entire Z_{vtx} distribution.

	A_1	B_1	B_2	C_1	C_2	D_1	D_2
ALL	0.0796	$4.27 \cdot 10^{-3}$	$6.47 \cdot 10^{-4}$	$3.64 \cdot 10^{-4}$	$3.11 \cdot 10^{-4}$	$1.65 \cdot 10^{-3}$	$8.20 \cdot 10^{-4}$
RH	0.0855	$8.13 \cdot 10^{-4}$	$1.18 \cdot 10^{-3}$	$3.15 \cdot 10^{-4}$	$1.15 \cdot 10^{-4}$	$1.03 \cdot 10^{-3}$	$7.18 \cdot 10^{-4}$
LH1	0.0859	$2.88 \cdot 10^{-3}$	$3.23 \cdot 10^{-3}$	$3.12 \cdot 10^{-4}$	$2.55 \cdot 10^{-4}$	$1.54 \cdot 10^{-3}$	$7.74 \cdot 10^{-4}$
LH2	0.0809	$5.10 \cdot 10^{-4}$	$5.87 \cdot 10^{-4}$	$2.89 \cdot 10^{-4}$	$6.91 \cdot 10^{-5}$	$3.26 \cdot 10^{-3}$	$1.21 \cdot 10^{-3}$

	a	b	c	σ_1	σ_2	σ_3
ALL	-0.597	-20.2	-4.16	8.35	9.82	7.77
RH	-0.993	-6.96	-2.86	8.85	10.65	6.95
LH1	-0.341	-16.9	-3.97	8.34	9.24	7.39
LH2	-0.680	-6.05	-3.78	9.14	14.7	7.13

Table 5.7: Parameters for the fit to the data Z_{vtx} distribution.

of the data, particularly during the LH2 period.

The results presented in 5.15 and 5.16 show the reconstructed Z_{vtx} from data along with the MC before and after the re-weighting procedure has been applied for two regions: from $-100 \text{ cm} < Z_{vtx} < 100 \text{ cm}$ and the restricted region of $-30 \text{ cm} < Z_{vtx} < 30 \text{ cm}$ used in the NC selection of this analysis. The improvement in the Z_{vtx} description by the MC can be clearly seen after the re-weighting procedure has been applied. The effect on the normalisation between data and the MC varies greatly between running periods, from increasing the amount of MC by 0.37% (RH) and decreasing the amount of MC by -2.5% (LH2).

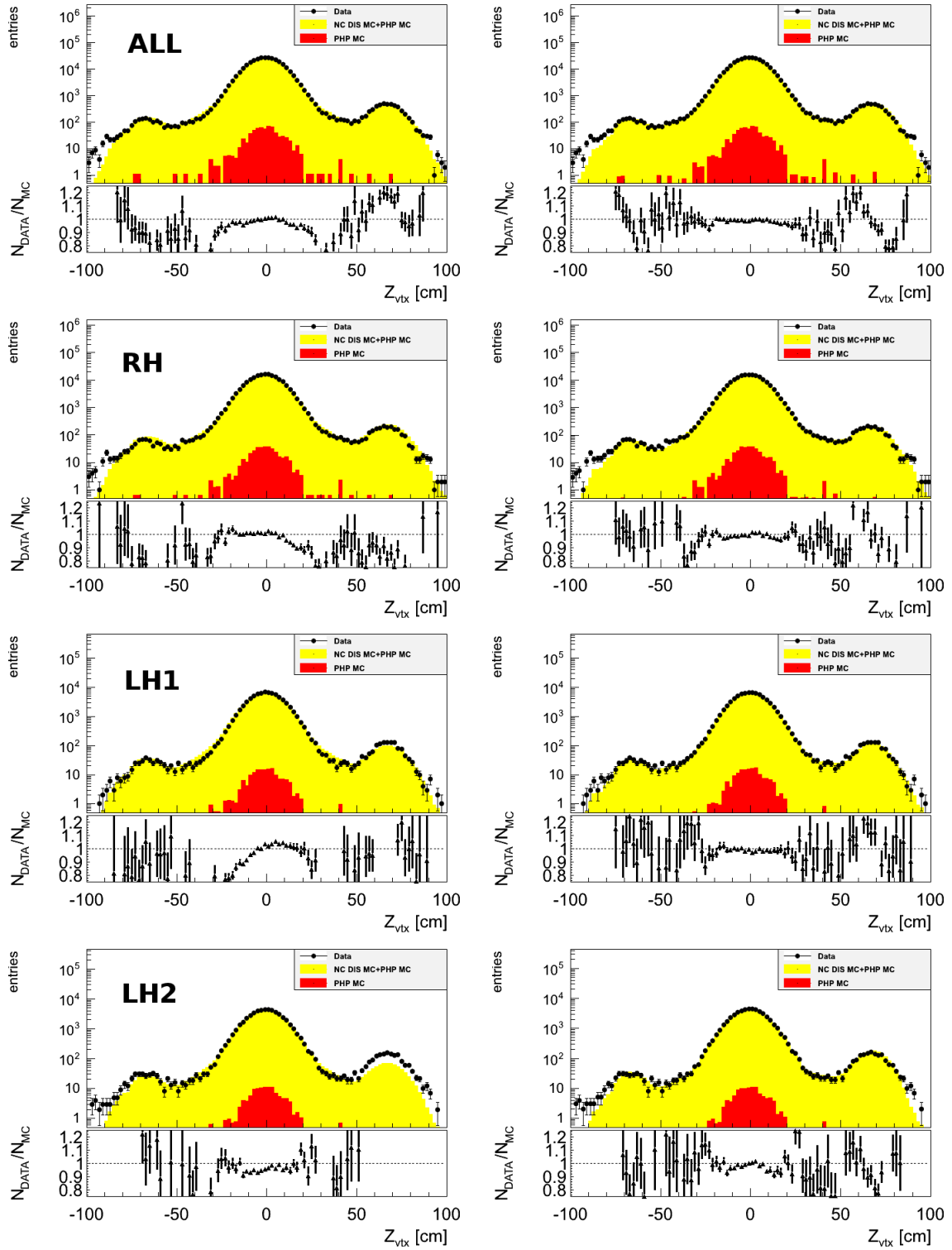


Figure 5.15: The Z_{vtx} distributions for the range $|Z_{vtx}| < 100\text{cm}$ before Z_{vtx} re-weighting (left) and after Z_{vtx} re-weighting (right) for the ALL, RH, LH1 and LH2 running periods. The data is shown as points, the yellow histogram is the NC DIS MC plus PHP MC and the red histogram is the contribution from the PHP MC. The ratio of data to MC is shown below each Z_{vtx} distribution.

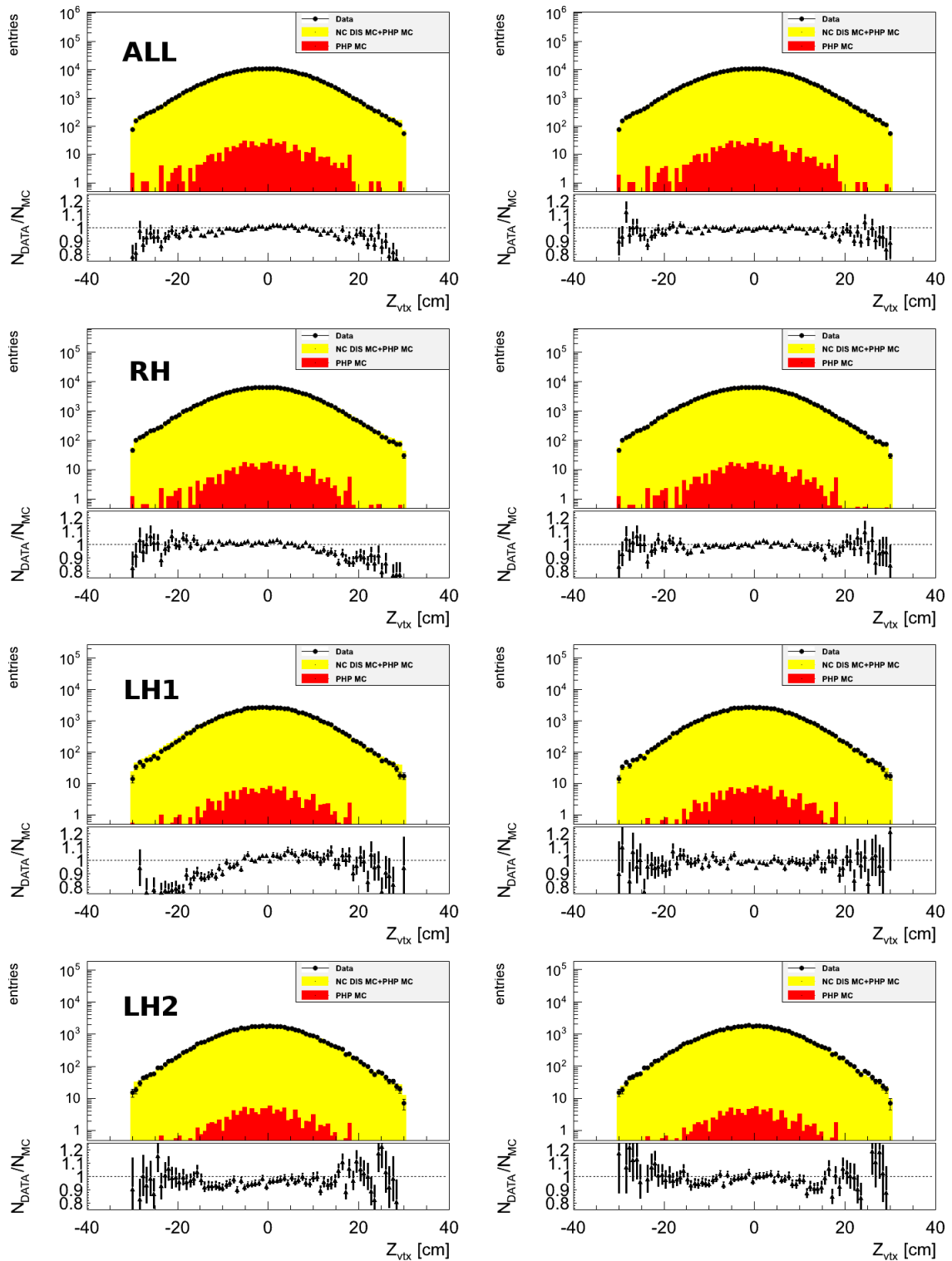


Figure 5.16: The Z_{vtx} distributions for the range $|Z_{vtx}| < 30$ cm before Z_{vtx} re-weighting (left) and after Z_{vtx} re-weighting (left) for the ALL, RH, LH1 and LH2 running periods. The data is shown as points, the yellow histogram is the NC DIS MC plus PHP MC and the red histogram is the contribution from the PHP MC. The ratio of data to MC is shown below each Z_{vtx} distribution.

Chapter 6

Data Selection

In Section 4.1 the characteristics of a NC event are discussed in broad terms: the presence of a scattered isolated electron in the calorimeter balanced in transverse momentum by the hadronic final state, consisting of a cluster of particles in the struck quark direction and the proton remnant in the forward direction. In addition to NC DIS events there are several background sources that can make energy deposits in the calorimeter that may be mistaken for an electron. This chapter begins by discussing the characteristics of NC DIS events in more detail, and the different background sources, in terms of observable quantities of the ZEUS detector. Sections 6.3 and 6.5 then present the preselection criteria, performed online by the trigger, and the offline requirements which select NC DIS events and reject background events.

6.1 NC event characteristics

The scattered electron is typically detected as an isolated shower contained in the electromagnetic calorimeter which is pointed to by a track originating from the interaction vertex. At low and medium Q^2 , where $Q^2 < 500 \text{ GeV}^2$, the electron is typically scattered at large angles¹ and is found in the RCAL. In events with higher Q^2 values, $Q^2 > 500 \text{ GeV}^2$, the electron is found in the BCAL or, for the highest Q^2 events,

¹The scattering angle is large due to the electron scattering angle being measured with respect to the proton beam.

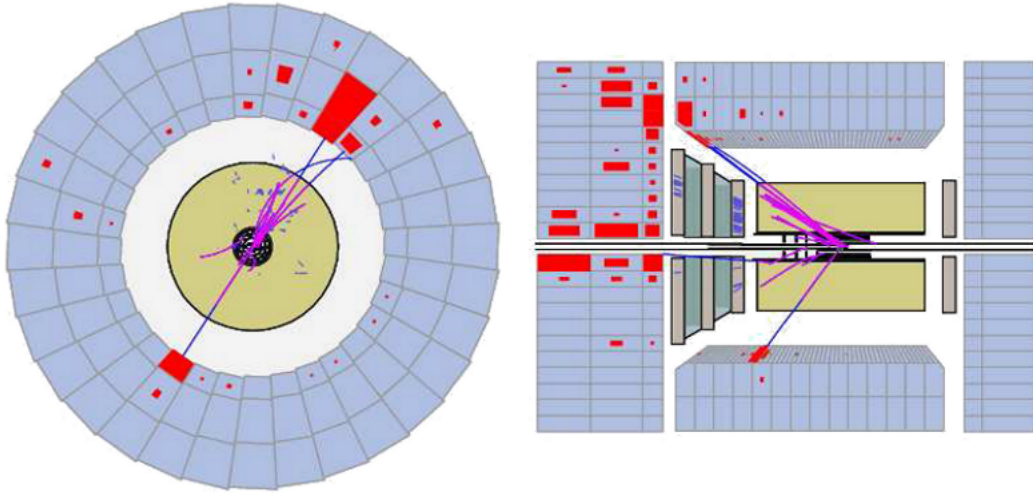


Figure 6.1: A typical NC event in the ZEUS detector. The $x - y$ -view is on the left and the $z - r$ -view is on the right. Lines emerging from the event vertex represent the tracks, while the red block depict energy deposits in the CAL.

in the FCAL. Equations 4.6 and 4.8 show that the energy of the scattered electron increases with both Q^2 and x . Momentum conservation requires that the transverse momentum of the electron be balanced by the hadronic transverse momentum. The scattering angle of the hadronic system is directly related to x . At low x , where the struck quark carries little of the proton's momentum, the hadronic system is scattered in the rear direction. At high x the quark carries a significant fraction of the incoming proton's momentum and is scattered in the forward direction.

The variable δ_{tot} is defined as (neglecting masses):

$$\delta_{tot} = \sum_i (E - P_z)_i = \sum_i (E_i - E_i \cos \theta_i), \quad (6.1)$$

where the sum runs over all the energy deposits in the calorimeter, E_i , with an angle θ_i as measured from the calorimeter position and the interaction point. In the initial state δ_{tot} can be written as:

$$\delta_{tot} = \delta_h + \delta_e = (E_p - E_p) + (E_e - (-E_e)) = 2E_e (= 55 \text{ GeV}). \quad (6.2)$$

Since both energy and momentum are conserved in the interaction, the value of δ_{tot} in the final state should also be equal to 55 GeV (assuming that $\delta_{beam\ pipe} = \sum_i E_i - P_{z,i} =$

$E_i(1 - \cos\theta_i) \approx 0$, where the sum runs over particles escaping down the forward beampipe) for well reconstructed NC DIS events.

Another variable that characterises NC DIS events is the net transverse momentum, P_T :

$$P_T^2 = p_x^2 + p_y^2 = \left(\sum_i E_i \sin\theta_i \cos\phi_i\right)^2 + \left(\sum_i E_i \sin\theta_i \sin\phi_i\right)^2, \quad (6.3)$$

where the sums run over all the energy deposits in the calorimeter, and ϕ_i is the azimuthal angle. Since the initial state has zero transverse momentum, P_T^2 for a well reconstructed NC DIS event should also be zero, again assuming negligible contribution from particles escaping down the beampipe.

6.2 Background Characteristics

6.2.1 Photoproduction

Photoproduction (PHP) (see figure 6.2), where the electron emits a quasi-real photon ($Q^2 \approx 0$) which scatters off the proton, is the most important background source for this analysis. The electron is deflected by a small angle and continues down the rear beampipe undetected. A PHP event can be misidentified as a NC event if one of the particles of the hadronic final state leaves a signal in the EMC portion of the calorimeter consistent with an electron (such as the decay of a π^0 into photons). There are several methods of rejecting these events. As discussed in section 6.1, δ_{tot} is insensitive to the loss of particles down the forward beampipe. This is not true for particles lost down the rear beampipe where E and P_z do not cancel but are additive, thus reducing the measured δ_{tot} by $\approx 2E_e$. Thus a lower cut on δ_{tot} helps to eliminate PHP events (see section 6.5). Also effective in rejecting PHP background is an isolation cut and minimum energy cut for the electron, since the fake electron in a PHP event is typically a low energy component of the hadronic final state.

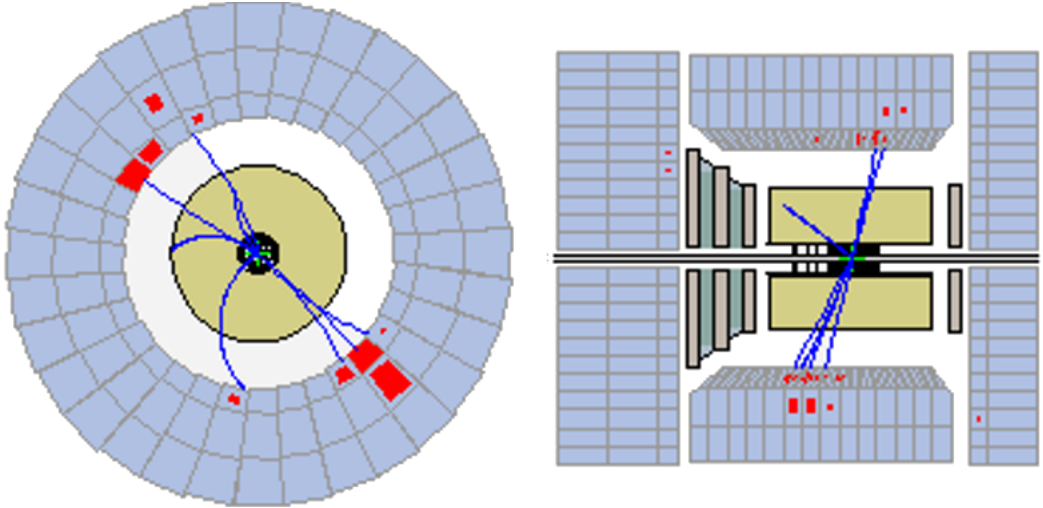


Figure 6.2: A typical PHP event in the ZEUS detector. The low energy deposits in the EMC section of the CAL can fake a NC event.

6.2.2 Elastic QEDC

QED Compton (QEDC) scattering denotes the reactions $ep \rightarrow e'\gamma p$ and $ep \rightarrow e'\gamma X$ where the incoming or scattered electron radiates a hard photon. Diagrams for QEDC are shown in fig 6.3. In QEDC events there are two distinct electromagnetic deposits in the calorimeter. This second electromagnetic cluster may be included in the hadronic system or be misidentified as the scattered electron, significantly altering the measured kinematic variables and migrating the event into high- Q^2 NC DIS events.

The first reaction $ep \rightarrow e'\gamma p$, where the proton stays intact and escapes down the beampipe, is called elastic QEDC. The event topology of elastic QEDC is two electromagnetic clusters balancing in transverse momentum, with no other energy deposits in the calorimeter. This simple topology of elastic QEDC events means that they can be easily rejected (details in section 6.5.4). The second reaction $ep \rightarrow e'\gamma X$, where the proton breaks up, is referred to as inelastic QEDC. Inelastic QEDC events exhibit a similar event topology to elastic QEDC but have hadronic energy deposits in the forward direction due to the breakup of the proton. Inelastic QEDC events are included in the DJANGO NC DIS MC used in this analysis. A previous study [78] showed that the DJANGO MC well describes the inelastic QEDC events selected from real data. Therefore they are not rejected in this analysis.

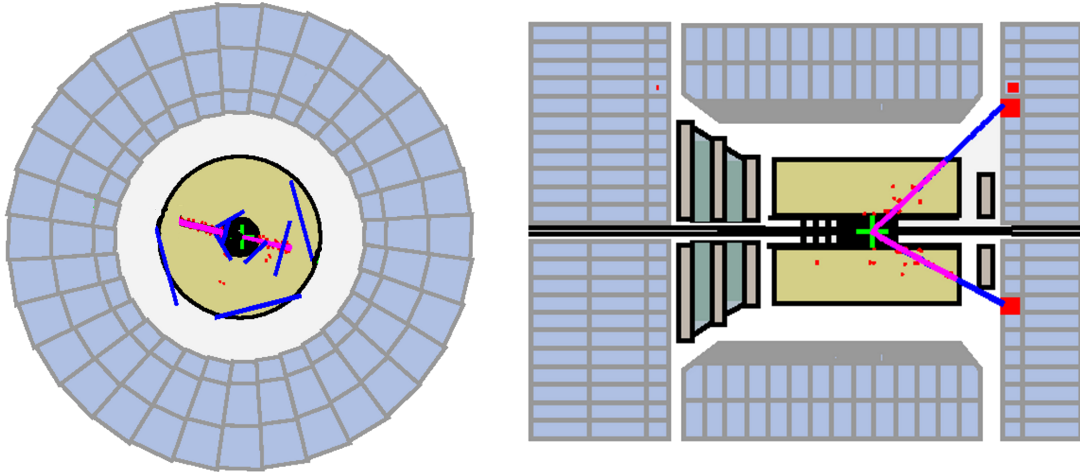


Figure 6.3: An elastic QEDC event in the ZEUS detector. The electron and photon are in the RCAL and balanced in P_T . Note the lack of energy deposits in the FCAL. Due to the distinct signature of elastic QEDC they can be easily rejected.

6.2.3 Beam-gas Interactions

The proton beam itself can act as a background source through two major processes: beam-gas interactions and beampipe collisions. Beam-gas interactions occur when protons in the beam interact with residual gas in the beampipe. Beam-gas events that occur upstream of the detector can be rejected by the veto wall (see section 2.2) and calorimeter timing cuts since these events do not occur at the ep bunch crossing time. Beam-gas interactions occurring within the ZEUS detector volume have most of their particles travelling at low polar angles in the FCAL and therefore have a low values of δ_{tot} . They can be rejected by the lower δ_{tot} cut used to reject PHP events.

The electron beam may also interact with the residual gas. Unlike proton beam-gas interactions, electron beam-gas interactions that occur in the detector volume are indistinguishable from normal DIS (equivalent to a electron scattering off a fixed target). A previous study [78] using the electron beam and an empty proton beam bunch, showed the contribution from this phenomenon can be ignored.

Due to the high rate at which beam-gas events occur compared to physics events, beam-gas events can occur during the same time as a NC DIS event. These events are known as overlay events and are rejected by an upper cut on the value of δ_{tot} (see section 6.5.4).

6.2.4 Cosmic and halo muons

There are two types of background sources involving muons, where the muon deposits energy in the EMC faking a scattered electron.

Cosmic muons (see figure 6.4) are produced from the interaction of high-energy cosmic rays with the upper atmosphere. Although the ZEUS detector is located 30 m underground, a fraction of high-energy cosmic muons can still reach the detector. Cosmic muons exhibit two main characteristics: they are independent of the beam crossing timing and they pass the upper part of the BCAL before reaching the bottom part of the BCAL. Thus, cosmic muons can be rejected by their timing information.

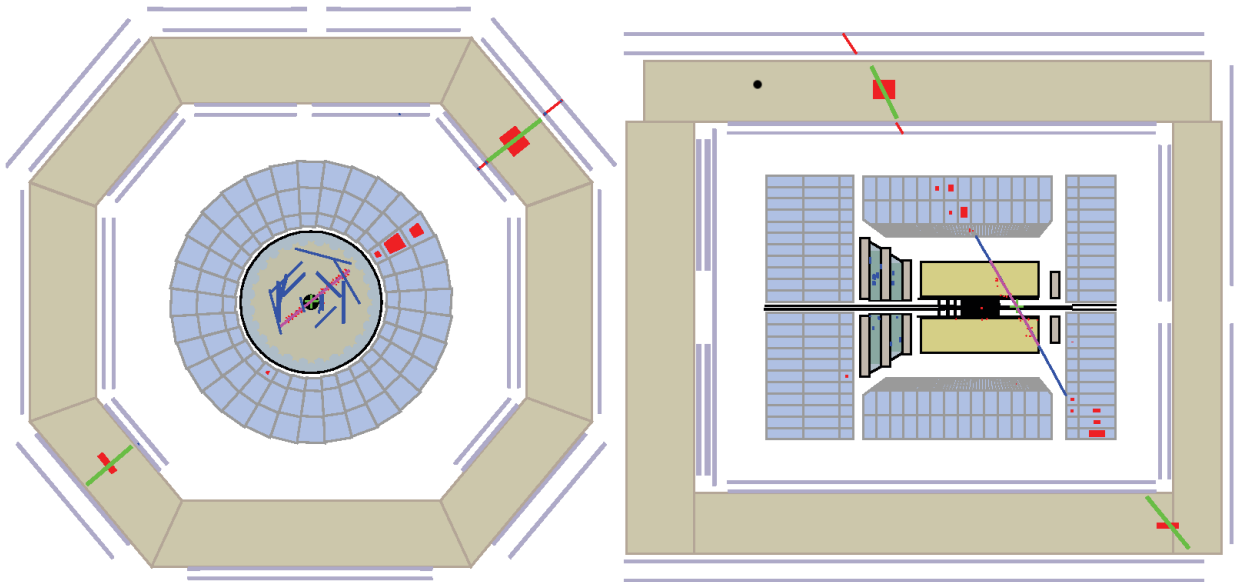


Figure 6.4: A cosmic muon event in the ZEUS detector. The muon enters the top of the detector, depositing energy in the BAC and BMUON chambers before passing through the central tracking region and out the other side of the detector.

Another type of muon background is that of halo muons (see figure 6.5), which are created from the decay of pions produced from the interactions of the proton beam halo with residual gas or accelerator components upstream of the detector. These muons pass through the veto wall and into the RCAL almost parallel to the beamline. Events that occur from ep bunch crossing within the detector have energy deposits in the FCAL and RCAL occurring at roughly the same time, while halo muons will first leave deposits in the RCAL then the FCAL. Thus halo muons can be

rejected easily using calorimeter timing information.

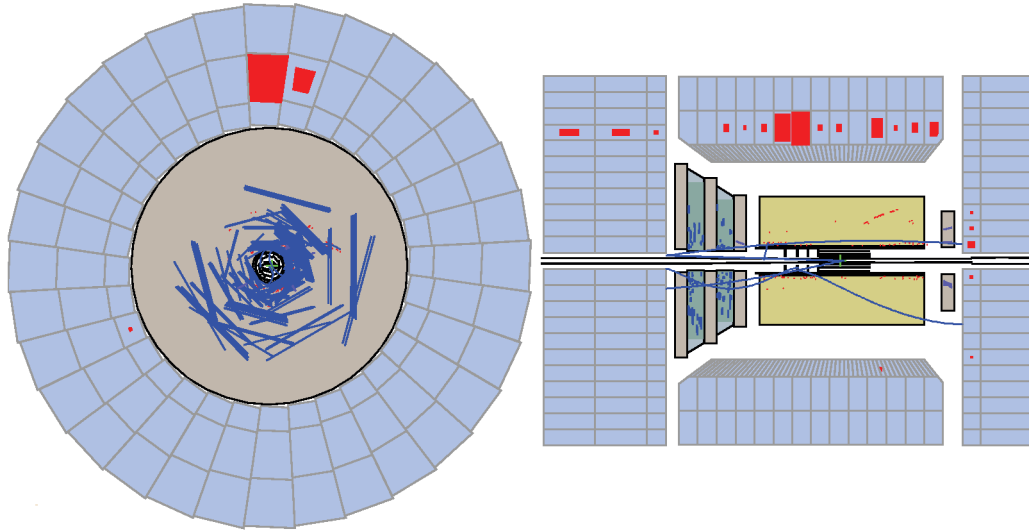


Figure 6.5: A halo muon event in the ZEUS detector. The muon passes through the calorimeter parallel to the beams and is not balanced in P_T .

Both halo and cosmic muons may be rejected using the total transverse momentum. Halo muons travel parallel to the beam, so energy deposits in the calorimeter will not be balanced in the transverse plane. The total transverse momentum of cosmic muon events will often be unbalanced if more energy is deposited on one side of the detector. The total vector sum of the transverse momentum P_T (see equation 6.3) and the scalar sum $E_{T,tot}$ are calculated, with $E_{T,tot}$ given as follows:

$$E_{T,tot} = \sum_i \sqrt{(p_{x,i})^2 + (p_{y,i})^2}, \quad (6.4)$$

where the index i runs over all calorimeter clusters. The total transverse momentum is expected to be close to zero for NC DIS events, but large for cosmic and halo muons. Background rejection using $P_{T,tot}$ and $E_{T,tot}$ is discussed further in section 6.5.4.

6.3 Trigger preselection

The event preselection by the ZEUS trigger aims to select NC DIS events, identified by the presence of a scattered electron, while rejecting as much background as possible. Thus the trigger must balance sometimes conflicting requirements of selecting a pure

NC DIS sample with as high efficiency as possible. To ensure the highest statistics at high Q^2 , where the cross section is six orders of magnitude smaller than in the lowest Q^2 bins, the trigger must be very efficient. The trigger preselection using the FLT, SLT and TLT are discussed in the following sections.

6.3.1 First level trigger

The FLT trigger bits in this analysis can be broadly divided into two categories: bits that detect the presence of an isolated electron (an isolated electron consists of a energy deposit in 1, 2, 3 or 4 sub-towers with no energy in the surrounding towers) in the calorimeter and inclusive bits that fire if a large energy deposit is found in the calorimeter. In addition to the isolated electron and calorimeter energy requirements most trigger bits have vetos based on the veto wall, C5, SRTD, timing information or the number of tracks. The tracking vetos require further explanation and careful analysis and are discussed in section 5.4.

Isolated electron bits

FLT 28 An isolated electron in either the RCAL or BCAL and track veto requirements.

FLT 30 An isolated electron in the EMC section of the RCAL with an energy greater than 4 GeV (15 GeV if in the first inner ring around the beampipe).

FLT 36 An isolated electron in the EMC section of the RCAL with an energy greater than 4 GeV (5 GeV if in the first inner ring around the beampipe) and track veto requirements.

FLT 39 An isolated electron in the EMC section of the BCAL with an energy greater than 3.5 GeV and track veto requirements.

FLT 46 An isolated electron in one of the quadrants of the EMC section, excluding the 3rd quadrant, of the RCAL with an energy greater than 2 GeV (4 GeV if in the first inner ring around the beampipe) and track veto requirements.

FLT 47 An isolated electron in one of the quadrants of the EMC section, excluding

the 3rd quadrant, of the RCAL with an energy greater than 2 GeV (4 GeV if in the first inner ring around the beampipe) and track and total calorimeter energy veto requirements.

Inclusive bits

FLT 40 A total energy in the EMC section of the calorimeter greater than 20 GeV and track veto requirements.

FLT 41 A transverse energy greater than 30 GeV in the calorimeter and track veto requirements.

FLT 43 A transverse energy greater than 15 GeV in the calorimeter and track veto requirements.

FLT 44 A total energy in the EMC section of the BCAL greater than 5 GeV or greater than 3.5 GeV in the EMC section of the FCAL and track veto requirements.

The event is accepted by the FLT if the logical OR of all the above FLT bits is true.

6.3.2 Second level trigger

At the second level trigger more time is available to reconstruct the event. This allows better electron finding algorithms to be used by dividing the CAL into finer segments, and the ability to use timing information to veto background events. The SLT reconstruction of the event is still coarse compared to the offline reconstruction. As with the FLT, the SLT bits used in this analysis can be divided into two categories: isolated electrons and inclusive bits.

Isolated electrons

DIS 07 An electron candidate with an energy greater than 5 GeV, $\delta_{tot} + 2E_{PCAL}$ more than 2.5 (10) GeV in the EMC section of the RCAL/BCAL (FCAL) and FLT bit 28, 30, 31, 36, 39, 40, 41, 43, 44, 46, 47 or 62.

Inclusive

EXO 01 A total transverse energy > 35 GeV.

EXO 02 A total transverse energy > 15 GeV if FLT28 is taken or a total transverse energy > 25 GeV and $\delta_{tot} > 15$ GeV.

EXO 03 A total transverse energy of 16 GeV and $\delta_{tot} > 34$ GeV.

6.3.3 Third level trigger

At the TLT information is available from all the detector components. The longer time available for processing the event, compared to the FLT and SLT, allows a slightly simplified version of the offline reconstruction software to be run. This allows an event to be reconstructed including tracking, which allows the Z_{vtx} to be reconstructed and therefore provides a more precise δ_{tot} determination. More complicated electron finders can be run to identify the scattered electron and classify the event as NC DIS. Additionally, the tracking information is used together with the muon chambers and calorimeter information to reject cosmic and halo muons.

Only one TLT bit is used in this analysis, **DIS 03**, which requires the following:

- DIS FLT and SLT trigger bits. The FLT bits require a certain amount of energy in the calorimeter and an isolated electron. The SLT trigger bits require the same information and add the measurement of δ_{tot} .
- $\delta_{tot} + 2E_{PCAL} > 30$ GeV.
- $\delta_{tot} < 100$ GeV.
- An electron candidate with an energy greater than 4 GeV (outside a 35 cm radius) in the RCAL.
- A reconstructed Z_{vtx} .

6.4 Data quality requirements

In order to ensure that all essential components of the ZEUS detector needed to measure each NC event are operational, additional data quality criteria are applied to each event. These criteria are called TAKES. For each run used in this analysis the following TAKES are required:

- **EVTAKE:**
 - The CTD must be at full voltage and have no large dead sections.
 - The lumi system must be functioning.
 - The magnetic field must be on and at full strength.
 - The calorimeter must be on and have few bad channels or holes.
- **MVDTAKE:**
 - The MVD must be on.
- **STTTAKE:**
 - The STT must be on.

The polarisation system must be operational as the analysis relies on an accurate determination of the average polarisation. This requirement is handled by two TAKES, TPOLTAKE and LPOLTAKE, and are treated differently from the above TAKES and must be applied for each event. As luminosity values are available for either the LPOL or the TPOL (see sections 2.1.4 and 2.2.7) a simple logical OR between the two takes cannot be used. TPOLTAKE is required when the TPOL luminosity value is used and LPOLTAKE is required when the LPOL luminosity is used.

6.5 Event Selection

Events that pass the trigger preselection, described in the previous section, are then required to pass further selection criteria. The final selection criteria can be divided

into several subcategories: positron selection, phase space, background suppression and MC validity. The description and motivation for each selection criterion are presented in the following sections. Accompanying the text are several figures which illustrate the applied cuts. These figures are presented with the entire selection criteria except for the requirement being discussed. This is done to make clear the reasons for each selection criterion.

6.5.1 Positron selection

The aim of the positron selection is to find the scattered positron with high efficiency and purity. The EM electron finder is described in section 4.3.4 and is used to select positron candidates that are then required to pass the following criteria:

- **Positron candidate:** If more than one positron candidate is found the candidate with the highest selection probability is selected.
- **Positron probability:** The EM grand probability, P_{grand} , is required to have a high value to ensure high purity:

$$P_{grand} > 10^{-3}. \quad (6.5)$$

Figure 6.6 shows the distribution of the grand probability for data and MC.

- **Positron energy:** The PHP background is relatively large at low E'_e where low energy pions decay into photons faking a positron (see figure 6.6). To ensure that the positron sample has a high purity E'_e is required to be:

$$E'_e > 10 \text{ GeV}. \quad (6.6)$$

- **Isolation Energy:** The scattered positron in NC DIS events are balanced back-to-back with the hadronic system, thus the scattered positron should be well isolated. Fake positron candidates in background events need not be isolated,

and are often surrounded by activity in the calorimeter not assigned to the positron. The positron isolation energy, E_{iso} , is defined as energy deposits not assigned to the positron candidate in a $\eta - \phi$ cone centred on the candidate with a radius of $R_{cone} = 0.8$. The cone radius R_{cone} is defined as $R_{cone} = \sqrt{(\Delta\phi)^2 + (\Delta\eta)^2}$, where $\Delta\eta$ ($\Delta\phi$) is the difference between the pseudorapidity (azimuthal angle) of the positron candidate and the calorimeter deposit. E_{iso} is required to be:

$$E_{iso} < 5 \text{ GeV}. \quad (6.7)$$

The E_{iso} distribution is shown in figure 6.7. Most NC DIS events have E_{iso} close to zero, while the PHP events have E_{iso} evenly distributed. Therefore the fractional contamination of PHP events at large values of E_{iso} is high.

- **Track matching:** A matched track is required if the positron is in the CTD acceptance (see section 5.5) to reject photons which have a calorimeter energy deposit similar to a positron but no track.
- **Track momentum:** The track momentum in the CTD acceptance region is required to be:

$$P_{e,trk} > 3 \text{ GeV} \quad (6.8)$$

in order to increase the purity of the positron sample. The increase of PHP at low values of $P_{e,trk}$ can be seen in figure 6.8.

- **Distance of closest approach:** The distance of closest approach (DCA) between the positron calorimeter cluster and the endpoint of the track extrapolated to the calorimeter surface is required to be:

$$DCA < 10 \text{ cm} \quad (6.9)$$

if the track is found in the CTD acceptance region (see figure 6.8). This rejects events where a track is incorrectly matched to a photon cluster.

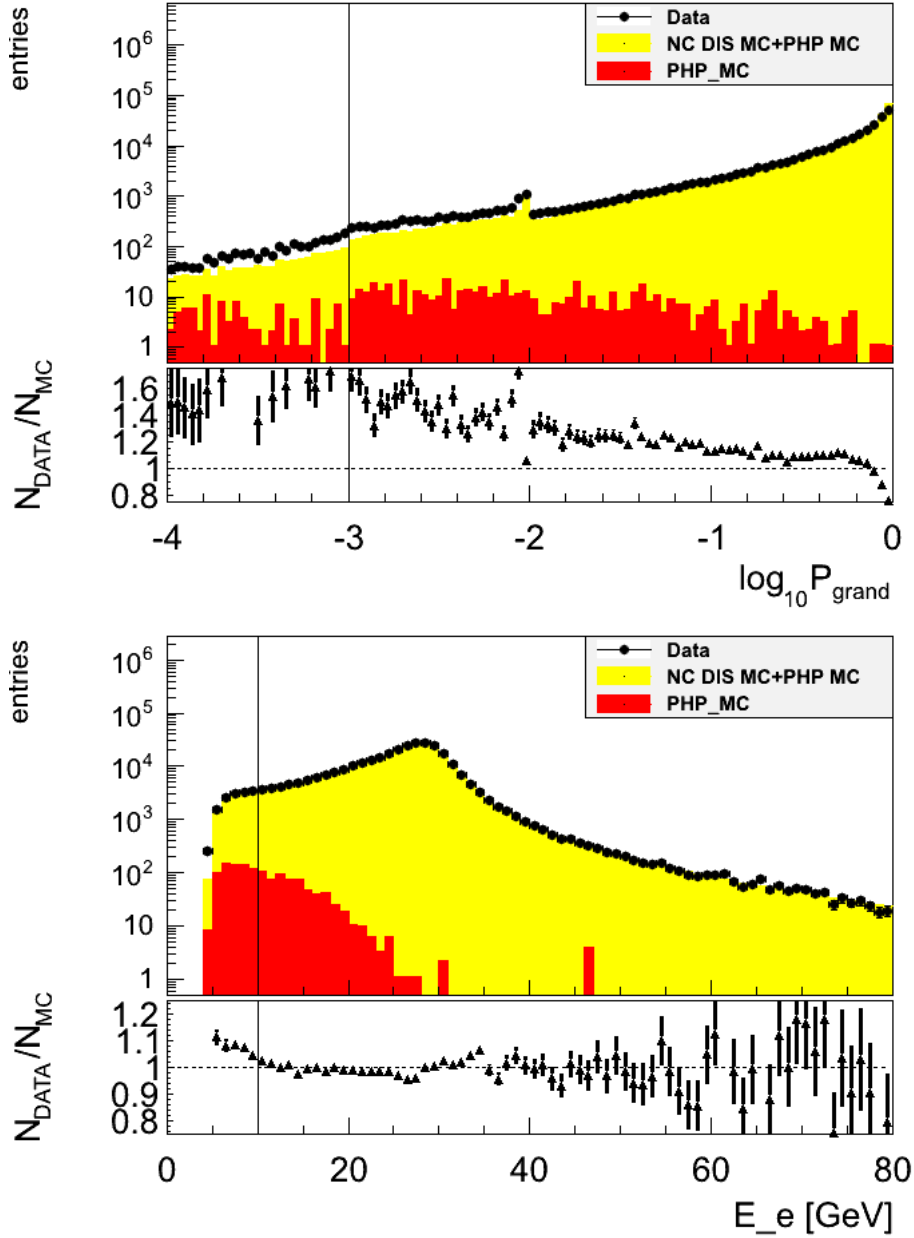


Figure 6.6: The grand probability (top) and the electron energy (bottom) of the scattered electron candidate. The points are data, the yellow histogram is NC DIS MC plus PHP MC and the red histogram is PHP MC. The vertical line indicates the cut value.

Events that are not in the CTD acceptance region are reconstructed using the electron position, θ_e and ϕ_e determined from the CAL and HES, while events in the CTD use variables determined from the matched track.

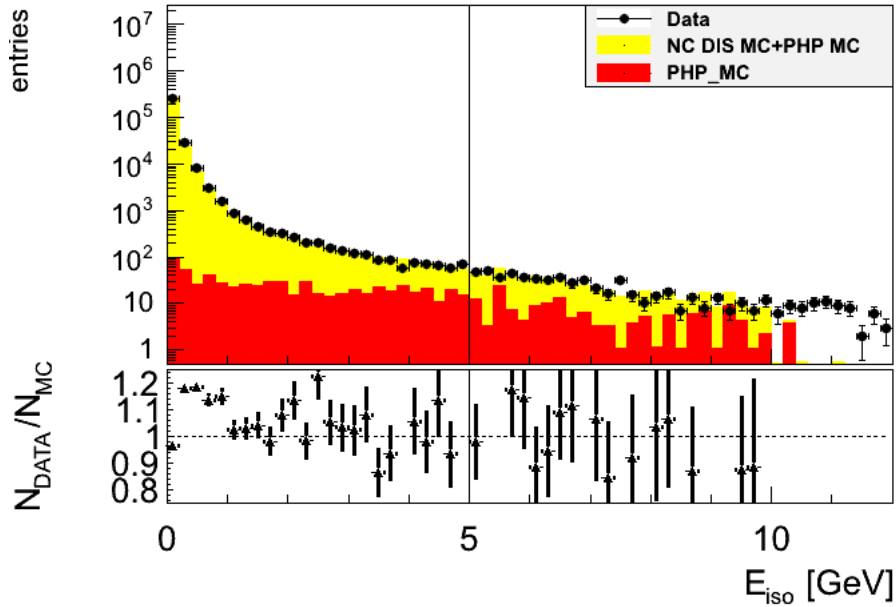


Figure 6.7: The isolation energy (bottom) of the scattered electron candidate. The points are data, the yellow histogram is NC DIS MC plus PHP MC and the red histogram is PHP MC. The vertical line indicates the cut value.

6.5.2 Vertex

- **Z_{vtx} position:** The position of the Z_{vtx} is important for the reconstruction of the kinematic variables of the event. The event vertex is required to lie within:

$$|Z_{vtx}| < 30 \text{ cm with } \chi_{vtx}^2 < 100. \quad (6.10)$$

The motivation to require the Z_{vtx} to be near the nominal Z_{vtx} position is twofold: the acceptance of the tracking and calorimeter is best understood in this region and non- ep background is rejected. This background occurs uniformly in the z position, unlike NC DIS events that distribute around the nominal Z_{vtx} position.

- To further ensure that the vertex is well measured, at least one track is required to be associated with the vertex with the following criteria:

$$p_{T,trk} > 0.2 \text{ GeV} \quad (6.11)$$

$$N_{SL} > 3, \quad (6.12)$$

where $p_{T, trk}$ is the transverse momentum of the track and N_{SL} is the number of superlayers passed by the track.

6.5.3 Detector Geometry

In some detector regions the measurement of the scattered positron is poor due to the construction of the detector. The following explains which regions of the detector are excluded:

- **Distance to module edge:** If the track is found in the CTD acceptance the distance to the calorimeter module edge (DME), see figure 6.9, is required to be:

$$DME > 1.5 \text{ cm}, \quad (6.13)$$

since the energy measurement close to the module edge is unreliable.

- **Supercrack:** Events are rejected if the positron is found in the edges of the BCAL, as part of the shower may leak into the FCAL or RCAL and the simulation of this area is not precise. Events are rejected if they are found with the following z_e position (the z-coordinate position of the electron):

$$-104 \text{ cm} < z_e < -98.5 \text{ cm} \text{ and } 164 \text{ cm} < z_e < 174 \text{ cm}. \quad (6.14)$$

- **Chimney cut:** The pipes that carry liquid to and from the solenoid partially cover the face of the RCAL and therefore there is a large amount of dead material in this region. Moreover, EMC cells do not exist in this region to allow room for a chimney enclosing the pipes. The positron energy measurement in this region is therefore poor and positrons reconstructed in the chimney region are excluded. A positron found in the RCAL is therefore excluded if:

$$|x_e| < 12 \text{ cm} \text{ and } y_e > 80 \text{ cm}. \quad (6.15)$$

The effect of this cut can be seen clearly in figure 6.9.

- **Electron radius in RCAL:** The outermost region of the RCAL is occluded by the BCAL which leads to poor energy measurement and is not well simulated in the MC [78]. Therefore events are accepted if found in the RCAL with a radius:

$$r_e < 175 \text{ cm.} \quad (6.16)$$

6.5.4 Background rejection

This section describes the selection cuts used to reject the background sources described in section 6.2.

- δ_{tot} : As discussed in section 6.2, δ_{tot} is very useful in rejecting PHP and cosmic and halo muons. NC DIS events are expected to have a peak at 55 GeV smeared by the detector resolution. This is not the case for the background sources (see figure 6.10). Therefore δ_{tot} is required to be:

$$38 < \delta_{tot} < 65 \text{ GeV.} \quad (6.17)$$

- **Transverse momentum balance:** The transverse momentum of a perfectly measured NC DIS event is zero. However with a real detector this should be measured with a finite resolution of approximately $\sqrt{E_T}$. Thus the ratio $P_T/\sqrt{E_T}$ is required to be small (see figure 6.11):

$$\frac{P_T}{\sqrt{E_T}} < 4\sqrt{\text{GeV}}. \quad (6.18)$$

Some events are found to have a small measured value of E_T but unusually large P_T and are not found in either the DIS NC or PHP MC. These events are cosmic or halo muons that pass the timing cuts of the SLT and TLT trigger bits (see sections 6.3.2 and 6.3.3) and are removed by the following cut (see figure

6.11):

$$\frac{P_T}{E_T} < 0.7. \quad (6.19)$$

- **y_{EL} cut:** PHP events can contaminate the NC DIS event sample despite the imposition of the $E'_e > 10$ GeV cut by faking a positron in the FCAL where tracking information is not available. These events are characterised by very high y_{EL} (see equation 4.7) close to 1. Therefore a cut on y_{EL} is required:

$$y_{EL} < 0.9. \quad (6.20)$$

- **At least one “good track”:** NC DIS events should have a number of tracks associated with the electron or the hadronic systems. High quality tracks are needed to reconstruct the Z_{vtx} . At least one “good track”² is required.
- **Elastic QEDC rejection:** Elastic QEDC events are described in section 6.2.2 and are characterised by the presence of two electromagnetic clusters in the calorimeter and little activity elsewhere in the detector. QEDC events are rejected by the following:
 - At least two good ($P_{grand} > 10^{-3}$) positron candidates found in the detector.
 - The difference in ϕ of the two candidates greater than 3 rad to ensure that the particles are produced back to back.

²A “good track” is defined to be a track passing the following criteria:

$$\begin{aligned} P_{trk} &> 0.2 \text{ GeV} \\ \text{Inner superlayer} &\leq 1 \\ \text{Outer superlayer} &\geq 3 \\ &\text{Fitted to the primary vertex.} \end{aligned}$$

- The transverse momentum of the candidates should be balanced:

$$0.8 < \frac{P_{T,1}}{P_{T,2}} < 1.2, \quad (6.21)$$

where $P_{T,1}$ ($P_{T,2}$) is the P_T of the first (second) positron candidate.

- The total energy in the calorimeter after subtracting the energy of the two electron candidates should be less than 3 GeV.

6.5.5 Phase space and MC validity:

- **Projection of γ_h on the FCAL:** Events with very low values of γ_h are not simulated well [79]. This is due to particles escaping down the beampipe. This is important as the DA method (see section 4.2.3), used to determine the event kinematics, is highly dependant on an accurate determination of γ_h . To avoid this region γ_h is projected onto the face of the FCAL and events are rejected if:

$$R_{\gamma_h,FCAL} < 18 \text{ cm}, \quad (6.22)$$

where $R_{\gamma_h,FCAL}$ is the radius of γ_h projected onto the face of the FCAL.

- The phase space is restricted to the high- Q^2 region by requiring:

$$Q_{DA}^2 > 185 \text{ GeV}^2. \quad (6.23)$$

This value is chosen to reject PHP background and to be consistent with previous NC DIS analyses [1].

- The MC simulation is not valid at high x and low y due to large virtual QED corrections [80]. Therefore the region is excluded with the cut (see figure 6.10):

$$y_{JB}(1 - x_{DA})^2 > 0.004. \quad (6.24)$$

6.6 Final data and MC samples

In total 302073 data events passed all the trigger and selection cuts, which after applying the RISOE trigger inefficiency correction (see section 5.3.1) corresponds to 302499 events. Out of 12459002 NC DIS MC events, 4826872 events pass the trigger and selection cuts, which after weighting for differing Q^2 cuts (see section 3.2.1) and applying all corrections, (see chapter 5) corresponds to 304641 events. The contribution from PHP MC is small with 1135 events passing the event selection out of 1600000, which after all corrections becomes 643 events.

The total event numbers for each run period (ALL, RH, LH, LH1 and LH2) are summarized in table 6.1. The number of MC events agree within the uncertainty of the luminosity measurement (see section 2.2.7) for all periods.

	Nr. DATA	Nr. MC	Nr. PHP	Norm. (%)
ALL	302073	304641	643	1.06
RH	179070	179826	371	0.63
LH	123429	124788	272	1.32
LH1	73247	73897.7	163.1	1.11
LH2	50182	50917.9	108.9	1.86

Table 6.1: Summary of the number of DATA, NC DIS MC, PHP MC events and the normalisation for each running period.

Figure 6.12 shows histograms for data and MC of the most important variables used to describe NC DIS events. Only events that passed the entire event selection and have had all corrections applied are presented. The data is shown compared to MC prediction, which includes both NC DIS and PHP MC events. The figures show good agreement between data and MC and therefore the MC can be used to determine the detector acceptance and unfold the cross-sections (see section 7).

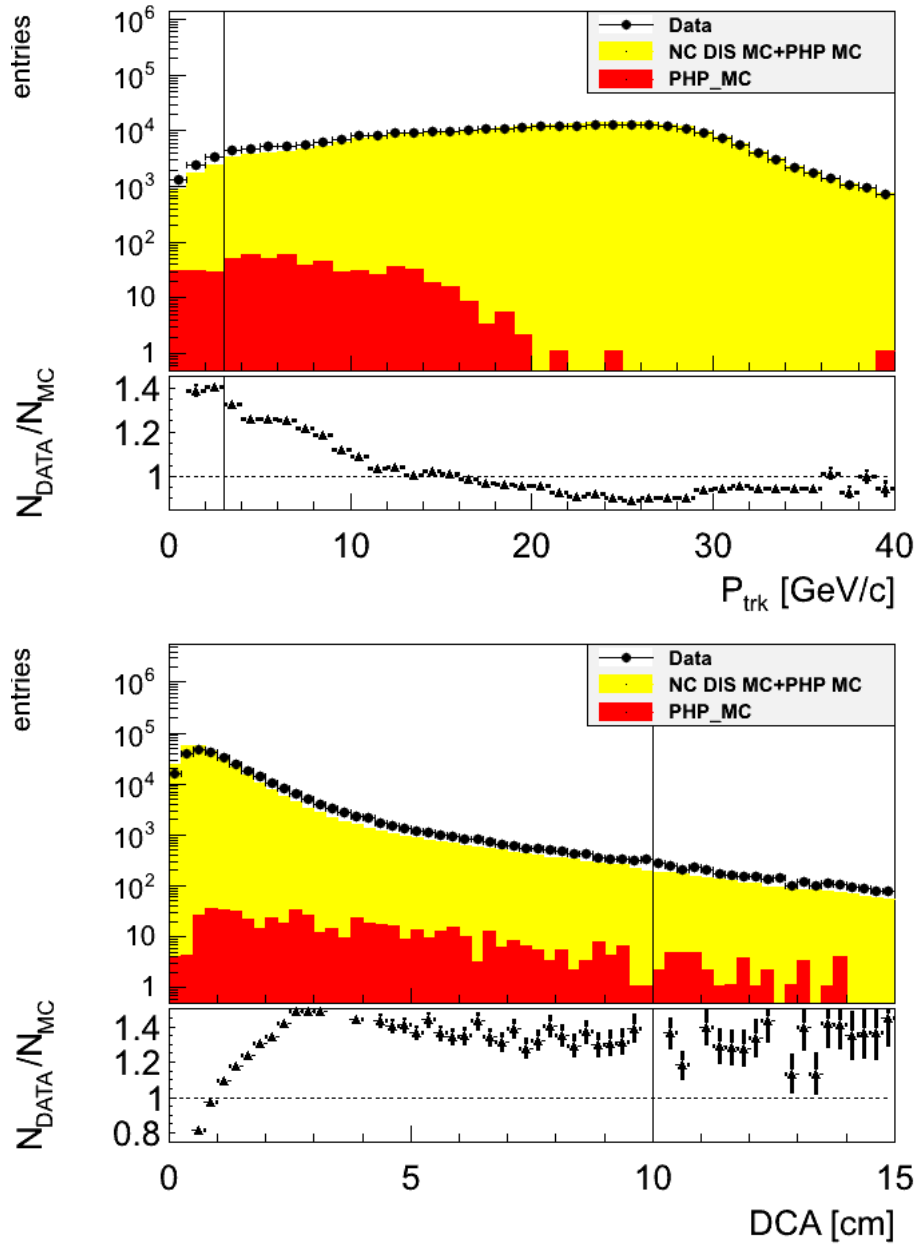


Figure 6.8: The track momentum (top) and the DCA (bottom) of the scattered electron candidate. The points are data, the yellow histogram is NC DIS MC plus PHP MC and the red histogram is PHP MC. The vertical line indicates the cut value.

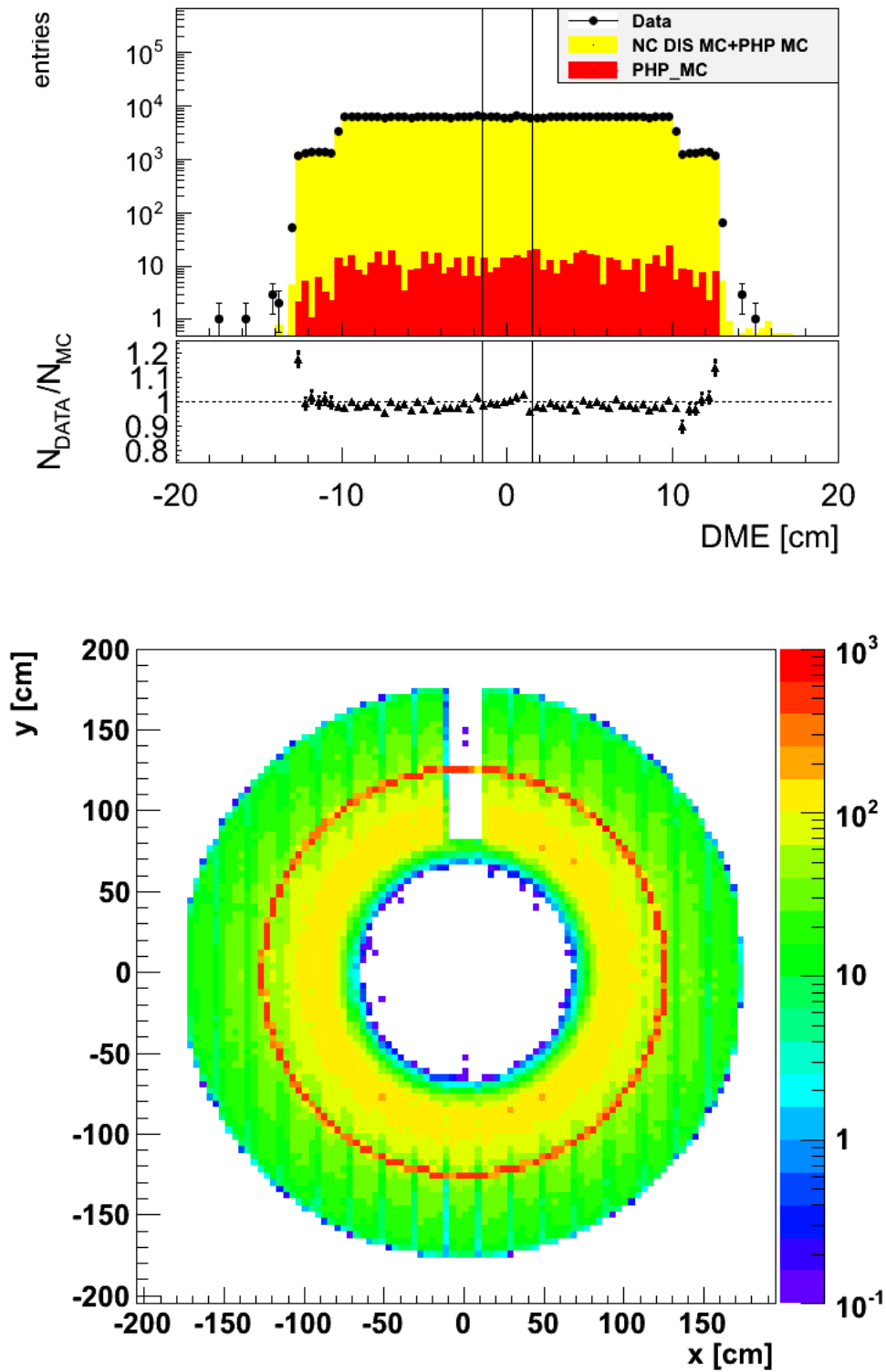


Figure 6.9: The DME (top) and the position on the RCAL surface (bottom) of the scattered electron candidate. The points are data, the yellow histogram is NC DIS MC plus PHP MC and the red histogram is PHP MC. The vertical line indicates the cut value, events between the vertical lines are excluded. The effect of the chimney cut can be seen as the region with no event entries.

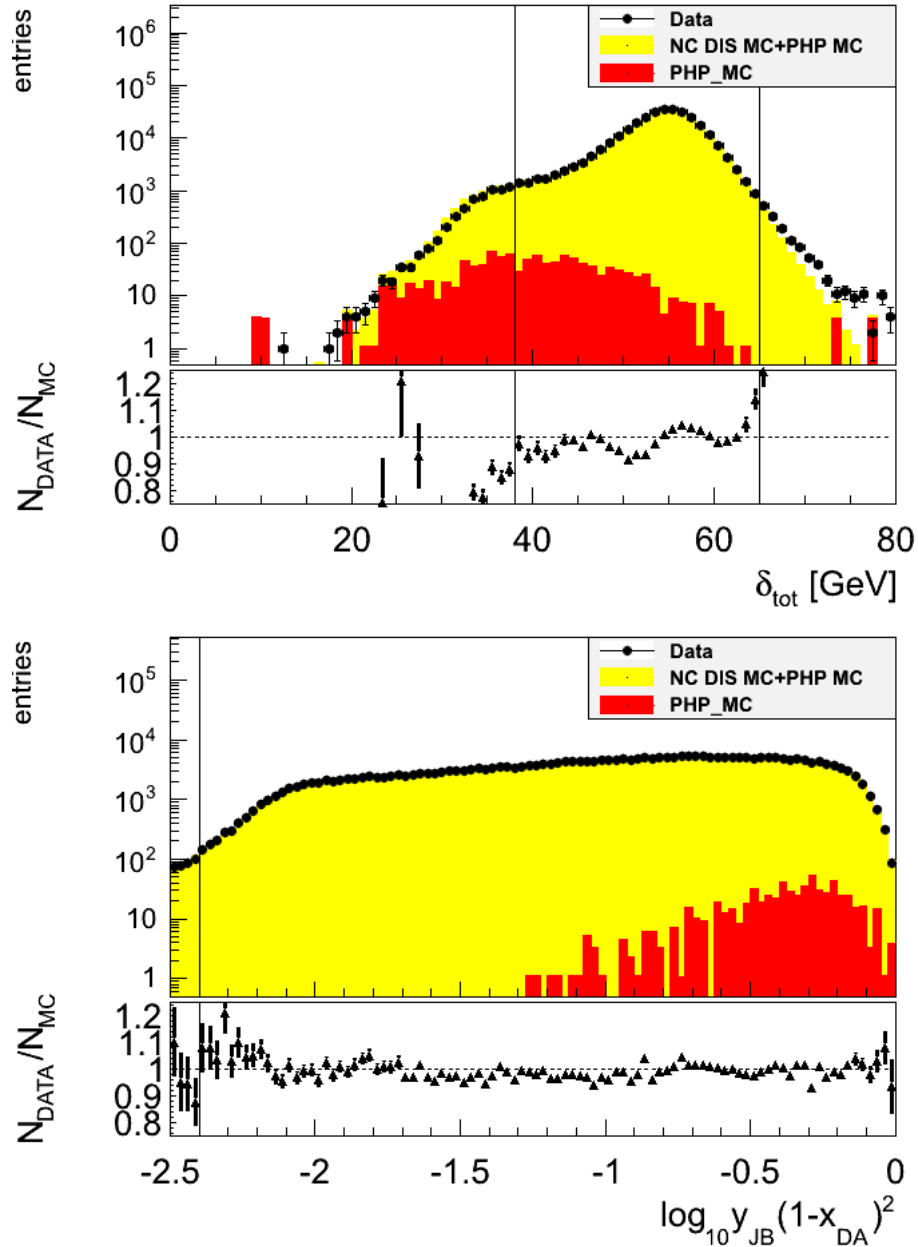


Figure 6.10: The difference of total energy and the longitudinal momentum, δ_{tot} (top) and $y_{JB}(1 - x_{DA})^2$ (bottom), where the points are data, the yellow histogram is NC DIS MC plus PHP MC and the red histogram is PHP MC. The vertical line indicates the cut value.

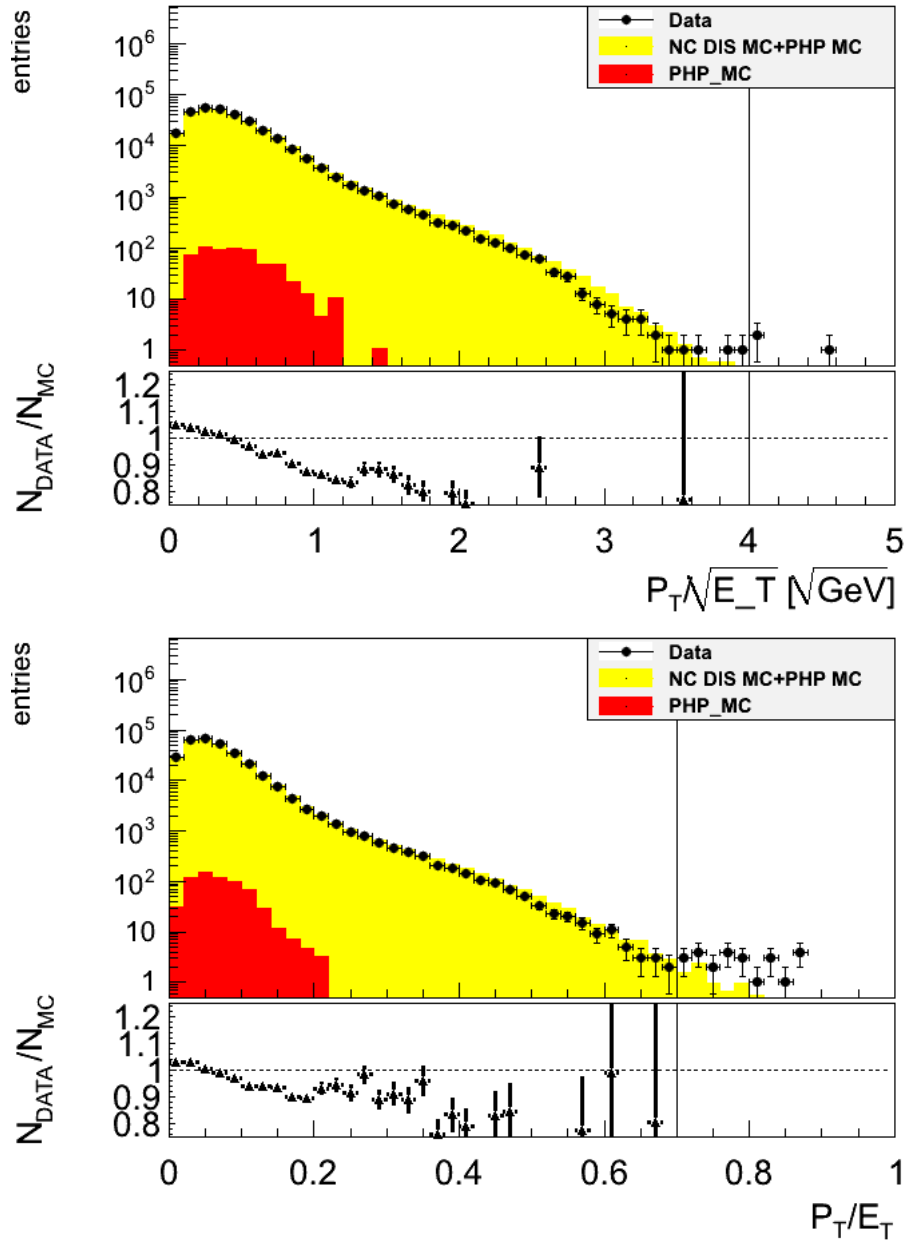


Figure 6.11: The ratio $\frac{P_T}{\sqrt{E_T}}$ (top) and $\frac{P_T}{E_T}$ (bottom), where the points are data, the yellow histogram is NC DIS MC plus PHP MC and the red histogram is PHP MC. The vertical line indicates the cut value.

ZEUS

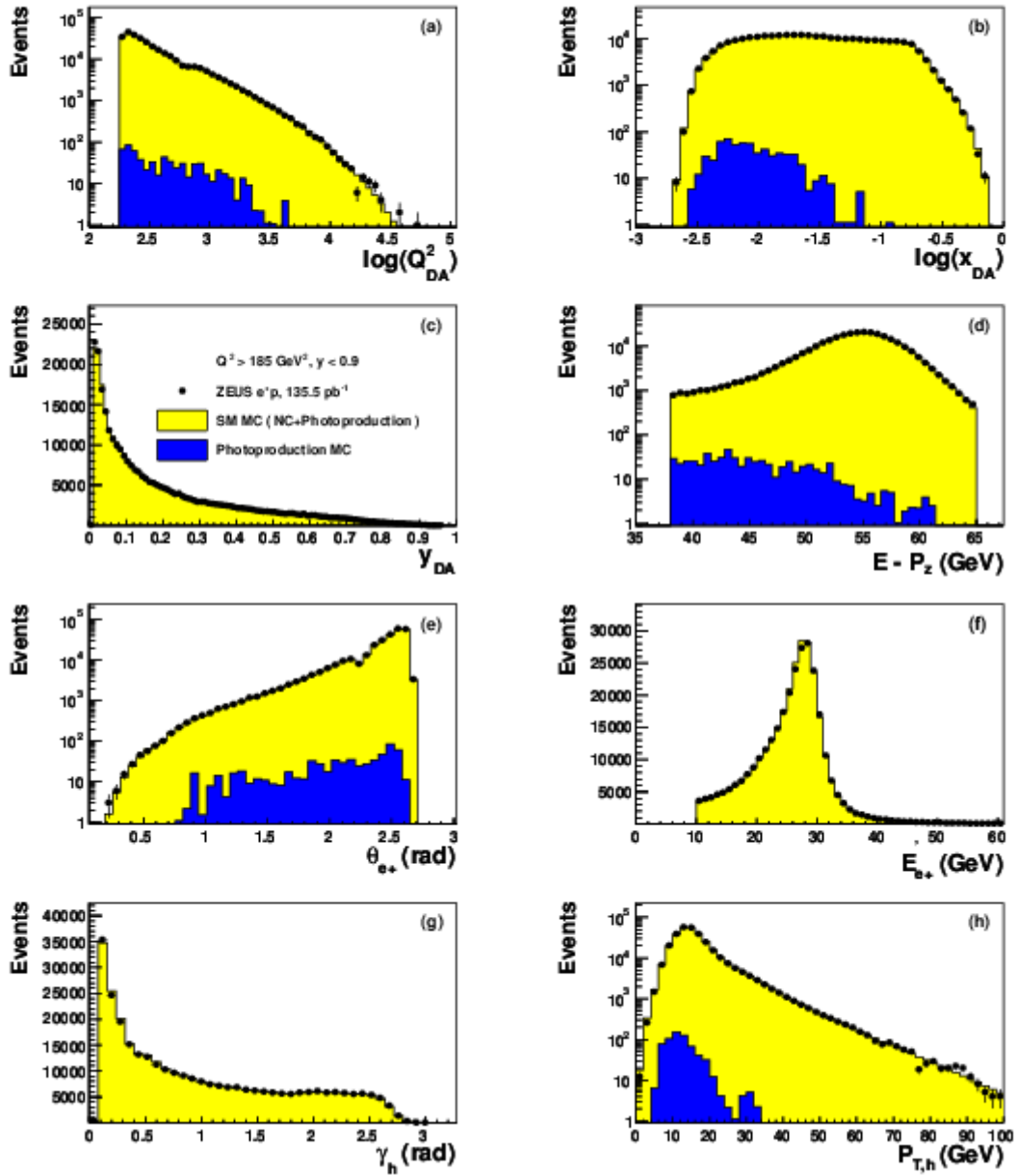


Figure 6.12: Distributions of some of the important variables from the NC DIS event selection. Data is represented by the black points, the yellow filled histogram is DIS NC MC and PHP MC and the dark blue filled histogram is PHP MC.

Chapter 7

Cross-Section Measurement and Systematic Uncertainties

In this chapter the method used for the unfolding of the NC DIS cross-sections is discussed. In section 7.1 the bins are defined for the polarised and unpolarised single differential cross-sections as a function of Q^2 , x and y and the reduced cross-section as function of x at fixed Q^2 . The method of unfolding the cross-section is explained in section 7.2. In the final part of this chapter, section 7.3, the statistical and systematic uncertainties are studied in detail.

7.1 Bin Selection

The first step required to determine the cross-sections is to divide the phase space into a number of bins in which the cross-sections are to be measured. Ideally, to get the most information from the measurement, one would define the bins to be very small. However the bin size is limited by two main considerations: statistics (i.e., the number of events in each bin) and the resolution of the measured variables, which cause events to migrate to neighbouring bins (see section 4.2.4 for an overview of the resolution of the DA method). To ensure a statistically significant number of events in each bin, bin sizes are increased as the cross-section decreases; this will be described in more detail in the following subsections. Migrations between bins can be managed by

choosing bins that are sufficiently wide with respect to the resolution of the variable being measured. One more item that must be considered is the measurement of the xF_3 structure function. In order to extract xF_3 it would be convenient to measure the cross-section in the same bins as the ZEUS e^-p measurement [1] as it would eliminate the need to rely on calculations using PDFs and their inherent uncertainty to swim the results to a common binning. As the measurement was done with the same detector and with a similar amount of luminosity, 135.5 pb^{-1} for e^+p and 169.9 pb^{-1} for e^-p , the bins from the e^-p measurement are used and checked for applicability to this analysis. This is done by checking the efficiency, E , purity, P , and acceptance, A , for each cross-section bin. These quantities E , P and A are estimated using the NC DIS MC as follows:

$$E = \frac{\# \text{ of events generated and reconstructed in bin } i}{\# \text{ of events generated in bin } i} \quad (7.1)$$

$$P = \frac{\# \text{ of events generated and reconstructed in bin } i}{\# \text{ of events reconstructed in bin } i} \quad (7.2)$$

$$A = \frac{\# \text{ of events reconstructed in bin } i}{\# \text{ of events generated in bin } i}. \quad (7.3)$$

MC events are counted as being generated in a bin if their generated (or true) kinematic variables fall within the bin edges and they pass the phase space cuts $Q_{true}^2 > 185 \text{ GeV}^2$, $y_{true} < 0.9$ and $y_{true} \times (1 - x_{true})^2 > 0.004$. Events are counted as reconstructed in a bin if their reconstructed kinematic variables fall within the bin edges, and pass all the trigger and selection cuts.

The efficiency quantifies how many events that are generated in a bin remain in that bin after reconstruction and passing the selection cuts. Low efficiency (below 50%) indicates that the majority of events generated in a bin either failed the selection cuts or migrated to other bins. This in itself is not a concern as long the MC simulation of the detector is accurate (see section 6.6) but reduces the number of events in the bin and thus increases the statistical uncertainty.

The purity quantifies how many events migrate from neighbouring bins into the bin being investigated. A low purity indicates that the bin is dominated by events

generated elsewhere in the kinematic plane, i.e., the bin is surrounded by bins with poor resolution. If the purity is too low, the danger is not measuring the cross-section well, the bin being biased by events from neighbouring bins, especially if the cross-section is falling or rising rapidly as a function of the binned variable.

The acceptance indicates the number of events reconstructed in a bin regardless if generated there. To measure the cross-section the number of events measured in a bin must be transformed into the true number of events in the bin by correcting for the effects of the analysis cuts and migrations from other bins. This is done by using the acceptance which can be defined in terms of the purity and efficiency as:

$$A = \frac{E}{P} \quad (7.4)$$

The use of the acceptance in extracting the cross-sections will be discussed further in section 7.2.

In the next three subsections it is shown that E , P and A are sufficiently good for this analysis using the e^-p binning.

7.1.1 Bin definition for $\frac{d\sigma}{dQ^2}$

The bins for the single differential cross-section $\frac{d\sigma}{dQ^2}$ cover a Q^2 range from a minimum of $Q^2 = 185 \text{ GeV}^2$ to a maximum of $Q^2 = 51200 \text{ GeV}^2$. This region is divided into 34 bins (see appendix A). The bin widths chosen for $Q^2 < 2000 \text{ GeV}^2$ have approximately logarithmically equal width, while higher Q^2 bins have been made wider due to statistical limitations. The bin centres are at the logarithmic centre of each bin. Figure 7.1 shows the purity, efficiency and acceptance for each $\frac{d\sigma}{dQ^2}$ bin.

The purity is on average 70%, never dropping below 60%. The increases in the purity and efficiency at 2000 GeV^2 and 10000 GeV^2 are due to the increase in bin size compared to the resolution (where the bin size is dominated by the statistics and not the resolution). The dips seen in both the acceptance and the efficiency are due to the supercrack between the RCAL and BCAL, where there is a drop in the number

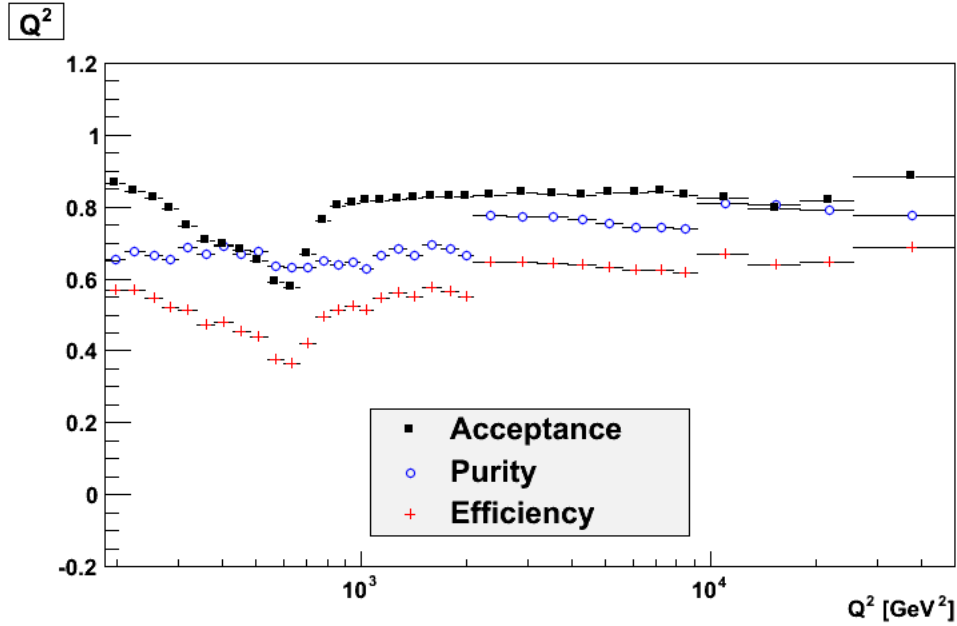


Figure 7.1: The acceptance (filled in squares), purity (open circles) and efficiency (crosses) for the cross-section $\frac{d\sigma}{dQ^2}$.

of events passing the selection cuts (see section 6.5).

7.1.2 Bin definition for $\frac{d\sigma}{dx}$

The single differential cross-section $\frac{d\sigma}{dx}$ is measured for two Q^2 regions: one with $Q^2 > 185 \text{ GeV}^2$, the other with $Q^2 > 3000 \text{ GeV}^2$. The higher Q^2 cut was done to extend the measurement to larger x with reasonable values of efficiency, purity and acceptance (see figure 7.2). The measurement for $Q^2 > 185 \text{ GeV}^2$ is divided into 8 x bins from 0.0063 to 0.25; for $Q^2 > 3000 \text{ GeV}^2$, 6 bins from 0.04 to 0.75. The bins are defined with an approximately logarithmically equal bin width for both cases. The bins are tabulated in Appendix A.

7.1.3 Bin definition for $\frac{d\sigma}{dy}$

As for $\frac{d\sigma}{dx}$, the cross-section $\frac{d\sigma}{dy}$ is measured for two Q^2 regions: $Q^2 > 185 \text{ GeV}^2$ and $Q^2 > 3000 \text{ GeV}^2$. For the $Q^2 > 185 \text{ GeV}^2$ measurement there are 15 bins from 0.0 to 0.75; for $Q^2 > 3000 \text{ GeV}^2$, 17 bins 0.0 to 0.9. The bins are of equal width, 0.05, for both cases. The efficiency, purity and acceptance are shown in figure 7.3. For the

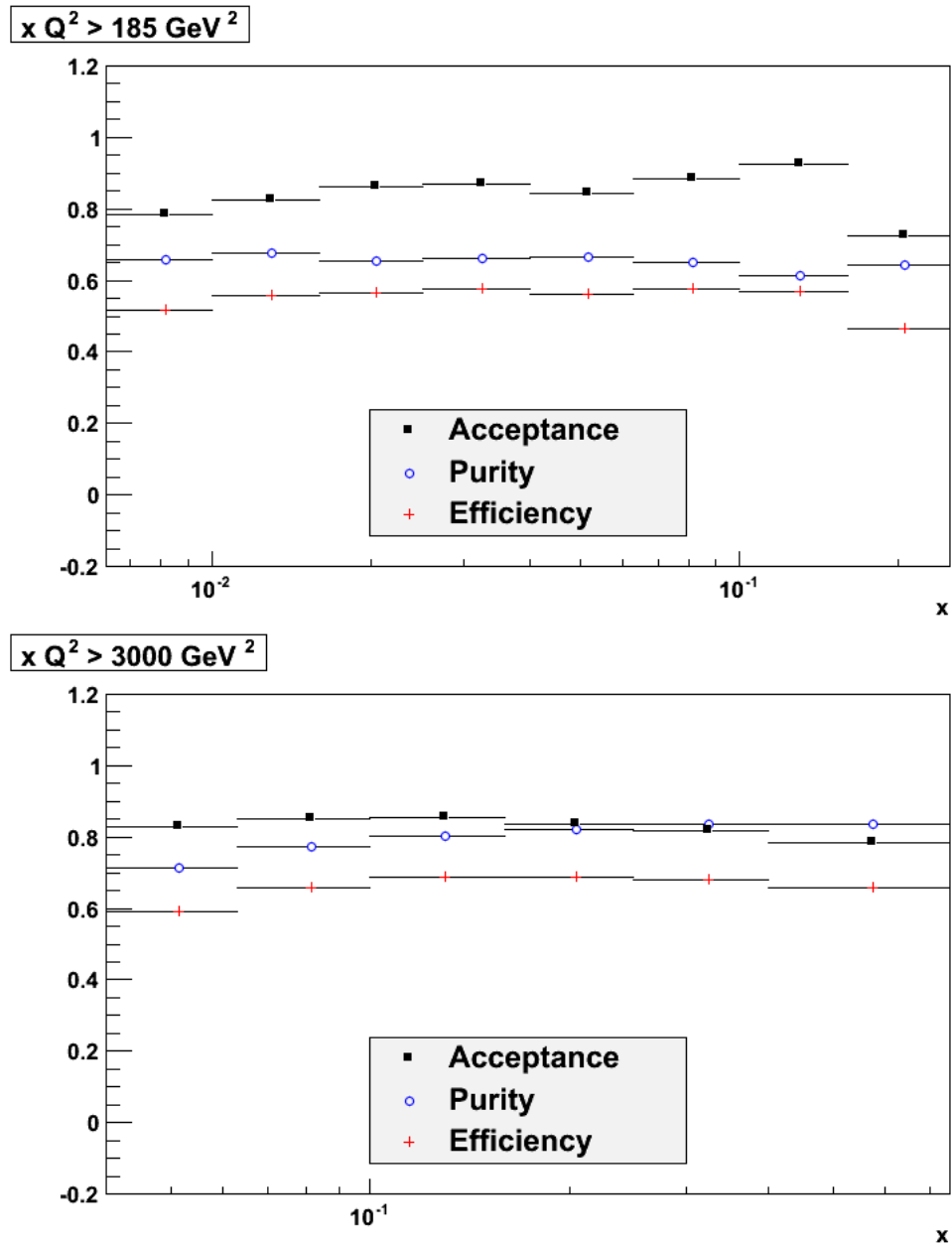


Figure 7.2: The acceptance (filled in squares), purity (open circles) and efficiency (crosses) for the cross-section $\frac{d\sigma}{dx}$ for $Q^2 > 185 \text{ GeV}^2$ (top) and $Q^2 > 3000 \text{ GeV}^2$ (bottom).

$Q^2 > 185 \text{ GeV}^2$ measurement the purity and efficiency drop from 85% to 45% and 70% to 20%, respectively, with increasing y . For the $Q^2 > 3000 \text{ GeV}^2$ measurement both the efficiency and purity drop but less, never dropping below 60% and 50%, respectively. The drop in the efficiency at high y is due to the strict cuts in this region to eliminate PHP background, chiefly the electron energy cut which puts an upper limit on y .

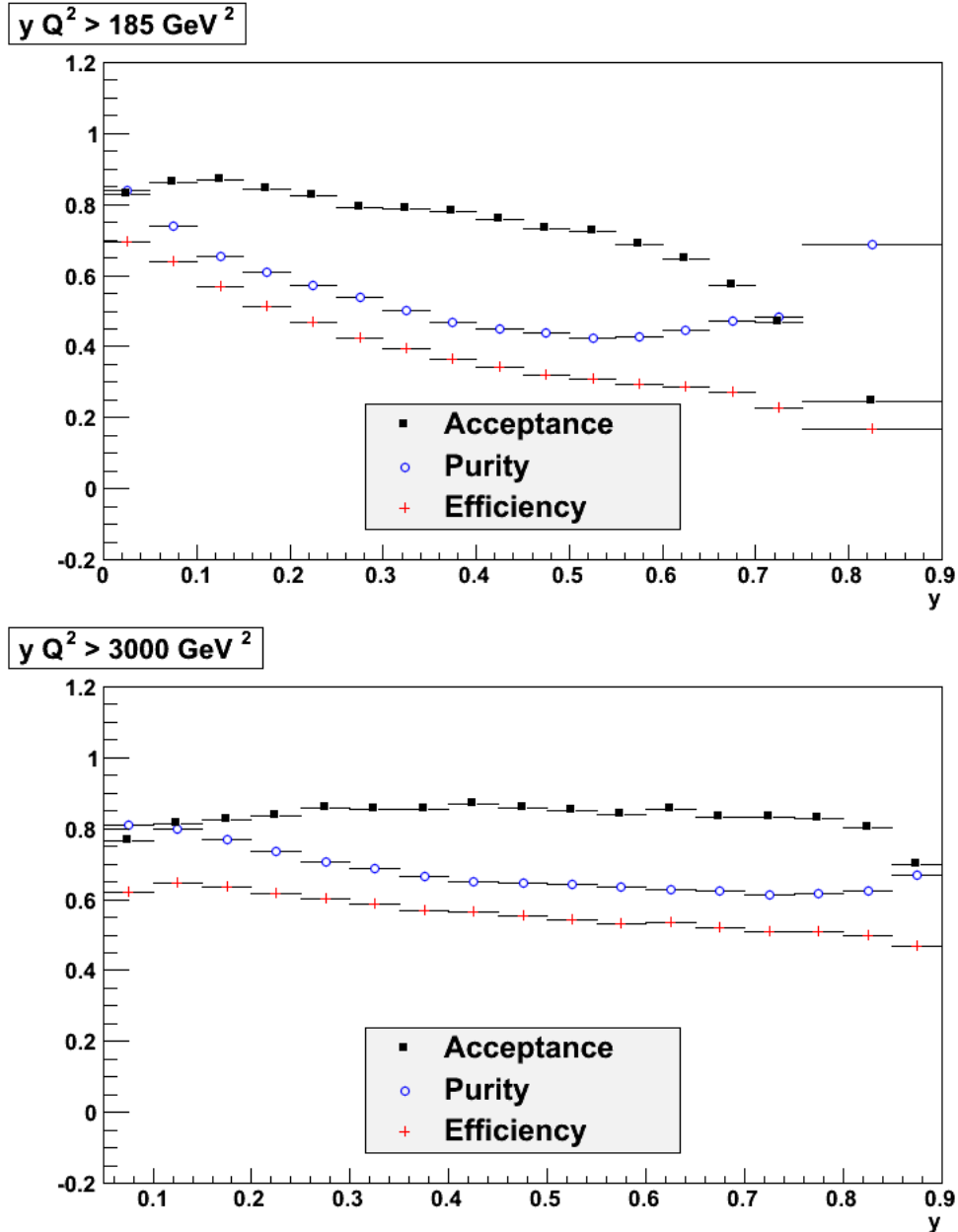


Figure 7.3: The acceptance (filled in squares), purity (open circles) and efficiency (crosses) for the cross-section $\frac{d\sigma}{dy}$ for $Q^2 > 185 \text{ GeV}^2$ (top) and $Q^2 > 3000 \text{ GeV}^2$ (bottom).

7.1.4 Bin definition for the reduced cross-section

The measurement of the reduced cross-section (see equation 1.46) is divided into 90 bins with Q^2 between 185 GeV² and 50000 GeV² and x between 0.0037 and 0.75 (tabulated in appendix A). The bin definition is determined mainly by resolution in the lower Q^2 bins and statistics in the higher Q^2 bins. The purity is above 50% for all bins, from a low of 60% at low Q^2 and x , due to the relatively small bins sizes, to over 80% at high Q^2 and high x (see figure 7.4). As also seen in section 7.1.1, the efficiency drops below 50% in the region of the crack between the RCAL and BCAL.

7.2 Unfolding the cross-section

For a detector with full solid angle coverage, perfect energy and angular resolution, the measurement of a cross-section σ would be a trivial calculation:

$$\sigma = \frac{N}{\mathcal{L}} \quad (7.5)$$

where N is the number of detected events and \mathcal{L} is the integrated luminosity. In a real experiment the detector has finite acceptance and detector resolution. The finite detector acceptance leads to the observation of only a subset of the actual number of events occurring, while the finite resolution smears the measured kinematic variables and as a consequence the cross-sections. Additionally, initial and final state radiation can lead to the migration of events to different regions of phase space. The cross-sections themselves must be estimated from the number of events observed in the detector. The method of extracting the true cross-section from the observed quantities is known as “unfolding”. This is typically done using MC simulations owing to the complexity of modern day experiments.

In order to extract the true cross-section from the observed quantities consider a density function $f(x)$ of a variable x that is measured by a detector with finite

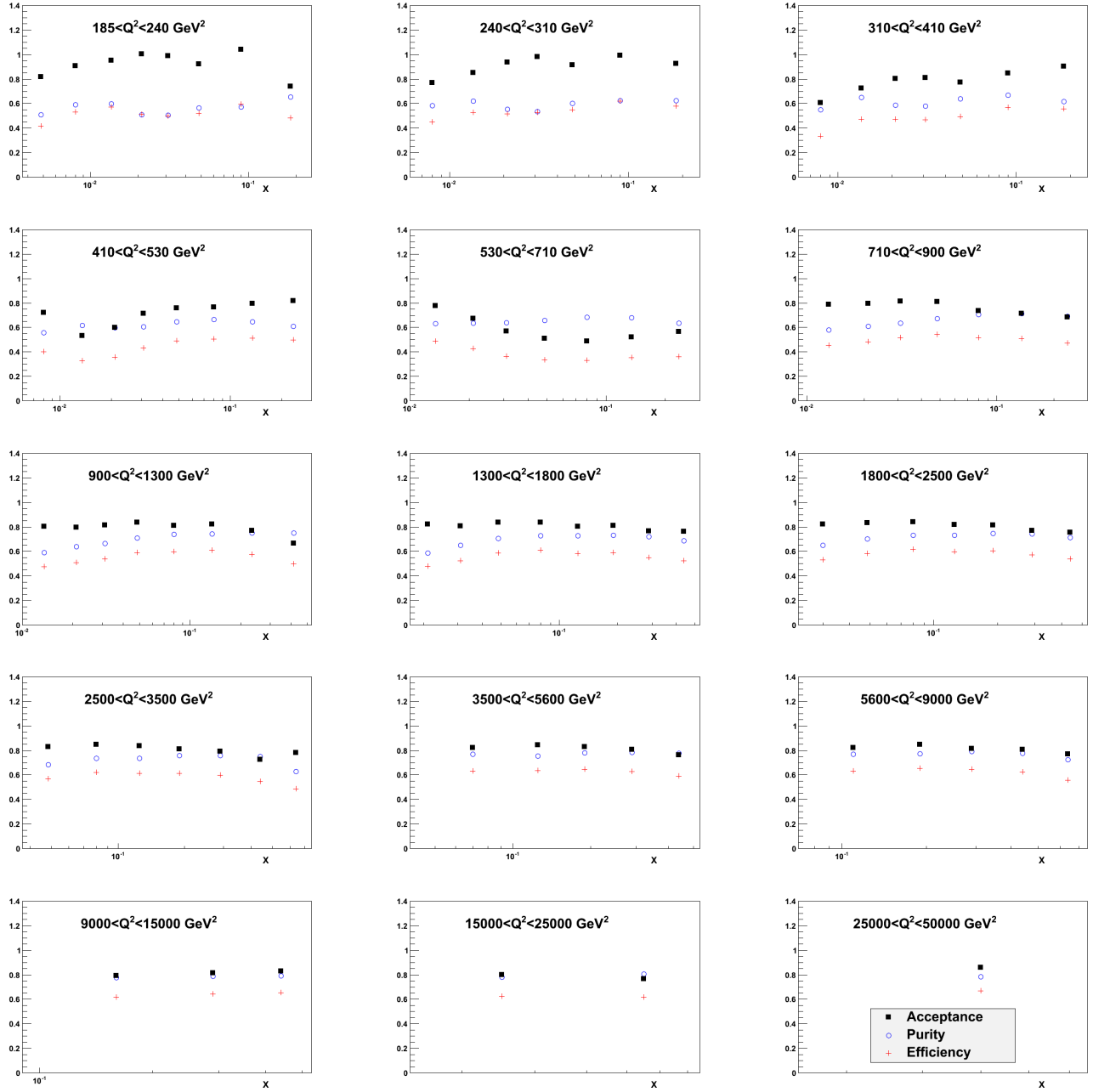


Figure 7.4: The acceptance (filled in squares), purity (open circles) and efficiency (crosses) for the reduced cross-section as a function of x in bins of Q^2 .

resolution. The function $f'(x')$, defined by [82]

$$f'(x') = \int_{-\infty}^{\infty} t(x, x') f(x) dx \quad (7.6)$$

is a probability function to measure the quantity x' , where $t(x, x')$ is called the transfer function which includes the effects of the detector resolution, finite acceptance of the detector and the analysis cuts. Thus the function $t(x, x')$ allows us to go from true quantities to those observed in the detector.

To deduce the transfer function the detector response is estimated from the MC simulation. The MC events are generated using a function $g(x)$ which is expected to be a close expectation for $f(x)$. The observed distribution $g'(x')$ is defined analogously to equation 7.6 replacing $f(x)$ and $f'(x')$ with $g(x)$ and $g'(x')$, respectively.

Usually the phase space is divided into bins of x or x' . The true (reconstructed) number of events in bin i are $N_{i,data}^{true}$ ($N_{i,data}^{reco}$) and $N_{i,MC}^{true}$ ($N_{i,MC}^{reco}$) for data and MC respectively. The integral 7.6 is transformed into sums over the bins:

$$N_{i,data}^{reco} = \sum_j T_{ij} N_{j,data}^{true} \quad (7.7)$$

$$N_{i,MC}^{reco} = \sum_j T_{ij} N_{j,MC}^{true}, \quad (7.8)$$

where $t(x, x')$ has become T_{ij} , the probability for an event from the true bin j to be reconstructed bin in i . The transfer matrix is given by:

$$T_{ij} = \frac{\int_i dx' \int_j t(x, x') f(x) dx}{\int_j f(x) dx} \quad (7.9)$$

$$\approx \frac{\int_i dx' \int_j t(x, x') g(x) dx}{\int_j g(x) dx} \quad (7.10)$$

$$= \frac{N_{ij,MC}^{reco \& true}}{N_{j,MC}^{true}}, \quad (7.11)$$

where the integration limits are over the bin boundaries. An estimate of T_{ij} can be determined from the MC simulation by replacing the integrals over the density

functions $f(x)$ and $f'(x')$ with equation 7.11, where $N_{ij,MC}^{reco \& true}$ is the number of MC events generated in bin j and reconstructed in bin i and passed the selection cuts, and $N_{j,MC}^{true}$ is the number of MC events generated in bin j .

In principle the estimated transfer matrix can be inverted to estimate the true number of events:

$$N_{j,data}^{true} = \sum_i (T^{-1})_{ji} N_{i,data}^{reco}. \quad (7.12)$$

This method, while correct, has a number of difficulties if the simulation does not describe the acceptance and resolution of the detector well. Additionally, the method is susceptible to statistical fluctuations in the data. Due to these difficulties this method is not used.

7.2.1 Bin-by-bin unfolding

The method used in this analysis to extract the cross-sections is equivalent to assuming that the transfer matrix T is diagonal. This method is referred to as “bin-by-bin” unfolding. In this method only net migrations of events into and out of each bin are considered, and the small correlations between bins are ignored. With this assumption, combining equations 7.11 and 7.12, the estimate of the true number of events in bin i :

$$N_{i,data}^{true} = T_{ii}^{-1} N_{i,data}^{reco} = \frac{N_{i,MC}^{true}}{N_{i,MC}^{reco}} N_{i,data}^{reco} \quad (7.13)$$

$$\sigma_i = \frac{\frac{N_{i,MC}^{true}}{N_{i,MC}^{reco}}}{\mathcal{L}} N_{i,data}^{reco} \quad (7.14)$$

$$\sigma_i = \frac{N_{i,data}^{reco}}{\mathcal{L} \times A_i}, \quad (7.15)$$

which accounts for the detector acceptance, resolution and selection cuts. Although the transfer matrix is not exactly diagonal in this analysis, the good agreement between data and MC as shown in figure 6.12 and the relatively high purities and efficiencies (see figures 7.1, 7.2, 7.3 and 7.4) resulting from the bin selection, indicates

that the net migration in and out of a bin should be the same in data and MC. The bin by bin unfolding technique is therefore reliable.

The cross-section, including electroweak radiative effects integrated over bin i (see equation 7.15), is extracted from the measured number of events in bin i from data, the total data luminosity and the detector acceptance.

7.2.2 Background subtraction

Events that pass the selection cuts include not only NC DIS events but also a background contribution, estimated from PHP MC (see section 3.2.2). This background sample needs to be subtracted from equation 7.15:

$$\sigma_i = \frac{N_{i,data}^{reco} - N_{i,PHP}^{reco}}{\mathcal{L} \times A_i}, \quad (7.16)$$

where $N_{i,PHP}^{reco}$ is the number of PHP events in bin i .

7.2.3 Radiative corrections

The measured integrated cross-section includes electroweak radiative effects and a correction factor must be applied to obtain the Born level cross-section, $\sigma_{i,Born}$. This correction is obtained from the ratio of the theoretical Born level cross-section, $\sigma_{i,Born,theory}$ and the theoretical cross-section including radiative corrections, $\sigma_{i,rad,theory}$:

$$\sigma_{i,Born} = \frac{N_{i,data}^{reco} - N_{i,PHP}^{reco}}{\mathcal{L} \times A_i} \frac{\sigma_{i,Born,theory}}{\sigma_{i,rad,theory}}. \quad (7.17)$$

To maintain consistency the theoretical cross-sections should be determined using the same PDFs as used in the MC.

7.2.4 Bin centring correction

The integrated cross $\sigma_{i,Born}$ can be transformed to a differential cross-section of a variable ν at a specific point ν_{point} by applying a correction factor calculated from

theoretical predictions:

$$C_i^{centre} = \frac{\left. \frac{d\sigma_{i,Born,theory}}{d\nu} \right|_{\nu_{point}}}{\sigma_{i,Born,theory}} \quad (7.18)$$

where C_i^{centre} is the bin centring correction, $\left. \frac{d\sigma_{i,Born,theory}}{d\nu} \right|_{\nu_{point}}$ is the theoretical prediction at the point ν_{point} . The cross-section at a point ν_{point} including radiative corrections and the bin centring correction is given by:

$$\left. \frac{d\sigma_{i,Born}}{d\nu} \right|_{\nu_{point}} = \frac{N_{i,data}^{reco} - N_{i,PHP}^{reco}}{\mathcal{L} \times A_i} \frac{\sigma_{i,Born,theory}}{\sigma_{i,rad,theory}} \times C_i^{centre} \quad (7.19)$$

$$= \frac{N_{i,data}^{reco} - N_{i,PHP}^{reco}}{\mathcal{L} \times A_i} \frac{\left. \frac{d\sigma_{i,Born,theory}}{d\nu} \right|_{\nu_{point}}}{\sigma_{i,rad,theory}}. \quad (7.20)$$

As was the case for the radiative correction, the PDFs used should be the same as those used in the MC for consistency.

7.2.5 Unfolded cross-section

If the NC DIS MC includes radiative processes and is based on the same PDFs at the same perturbation theory order as the theoretical prediction $\left. \frac{d\sigma_{i,Born,theory}}{d\nu} \right|_{\nu_{point}}$ then:

$$\mathcal{L} \sigma_{i,rad,theory} A_i = N_{i,MC}^{reco}, \quad (7.21)$$

where $N_{i,MC}^{reco}$ is the number of reconstructed NC DIS MC events in bin i .

The NC DIS MC (see section 3.2.1) satisfies these conditions, since both the MC and the theoretical prediction using HECTOR are based on HERACLES and CTEQ5D at leading order. Thus the cross-section at the Born level can be extracted using the following equation:

$$\left. \frac{d\sigma_{i,Born}}{d\nu} \right|_{\nu_{point}} = \frac{N_{i,data}^{reco} - N_{i,PHP}^{reco}}{N_{i,MC}^{reco}} \frac{d\sigma_{i,Born,theory}}{d\nu} \Big|_{\nu_{point}}. \quad (7.22)$$

7.3 Systematic uncertainties

Systematic uncertainties are fundamentally different from statistical uncertainties, since they arise from the imperfect understanding of the ZEUS detector. First the major error sources must be determined. Then the associated uncertainties must be quantified and combined to determine a total value for the systematic error. This analysis estimates systematic uncertainties for the following sources: the reconstruction of the electron and hadronic systems, the estimation of the background PHP events and the selection cuts and the corrections applied to the MC (see section 5). These are discussed in detail in the following sections.

The uncertainty arising from each source is quantified using the following procedure. Each systematic source i (e.g., electron energy scale or δ_{tot}) is changed by its estimated error in the analysis, implemented for data and MC where appropriate, and the cross-sections re-evaluated. The relative difference, δ_i , between the re-evaluated cross-sections, σ_i , and the nominal cross-sections, σ are calculated. This is taken to be the relative systematic uncertainty from source i . The systematic uncertainties from each source are then combined in quadrature for each bin of a cross-section, separately for positive and negative deviations from the nominal cross-section, using the following:

$$\frac{\sigma_{syst}^+}{\sigma} = \sqrt{\sum_i \delta_i^2} = \sqrt{\sum_i \left(\frac{\sigma_i - \sigma}{\sigma}\right)^2} \text{ where } \sigma_i - \sigma > 0 \quad (7.23)$$

$$\frac{\sigma_{syst}^-}{\sigma} = \sqrt{\sum_i \delta_i^2} = \sqrt{\sum_i \left(\frac{\sigma_i - \sigma}{\sigma}\right)^2} \text{ where } \sigma_i - \sigma < 0. \quad (7.24)$$

Here σ_{syst}^+ is the total positive systematic uncertainty and σ_{syst}^- the total negative systematic uncertainty. This can result in an asymmetric total systematic uncertainty. For some sources of systematic uncertainty, the deviation for varying a cut up and down in a given cross-section bin may result in deviations in the same direction (i.e., both up, or down). In this case the largest relative difference, δ_i , is taken and the deviation in the opposite direction is set to zero. Similarly, for a source which is

varied by using a different procedure (e.g., using a different electron finder), the δ_i is added to σ_{syst}^+ or σ_{syst}^- depending on its sign.

7.3.1 Reconstruction of the scattered electron

- **Dependence of the electron finder**

The Sinistra electron finder [110], briefly introduced in section 4.3.4, is used as an alternative to the EM electron finder. This introduces a problem: the BCAL energy corrections cannot be applied to the data and MC when the Sinistra electron finder is used. To overcome this difficulty, the nominal cross-sections are re-evaluated using the EM electron finder but with the BCAL energy corrections turned off. This cross-section is then compared to cross-sections determined using Sinistra to evaluate the systematic uncertainty due to changing the electron finder. The use of Sinistra tends to increase the cross-sections with respect to EM, the difference being approximately 0.5-2% but rising to almost 10% in high- y and high- Q^2 bins. Since Sinistra was developed primarily for low Q^2 events, differences from EM are possible at high Q^2 . This is acceptable as the total uncertainty in these high Q^2 bins is dominated by the statistical uncertainty.

- **Electron energy scale**

The uncertainty in the electron energy scale is discussed in section 5.6.3. The average uncertainty across the entire kinematic region is estimated to be 1%. To estimate the systematic uncertainty, the electron energy scale in MC is varied by $\pm 1\%$. The effect on the measurement of the kinematic variables is small, typically less than 0.5%, due to the use of the DA method (see section 4.2.3). The uncertainty in the cross-section rises up to 3% at high y , where the electron energy is low, due to threshold effects at the $E'_e > 10$ GeV cut.

- **Electron energy smearing**

The electron energy resolution in MC is better than that observed in data. To

correct for this difference MC events are smeared as described in section 5.6.3. The uncertainty on the smearing was found to be approximately 1%. To evaluate the systematic uncertainty due to the electron energy smearing in MC, the smearing factors are varied by $\pm 1\%$. The effect is found to be negligible, generally 0.1% but never larger than 0.3%.

- **Electron track momentum**

The cut threshold on p_{trk} is varied by ± 1 GeV to determine the systematic uncertainty from the disagreement in the electron track momentum distribution shown in figure 6.8. This systematic additionally tests the background contamination due to low momentum hadronic particles which are misidentified as the scattered electron (see section 6.2.1). The systematic uncertainty is typically less than 0.5% across the entire kinematic range.

- **Electron isolation**

The cut on the energy in a cone around the electron candidate (see section 6.5) not assigned to the electron candidate is investigated by varying the cut by ± 2 GeV. The systematic uncertainty is generally negligible except at high Q^2 where it rises to almost 5%. The reason for this large uncertainty at high Q^2 is that the electron is found in the FCAL and therefore close to the hadronic final state.

- **Distance of closest approach**

To estimate the systematic uncertainty of misidentified electrons due to the discrepancy in the DCA distribution between data and MC as seen in figure 6.8, the threshold of the DCA is decreased from 10 cm to 8 cm. The effect on the cross-section is typically less than 0.3%.

7.3.2 Reconstruction of the hadronic system

- **Parton shower model**

In section 3.2.1 two possible parton shower models are discussed: ARIADNE and Lepto MEPS. To estimate the systematic uncertainty due to the choice of parton shower model, Lepto MEPS is used to calculate the acceptance corrections instead of ARIADNE. The main difference between ARIADNE and MEPS is the description of the hadronic variables. The systematic uncertainty due to the change to MEPS is typically 1-2% but increases to 10% in bins with low statistics.

- **Hadronic energy scale**

The relative hadronic energy scale between data and MC is estimated to be 2% as discussed in section 4.3.5. To estimate the systematic uncertainty the hadronic energy in MC is varied by $\pm 1\%$. The effect is small, typically less than 0.1% and never reaching more than 0.7%. This is expected due to the use of the DA method for the reconstruction of the kinematic variables as described in section 4.2.3.

- **Projection of γ_h onto the FCAL**

The cut on the projection of γ_h onto the FCAL, $R_{\gamma_h,FCAL} < 18$ cm, is varied by 2 cm in each direction. This cut chiefly affects high- x events, where the struck quark is very forward and close to the FCAL beampipe. The systematic uncertainty due to this variation is less than 0.2% for the single differential cross-sections but rises to 6% for some high- x reduced cross-section bins.

7.3.3 Background estimation

- **Normalization of photoproduction MC**

The normalization of the PHP MC is somewhat uncertain as described in section 3.2.2 [111]. The systematic uncertainty due to PHP normalization is estimated by varying the PHP MC normalization by $\pm 50\%$. The systematic un-

certainty is typically 0.1-0.2% but rises to 1.5% in the middle- Q^2 region (where the electron is found in the BCAL).

- δ_{tot}

In section 6.2 the role of δ_{tot} in suppressing PHP, overlay, and cosmic and halo muons backgrounds is discussed. To estimate the systematic uncertainty due to the choice of upper (65 GeV) and lower (38 GeV) cuts on δ_{tot} , the δ_{tot} interval is changed symmetrically by ± 4 GeV (40-63 and 36-67 GeV). The effect is less than 1% for most bins, but rises to 5% at high x and high Q^2 .

- $\frac{P_T}{\sqrt{E_T}}$

The cut on $\frac{P_T}{\sqrt{E_T}}$ (see section 6.5.4) is varied by $\pm 1 \sqrt{\text{GeV}}$. This cut influences the amount of background from cosmic and halo muons. The systematic uncertainty due to the variation of the $\frac{P_T}{\sqrt{E_T}}$ cut is less than 1% across the entire kinematic range.

- Z_{vtx}

The cut on Z_{vtx} (see section 6.5.2) is varied by ± 5 cm. This cut influences the amount of non- ep background that is in the sample and restricts NC events to the well understood central region of the detector. The systematic uncertainties due to the Z_{vtx} are typically less than 1% but rise to 7% in the highest $d\sigma/dQ^2$ cross-section bin.

7.3.4 Effect of MC corrections

The corrections applied to the MC simulation to improve the MC description of data are discussed in chapter 5. To evaluate the systematic uncertainties due to the use of these corrections the following is done:

- **Track veto efficiency correction**

The uncertainty of the fit used for the TVE correction is large (see section 5.4). Thus the TVE correction is varied up and down by 50%. The systematic uncer-

tainty due to the TVE is typically less than 1.5% with the maximum uncertainty at medium Q^2 .

- **Track matching efficiency correction**

To estimate the systematic uncertainty of the TME correction (see section 5.5) the requirement for the electron polar angle θ is varied by ± 0.1 radian. Figure 5.8 shows that varying the cut by this amount is reasonable. The overall systematic uncertainty is less than 1%, rising to 2% at low Q^2 .

The description of the Z_{vtx} distribution in data by the MC after re-weighting (see section 5.7) is good, and therefore the systematic uncertainty due to the Z_{vtx} re-weighting is expected to be small. The cut based Z_{vtx} systematic uncertainty described in section 7.3.3 is sufficient to determine the uncertainty due to any remaining difference between the data and MC Z_{vtx} distributions.

The systematic uncertainties due to the RISOE, F_L , and polarisation corrections are not considered in this analysis. The effect of the RISOE correction is small, a 0.15% influence on the normalisation of MC to data, therefore the systematic uncertainty is also expected to be negligible. The F_L correction is only used to demonstrate that the data are well described by the MC and is not used in the unfolding of the cross-sections (see section 7.2), thus the systematic uncertainty due to the F_L correction is not investigated. The systematic uncertainty due to the polarisation correction is not evaluated in this analysis since the effects are expected mainly at high Q^2 where the statistical error dominates.

Chapter 8

Results

The event reconstruction and selection are outlined in chapters 4, 5 and 6. In this chapter, the selected events are used to determine the cross-sections in the bins described in section 7.1. The cross-section results are presented with both statistical and systematic uncertainties as described in section 7.3. The results are compared to the SM predictions evaluated using the HERAPDF1.5 PDFs.

In section 8.1 the unpolarised cross-section measurements are obtained by combining the positive and negative polarisation samples. The unpolarised reduced cross-sections are combined with the previously measured e^-p unpolarised reduced cross-sections [1] to extract the structure function $x\tilde{F}_3$ and the γ/Z interference structure function $x\tilde{F}_3^{\gamma Z}$. The cross-section measurements for the positive and negative polarisation samples are presented separately in section 8.2. Finally, the polarisation asymmetry is extracted to investigate parity violation in NC DIS.

8.1 Unpolarised cross-sections

The average polarisation of the entire e^+p data sample is $P_e = +0.03$. Therefore, it is possible to use a small theoretical correction to extract unpolarised ($P_e = 0$) cross-sections. The average polarisation is corrected for by using the SM predictions

of the cross-section:

$$\frac{d\sigma_{i,born}}{d\nu}|_{P_e=0} = \frac{d\sigma_{i,born}}{d\nu}|_{P_e=+0.03} \frac{\frac{d\sigma_{i,born,theory}}{d\nu}|_{P_e=0}}{\frac{d\sigma_{i,born,theory}}{d\nu}|_{P_e=+0.03}} \quad (8.1)$$

where $\frac{d\sigma_{i,born}}{d\nu}|_{P_e=+0.03}$ is the measured cross-section, $\frac{d\sigma_{i,born,theory}}{d\nu}|_{P_e=0}$ is the unpolarised theoretical cross-section, $\frac{d\sigma_{i,born,theory}}{d\nu}|_{P_e=+0.03}$ is the theoretical cross-section at $P_e = +0.03$. The single differential cross-sections are presented in section 8.1.1, the reduced cross-section in 8.1.2 and the structure functions $x\tilde{F}_3$ and $xF_3^{\gamma Z}$ in sections 8.1.3 and 8.1.3.

Tables of the results and their uncertainties are given in appendix A.

8.1.1 Single differential cross-sections

$d\sigma/dQ^2$

$d\sigma/dQ^2$ is obtained by integrating the expression for $\frac{d\sigma^2}{dx dQ^2}$ (equation 1.40) over x . Figure 8.1 shows the measured cross-section $d\sigma/dQ^2$, as a function of Q^2 , in the interval $185 \text{ GeV}^2 < Q^2 < 50000 \text{ GeV}^2$. Further restrictions on the phase space are $y < 0.9$ and $y(1-x)^2 > 0.004$. The measurement is found to fall by over six orders of magnitude in the measured interval, as expect from the $1/Q^4$ dependence of the cross-section. The agreement between the SM prediction using HERAPDF1.5 is good. This can be clearly seen in the bottom plot in figure 8.1, which shows the ratio of the measured cross-section to the SM prediction.

The contributions of each systematic uncertainty are shown in figure 8.2.

$d\sigma/dx$

$d\sigma/dx$ is measured in two kinematic regions, $Q^2 > 185 \text{ GeV}^2$ and $Q^2 > 3000 \text{ GeV}^2$, for $y < 0.9$ and $y(1-x)^2 > 0.004$. As is shown in figure 8.3 (top left), the $Q^2 > 185 \text{ GeV}^2$ cross-section is restricted to $x \leq 0.2$, due to the $R_{\gamma_h,FCAL}$ cut described in section 6.5. To make a cross-section measurement at values of x larger than 0.2 the minimum Q^2 requirement is raised to $Q^2 > 3000 \text{ GeV}^2$ (see 8.3) (bottom left). The decrease in the

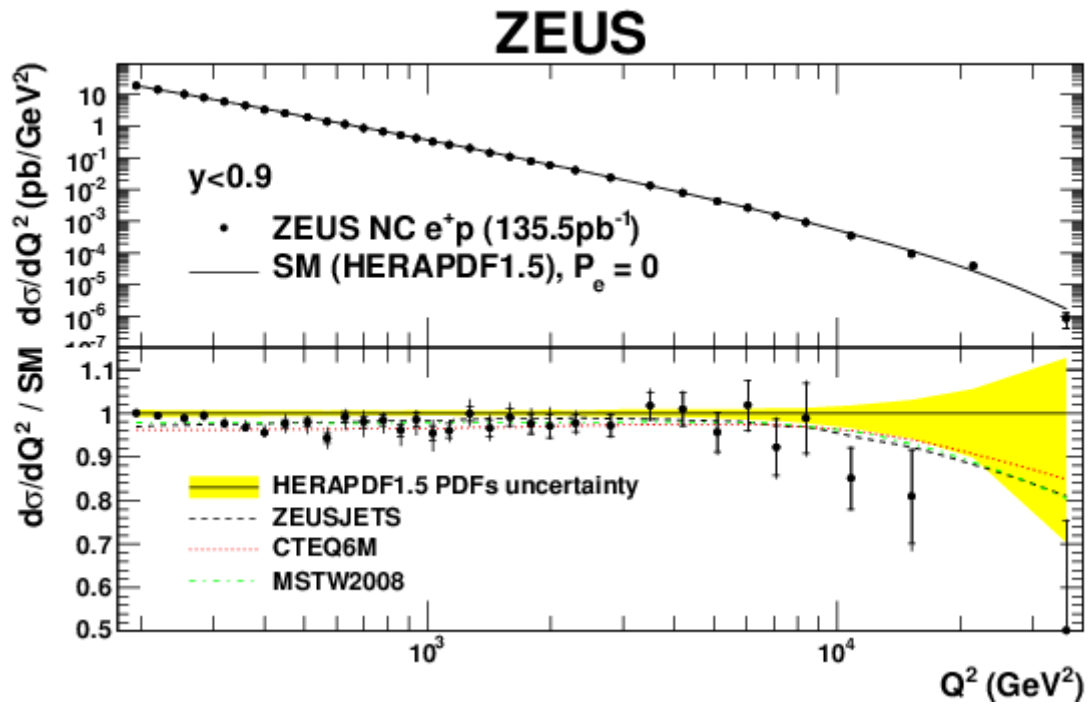


Figure 8.1: The $P_e = 0$ cross-section $d\sigma/dQ^2$ for $y < 0.9$ and $y(1-x)^2 > 0.004$ (top) and the ratio to the SM prediction (bottom). The closed circles represent the measured values, the inner error bars show the statistical uncertainty and the outer bars show the statistical and systematic uncertainties added in quadrature. The curves show the SM predictions evaluated using the HERAPDF1.5 (black solid line), ZEUSJETS (black dashed line), CTEQ6M (red dashed line) and MSTW2008 (green dashed line) PDFs. The shaded band on the bottom plot shows the uncertainties from the HERAPDF1.5 PDFs.

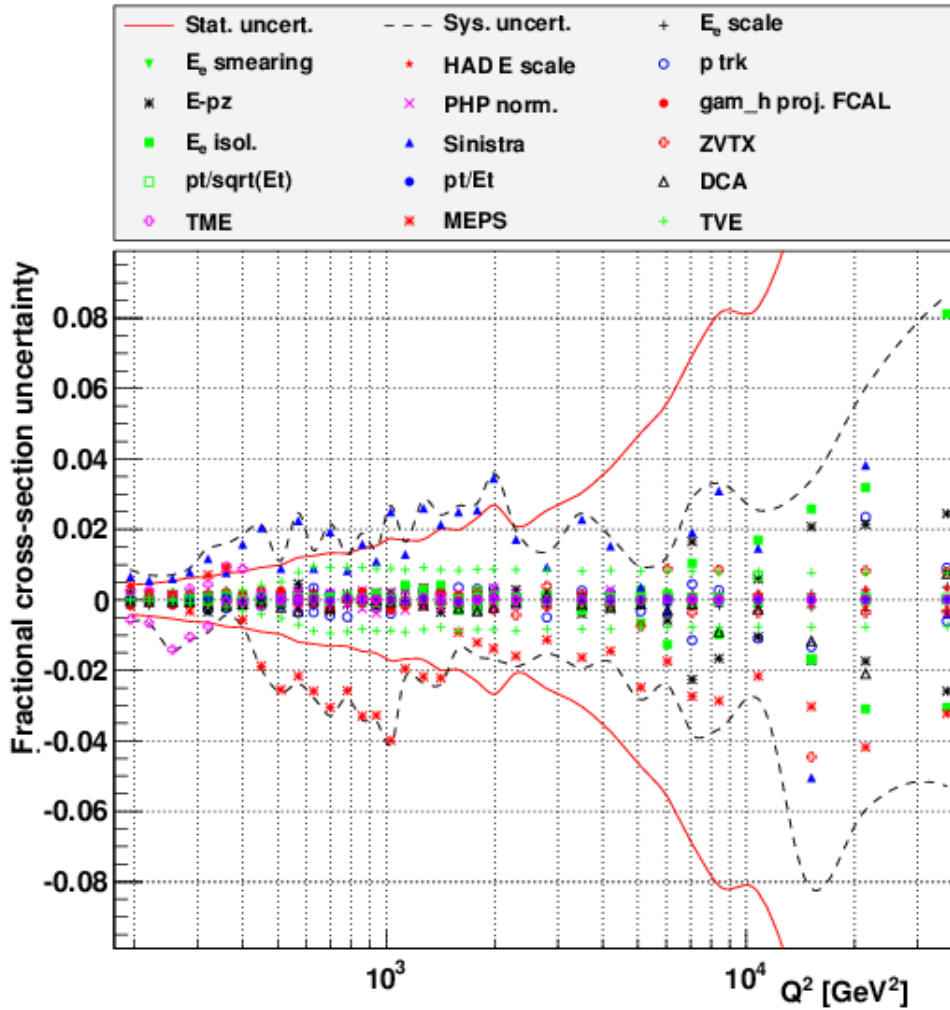


Figure 8.2: The systematic uncertainties for $d\sigma/dQ^2$. The coloured markers represent each systematic uncertainty, the red line shows the total statistical uncertainty.

cross-section toward high x reflects the low probability of striking a quark carrying a large fraction of the proton momentum. The ratios of the measured cross-sections for $Q^2 > 185 \text{ GeV}^2$ and $Q^2 > 3000 \text{ GeV}^2$ to the SM predictions are shown at the top and bottom left plots of figure 8.4. The SM predictions are in good agreement with the measured cross-sections.

The contributions of each systematic uncertainty are shown in figures 8.5 and 8.6.

$d\sigma/dy$

The single differential cross as a function of y , $d\sigma/dy$, is measured in the same kinematic region as $d\sigma/dx$. The positron energy requirement restricts the measurement of

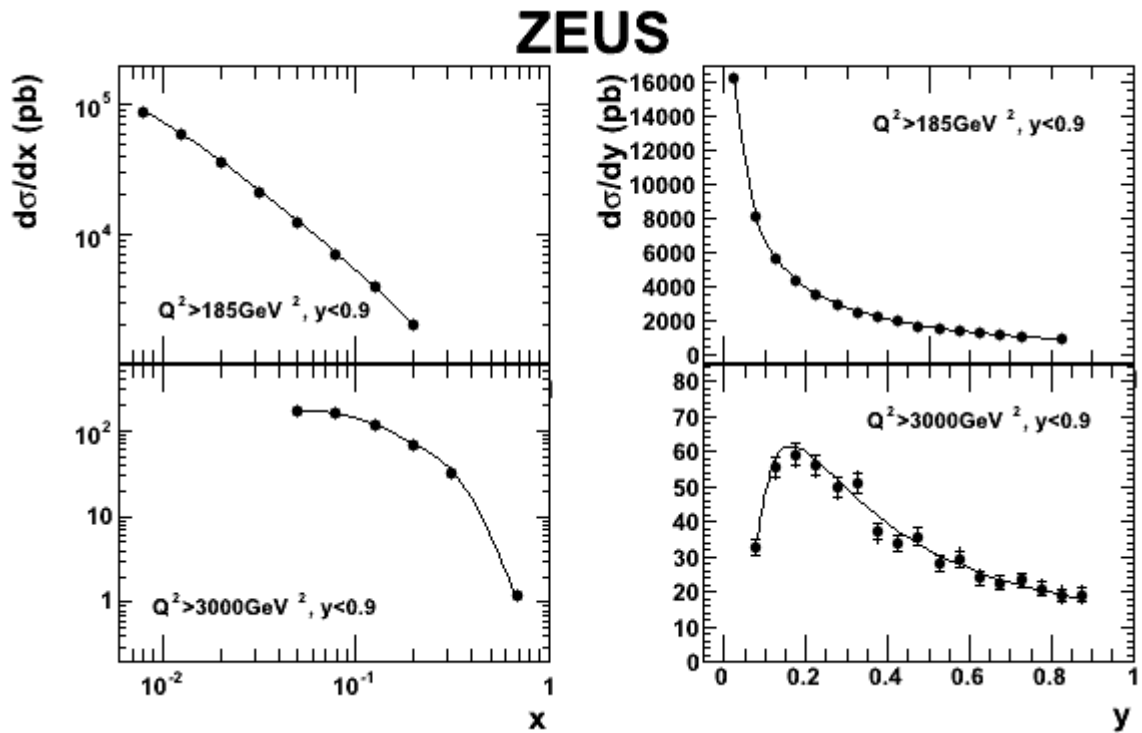


Figure 8.3: The $P_e = 0$ cross-sections $d\sigma/dx$ for $Q^2 > 185 \text{ GeV}^2$ (top left), $d\sigma/dy$ for $Q^2 > 185 \text{ GeV}^2$ (top right), $d\sigma/dx$ for $Q^2 > 3000 \text{ GeV}^2$ (bottom left) and $d\sigma/dy$ for $Q^2 > 3000 \text{ GeV}^2$ (bottom right). The closed circles represent the data points, the inner error bars show the statistical uncertainty and the outer bars show the statistical and systematic uncertainties added in quadrature. The curves show the SM predictions evaluated using the HERAPDF1.5 PDFs.

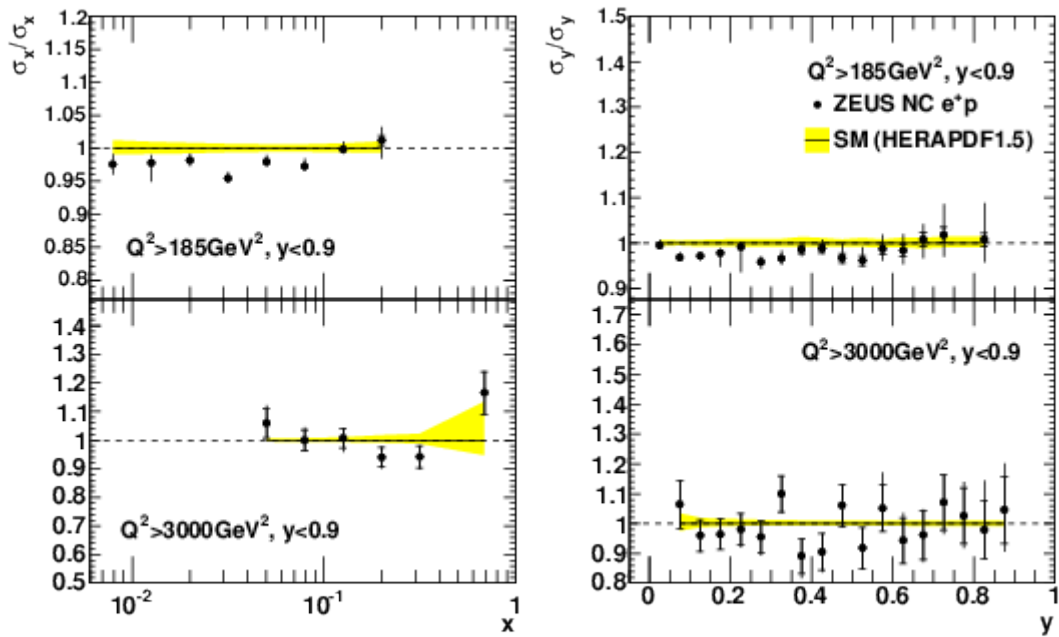


Figure 8.4: The ratios of the $P_e = 0$ cross-sections $d\sigma/dx$ for $Q^2 > 185 \text{ GeV}^2$ (top left), $d\sigma/dy$ for $Q^2 > 185 \text{ GeV}^2$ (top right), $d\sigma/dx$ for $Q^2 > 3000 \text{ GeV}^2$ (bottom left) and $d\sigma/dy$ for $Q^2 > 3000 \text{ GeV}^2$ (bottom right) to the SM predictions evaluated using HERAPDF1.5 PDFs. The closed circles represent the measured values, the inner error bars show the statistical uncertainty and the outer bars show the statistical and systematic uncertainties added in quadrature. The shaded band shows the uncertainties from the HERAPDF1.5 PDFs.

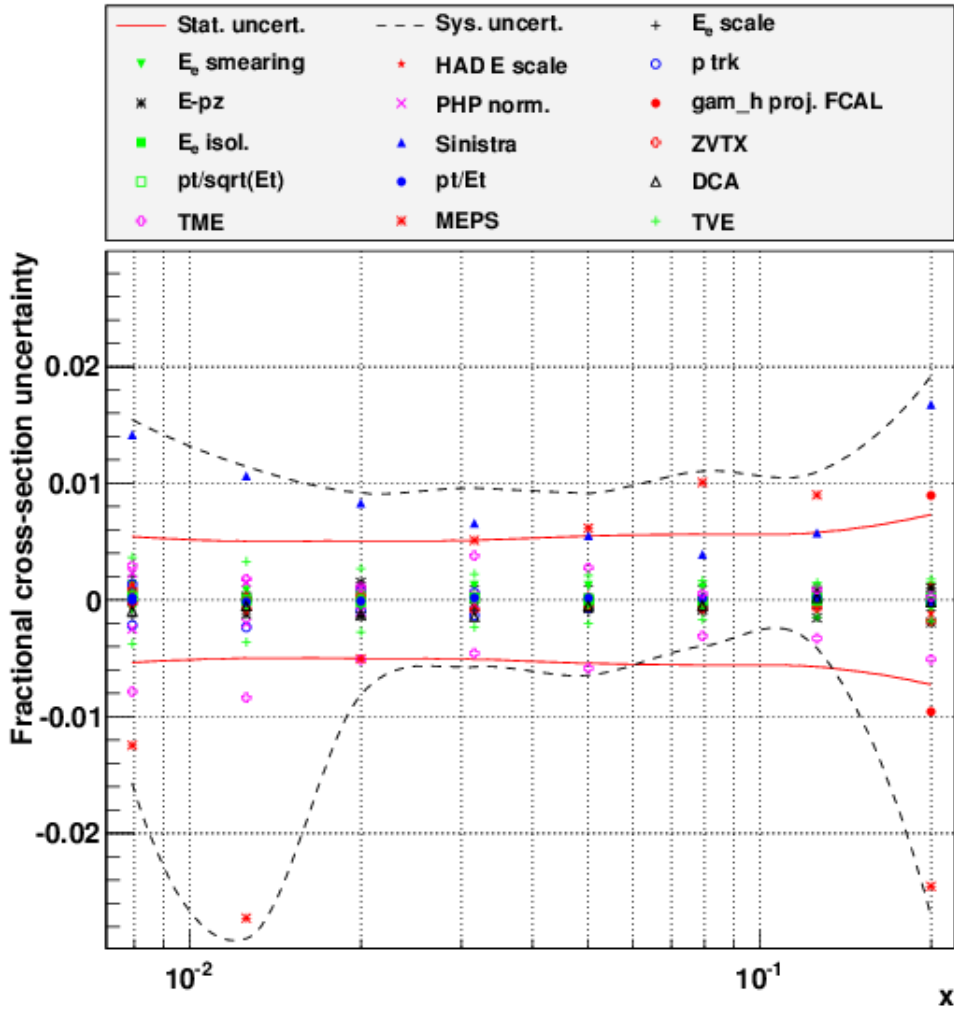


Figure 8.5: The systematic uncertainties for $d\sigma/dx$ for $Q^2 > 185 \text{ GeV}^2$. The coloured markers represent each systematic uncertainty, the red line shows the total statistical uncertainty.

$d\sigma/dy$ for $Q^2 > 185 \text{ GeV}^2$ to $y \leq 0.7$. One large bin $0.75 < y < 0.9$ is used to obtain the necessary statistics to make a measurement at high y at the cost of information on the shape of the cross-section. Increasing the minimum Q^2 to 3000 GeV^2 allows the cross-section to be measured up to 0.9 without the need to increase the bin width. The measured cross-sections for $Q^2 > 185 \text{ GeV}^2$ and $Q^2 > 3000 \text{ GeV}^2$ are shown in the top and bottom right plots of figure 8.3, respectively. The SM predictions agree within uncertainties with the measured cross-sections as can be seen in the top and bottom right plots of figure 8.4.

The contributions of each systematic uncertainty are shown in figures 8.7 and 8.8.

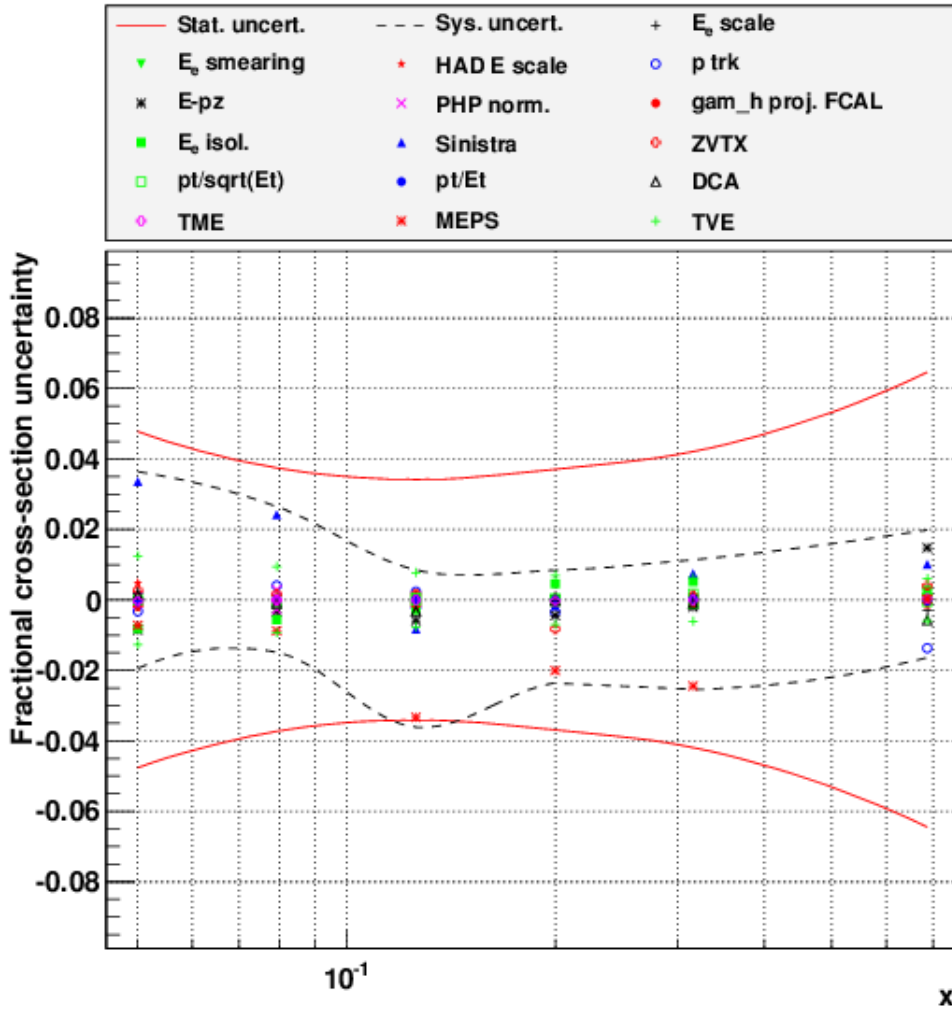


Figure 8.6: The systematic uncertainties for $d\sigma/dx$ for $Q^2 > 3000 \text{ GeV}^2$. The coloured markers represent each systematic uncertainty, the red line shows the total statistical uncertainty.

8.1.2 Reduced cross-sections

Figure 8.9 shows the unpolarised reduced cross-sections (see section 7.1.4) plotted as a function of x in bins of Q^2 . Plotted along with the e^+p reduced cross-sections are the previously published ZEUS e^-p results [1]. The e^-p cross-sections are corrected for the remaining polarisation in the same manner as the e^+p cross-sections (see section 8.1). The e^+p and e^-p cross-sections diverge at high Q^2 , where the structure function $x\tilde{F}_3$ (see equation 1.42) becomes sizeable. At low Q^2 $x\tilde{F}_3$ is negligible compared to the pure photon exchange term. As Q^2 increases $x\tilde{F}_3$ becomes relevant due to the γZ interference and Z exchange terms.

The ratio of the measured cross-sections and the SM predictions from the HERA-

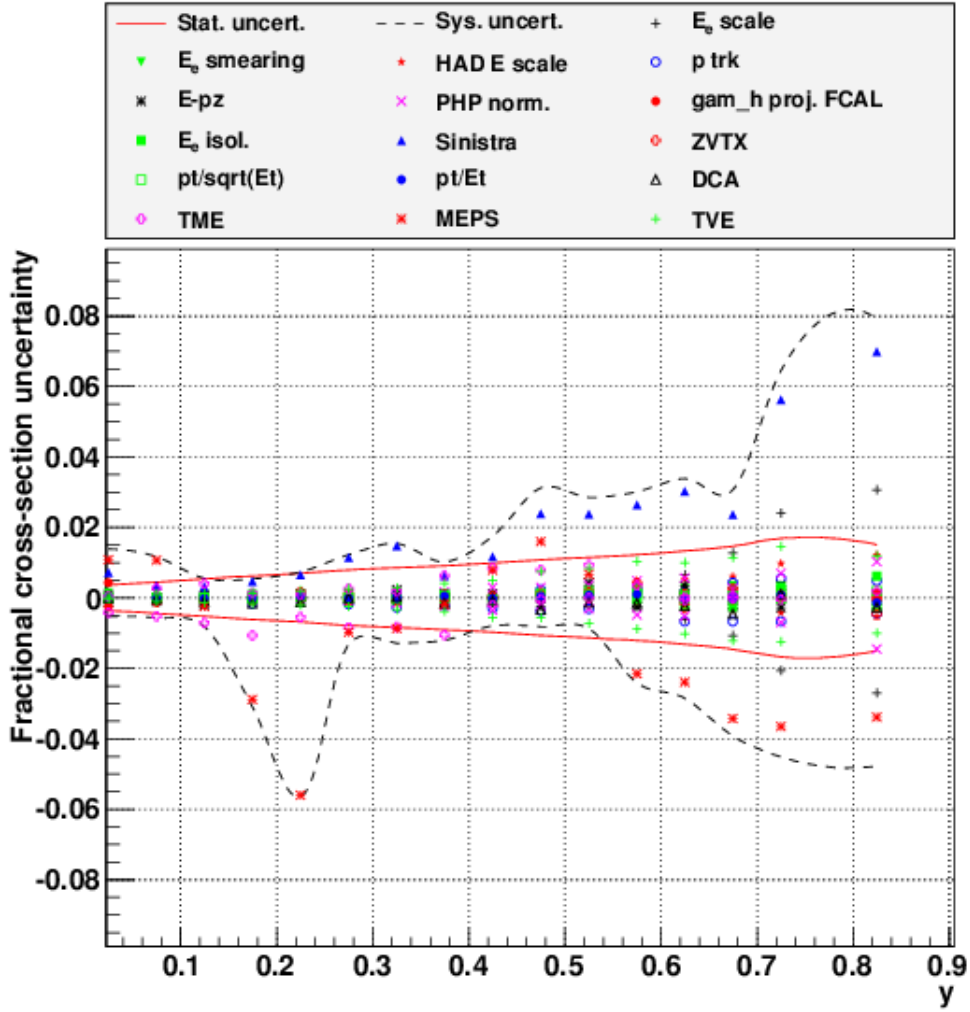


Figure 8.7: The systematic uncertainties for $d\sigma/dy$ for $Q^2 > 185 \text{ GeV}^2$. The coloured markers represent each systematic uncertainty, the red line shows the total statistical uncertainty.

PDF1.5 PDFs in figure 8.10 show that SM predictions agree well with the data over two orders of magnitude in Q^2 and x .

The contributions of each systematic uncertainty are shown in figure 8.11.

8.1.3 $x\tilde{F}_3$

The reduced cross-sections measured in this analysis together with the previously published e^-p results (see section 8.1.2) can be used to extract the $x\tilde{F}_3$ structure function. The sign of $x\tilde{F}_3$ in equation 1.46 increases the e^-p reduced cross-sections and decreases the e^+p reduced cross-sections. Thus, $x\tilde{F}_3$ can be extracted from the

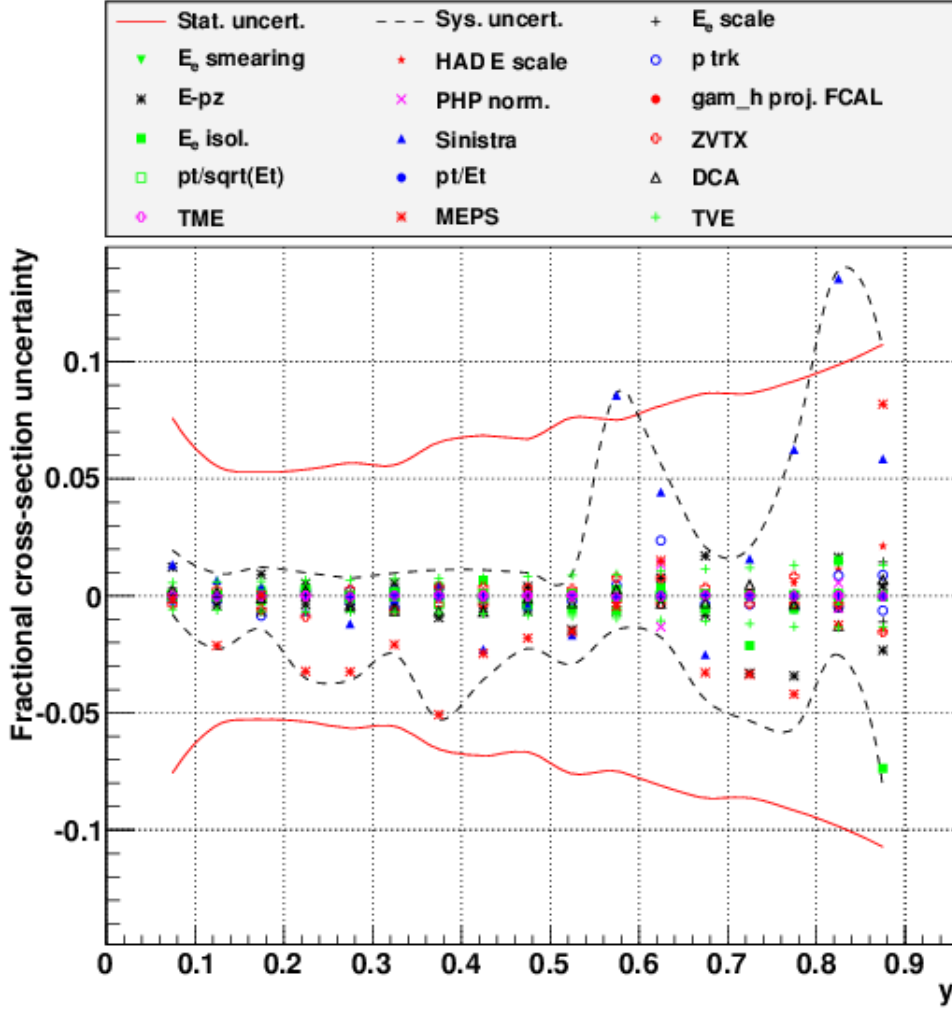


Figure 8.8: The systematic uncertainties for $d\sigma/dy$ for $Q^2 > 3000 \text{ GeV}^2$. The coloured markers represent each systematic uncertainty, the red line shows the total statistical uncertainty.

difference of the e^-p and e^+p cross-sections as:

$$x\tilde{F}_3 = \frac{Y_+}{2Y_-}(\tilde{\sigma}^{e^-p} - \tilde{\sigma}^{e^+p}). \quad (8.2)$$

The $x\tilde{F}_3$ results are shown as a function of x and in bins of Q^2 ($Q^2 > 1500 \text{ GeV}^2$) in figure 8.12. As expected the measured values of $x\tilde{F}_3$ at low Q^2 are small, but increase with Q^2 . The errors are conservative, since the systematic errors are treated as uncorrelated between the e^+p and e^-p analyses. This is a reasonable for the low Q^2 bins as they are dominated by systematics such as the TVE and TME¹, which

¹See section 5.4 and 5.5 for a description of the TVE and TME respectively. The systematic uncertainty from the TVE and TME are described in section 7.3.

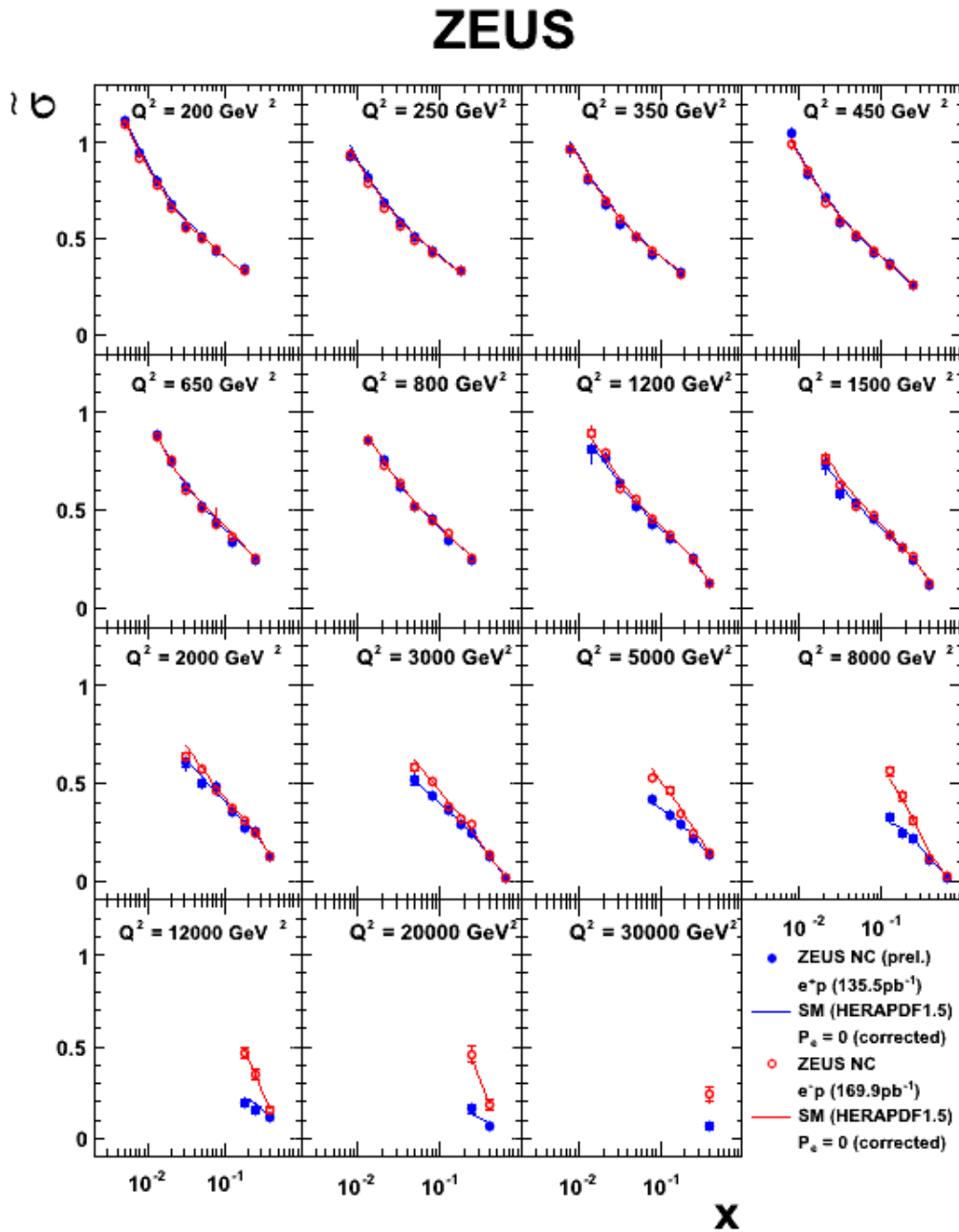


Figure 8.9: The reduced cross-section of $e^\pm p$ NC DIS with unpolarised e^\pm beams as a function of x for fixed Q^2 values. The blue closed circles represent the measured values, the inner error bars show the statistical uncertainty and the outer bars show the statistical and systematic uncertainties added in quadrature, although the errors are too small to be visible in most cases. The previously measured e^-p reduced cross-sections are shown as red open circles. The blue and red curves show the SM predictions evaluated using the HERAPDF1.5 PDFs for e^+ and e^- , respectively.

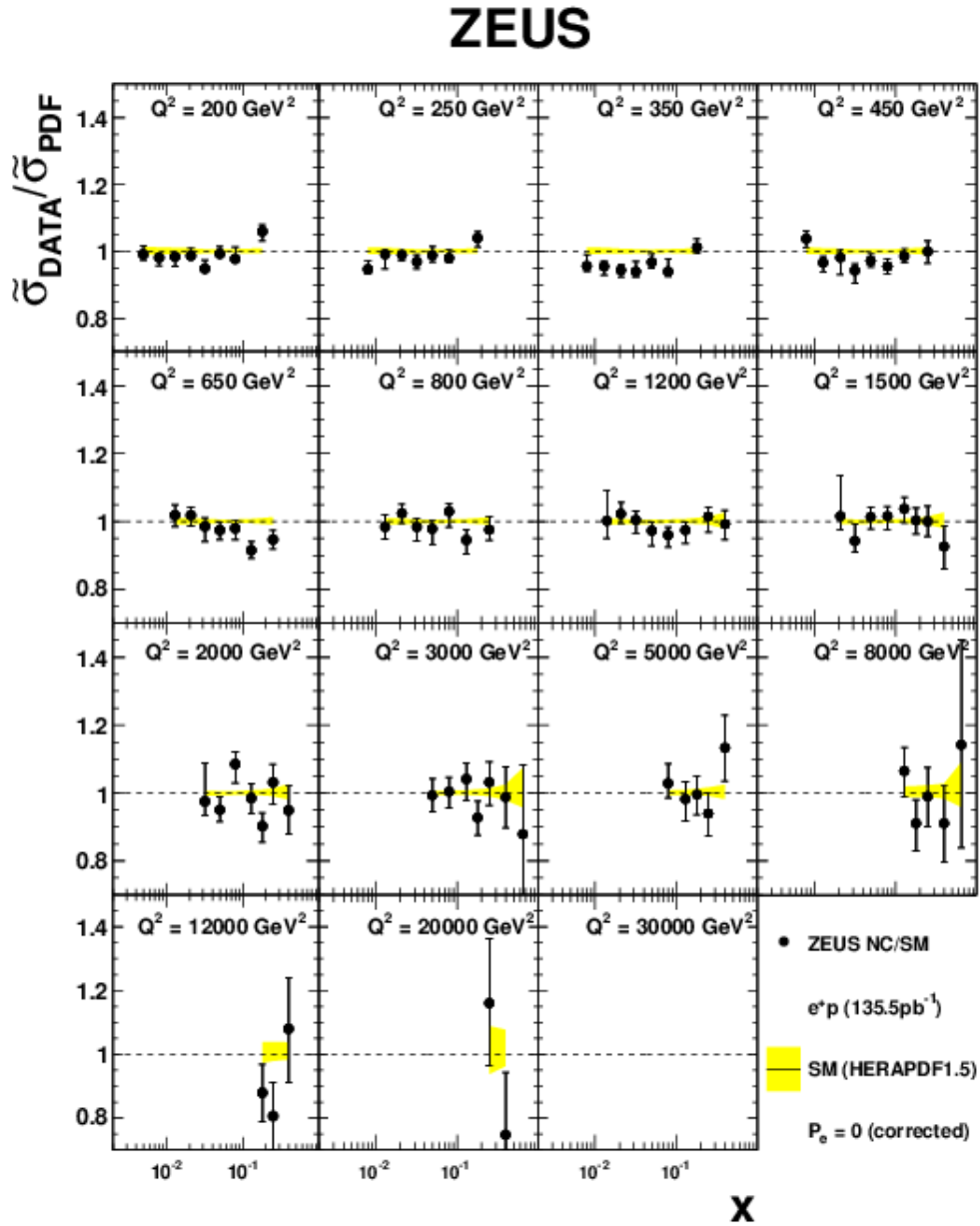


Figure 8.10: The ratio of the reduced cross-section of e^+ as a function of x at fixed values of Q^2 to the SM prediction evaluated using the HERAPDF1.5 PDFs. The points represent the measured values, the inner error bars show the statistical uncertainty and the outer bars show the statistical and systematic uncertainties added in quadrature. The shaded band shows the uncertainties from the HERAPDF1.5 PDFs.

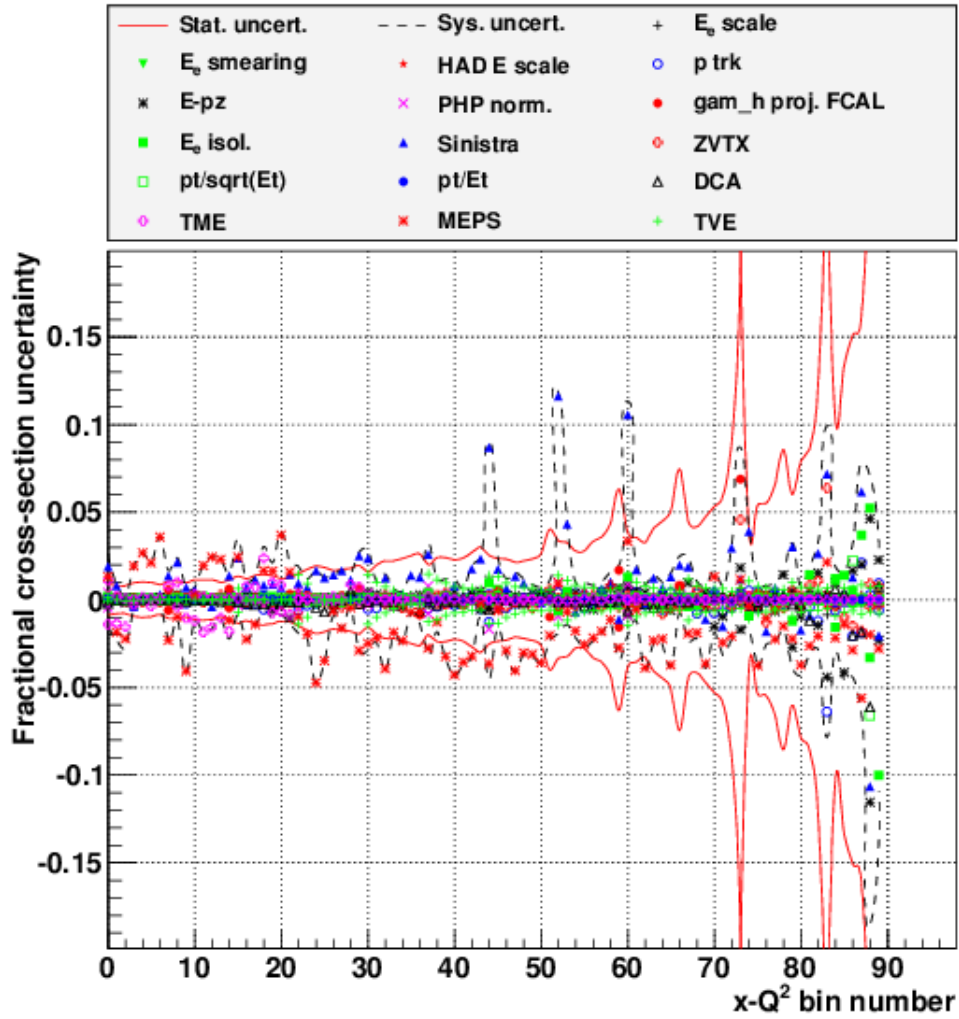


Figure 8.11: The systematic uncertainties for the reduced cross-section in terms of $x - Q^2$ bin number. The coloured markers represent each systematic uncertainty, the red line shows the total statistical uncertainty.

are not included in the e^-p analysis. The systematic uncertainties in the higher Q^2 bins are dominated by uncertainties correlated between the e^+p and e^-p analyses. Thus, the uncertainties are treated as uncorrelated in order not to underestimate the uncertainties at low Q^2 .

The SM prediction from the HERAPDF1.5 PDFs describe the measured values of $x\tilde{F}_3$ well across the entire Q^2 region.

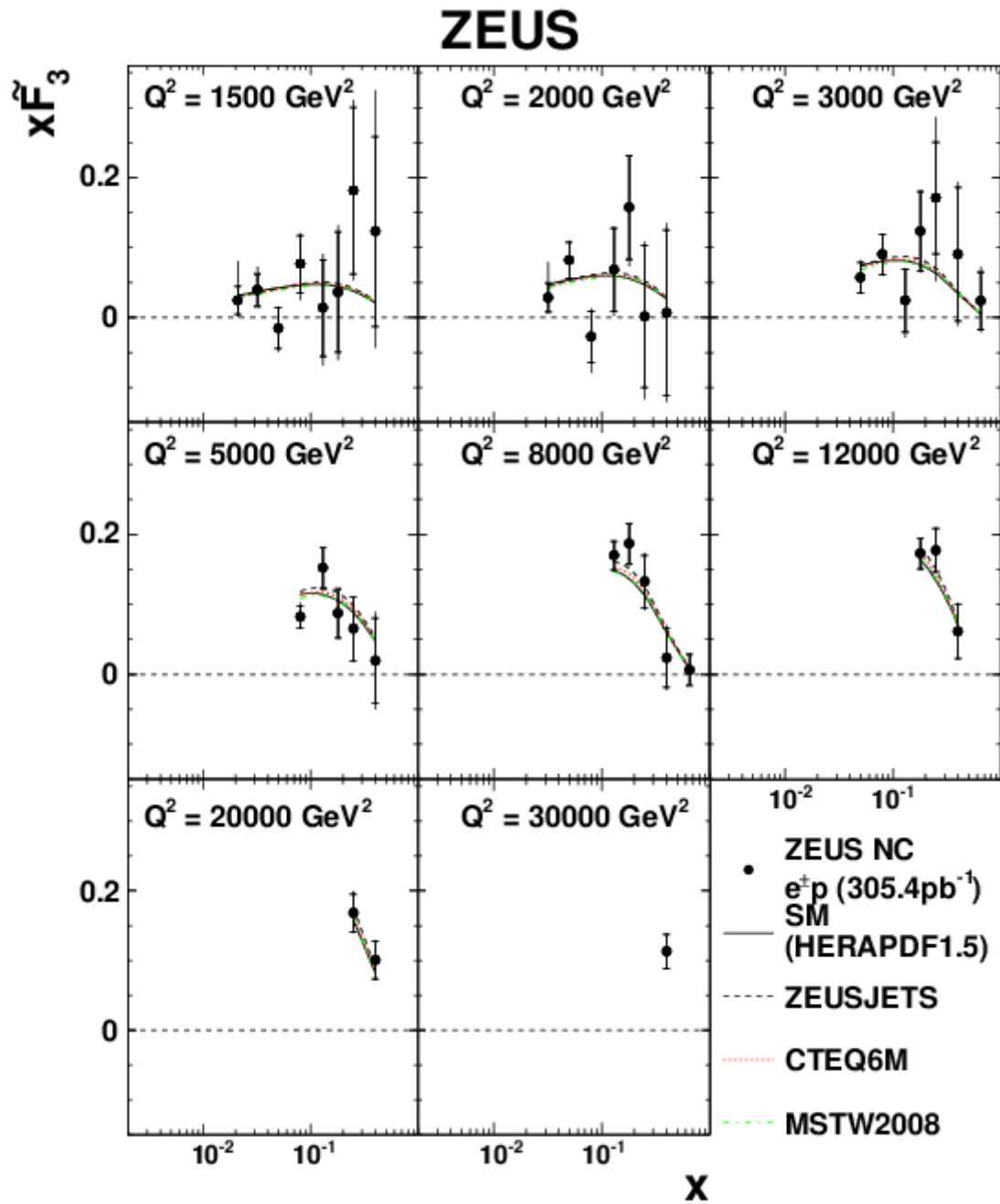


Figure 8.12: The structure function $x\tilde{F}_3$ as a function of x at fixed values of Q^2 . The points represent the measured values, the inner error bars show the statistical uncertainty and the outer bars show the statistical and systematic uncertainties added in quadrature. The solid curves show the SM prediction using the HERAPDF1.5 PDFs.

$x F_3^{\gamma Z}$

The structure function $x\tilde{F}_3$ is given by the equation 1.42. For the case of $P_e = 0$ the equation for $x\tilde{F}_3$ simplifies to:

$$x\tilde{F}_3 = -a_e \kappa x F_3^{\gamma Z} + 2v_e a_e \kappa^2 x F_3^Z. \quad (8.3)$$

The $x F_3^Z$ term is suppressed by the small value of v_e (≈ 0.04 see table 1.5) and the small value of κ^2 in the measured Q^2 region of $1500 - 30000 \text{ GeV}^2$. Thus, $x F_3^{\gamma Z}$ dominates the $x\tilde{F}_3$ structure function in the measured Q^2 region. $x F_3^{\gamma Z}$ can be approximated as:

$$x F_3^{\gamma Z} \approx \frac{x\tilde{F}_3}{a_e \kappa}. \quad (8.4)$$

It does not depend strongly on Q^2 , since it is proportional to the difference between the quark and anti-quark distributions as shown in equation 1.45. This is approximately the valance quark distribution, and therefore has little dependence on Q^2 . To improve the precision of $x F_3^{\gamma Z}$ the measurements are extracted at a single Q^2 point, $Q^2 = 1500 \text{ GeV}^2$, for each value of x using small theoretical corrections as follows:

$$x F_3^{\gamma Z}|_{1500 \text{ GeV}^2} = -\frac{x F_3^{\gamma Z}|_{point}}{a_e \chi_Z} \cdot \frac{x F_3^{\gamma Z}|_{1500 \text{ GeV}^2}^{Theory}}{x F_3^{\gamma Z}|_{point}^{Theory}} \quad (8.5)$$

where $x F_3^{\gamma Z}|_{1500 \text{ GeV}^2}$ and $x F_3^{\gamma Z}|_{1500 \text{ GeV}^2}^{Theory}$ are the measured and SM value of $x F_3^{\gamma Z}$ at $Q^2 = 1500 \text{ GeV}^2$, and $x F_3^{\gamma Z}|_{point}$ and $x F_3^{\gamma Z}|_{point \text{ GeV}^2}^{Theory}$ the measured and SM value of $x F_3^{\gamma Z}$ at the measured Q^2 value. The $x F_3^{\gamma Z}|_{1500 \text{ GeV}^2}$ values for each value of x are fitted with a 0th order polynomial to obtain a single $x F_3^{\gamma Z}$ value.

The result of this procedure is shown in figure 8.13. This is the most precise measurement of $x F_3^{\gamma Z}$ at ZEUS due to the combination of the two large statistics HERA-II e^+p and e^-p data sets. The statistical and systematic uncertainties are calculated from the fit used to average the $x F_3^{\gamma Z}$ values at a single x point. The SM predictions from the HERAPDF1.5 PDFs are in good agreement with the data.

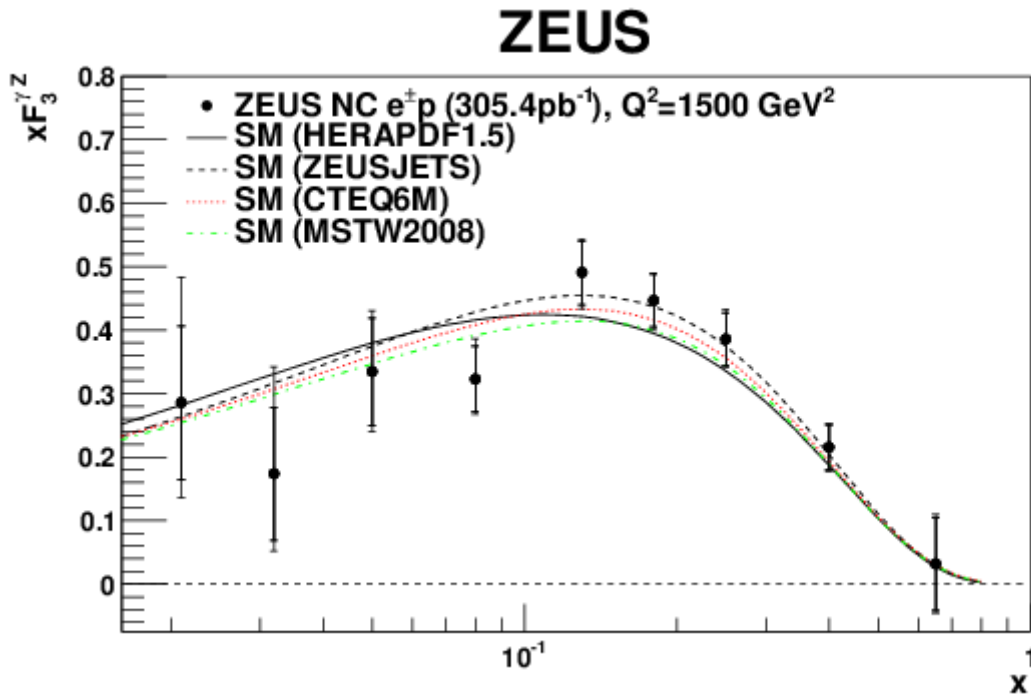


Figure 8.13: The structure function $xF_3^{\gamma Z}$ as a function of x at $Q^2 = 1500\text{ GeV}^2$. The points represent the measured values, the inner error bars show the statistical uncertainty and the outer bars show the statistical and systematic uncertainties added in quadrature. The solid curve shows the SM prediction using the HERAPDF1.5 (black solid line), ZEUSJETS (black dashed line), CTEQ6M (red dashed line) and MSTW2008 (green dashed line) PDFs.

8.2 Polarised cross-sections

The NC cross-section results using a longitudinally polarised positron (see section 1.7.2 for more information of the effects of longitudinal polarisation on the NC cross-sections) beam are presented in this section.

The single differential cross-sections $d\sigma/dQ^2$, $d\sigma/dx$, $d\sigma/dy$ and the reduced cross-sections are measured for e^+p data samples of both positive and negative polarisations. Details of each data sample are described in section 3.1. The phase space and the binning for each cross-section measurement are identical to those for the corresponding unpolarised cross-sections (see sections 8.1.1 and 8.1.2). In addition to the polarised cross-section measurements the polarisation asymmetry is extracted in order to quantify the amount of parity violation.

Tables of the polarised results and their uncertainties are given in appendix A.

8.2.1 Single differential cross-sections

$d\sigma/dQ^2$ and the polarisation asymmetry

In figure 8.14 (top) the measurement of the positive polarised cross-section $d\sigma/dQ^2$ is shown, while the negative polarised results are shown in 8.14 (bottom). The ratios of the measured cross-sections to the SM predictions are shown as insets in figure 8.14. The SM predictions are in good agreement with the measured positively and negatively polarised cross-sections. Parity violating effects are expected to appear only at high Q^2 where the measurement is statistically limited. However, the e^+p HERA-II data sample is large and approximately equally divided between positive and negative polarised positrons. Therefore, it is possible to compare the positive and negative polarised measurements at high Q^2 in a statistically meaningful manner. The effects of parity violation at high Q^2 are clearly seen in the rise of the ratio of the positive and negative polarised cross-sections seen in figure 8.15 (top).

Parity violation is clearly observed in the polarisation asymmetry, A^+ , extracted according to equation 1.47 as shown in figure 8.15 (bottom). Only statistical uncer-

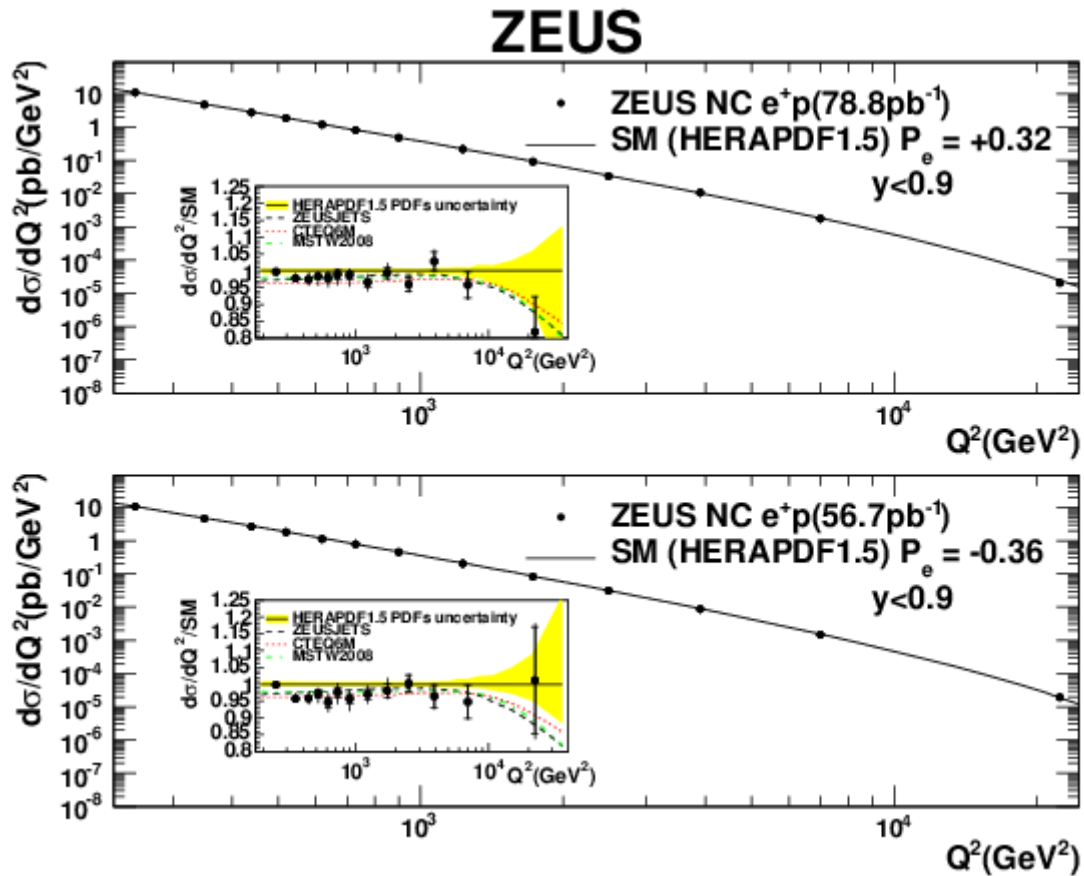


Figure 8.14: The cross-section $d\sigma/dQ^2$ for $y < 0.9$ and $y(1-x)^2 > 0.004$ for positive (top) and negative (bottom) polarisation. The closed circles represent the measured values, the inner error bars show the statistical uncertainty and the outer bars show the statistical and systematic uncertainties added in quadrature. The curves show the SM predictions evaluated using the HERAPDF1.5 PDFs. The inset shows the ratio to the SM prediction. The shaded bands on the inset show the uncertainties from the HERAPDF1.5 (black solid line), ZEUSJETS (black dashed line), CTEQ6M (red dashed line) and MSTW2008 (green dashed line) PDFs.

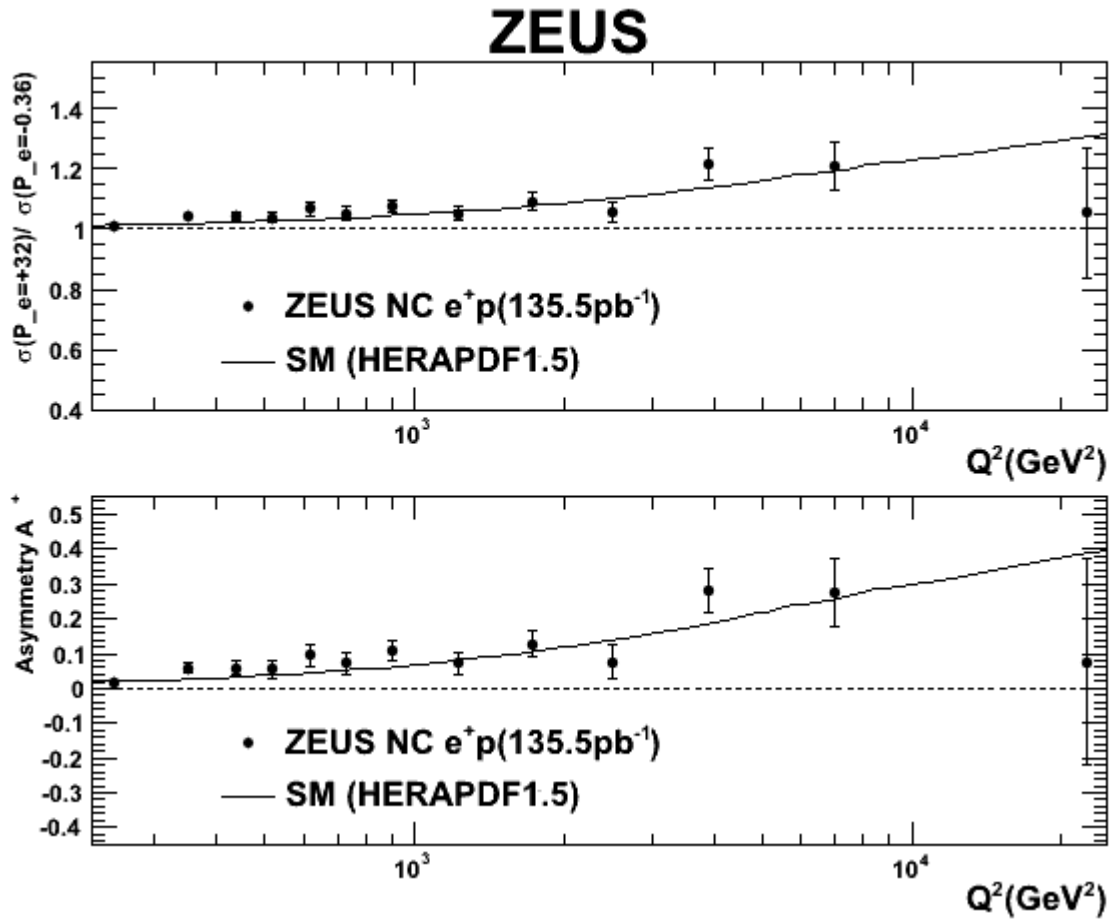


Figure 8.15: The measured ratio of the $d\sigma/dQ^2$ cross-sections for positive and negative polarisation (top) and the polarisation asymmetry A^+ as a function of Q^2 . The closed circles represent the measured values, where only the statistical uncertainties are considered as the systematic uncertainties are assumed to cancel. The curves show the SM predictions evaluated using the HERAPDF1.5 PDFs.

tainties are considered as the systematic uncertainties cancel.

The significance of the measured parity violating effects can be quantified via a χ^2 test, defined using the following [112]:

$$\chi^2 = \sum_i \frac{(A_{meas}^+ - A_{pred}^+)^2}{\delta_{meas}^2}, \quad (8.6)$$

where the sum runs over the asymmetry bins, A_{meas}^+ and A_{pred}^+ are the measured and predicted polarisation asymmetry values in bin i and δ_{meas} is the uncertainty on the measured value in bin i . The predicted polarisation asymmetry value is taken to be the SM prediction (the case of parity violation) or zero (the case of no parity violation). The χ^2 value is divided by the number of degrees of freedom (ndf). The expected value of χ^2/ndf is unity if the data is consistent with the prediction. The case of no parity violation gives $\chi^2/ndf = 8.7$ while the parity violation case yields a $\chi^2/ndf = 1.4$. Thus, the case of parity violation is clearly preferred over that of no parity violation.

$d\sigma/dx$ and $d\sigma/dy$

Figures 8.16 and 8.17 show for positive and negative polarisations respectively, the cross-sections $d\sigma/dx$ and $d\sigma/dy$ for $Q^2 > 185 \text{ GeV}^2$ and $Q^2 > 3000 \text{ GeV}^2$. The SM predictions agree well with all measurements. The effect of parity violation is expected to be relatively constant with x and y as is observed in figure 8.18 where the ratios of the positive and negative polarised cross-sections are shown. As expected, positive polarisation increases the cross-section while negative polarisation decreases it. An increase of the effect of parity violation is observed in the $Q^2 > 3000 \text{ GeV}^2$ cross-section compared to the $Q^2 > 185 \text{ GeV}^2$ cross-section, again as expected.

8.2.2 Reduced cross-sections

The polarised reduced cross-sections for e^+p are shown in figure 8.19 for positive and negative polarisations as a function of x and in bins of Q^2 . The measured cross-

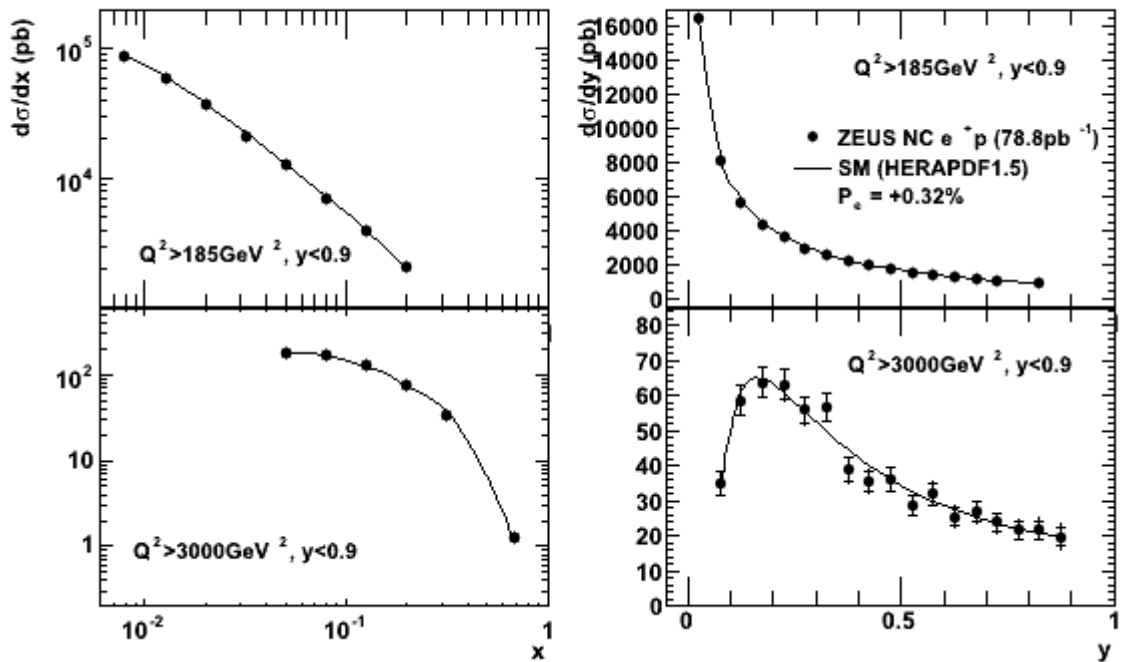


Figure 8.16: The cross-sections $d\sigma/dx$ for $Q^2 > 185 \text{ GeV}^2$ (top left), $d\sigma/dy$ for $Q^2 > 185 \text{ GeV}^2$ (top right), $d\sigma/dx$ for $Q^2 > 3000 \text{ GeV}^2$ (bottom left) and $d\sigma/dy$ for $Q^2 > 3000 \text{ GeV}^2$ (bottom right) for positive polarisation. The closed circles represent the data points, the inner error bars show the statistical uncertainty and the outer bars show the statistical and systematic uncertainties added in quadrature. The curves show the SM predictions evaluated using the HERAPDF1.5 PDFs.

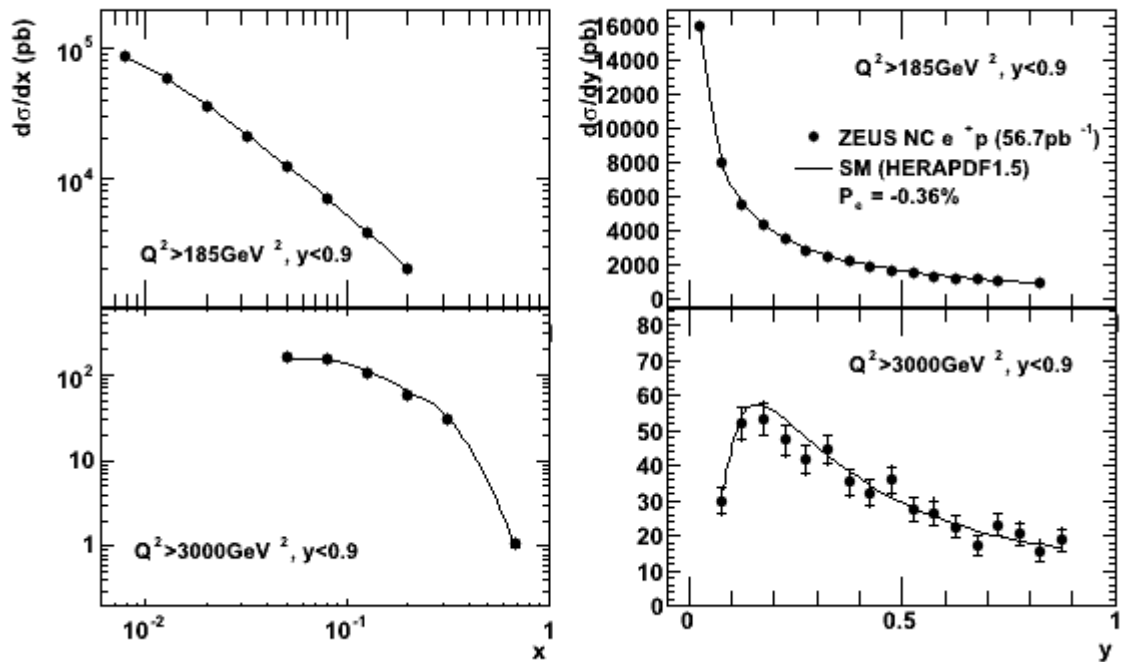


Figure 8.17: The cross-sections $d\sigma/dx$ for $Q^2 > 185 \text{ GeV}^2$ (top left), $d\sigma/dy$ for $Q^2 > 185 \text{ GeV}^2$ (top right), $d\sigma/dx$ for $Q^2 > 3000 \text{ GeV}^2$ (bottom left) and $d\sigma/dy$ for $Q^2 > 3000 \text{ GeV}^2$ (bottom right) for negative polarisation. The closed circles represent the data points, the inner error bars show the statistical uncertainty and the outer bars show the statistical and systematic uncertainties added in quadrature. The curves show the SM predictions evaluated using the HERAPDF1.5 PDFs.

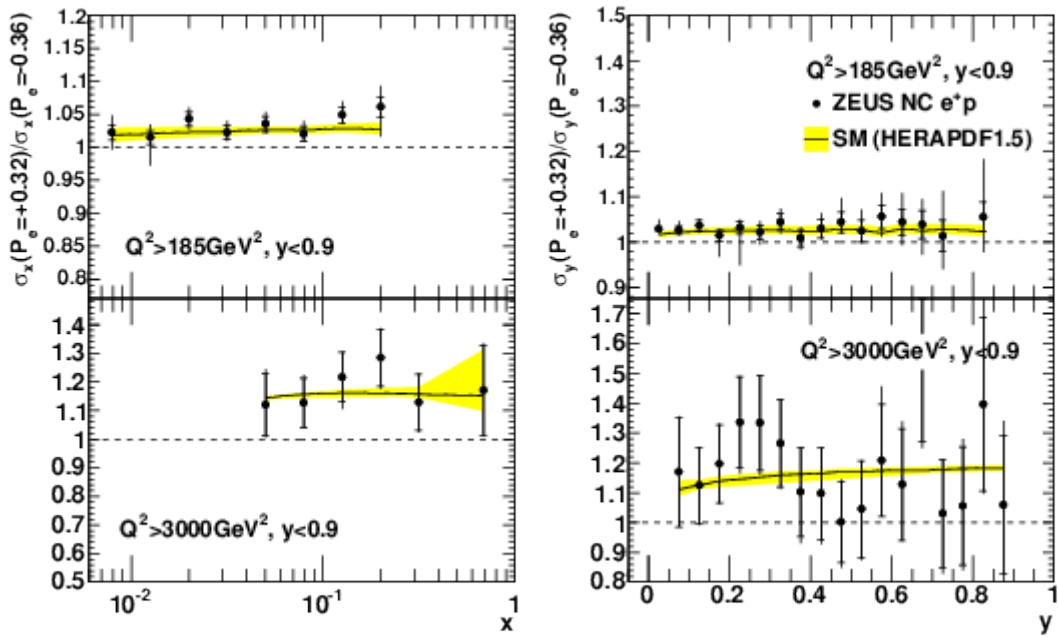


Figure 8.18: The ratio of the positive and negative polarised cross-sections $d\sigma/dx$ for $Q^2 > 185 \text{ GeV}^2$ (top left), $d\sigma/dy$ for $Q^2 > 185 \text{ GeV}^2$ (top right), $d\sigma/dx$ for $Q^2 > 3000 \text{ GeV}^2$ (bottom left) and $d\sigma/dy$ for $Q^2 > 3000 \text{ GeV}^2$ (bottom right). The closed circles represent the data points, the inner error bars show the statistical uncertainty and the outer bars show the statistical and systematic uncertainties added in quadrature. The curves show the SM predictions evaluated using the HERAPDF1.5 PDFs. The shaded bands on the plot show the uncertainties from the HERAPDF1.5 PDFs.

sections are well described by the SM predictions using the HERAPDF1.5 PDFs. Figure 8.20 shows the ratios of the positive and negative polarised cross-sections.

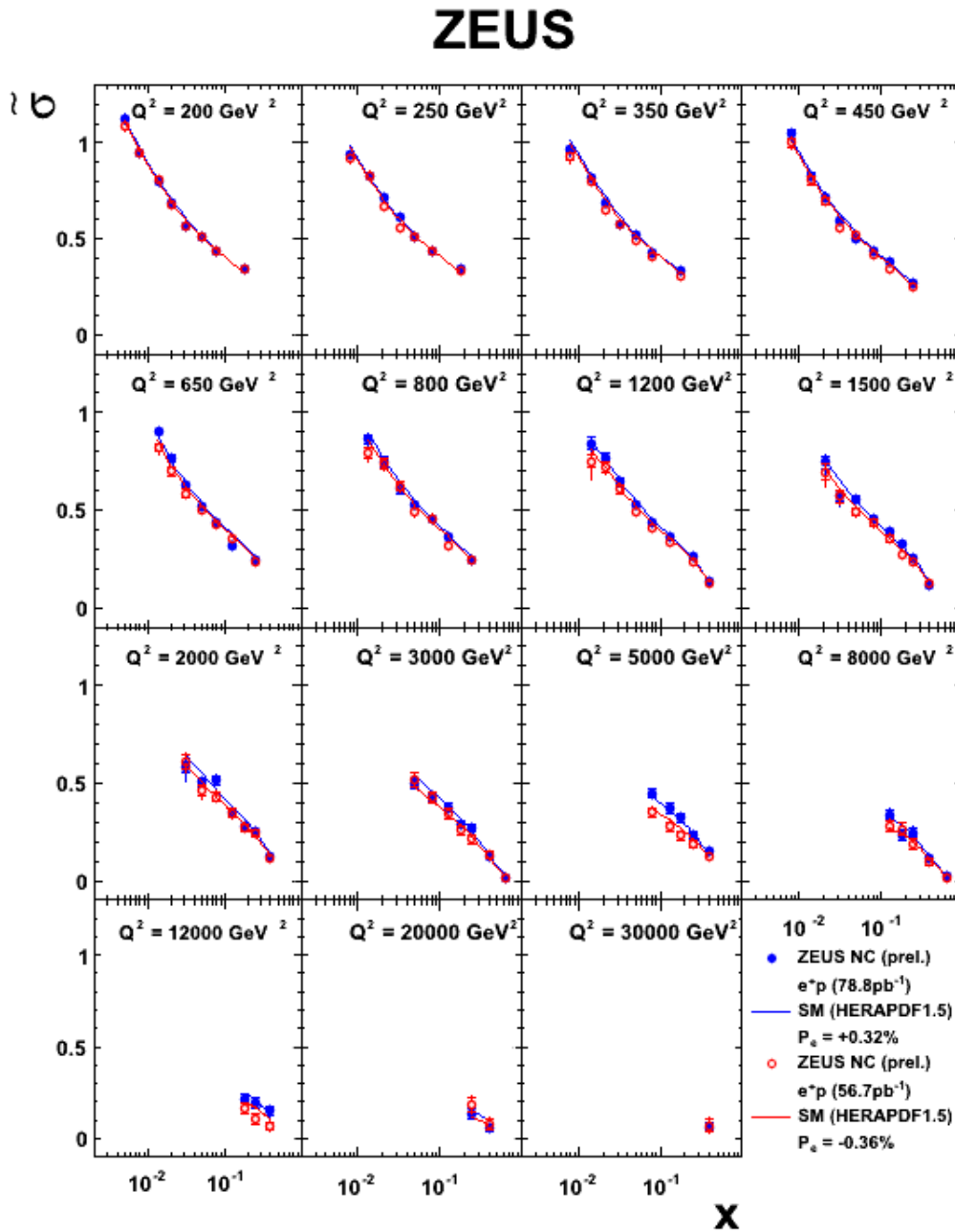


Figure 8.19: The reduced cross-section for e^+p NC DIS with polarised e^+ beams as a function of x for fixed Q^2 values. The blue closed (red open) circles represent the measured values for positive (negative) polarisation, the inner error bars show the statistical uncertainty and the outer bars show the statistical and systematic uncertainties added in quadrature, although the errors are too small to be visible in most cases. The blue and red curves show the SM predictions evaluated using the HERAPDF1.5 PDFs at the measured polarisation value.

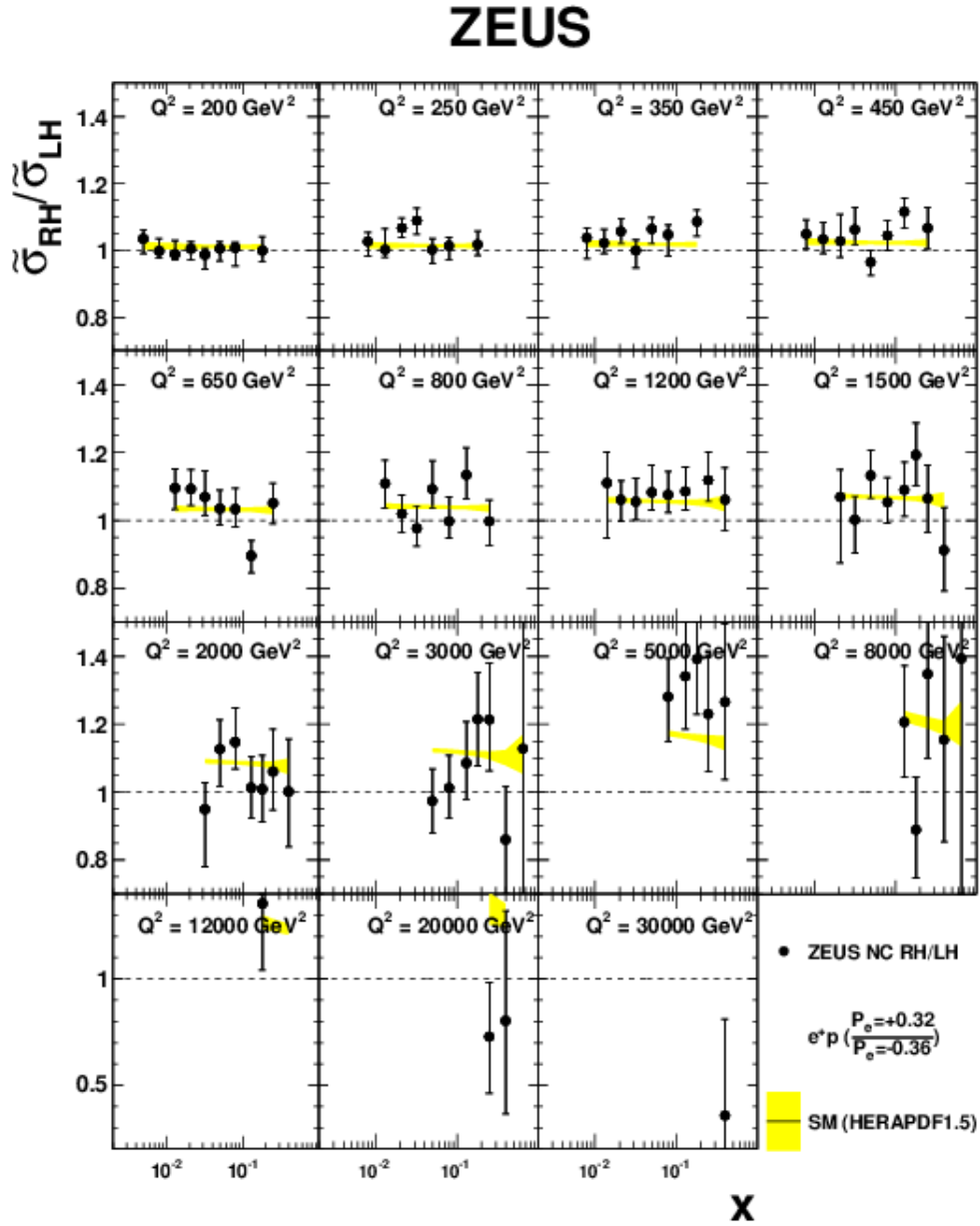


Figure 8.20: The ratios of the reduced cross-section with polarised e^+ beams as a function of x at fixed values of Q^2 to the SM predictions evaluated using the HERAPDF1.5 PDFs. The points represent the measured ratios, the inner error bars show the statistical uncertainty and the outer bars show the statistical and systematic uncertainties added in quadrature. The shaded band shows the uncertainties from the HERAPDF1.5 PDFs.

Chapter 9

Summary and conclusions

This thesis presents the ZEUS measurement of the 2006/2007 e^+p NC DIS cross-sections for $Q^2 > 185 \text{ GeV}^2$, $y < 0.9$ and $y(1-x)^2 > 0.004$, with an integrated luminosity of 135.5 pb^{-1} . The measured cross-sections are based on 4.7 times the integrated luminosity of the previously published HERA-II ZEUS e^+p NC DIS results [113]. The single-differential cross-sections $d\sigma/dQ^2$, $d\sigma/dx$ and $d\sigma/dy$ are presented for both an unpolarised positron beam and with positive and negative polarisation of the positron beam. The ratio of the positive and negative polarised $d\sigma/dQ^2$ cross-section and the polarisation asymmetry A^+ verify parity violation in e^+p NC DIS. The SM predictions agree reasonably well with all single differential cross-sections.

The results for the reduced cross-section, $\tilde{\sigma}$, are also presented for an unpolarised positron beam and positive and negative polarisation of the positron beam, in bins of Q^2 and x . The unpolarised cross-sections are compared to the previously published e^-p results from ZEUS [1]. The difference between the e^-p and e^+p cross-sections is used to extract the $x\tilde{F}_3$ and $xF_3^{\gamma Z}$ structure functions. These are the most precise measurements of $x\tilde{F}_3$ and $xF_3^{\gamma Z}$ to date, due to the large combined luminosity of 305.4 pb^{-1} . The SM predictions are in good agreement with all the results for $\tilde{\sigma}$, $x\tilde{F}_3$ and $xF_3^{\gamma Z}$.

The H1 and ZEUS collaborations have already released HERAPDF1.5, which

includes some of the HERA-II results. The inclusion of these new results will lead to a reduction of uncertainties in the PDFs, especially for the high- x gluon and u valence quark. Preliminary results from the inclusion of these results are shown in figure 9.1. These results will not only benefit the HERAPDF fits but will also serve as input into the work of other major fitting groups. Constraining the PDF fits is of great importance, as a precise knowledge of the PDFs is required for future measurements at the LHC.

In addition to further constraining the PDF fits, these measurements will allow further improvement in the precision of the axial and vector couplings, a_u , a_d , v_u and v_d , of the u and d quarks to the Z^0 boson.

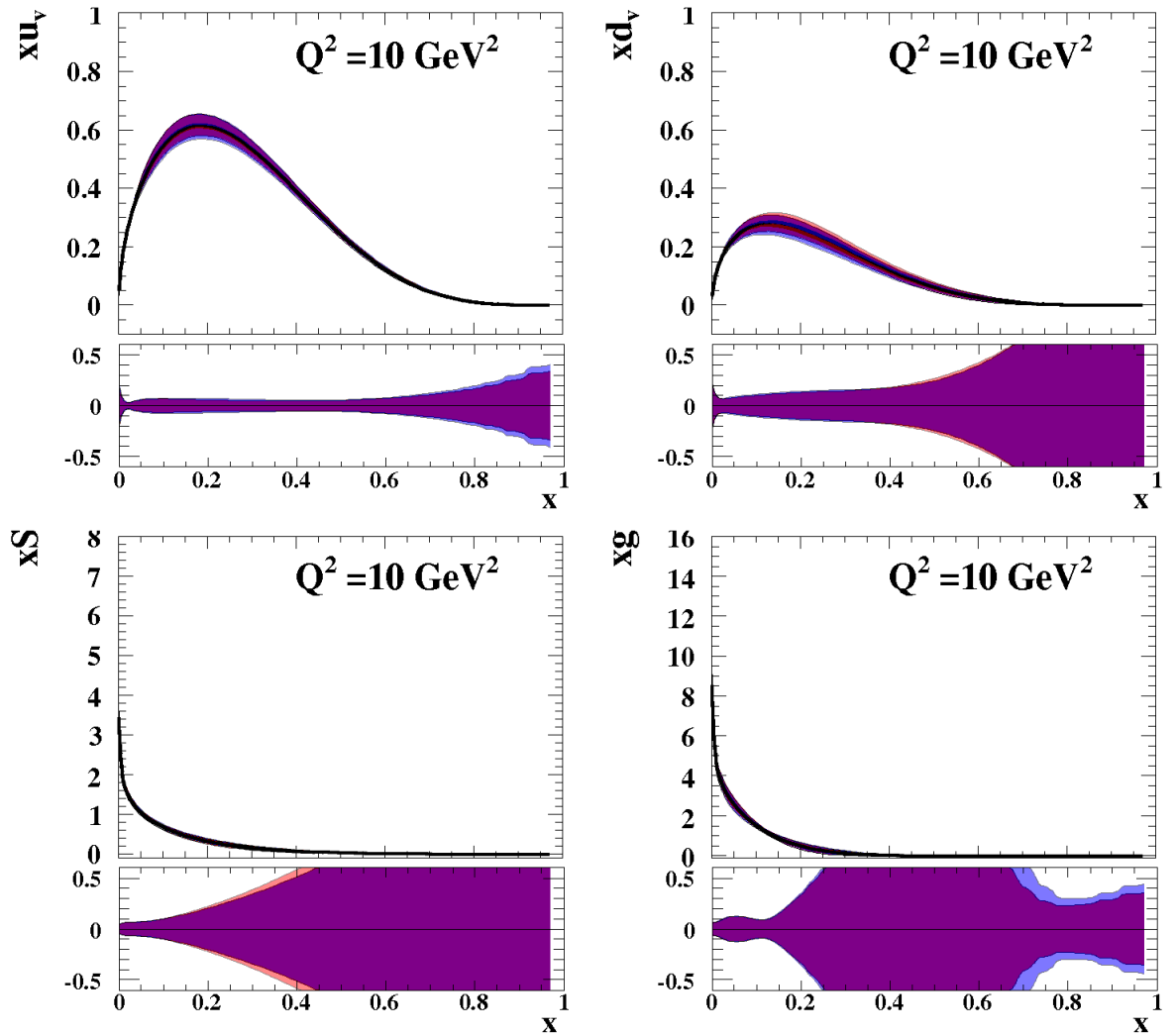


Figure 9.1: Parton densities for the u_v (top left), d_v (top right) valence quarks, the sea quarks (bottom left) and the gluon (bottom right). The fractional error is shown as the purple band below each distribution.

Appendix A

Cross section tables

A.1 List of included systematics

- δ_1 : Electron energy scale.
- δ_2 : δ_{tot} .
- δ_3 : Normalization of photoproduction MC.
- δ_4 : Dependence of the electron finder.
- δ_5 : Track matching efficiency correction.
- δ_6 : Parton shower model.
- δ_7 : Track veto efficiency correction.
- δ_8 : Electron energy smearing.
- δ_9 : Electron track momentum.
- δ_{10} : Electron isolation.
- δ_{11} : Distance of closest approach.
- δ_{12} : Hadronic energy scale.
- δ_{13} : Projection of γ_h onto the FCAL.

- $\delta_{14}: \frac{P_T}{\sqrt{E_T}}$.
- $\delta_{15}: Z_{vtx}$.

Q^2 range (GeV ²)	Q_c^2 (GeV ²)	$d\sigma/dQ^2$ (pb/GeV ²)	N_{data}	$N_{\text{bg}}^{\text{MC}}$
185 – 210	195	$(1.91 \pm 0.01^{+0.02}_{-0.01}) \times 10^1$	55281	110.1
210 – 240	220	$(1.43 \pm 0.01^{+0.01}_{-0.01}) \times 10^1$	47861	73.8
240 – 270	255	$(1.01 \pm 0.01^{+0.01}_{-0.01}) \times 10^1$	34808	59.2
270 – 300	285	$(7.79 \pm 0.05^{+0.07}_{-0.09})$	25835	18.9
300 – 340	320	$(5.79 \pm 0.04^{+0.09}_{-0.05})$	24184	32.8
340 – 380	360	$(4.35 \pm 0.03^{+0.07}_{-0.02})$	17201	22.8
380 – 430	400	$(3.33 \pm 0.03^{+0.06}_{-0.03})$	15791	28.5
430 – 480	450	$(2.56 \pm 0.02^{+0.05}_{-0.05})$	11903	40.1
480 – 540	510	$(1.89 \pm 0.02^{+0.02}_{-0.05})$	10365	19.9
540 – 600	570	$(1.39 \pm 0.02^{+0.03}_{-0.03})$	6943	36.2
600 – 670	630	$(1.14 \pm 0.01^{+0.02}_{-0.03})$	6366	20.1
670 – 740	700	$(8.70 \pm 0.12^{+0.19}_{-0.29}) \times 10^{-1}$	5655	22.5
740 – 820	780	$(6.65 \pm 0.09^{+0.09}_{-0.19}) \times 10^{-1}$	5750	16.9
820 – 900	860	$(5.08 \pm 0.07^{+0.09}_{-0.17}) \times 10^{-1}$	4654	25.0
900 – 990	940	$(4.16 \pm 0.06^{+0.06}_{-0.14}) \times 10^{-1}$	4295	15.6
990 – 1080	1030	$(3.20 \pm 0.06^{+0.09}_{-0.14}) \times 10^{-1}$	3304	10.5
1080 – 1200	1130	$(2.55 \pm 0.04^{+0.04}_{-0.06}) \times 10^{-1}$	3522	18.1
1200 – 1350	1270	$(1.96 \pm 0.03^{+0.06}_{-0.05}) \times 10^{-1}$	3439	14.6
1350 – 1500	1420	$(1.42 \pm 0.03^{+0.03}_{-0.03}) \times 10^{-1}$	2501	16.4
1500 – 1700	1590	$(1.08 \pm 0.02^{+0.03}_{-0.02}) \times 10^{-1}$	2549	8.3
1700 – 1900	1790	$(7.84 \pm 0.18^{+0.21}_{-0.13}) \times 10^{-2}$	1849	8.5
1900 – 2100	1990	$(5.88 \pm 0.16^{+0.13}_{-0.10}) \times 10^{-2}$	1393	9.1
2100 – 2600	2300	$(4.02 \pm 0.08^{+0.08}_{-0.08}) \times 10^{-2}$	2311	7.2
2600 – 3200	2800	$(2.34 \pm 0.06^{+0.03}_{-0.04}) \times 10^{-2}$	1565	3.3
3200 – 3900	3500	$(1.31 \pm 0.04^{+0.03}_{-0.03}) \times 10^{-2}$	1083	1.1
3900 – 4700	4200	$(7.77 \pm 0.29^{+0.14}_{-0.14}) \times 10^{-3}$	715	3.9
4700 – 5600	5100	$(4.18 \pm 0.20^{+0.04}_{-0.12}) \times 10^{-3}$	447	0.0
5600 – 6600	6050	$(2.66 \pm 0.15^{+0.03}_{-0.06}) \times 10^{-3}$	320	0.0
6600 – 7800	7100	$(1.47 \pm 0.10^{+0.04}_{-0.06}) \times 10^{-3}$	208	0.0
7800 – 9200	8400	$(9.20 \pm 0.74^{+0.31}_{-0.34}) \times 10^{-4}$	152	0.0
9200 – 12800	10800	$(3.40 \pm 0.28^{+0.09}_{-0.10}) \times 10^{-4}$	145	0.0
12800 – 18100	15200	$(9.21 \pm 1.21^{+0.31}_{-0.76}) \times 10^{-5}$	57	0.0
18100 – 25600	21500	$(3.81^{+0.76}_{-0.64} \text{ } ^{+0.23}_{-0.23}) \times 10^{-5}$	35	0.0
25600 – 50000	36200	$(8.23^{+6.51}_{-3.94} \text{ } ^{+0.71}_{-0.44}) \times 10^{-7}$	4	0.0

Table A.1: The single differential cross section $d\sigma/dQ^2$ ($y < 0.9$, $y(1-x)^2 > 0.004$) ($\mathcal{L} = 135.5\text{pb}^{-1}$, $P_e = 0$). The bin range, bin centre (Q_c^2) and measured cross section are shown. The first (second) error on the cross section corresponds to the statistical (systematic) uncertainties. The number of observed data events (N_{data}) and simulated background events ($N_{\text{bg}}^{\text{MC}}$) are also shown.

A.2 Tables of cross-sections

Q_c^2 (GeV ²)	$d\sigma/dQ^2$ (pb/GeV ²)	stat. (%)	sys. (%)	δ_1 (%)	δ_2 (%)	δ_3 (%)	δ_4 (%)	δ_5 (%)	δ_6 (%)	δ_7 (%)	$\delta_8 - \delta_{15}$ (%)
195	1.91×10^1	± 0.4	+0.9 -0.6	+0.2 -0.2	+0.2 -0.0	+0.1 -0.1	+0.6 -0.0	+0.2 -0.6	+0.4 -0.0	+0.0 -0.0	+0.1 -0.2
220	1.43×10^1	± 0.5	+0.7 -0.7	+0.2 +0.2	+0.0 -0.1	+0.1 -0.1	+0.5 +0.3	+0.3 -0.7	+0.1 +0.1	+0.1 +0.0	+0.3 -0.1
255	1.01×10^1	± 0.5	+0.7 -1.4	+0.2 -0.2	+0.1 -0.1	+0.1 -0.1	+0.3 -0.0	+0.1 -1.4	+0.1 -0.0	+0.0 +0.1	+0.2 -0.2
285	7.79	± 0.6	+0.9 -1.1	+0.2 -0.2	+0.0 -0.1	+0.0 -0.1	+0.8 -0.0	+0.3 -1.1	+0.0 -0.3	+0.1 -0.1	+0.2 -0.2
320	5.79	± 0.6	+1.5 -0.9	+0.2 -0.2	+0.1 -0.3	+0.1 -0.1	+1.2 -0.0	+0.4 -0.8	+0.7 -0.0	+0.1 -0.1	+0.2 -0.4
360	4.35	± 0.8	+1.6 -0.4	+0.3 -0.1	+0.0 -0.2	+0.1 -0.1	+0.8 -0.0	+0.9 -0.0	+0.9 -0.0	+0.2 -0.2	+0.3 -0.3
400	3.33	± 0.8	+1.8 -0.8	+0.2 +0.2	+0.0 +0.0	+0.1 +0.2	+1.6 +2.0	+0.9 +0.2	+0.0 +0.0	+0.3 +0.4	+0.2 +0.3
450	2.56	± 0.9	+2.1 -2.0	+0.2 -0.2	+0.0 -0.1	+0.2 -0.2	+2.0 -0.0	+0.2 -0.9	+0.0 +0.0	+0.4 -0.4	+0.3 -0.2
510	1.89	± 1.0	+1.1 -2.6	+0.2 -0.2	+0.0 -0.1	+0.1 -0.1	+0.9 -0.0	+0.0 -0.0	+0.0 -2.6	+0.5 -0.5	+0.3 -0.3
570	1.39	± 1.2	+2.5 -2.4	+0.3 -0.3	+0.5 -0.0	+0.2 -0.2	+2.2 -0.0	+0.1 -0.0	+0.0 -2.2	+0.8 -0.7	+0.3 -0.5
630	1.14	± 1.3	+1.4 -2.8	+0.3 -0.2	+0.1 -0.0	+0.2 -0.1	+0.9 -0.0	+0.0 +0.0	+0.0 -2.6	+0.9 -0.9	+0.4 -0.4
700	8.70×10^{-1}	± 1.3	+2.2 -3.3	+0.2 -0.2	+0.0 -0.3	+0.2 -0.2	+1.9 -0.0	+0.0 -0.1	+0.0 -3.1	+0.9 -1.0	+0.2 -0.6
780	6.65×10^{-1}	± 1.3	+1.3 -2.8	+0.2 -0.2	+0.1 -0.0	+0.2 -0.1	+0.8 -0.0	+0.0 -0.0	+0.0 -2.6	+0.9 -0.9	+0.2 -0.5
860	5.08×10^{-1}	± 1.5	+1.9 -3.4	+0.2 -0.2	+0.1 -0.0	+0.3 -0.3	+1.6 -0.0	+0.1 -0.0	+0.0 -3.3	+0.9 -0.8	+0.3 -0.1
940	4.16×10^{-1}	± 1.5	+1.4 -3.4	+0.1 -0.1	+0.2 -0.2	+0.2 -0.4	+1.1 -0.0	+0.0 -0.0	+0.0 -3.3	+0.9 -0.9	+0.2 -0.3
1030	3.20×10^{-1}	± 1.7	+2.7 -4.1	+0.1 -0.1	+0.2 -0.2	+0.2 -0.2	+2.5 -0.0	+0.0 -0.0	+0.0 -4.0	+0.9 -0.9	+0.1 -0.5
1130	2.55×10^{-1}	± 1.7	+1.6 -1.7	+0.1 -0.2	+0.3 -0.0	+0.2 -0.3	+1.3 -0.0	+0.0 -0.0	+0.0 -2.0	+0.8 +0.9	+0.4 -0.4
1270	1.96×10^{-1}	± 1.7	+2.8 -2.4	+0.2 -0.1	+0.3 -0.0	+0.2 -0.2	+2.6 -0.0	+0.0 -0.0	+0.0 -2.2	+0.9 -0.8	+0.5 -0.2
1420	1.42×10^{-1}	± 2.0	+2.4 -2.4	+0.3 -0.1	+0.4 -0.4	+0.3 -0.2	+2.1 -0.0	+0.1 -0.0	+0.0 -2.2	+0.9 -0.8	+0.5 -0.2
1590	1.08×10^{-1}	± 2.0	+2.7 -1.4	+0.1 -0.1	+0.0 -0.1	+0.2 -0.2	+2.5 -0.0	+0.0 -0.1	+0.0 -0.9	+0.8 -0.9	+0.4 -0.4
1790	7.84×10^{-2}	± 2.3	+2.7 -1.6	+0.2 -0.1	+0.0 -0.3	+0.2 -0.2	+2.5 -0.0	+0.0 -0.0	+0.0 -1.2	+0.9 +0.8	+0.4 -0.5
1990	5.88×10^{-2}	± 2.7	+3.6 -1.7	+0.2 -0.2	+0.3 -0.0	+0.3 -0.3	+3.4 -0.0	+0.0 -0.0	+0.0 -1.4	+0.9 +0.8	+0.4 +0.1
2300	4.02×10^{-2}	± 2.1	+1.9 -1.9	+0.1 -0.1	+0.3 -0.1	+0.2 -0.2	+1.7 -0.0	+0.0 -0.0	+0.0 -1.6	+0.8 -0.9	+0.1 -0.5
2800	2.34×10^{-2}	± 2.5	+1.3 -1.5	+0.1 -0.2	+0.0 -0.1	+0.1 -0.1	+0.9 -0.0	+0.0 -0.0	+0.0 -1.1	+0.8 -0.8	+0.5 -0.5
3500	1.31×10^{-2}	± 3.0	+2.4 -1.9	+0.2 -0.1	+0.1 -0.4	+0.1 -0.1	+2.3 +1.5	+0.0 +0.0	+0.0 -1.6	+0.8 +0.8	+0.3 -0.4
4200	7.77×10^{-3}	± 3.7	+1.8 -1.8	+0.2 -0.2	+0.0 -0.2	+0.3 -0.3	+1.5 -0.0	+0.0 -0.0	+0.0 -1.5	+0.8 +0.8	+0.2 -0.4
5100	4.18×10^{-3}	± 4.7	+0.9 -2.8	+0.2 -0.2	+0.1 -0.1	+0.0 -0.0	+0.4 -0.0	+0.0 -0.0	+0.0 -2.5	+0.8 +0.8	+0.3 -1.1
6050	2.66×10^{-3}	± 5.6	+1.2 -2.4	+0.2 -0.2	+0.0 -0.6	+0.0 -0.0	+0.0 -0.3	+0.0 -0.0	+0.0 -1.8	+0.8 -0.8	+0.9 -1.3
7100	1.47×10^{-3}	± 6.9	+2.9 -3.8	+0.2 -0.2	+1.6 -2.3	+0.0 -0.0	+1.9 -0.0	+0.0 -0.0	+0.0 -2.7	+0.8 -0.8	+1.1 -1.2
8400	9.20×10^{-4}	± 8.1	+3.3 -3.7	+0.2 -0.2	+0.0 -1.7	+0.0 +0.0	+3.1 -0.0	+0.0 +0.0	+0.0 -2.9	+0.8 +0.8	+0.9 -1.4
10800	3.40×10^{-4}	± 8.3	+2.5 -2.8	+0.1 +0.2	+0.6 -1.1	+0.0 -0.0	+1.5 -0.0	+0.0 -0.0	+0.0 -2.2	+0.8 +0.8	+1.8 -1.2
15200	9.21×10^{-5}	± 13.2	+3.4 -8.2	+0.2 -0.2	+2.1 -1.7	+0.0 -0.0	+0.0 -5.1	+0.0 -0.0	+0.0 -3.0	+0.8 -0.8	+2.6 -5.4
21500	3.81×10^{-5}	+19.9 -16.6	+6.0 -6.0	+0.3 -0.3	+2.1 -1.8	+0.0 -0.0	+3.8 -0.0	+0.0 -0.0	+0.0 -4.2	+0.8 -0.8	+4.1 -3.8
36200	8.23×10^{-7}	+79.1 -47.1	+8.6 -5.3	+0.4 -0.3	+2.4 -2.6	+0.0 -0.0	+0.0 -0.4	+0.0 -0.0	+0.0 -3.2	+0.8 -0.8	+8.2 -3.2

Table A.2: Systematic uncertainties for $d\sigma/dQ^2$ ($y < 0.9$, $y(1-x)^2 > 0.004$) ($\mathcal{L} = 135.5\text{pb}^{-1}$, corrected to $P_e = 0$). The left four columns of the table contain the bin centre (Q_c^2), the measured cross section, the statistical uncertainty and the total systematic uncertainty. The right eight columns of the table list the systematic uncertainties for $\delta_1 - \delta_7$, and the systematic uncertainties summed in quadrature for $\delta_8 - \delta_{15}$. The upper and lower uncertainties correspond to a positive or negative variation of a cut value.

$Q^2 >$ (GeV ²)	x range	x_c	$d\sigma/dx$ (pb)	N_{data}	$N_{\text{bg}}^{\text{MC}}$
185	$(0.63 - 1.00) \times 10^{-2}$	0.794×10^{-2}	$(8.71 \pm 0.05^{+0.13}_{-0.14}) \times 10^4$	34570	161.0
	$(0.10 - 0.16) \times 10^{-1}$	0.126×10^{-1}	$(5.84 \pm 0.03^{+0.07}_{-0.17}) \times 10^4$	39862	122.5
	$(0.16 - 0.25) \times 10^{-1}$	0.200×10^{-1}	$(3.63 \pm 0.02^{+0.03}_{-0.03}) \times 10^4$	39233	82.9
	$(0.25 - 0.40) \times 10^{-1}$	0.316×10^{-1}	$(2.10 \pm 0.01^{+0.02}_{-0.01}) \times 10^4$	38384	30.2
	$(0.40 - 0.63) \times 10^{-1}$	0.501×10^{-1}	$(1.24 \pm 0.01^{+0.01}_{-0.01}) \times 10^4$	33557	5.5
	$(0.63 - 1.00) \times 10^{-1}$	0.794×10^{-1}	$(6.90 \pm 0.04^{+0.08}_{-0.04}) \times 10^3$	31825	5.1
	0.10 - 0.16	0.126	$(3.89 \pm 0.02^{+0.03}_{-0.02}) \times 10^3$	30244	1.4
	0.16 - 0.25	0.200	$(2.04 \pm 0.01^{+0.04}_{-0.06}) \times 10^3$	18768	0.0
3000	$(0.40 - 0.63) \times 10^{-1}$	0.501×10^{-1}	$(1.71 \pm 0.08^{+0.06}_{-0.03}) \times 10^2$	440	1.1
	$(0.63 - 1.00) \times 10^{-1}$	0.794×10^{-1}	$(1.60 \pm 0.06^{+0.04}_{-0.02}) \times 10^2$	714	3.9
	0.10 - 0.16	0.126	$(1.18 \pm 0.04^{+0.01}_{-0.04}) \times 10^2$	859	0.0
	0.16 - 0.25	0.200	$(6.72 \pm 0.25^{+0.06}_{-0.16}) \times 10^1$	730	0.0
	0.25 - 0.40	0.316	$(3.22 \pm 0.14^{+0.04}_{-0.08}) \times 10^1$	567	0.0
	0.40 - 0.75	0.687	$(1.20 \pm 0.08^{+0.02}_{-0.02})$	240	0.0

Table A.3: The single differential cross section $d\sigma/dx$ ($y < 0.9$, $y(1-x)^2 > 0.004$) for $Q^2 > 185\text{GeV}^2$ and $Q^2 > 3000\text{GeV}^2$ ($\mathcal{L} = 135.5\text{pb}^{-1}$, corrected to $P_e = 0$). The Q^2 and bin range, bin centre (x_c) and measured cross section are shown. The first (second) error on the cross section corresponds to the statistical (systematic) uncertainties. The number of observed data events (N_{data}) and simulated background events ($N_{\text{bg}}^{\text{MC}}$) are also shown.

$Q^2 >$ (GeV ²)	x_c	$d\sigma/dx$ (pb)	stat. (%)	sys. (%)	δ_1 (%)	δ_2 (%)	δ_3 (%)	δ_4 (%)	δ_5 (%)	δ_6 (%)	δ_7 (%)	$\delta_8 - \delta_{15}$ (%)
185	0.794×10^{-2}	8.71×10^4	± 0.5	$+1.5$ -1.6	$+0.2$ -0.1	$+0.1$ -0.0	$+0.2$ -0.3	$+1.4$ -0.0	$+0.3$ -0.8	$+0.0$ -1.2	$+0.4$ -0.4	$+0.2$ -0.3
	0.126×10^{-1}	5.84×10^4	± 0.5	$+1.1$ -2.9	$+0.1$ -0.1	$+0.0$ -0.1	$+0.1$ -0.2	$+1.1$ -0.0	$+0.2$ -0.8	$+0.0$ -2.7	$+0.3$ -0.4	$+0.1$ -0.3
	0.200×10^{-1}	3.63×10^4	± 0.5	$+0.9$ -0.8	$+0.1$ $+1.0$	$+0.1$ $+0.1$	$+0.1$ $+0.0$	$+0.8$ $+0.0$	$+0.1$ $+0.2$	$+0.0$ -0.5	$+0.3$ $+0.3$	$+0.1$ -0.2
	0.316×10^{-1}	2.10×10^4	± 0.5	$+0.6$ $+0.9$	-0.1 $+0.1$	-0.1 $+0.0$	-0.0 $+0.0$	-0.0 $+0.5$	-0.5 $+0.3$	-0.0 $+0.6$	-0.2 $+0.2$	-0.2 $+0.1$
	0.501×10^{-1}	1.24×10^4	± 0.5	-0.6 $+1.1$	-0.1 $+0.1$	-0.1 $+0.0$	-0.0 -0.0	-0.0 $+0.4$	-0.6 $+0.1$	-0.0 $+1.0$	-0.2 $+0.2$	-0.1 $+0.1$
	0.794×10^{-1}	6.90×10^3	± 0.6	-0.4 $+1.1$	-0.1 $+0.1$	-0.1 $+0.1$	-0.0 $+0.0$	-0.0 $+0.6$	-0.3 $+0.1$	-0.0 $+0.9$	-0.2 $+0.1$	-0.1 $+0.1$
	0.126	3.89×10^3	± 0.6	-0.4 $+1.9$	-0.1 $+0.1$	-0.2 $+0.1$	-0.0 $+0.0$	-0.0 $+1.7$	-0.3 $+0.0$	-0.0 $+0.0$	-0.1 $+0.2$	-0.1 $+0.9$
	0.200	2.04×10^3	± 0.7	-2.7 $+3.6$	-0.1 $+0.2$	-0.2 $+0.1$	-0.0 $+0.1$	-0.0 $+3.4$	-0.5 $+0.0$	-2.5 $+0.0$	-0.2 $+1.2$	-1.0 $+0.6$
	3000	0.501×10^{-1}	1.71×10^2	± 4.8	-1.9 $+2.6$	-0.2 $+0.1$	-0.9 $+0.0$	-0.1 $+0.3$	-0.0 $+2.4$	-0.0 $+0.0$	-0.7 $+0.0$	-1.3 $+0.9$
0.794×10^{-1}		1.60×10^2	± 3.7	-1.5 $+0.8$	-0.1 $+0.1$	-0.3 $+0.0$	-0.3 $+0.0$	-0.0 $+0.0$	-0.0 $+0.0$	-0.9 $+0.0$	-0.9 $+0.8$	-0.6 $+0.3$
0.126		1.18×10^2	± 3.4	-3.6 $+0.8$	-0.1 $+0.1$	-0.6 $+0.0$	-0.0 $+0.0$	-0.8 $+0.0$	-0.0 $+0.0$	-3.3 $+0.0$	-0.8 $+0.7$	-0.5 $+0.5$
0.200		6.72×10^1	± 3.7	-2.4 $+1.1$	-0.1 $+0.1$	-0.5 $+0.0$	-0.0 $+0.0$	-0.2 $+0.7$	-0.0 $+0.0$	-2.0 $+0.0$	-0.7 $+0.6$	-0.9 $+0.6$
0.316		3.22×10^1	± 4.2	-2.5 $+2.0$	-0.1 $+0.3$	-0.2 $+1.5$	-0.0 $+0.0$	-0.0 $+1.0$	-0.0 $+0.0$	-2.5 $+0.0$	-0.6 $+0.6$	-0.2 $+0.6$
0.687		1.20	± 6.5	-1.6 $+0.3$	-0.3 -0.0	-0.0 -0.0	-0.0 -0.0	-0.0 -0.0	-0.0 -0.0	-0.0 -0.0	-0.6 -0.6	-1.5 -1.5

Table A.4: Systematic uncertainties for $d\sigma/dx$ ($y < 0.9$, $y(1-x)^2 > 0.004$) for $Q^2 > 185\text{GeV}^2$ and $Q^2 > 3000\text{GeV}^2$ ($\mathcal{L} = 135.5\text{pb}^{-1}$, corrected to $P_e = 0$). The left five columns of the table contain the Q^2 range, bin centre (x_c), the measured cross section, the statistical uncertainty and the total systematic uncertainty. The right eight columns of the table list the systematic uncertainties for $\delta_1 - \delta_7$, and the systematic uncertainties summed in quadrature for $\delta_8 - \delta_{15}$. The upper and lower uncertainties correspond to a positive or negative variation of a cut value.

$Q^2 >$ (GeV ²)	y range	y_c	$d\sigma/dy$ (pb)	N_{data}	$N_{\text{bg}}^{\text{MC}}$
185	0.00 – 0.05	0.025	$(1.63 \pm 0.01^{+0.02}_{-0.01}) \times 10^4$	75314	0.0
	0.05 – 0.10	0.075	$(8.10 \pm 0.04^{+0.09}_{-0.05}) \times 10^3$	50532	7.4
	0.10 – 0.15	0.125	$(5.64 \pm 0.03^{+0.03}_{-0.05}) \times 10^3$	34944	11.6
	0.15 – 0.20	0.175	$(4.37 \pm 0.03^{+0.02}_{-0.14}) \times 10^3$	26237	24.7
	0.20 – 0.25	0.225	$(3.61 \pm 0.03^{+0.03}_{-0.20}) \times 10^3$	20974	19.8
	0.25 – 0.30	0.275	$(2.93 \pm 0.02^{+0.04}_{-0.04}) \times 10^3$	16254	17.7
	0.30 – 0.35	0.325	$(2.53 \pm 0.02^{+0.04}_{-0.03}) \times 10^3$	13919	44.6
	0.35 – 0.40	0.375	$(2.24 \pm 0.02^{+0.02}_{-0.03}) \times 10^3$	12202	43.8
	0.40 – 0.45	0.425	$(1.98 \pm 0.02^{+0.03}_{-0.02}) \times 10^3$	10402	62.6
	0.45 – 0.50	0.475	$(1.73 \pm 0.02^{+0.05}_{-0.01}) \times 10^3$	8761	50.6
	0.50 – 0.55	0.525	$(1.54 \pm 0.02^{+0.04}_{-0.01}) \times 10^3$	7661	54.4
	0.55 – 0.60	0.575	$(1.42 \pm 0.02^{+0.04}_{-0.03}) \times 10^3$	6794	64.1
	0.60 – 0.65	0.625	$(1.29 \pm 0.02^{+0.04}_{-0.04}) \times 10^3$	5723	63.0
	0.65 – 0.70	0.675	$(1.21 \pm 0.02^{+0.04}_{-0.05}) \times 10^3$	4671	25.1
	0.70 – 0.75	0.725	$(1.12 \pm 0.02^{+0.07}_{-0.05}) \times 10^3$	3542	48.3
	0.75 – 0.90	0.825	$(9.54 \pm 0.14^{+0.76}_{-0.46}) \times 10^2$	4433	103.8
3000	0.05 – 0.10	0.075	$(3.27 \pm 0.25^{+0.06}_{-0.03}) \times 10^1$	174	0.0
	0.10 – 0.15	0.125	$(5.56 \pm 0.31^{+0.05}_{-0.13}) \times 10^1$	326	0.0
	0.15 – 0.20	0.175	$(5.91 \pm 0.31^{+0.07}_{-0.08}) \times 10^1$	357	0.0
	0.20 – 0.25	0.225	$(5.62 \pm 0.30^{+0.05}_{-0.20}) \times 10^1$	345	0.0
	0.25 – 0.30	0.275	$(4.97 \pm 0.28^{+0.04}_{-0.18}) \times 10^1$	312	0.0
	0.30 – 0.35	0.325	$(5.13 \pm 0.29^{+0.05}_{-0.13}) \times 10^1$	321	0.0
	0.35 – 0.40	0.375	$(3.72 \pm 0.24^{+0.04}_{-0.20}) \times 10^1$	233	0.0
	0.40 – 0.45	0.425	$(3.40 \pm 0.23^{+0.04}_{-0.12}) \times 10^1$	214	0.0
	0.45 – 0.50	0.475	$(3.59 \pm 0.24^{+0.04}_{-0.08}) \times 10^1$	224	0.0
	0.50 – 0.55	0.525	$(2.82 \pm 0.21^{+0.04}_{-0.08}) \times 10^1$	173	0.0
	0.55 – 0.60	0.575	$(2.94 \pm 0.22^{+0.03}_{-0.04}) \times 10^1$	178	0.0
	0.60 – 0.65	0.625	$(2.41 \pm 0.20^{+0.04}_{-0.04}) \times 10^1$	152	3.9
	0.65 – 0.70	0.675	$(2.27 \pm 0.20^{+0.05}_{-0.10}) \times 10^1$	134	0.0
	0.70 – 0.75	0.725	$(2.35 \pm 0.20^{+0.05}_{-0.13}) \times 10^1$	134	0.0
	0.75 – 0.80	0.775	$(2.10 \pm 0.19^{+0.14}_{-0.12}) \times 10^1$	119	0.0
	0.80 – 0.85	0.825	$(1.89 \pm 0.19^{+0.26}_{-0.05}) \times 10^1$	103	1.1
0.85 – 0.90	0.875	$(1.92 \pm 0.21^{+0.20}_{-0.16}) \times 10^1$	87	0.0	

Table A.5: The single differential cross section $d\sigma/dy$ ($y < 0.9$, $y(1-x)^2 > 0.004$) for $Q^2 > 185\text{GeV}^2$ and $Q^2 > 3000\text{GeV}^2$ ($\mathcal{L} = 135.5\text{pb}^{-1}$, corrected to $P_e = 0$). The Q^2 and bin range, bin centre (x_c) and measured cross section are shown. The first (second) error on the cross section corresponds to the statistical (systematic) uncertainties. The number of observed data events (N_{data}) and simulated background events ($N_{\text{bg}}^{\text{MC}}$) are also shown.

$Q^2 >$ (GeV ²)	y_c	$d\sigma/dy$ (pb)	stat. (%)	sys. (%)	δ_1 (%)	δ_2 (%)	δ_3 (%)	δ_4 (%)	δ_5 (%)	δ_6 (%)	δ_7 (%)	$\delta_8 - \delta_{15}$ (%)
185	0.025	1.63×10^4	± 0.4	+1.4 -0.5	+0.1 -0.1	+0.1 -0.1	+0.0 -0.0	+0.7 -0.0	+0.0 -0.4	+1.1 -0.0	+0.0 -0.0	+0.5 -0.3
	0.075	8.10×10^3	± 0.4	+1.2 -0.6	+0.1 -0.1	+0.0 -0.0	+0.0 -0.0	+0.3 -0.0	+0.3 -0.5	+1.1 -0.0	+0.1 -0.0	+0.1 -0.2
	0.125	5.64×10^3	± 0.5	+0.5 -0.8	+0.1 -0.1	+0.1 -0.2	+0.0 -0.0	+0.3 -0.0	+0.4 -0.7	+0.0 -0.2	+0.1 -0.1	+0.1 -0.2
	0.175	4.37×10^3	± 0.6	+0.5 -3.1	+0.1 -0.1	+0.0 -0.1	+0.0 -0.1	+0.5 -0.0	+0.1 -1.1	+0.0 -2.9	+0.1 -0.2	+0.1 -0.3
	0.225	3.61×10^3	± 0.7	+0.7 -5.6	+0.1 -0.1	+0.1 -0.0	+0.1 -0.0	+0.6 -0.0	+0.1 -0.6	+0.0 -5.6	+0.2 -0.2	+0.2 -0.2
	0.275	2.93×10^3	± 0.8	+1.2 -1.3	+0.1 -0.0	+0.1 -0.1	+0.1 -0.1	+1.1 -0.0	+0.3 -0.8	+0.0 -1.0	+0.3 -0.3	+0.2 -0.2
	0.325	2.53×10^3	± 0.8	+1.5 -1.3	+0.1 -0.1	+0.2 -0.2	+0.2 -0.0	+1.5 -0.0	+0.2 -0.8	+0.0 -0.9	+0.3 -0.3	+0.2 -0.3
	0.375	2.24×10^3	± 0.9	+1.0 -1.2	+0.0 -0.0	+0.1 -0.2	+0.2 -0.2	+0.6 -0.0	+0.6 -1.1	+0.0 -0.2	+0.4 -0.4	+0.2 -0.3
	0.425	1.98×10^3	± 1.0	+1.7 -0.8	+0.0 -0.0	+0.1 -0.1	+0.3 -0.4	+1.2 -0.0	+0.8 -0.2	+0.8 -0.0	+0.5 -0.6	+0.1 -0.3
	0.475	1.73×10^3	± 1.1	+3.1 -1.1	+0.1 -0.8	+0.0 -0.2	+0.3 -0.2	+2.4 -0.0	+0.8 -0.0	+1.6 -0.0	+0.7 -0.6	+0.4 -0.5
	0.525	1.54×10^3	± 1.2	+2.8 -1.1	+0.1 -0.9	+0.4 -0.0	+0.4 -0.3	+2.4 -0.0	+0.9 -0.0	+0.7 -0.0	+0.8 -0.7	+0.4 -0.4
	0.575	1.42×10^3	± 1.2	+3.0 -2.4	+0.3 -0.1	+0.5 -0.3	+2.6 -0.5	+0.3 -0.0	+0.0 -0.0	+0.0 -2.2	+1.0 -0.9	+0.8 -0.2
	0.625	1.29×10^3	± 1.3	+3.4 -1.3	+0.6 -0.6	+0.3 -0.0	+0.6 -0.5	+3.0 -0.0	+0.0 -0.1	+0.0 -2.4	+1.0 -1.0	+0.6 -0.9
	0.675	1.21×10^3	± 1.5	+3.1 -1.5	+1.3 -0.9	+0.2 -0.2	+0.3 -0.3	+2.4 -0.0	+0.1 -0.0	+0.0 -3.4	+1.1 -1.2	+0.9 -1.0
	0.725	1.12×10^3	± 1.7	+6.4 -1.7	+2.4 -4.5	+0.3 -2.1	+0.7 -0.3	+5.6 -0.0	+0.0 -0.2	+0.0 -3.7	+0.0 -1.2	+1.5 -1.2
	0.825	9.54×10^2	± 1.5	+7.9 -1.5	+3.1 -4.8	+0.0 -2.7	+1.0 -0.2	+7.0 -1.5	+0.0 -0.0	+0.2 -3.4	+0.0 -3.4	+1.2 -0.9
3000	0.075	3.27×10^1	± 7.6	+1.9 -0.8	+0.3 -0.3	+1.2 -0.0	+0.0 -0.0	+1.3 -0.0	+0.0 -0.0	+0.0 -0.0	+0.0 -0.6	+0.6 -0.4
	0.125	5.56×10^1	± 5.5	+1.0 -2.3	+0.2 -0.2	+0.0 -0.4	+0.0 -0.0	+0.7 -0.0	+0.0 -0.0	+0.0 -2.1	+0.0 -0.6	+0.6 -0.2
	0.175	5.91×10^1	± 5.3	+1.2 -1.4	+0.1 -0.2	+0.9 -0.7	+0.0 -0.0	+0.4 -0.0	+0.0 -0.0	+0.0 -0.0	+0.0 -0.7	+0.2 -1.1
	0.225	5.62×10^1	± 5.4	+1.0 -3.5	+0.2 -0.2	+0.5 -0.0	+0.0 -0.0	+0.0 -0.7	+0.0 -0.0	+0.0 -3.2	+0.0 -0.7	+0.5 -0.9
	0.275	4.97×10^1	± 5.7	+0.8 -3.6	+0.1 -0.2	+0.0 -0.9	+0.0 -0.0	+0.0 -0.0	+0.0 -0.1	+0.0 -3.2	+0.0 -0.7	+0.3 -0.3
	0.325	5.13×10^1	± 5.6	+1.0 -2.5	+0.2 -0.1	+1.2 -0.4	+0.0 -0.0	+1.3 -0.2	+0.0 -0.0	+0.0 -2.1	+0.0 -0.7	+0.3 -1.1
	0.375	3.72×10^1	± 6.6	+1.1 -5.3	+0.1 -0.1	+0.0 -0.9	+0.0 -0.0	+0.5 -0.0	+0.0 -0.0	+0.0 -5.1	+0.0 -0.7	+0.7 -0.8
	0.425	3.40×10^1	± 6.8	+1.1 -3.6	+0.1 -0.1	+0.0 -0.5	+0.0 -0.0	+0.0 -2.3	+0.0 -0.0	+0.0 -2.5	+0.0 -0.8	+0.8 -0.8
	0.475	3.59×10^1	± 6.7	+1.0 -2.3	+0.1 -0.1	+0.4 -0.7	+0.0 -0.0	+0.0 -0.4	+0.0 -0.0	+0.0 -1.8	+0.0 -0.8	+0.4 -0.7
	0.525	2.82×10^1	± 7.6	+0.9 -8.7	+0.1 -0.1	+0.0 -0.0	+0.0 -0.0	+0.0 -0.0	+0.0 -8.6	+0.0 -0.0	+0.0 -0.9	+0.9 -0.7
	0.575	2.94×10^1	± 7.5	+1.0 -1.4	+0.2 -0.1	+0.0 -0.7	+0.0 -0.0	+0.0 -0.0	+0.0 -0.0	+0.0 -0.5	+0.0 -1.5	+1.0 +2.5
	0.625	2.41×10^1	± 8.1	+5.6 -1.8	+0.1 -0.1	+0.8 -0.0	+1.3 -1.3	+4.4 -0.0	+0.0 -0.0	+0.0 -0.0	+1.5 -1.1	+1.1 -0.5
	0.675	2.27×10^1	± 8.6	+2.1 -4.4	+0.0 -0.0	+1.7 -0.8	+0.0 -0.0	+0.0 -2.5	+0.0 -0.0	+0.0 -3.3	+0.0 -1.1	+1.1 -0.8
	0.725	2.35×10^1	± 8.6	+2.1 -5.4	+0.0 -0.0	+0.0 -3.3	+0.0 -0.0	+1.6 -0.0	+0.0 -0.0	+0.0 -3.4	+0.0 -1.2	+1.2 -2.2
	0.775	2.10×10^1	± 9.2	+6.5 -5.7	+0.1 -0.1	+0.0 -3.4	+0.0 -0.0	+6.2 -0.0	+0.0 -0.0	+0.0 -4.2	+0.0 -1.3	+1.3 -1.0
	0.825	1.89×10^1	± 9.9	+13.9 -2.5	+0.1 -0.1	+1.6 -0.5	+0.5 -0.5	+13.6 -0.0	+0.0 -0.0	+0.0 -1.3	+0.0 -1.3	+1.4 -1.4
0.875	1.92×10^1	± 10.7	+10.5 -8.2	+1.4 -1.1	+0.4 -2.3	+0.0 -0.0	+5.9 -0.0	+0.0 -0.0	+8.2 -0.0	+1.3 -1.3	+2.4 -7.7	

Table A.6: Systematic uncertainties for $d\sigma/dy$ ($y < 0.9$, $y(1-x)^2 > 0.004$) for $Q^2 > 185\text{GeV}^2$ and $Q^2 > 3000\text{GeV}^2$ ($\mathcal{L} = 135.5\text{pb}^{-1}$, corrected to $P_e = 0$). The left five columns of the table contain the Q^2 range, bin centre (x_c), the measured cross section, the statistical uncertainty and the total systematic uncertainty. The right eight columns of the table list the systematic uncertainties for $\delta_1 - \delta_7$, and the systematic uncertainties summed in quadrature for $\delta_8 - \delta_{15}$. The upper and lower uncertainties correspond to a positive or negative variation of a cut value.

Q^2 range (GeV ²)	Q_c^2 (GeV ²)	x range	x_c	$\tilde{\sigma}$	N_{data}	$N_{\text{bg}}^{\text{MC}}$
185 – 240	200	0.004 – 0.006	0.005	$(1.110 \pm 0.010^{+0.029}_{-0.017})$	13313	108.0
	200	0.006 – 0.010	0.008	$(0.945 \pm 0.008^{+0.008}_{-0.022})$	15647	38.8
	200	0.010 – 0.017	0.013	$(0.801 \pm 0.006^{+0.022}_{-0.022})$	16074	14.1
	200	0.017 – 0.025	0.021	$(0.680 \pm 0.006^{+0.013}_{-0.004})$	11107	5.1
	200	0.025 – 0.037	0.032	$(0.566 \pm 0.006^{+0.015}_{-0.001})$	9767	0.0
	200	0.037 – 0.060	0.050	$(0.511 \pm 0.005^{+0.011}_{-0.002})$	10375	1.1
	200	0.060 – 0.120	0.080	$(0.433 \pm 0.004^{+0.016}_{-0.001})$	13867	0.0
240 – 310	200	0.120 – 0.250	0.180	$(0.346 \pm 0.004^{+0.006}_{-0.008})$	8823	0.0
	250	0.006 – 0.010	0.008	$(0.929 \pm 0.010^{+0.022}_{-0.011})$	9190	34.9
	250	0.010 – 0.017	0.013	$(0.821 \pm 0.008^{+0.006}_{-0.035})$	10611	10.0
	250	0.017 – 0.025	0.021	$(0.692 \pm 0.008^{+0.005}_{-0.008})$	7770	6.4
	250	0.025 – 0.037	0.032	$(0.585 \pm 0.007^{+0.012}_{-0.011})$	7466	1.1
	250	0.037 – 0.060	0.050	$(0.513 \pm 0.006^{+0.011}_{-0.008})$	7740	0.0
	250	0.060 – 0.120	0.080	$(0.435 \pm 0.004^{+0.010}_{-0.005})$	10142	0.0
310 – 410	250	0.120 – 0.250	0.180	$(0.337 \pm 0.004^{+0.005}_{-0.008})$	8042	0.0
	350	0.006 – 0.010	0.008	$(0.948 \pm 0.013^{+0.033}_{-0.008})$	5579	27.3
	350	0.010 – 0.017	0.013	$(0.809 \pm 0.010^{+0.009}_{-0.019})$	7000	6.1
	350	0.017 – 0.025	0.021	$(0.673 \pm 0.009^{+0.009}_{-0.010})$	5167	0.9
	350	0.025 – 0.037	0.032	$(0.575 \pm 0.008^{+0.017}_{-0.004})$	4869	1.1
	350	0.037 – 0.060	0.050	$(0.507 \pm 0.007^{+0.011}_{-0.005})$	5306	1.1
	350	0.060 – 0.120	0.080	$(0.418 \pm 0.005^{+0.016}_{-0.004})$	6823	0.0
410 – 530	350	0.120 – 0.250	0.180	$(0.325 \pm 0.004^{+0.007}_{-0.005})$	6340	0.0
	450	0.006 – 0.010	0.008	$(1.023 \pm 0.015^{+0.019}_{-0.020})$	4548	44.9
	450	0.010 – 0.017	0.013	$(0.816 \pm 0.014^{+0.010}_{-0.018})$	3304	6.8
	450	0.017 – 0.025	0.021	$(0.706 \pm 0.014^{+0.012}_{-0.034})$	2711	2.2
	450	0.025 – 0.037	0.032	$(0.582 \pm 0.011^{+0.007}_{-0.021})$	2962	1.1
	450	0.037 – 0.060	0.050	$(0.511 \pm 0.008^{+0.007}_{-0.005})$	3618	0.0
	450	0.060 – 0.100	0.080	$(0.425 \pm 0.007^{+0.007}_{-0.007})$	3305	0.0
	450	0.100 – 0.170	0.130	$(0.365 \pm 0.007^{+0.005}_{-0.002})$	3094	0.0
450	0.170 – 0.300	0.250	$(0.257 \pm 0.005^{+0.007}_{-0.007})$	2612	0.0	

Table A.7: The reduced cross section $\tilde{\sigma}$ ($y < 0.9$, $y(1-x)^2 > 0.004$) ($\mathcal{L} = 135.5 \text{ textrmpb}^{-1}$, $P_e = 0$). The bin range, bin centre (Q_c^2) and measured cross section are shown. The first (second) error on the cross section corresponds to the statistical (systematic) uncertainties. The number of observed data events (N_{data}) and simulated background events ($N_{\text{bg}}^{\text{MC}}$) are also shown.

Q^2 range (GeV ²)	Q_c^2 (GeV ²)	x range	x_c	$\tilde{\sigma}$	N_{data}	$N_{\text{bg}}^{\text{MC}}$
530 – 710	650	0.010 – 0.017	0.013	$(0.865 \pm 0.014^{+0.024}_{-0.025})$	4045	29.0
	650	0.017 – 0.025	0.021	$(0.735 \pm 0.015^{+0.008}_{-0.018})$	2564	0.0
	650	0.025 – 0.037	0.032	$(0.609 \pm 0.013^{+0.009}_{-0.025})$	2043	1.1
	650	0.037 – 0.060	0.050	$(0.512 \pm 0.011^{+0.003}_{-0.010})$	2028	0.0
	650	0.060 – 0.100	0.080	$(0.434 \pm 0.010^{+0.002}_{-0.011})$	1809	0.0
	650	0.100 – 0.170	0.130	$(0.335 \pm 0.008^{+0.005}_{-0.003})$	1598	0.0
710 – 900	650	0.170 – 0.300	0.250	$(0.238 \pm 0.006^{+0.003}_{-0.003})$	1453	0.0
	800	0.009 – 0.017	0.013	$(0.836 \pm 0.017^{+0.027}_{-0.027})$	2600	41.2
	800	0.017 – 0.025	0.021	$(0.741 \pm 0.018^{+0.009}_{-0.014})$	1757	3.3
	800	0.025 – 0.037	0.032	$(0.610 \pm 0.015^{+0.007}_{-0.021})$	1747	7.9
	800	0.037 – 0.060	0.050	$(0.514 \pm 0.012^{+0.006}_{-0.022})$	1966	1.1
	800	0.060 – 0.100	0.080	$(0.454 \pm 0.011^{+0.003}_{-0.017})$	1768	0.0
900 – 1300	800	0.100 – 0.170	0.130	$(0.344 \pm 0.009^{+0.007}_{-0.011})$	1387	0.0
	800	0.170 – 0.300	0.250	$(0.243 \pm 0.007^{+0.006}_{-0.002})$	1110	0.0
	1200	0.010 – 0.017	0.014	$(0.815 \pm 0.021^{+0.073}_{-0.037})$	1631	36.5
	1200	0.017 – 0.025	0.021	$(0.737 \pm 0.017^{+0.021}_{-0.018})$	1819	12.2
	1200	0.025 – 0.037	0.032	$(0.626 \pm 0.014^{+0.007}_{-0.020})$	1863	0.0
	1200	0.037 – 0.060	0.050	$(0.513 \pm 0.011^{+0.008}_{-0.021})$	2209	0.0
1300 – 1800	1200	0.060 – 0.100	0.080	$(0.423 \pm 0.009^{+0.005}_{-0.013})$	2037	1.1
	1200	0.100 – 0.170	0.130	$(0.352 \pm 0.008^{+0.003}_{-0.011})$	1845	0.0
	1200	0.170 – 0.300	0.250	$(0.247 \pm 0.006^{+0.002}_{-0.009})$	1459	0.0
	1200	0.300 – 0.530	0.400	$(0.129 \pm 0.005^{+0.001}_{-0.003})$	624	0.0
	1500	0.017 – 0.025	0.021	$(0.724 \pm 0.024^{+0.086}_{-0.014})$	924	17.5
	1500	0.025 – 0.037	0.032	$(0.583 \pm 0.019^{+0.026}_{-0.008})$	952	1.5
1800 – 2500	1500	0.037 – 0.060	0.050	$(0.532 \pm 0.015^{+0.005}_{-0.012})$	1309	1.1
	1500	0.060 – 0.100	0.080	$(0.446 \pm 0.012^{+0.004}_{-0.012})$	1303	0.0
	1500	0.100 – 0.150	0.130	$(0.373 \pm 0.012^{+0.003}_{-0.009})$	902	0.3
	1500	0.150 – 0.230	0.180	$(0.306 \pm 0.011^{+0.003}_{-0.006})$	789	0.0
	1500	0.230 – 0.350	0.250	$(0.242 \pm 0.011^{+0.004}_{-0.003})$	528	0.0
	1500	0.350 – 0.530	0.400	$(0.119 \pm 0.007^{+0.002}_{-0.004})$	251	0.0
1800 – 2500	2000	0.023 – 0.037	0.032	$(0.594 \pm 0.023^{+0.067}_{-0.012})$	701	12.2
	2000	0.037 – 0.060	0.050	$(0.495 \pm 0.018^{+0.011}_{-0.006})$	790	1.9
	2000	0.060 – 0.100	0.080	$(0.474 \pm 0.015^{+0.004}_{-0.019})$	940	1.1
	2000	0.100 – 0.150	0.130	$(0.352 \pm 0.014^{+0.005}_{-0.009})$	607	1.1
	2000	0.150 – 0.230	0.180	$(0.273 \pm 0.012^{+0.003}_{-0.007})$	499	0.0
	2000	0.230 – 0.350	0.250	$(0.247 \pm 0.013^{+0.004}_{-0.009})$	387	0.0
	2000	0.350 – 0.530	0.400	$(0.119 \pm 0.009^{+0.003}_{-0.001})$	180	0.0

Table 7: Continuation 1.

Q^2 range (GeV ²)	Q_c^2 (GeV ²)	x range	x_c	$\bar{\sigma}$	N_{data}	$N_{\text{bg}}^{\text{MC}}$
2500 – 3500	3000	0.037 – 0.060	0.050	$(0.500 \pm 0.022^{+0.012}_{-0.012})$	502	2.2
	3000	0.060 – 0.100	0.080	$(0.429 \pm 0.018^{+0.004}_{-0.010})$	575	0.0
	3000	0.100 – 0.150	0.130	$(0.366 \pm 0.017^{+0.003}_{-0.004})$	448	0.0
	3000	0.150 – 0.230	0.180	$(0.276 \pm 0.015^{+0.002}_{-0.005})$	356	0.0
	3000	0.230 – 0.350	0.250	$(0.243 \pm 0.014^{+0.002}_{-0.008})$	286	0.0
	3000	0.350 – 0.530	0.400	$(0.121 \pm 0.011^{+0.004}_{-0.003})$	127	0.0
3500 – 5600	3000	0.530 – 0.750	0.650	$(0.015^{+0.004}_{-0.003} \text{ } ^{+0.001}_{-0.000})$	21	0.0
	5000	0.040 – 0.100	0.080	$(0.405 \pm 0.016^{+0.017}_{-0.007})$	628	3.9
	5000	0.100 – 0.150	0.130	$(0.328 \pm 0.018^{+0.003}_{-0.013})$	344	0.0
	5000	0.150 – 0.230	0.180	$(0.286 \pm 0.016^{+0.002}_{-0.007})$	333	0.0
	5000	0.230 – 0.350	0.250	$(0.215 \pm 0.014^{+0.002}_{-0.005})$	232	0.0
	5000	0.350 – 0.530	0.400	$(0.135 \pm 0.012^{+0.002}_{-0.002})$	137	0.0
5600 – 9000	8000	0.070 – 0.150	0.130	$(0.312 \pm 0.019^{+0.010}_{-0.012})$	277	0.0
	8000	0.150 – 0.230	0.180	$(0.239 \pm 0.019^{+0.002}_{-0.010})$	161	0.0
	8000	0.230 – 0.350	0.250	$(0.213 \pm 0.018^{+0.004}_{-0.007})$	136	0.0
	8000	0.350 – 0.530	0.400	$(0.104 \pm 0.013^{+0.003}_{-0.003})$	66	0.0
	8000	0.530 – 0.750	0.650	$(0.017^{+0.006}_{-0.004} \text{ } ^{+0.002}_{-0.001})$	15	0.0
9000 – 15000	12000	0.090 – 0.230	0.180	$(0.192 \pm 0.020^{+0.004}_{-0.006})$	95	0.0
	12000	0.230 – 0.350	0.250	$(0.152 \pm 0.020^{+0.002}_{-0.007})$	56	0.0
	12000	0.350 – 0.530	0.400	$(0.115 \pm 0.017^{+0.004}_{-0.005})$	44	0.0
15000 – 25000	20000	0.150 – 0.350	0.250	$(0.154^{+0.029}_{-0.025} \text{ } ^{+0.012}_{-0.010})$	38	0.0
	20000	0.350 – 0.750	0.400	$(0.064^{+0.021}_{-0.016} \text{ } ^{+0.005}_{-0.012})$	15	0.0
25000 – 50000	30000	0.250 – 0.750	0.400	$(0.040^{+0.024}_{-0.016} \text{ } ^{+0.001}_{-0.004})$	6	0.0

Table 7: Continuation 2.

Q_c^2 (GeV ²)	x_c	$\tilde{\sigma}$	stat. (%)	sys. (%)	δ_1 (%)	δ_2 (%)	δ_3 (%)	δ_4 (%)	δ_5 (%)	δ_6 (%)	δ_7 (%)	$\delta_8 - \delta_{15}$ (%)	
200	0.005	1.110	± 0.9	+2.6 -1.5	+0.1 -0.0	+0.1 -0.1	+0.4 -0.4	+1.9 +0.8	+1.1 +0.2	+1.3 +0.0	+0.2 +0.0	+0.4 -0.3	
	0.008	0.945	± 0.8	+0.9 -2.3	+0.1 -0.0	+0.1 -0.0	+0.1 -0.1	+0.8 +0.1	+0.2 +0.1	+0.0 +0.0	+0.0 +0.0	+0.2 -0.1	
	0.013	0.801	± 0.8	+0.2 -2.7	+0.1 -0.1	+0.1 -0.2	+0.0 -0.1	+0.1 +0.1	+0.1 +0.1	+0.0 +1.5	+0.0 -2.2	+0.1 -0.1	
	0.021	0.680	± 0.9	+1.9 -0.6	+0.1 -0.1	+0.1 -0.2	+0.0 -0.0	+0.0 +0.4	+0.0 -0.3	+0.0 +0.3	+1.9 -0.0	+0.0 -0.1	
	0.032	0.566	± 1.0	+2.7 -0.2	+0.1 -0.1	+0.0 -0.1	+0.0 -0.0	+0.0 -0.0	+0.0 -0.0	+0.1 -0.0	+2.7 -0.0	+0.0 -0.1	
	0.050	0.511	± 1.0	+2.1 -0.4	+0.1 -0.1	+0.0 -0.0	+0.0 -0.0	+0.0 -0.0	+0.1 +0.3	+0.1 -0.4	+0.1 -0.0	+0.0 -0.0	+0.1 -0.1
	0.080	0.433	± 0.8	+3.6 -0.2	+0.1 -0.1	+0.1 -0.0	+0.1 -0.0	+0.0 -0.0	+0.0 -0.0	+0.0 -0.0	+0.0 -0.0	+0.0 -0.0	+0.6 -0.2
	0.180	0.346	± 1.1	+1.7 -2.4	+0.1 -0.1	+0.0 -0.1	+0.0 -0.0	+0.0 -0.0	+1.4 +0.1	+0.8 -0.0	+0.0 -2.3	+0.0 +0.0	+0.6 -0.6
	250	0.008	0.929	± 1.0	+2.4 -1.1	+0.0 -0.0	+0.3 -0.3	+0.2 -0.2	+2.1 -0.0	+1.0 -0.4	+0.0 +0.0	+0.0 -1.0	+0.3 -0.1
0.013	0.821	± 1.0	+0.7 -4.2	+0.1 -0.1	+0.0 -0.1	+0.0 -0.0	+0.0 -0.0	+0.7 -0.0	+0.0 -1.0	+0.0 -4.1	+0.0 -0.0	+0.2 -0.2	
0.021	0.692	± 1.1	+0.7 -1.2	+0.1 -0.1	+0.2 -0.0	+0.0 -0.1	+0.0 -0.0	+0.5 +0.1	+0.3 +0.2	+0.3 -0.0	+0.0 -0.0	+0.1 -0.1	
0.032	0.585	± 1.2	+2.0 -1.9	+0.1 -0.1	+0.0 -0.1	+0.0 -0.0	+0.0 -0.0	+0.1 -0.0	+0.2 -0.0	+1.9 -0.0	+0.0 -0.0	+0.2 -0.2	
0.050	0.513	± 1.1	+2.4 -1.6	+0.1 -0.1	+0.0 -0.1	+0.0 -0.1	+0.0 -0.0	+0.0 -0.4	+0.1 -1.6	+2.4 -0.0	+0.0 +0.0	+0.2 -0.1	
0.080	0.435	± 1.0	+2.3 -1.1	+0.1 -0.1	+0.1 -0.2	+0.0 -0.0	+0.0 -0.1	+0.0 -1.0	+0.0 -1.0	+2.3 -0.0	+0.0 -0.0	+0.3 -0.1	
0.180	0.337	± 1.1	+1.5 -2.2	+0.1 -0.1	+0.2 -0.0	+0.0 -0.0	+1.4 -0.0	+0.1 -0.0	+0.0 -1.8	+0.0 -1.2	+0.0 +0.6	+0.6 +0.3	
350	0.008	0.948	± 1.3	+3.5 -0.8	+0.1 -0.1	+0.0 -0.2	+0.2 -0.3	+0.0 -0.0	+2.4 +0.7	+0.1 -0.0	+2.4 -0.0	+0.6 -0.7	
0.013	0.809	± 1.2	+1.1 -2.3	+0.0 -0.0	+0.2 -0.3	+0.0 -0.1	+0.0 -0.0	+0.7 -0.0	+0.0 -2.3	+0.0 -0.1	+0.1 +0.0	+0.1 -0.3	
0.021	0.673	± 1.4	+1.4 -1.5	+0.1 -0.0	+0.2 -0.1	+0.0 -0.0	+0.0 -0.0	+1.1 -0.0	+0.0 -0.0	+0.7 -1.4	+0.0 -0.0	+0.2 -0.4	
0.032	0.575	± 1.4	+3.0 -0.6	+0.1 -0.0	+0.0 -0.0	+0.0 -0.0	+0.8 -0.0	+0.0 -0.1	+0.0 -0.0	+2.4 -0.0	+1.7 -0.0	+0.4 -0.6	
0.050	0.507	± 1.4	+2.1 -1.1	+0.1 -0.0	+0.0 -0.6	+0.0 -0.0	+0.0 -0.0	+0.9 -0.0	+0.1 -0.8	+0.0 -0.0	+0.0 -0.0	+0.2 -0.4	
0.080	0.418	± 1.2	+3.8 -0.8	+0.0 -0.0	+0.0 -0.4	+0.0 -0.0	+0.7 -0.0	+0.8 +0.0	+3.7 +1.6	+0.0 +0.0	+0.0 +0.0	+0.1 +0.4	
0.180	0.325	± 1.3	+2.2 -1.4	+0.1 -0.0	+0.0 -1.1	+0.0 -0.0	+1.5 -0.0	+0.0 +0.9	+0.0 +0.0	+1.6 -0.9	+0.0 -0.0	+0.4 -0.2	
450	0.008	1.023	± 1.5	+1.9 -1.9	+0.4 -0.4	+0.0 -0.1	+0.5 -0.5	+0.9 -0.0	+0.0 -0.0	+0.0 -1.0	+1.4 -1.4	+0.6 -0.7	
0.013	0.816	± 1.7	+1.2 -2.2	+0.1 -0.0	+0.0 -0.1	+0.0 -0.1	+0.1 -0.0	+0.7 -0.0	+0.0 -0.0	+0.0 -2.0	+0.9 -1.0	+0.2 -0.3	
0.021	0.706	± 1.9	+1.7 -4.8	+0.1 -0.1	+0.0 -0.1	+0.0 -0.0	+0.0 -0.0	+1.7 -0.0	+0.0 -0.0	+0.0 -4.7	+0.0 -0.2	+0.2 -0.5	
0.032	0.582	± 1.8	+1.3 -3.6	+0.1 -0.1	+0.1 -0.1	+0.0 -0.0	+0.0 -0.0	+1.2 -0.0	+0.1 -0.0	+0.0 -3.5	+0.1 -0.1	+0.1 -0.7	
0.050	0.511	± 1.7	+1.4 -0.9	+0.1 -0.1	+0.0 -0.5	+0.0 -0.0	+1.4 -0.0	+0.2 -0.0	+0.0 -0.1	+0.2 -0.7	+0.0 +0.0	+0.1 -0.3	
0.080	0.425	± 1.7	+1.7 -1.7	+0.1 -0.1	+0.1 -0.2	+0.0 -0.0	+0.0 -0.0	+1.7 -0.0	+0.1 -0.0	+0.0 -1.6	+0.0 -0.1	+0.3 -0.5	
0.130	0.365	± 1.8	+1.5 -0.5	+0.1 -0.0	+0.2 -0.0	+0.0 -0.0	+0.0 +0.0	+1.1 +2.5	+0.8 +0.7	+0.0 -0.4	+0.1 +0.0	+0.5 +0.7	
0.250	0.257	± 2.0	+2.7 -2.9	+0.1 -0.0	+0.2 -0.0	+0.0 -0.0	+0.0 -0.0	+0.0 -0.0	+0.7 -0.1	+0.0 -2.9	+0.0 -0.0	+0.7 -0.4	

Table A.8: Systematic uncertainties for the reduced cross section $\tilde{\sigma}$ ($\mathcal{L} = 135.5\text{pb}^{-1}$, $P_e = 0$). The left five columns of the table contain the bin centres, Q_c^2 and x_c , the measured cross section, the statistical uncertainty and the total systematic uncertainty. The right eight columns of the table list the systematic uncertainties for $\delta_1 - \delta_7$, and the systematic uncertainties summed in quadrature for $\delta_8 - \delta_{15}$. The upper and lower uncertainties correspond to a positive or negative variation of a cut value. This table has two continuations.

Q_c^2 (GeV ²)	x_c	$\bar{\sigma}$	stat. (%)	sys. (%)	δ_1 (%)	δ_2 (%)	δ_3 (%)	δ_4 (%)	δ_5 (%)	δ_6 (%)	δ_7 (%)	$\delta_8 - \delta_{13}$ (%)	
650	0.013	0.865	± 1.6	+2.8 -2.9 +1.1	+0.0 -0.0 +0.3	+0.4 -0.0 +0.3	+0.4 -0.3 +0.0	+2.4 -0.0 +0.0	+0.0 -0.0 +0.0	+0.0 -2.5 +0.0	+1.5 -1.4 +1.0	+0.3 -0.6 +0.2	
	0.021	0.735	± 2.0	-2.4 +1.5	-0.1 +0.1	-0.0 +0.0	-0.0 +0.0	-0.0 +1.2	-0.0 +0.0	-2.2 +0.0	-1.0 +0.7	-0.5 +0.3	
	0.032	0.609	± 2.2	-4.0 +0.6	-0.2 +0.1	-0.2 +0.0	-0.0 +0.0	-0.0 +0.3	-0.0 +0.0	-3.9 +0.0	-0.7 +0.5	-0.3 +0.2	
	0.050	0.512	± 2.2	-2.0 -2.4	-0.2 -0.1	-0.2 +0.0	-0.0 +0.0	-0.0 +0.3	-0.0 +0.0	-1.9 +0.0	-0.5 +0.3	-0.4 +0.2	
	0.080	0.434	± 2.4	+1.4 -0.8	+0.1 -0.1	+0.1 -0.0	+0.0 -0.0	+1.4 -0.0	+0.0 +0.0	-2.3 +0.0	-0.3 +0.0	-0.5 +0.2	
	0.130	0.335	± 2.5	+1.3 -1.4	+0.2 -0.2	+0.3 -0.0	+0.0 -0.0	+1.3 -0.0	+0.0 -0.1	+0.0 -0.7	+0.0 +1.5	+0.2 +0.7	
	0.250	0.238	± 2.6	+3.2 -3.2	+0.3 -0.3	+0.2 -0.3	+0.8 -0.8	+2.6 -0.0	+0.2 -0.0	+0.0 -2.8	+0.0 +1.1	+1.5 +1.2	+0.7 -0.5
800	0.013	0.836	± 2.0	+1.2 -1.8	+0.1 -0.1	+0.0 -0.1	+0.1 -0.1	+0.0 -0.1	+0.0 -0.0	+0.0 -1.3	+0.0 -1.2	+0.3 -0.6	
	0.021	0.741	± 2.4	+1.2 -3.4	+0.1 -0.1	+0.1 +0.1	+0.3 +0.4	+0.4 +0.1	+0.1 +0.0	+0.0 +1.0	+1.0 +0.9	+0.5 -0.3	
	0.032	0.610	± 2.4	+1.2 -4.4	+0.2 -0.1	+0.4 -0.2	+0.0 -0.0	+0.8 +0.0	+0.0 +0.0	+0.0 -4.3	+0.7 +0.6	+0.1 -0.3	
	0.050	0.514	± 2.3	+0.7 -3.7	+0.1 -0.2	+0.0 -0.3	+0.0 -0.0	+0.0 -0.1	+0.0 -0.0	+0.0 -3.6	+0.0 +0.6	+0.6 -0.7	
	0.080	0.454	± 2.4	+1.9 -3.3	+0.1 -0.0	+0.4 -0.0	+0.0 -0.0	+1.8 -0.0	+0.0 -0.0	+0.0 -3.2	+0.0 +0.6	+0.6 -0.1	
	0.130	0.344	± 2.7	+2.5 -1.0	+0.1 -0.1	+0.5 -0.5	+0.0 -0.0	+2.3 -0.0	+0.0 -0.0	+0.0 -0.3	+0.0 +1.4	+0.6 +1.5	+0.2 -0.6
	0.250	0.243	± 3.0	+9.0 -4.5	+0.3 -0.3	+0.1 +0.4	+1.1 -1.7	+8.7 -0.0	+0.0 +0.0	+0.0 -3.6	+0.0 +0.0	+1.4 +1.4	+1.5 -1.5
1200	0.014	0.815	± 2.5	+2.4 -1.6	+0.0 -0.0	+0.4 -0.5	+0.3 -0.3	+1.7 -0.0	+0.0 -0.0	+0.0 -0.6	+0.0 +1.0	+1.3 +0.2	+0.8 +0.2
	0.021	0.737	± 2.4	+1.2 -3.1	+0.1 -0.1	+0.3 -0.0	+0.0 -0.0	+0.6 -0.0	+0.0 -0.0	+0.0 -2.9	+0.0 +0.8	+1.0 +0.1	+0.7 -0.7
	0.032	0.626	± 2.3	+1.6 -4.1	+0.1 -0.2	+0.2 -0.2	+0.0 -0.0	+1.3 +0.9	+0.0 +0.0	+0.0 -4.0	+0.0 +0.7	+0.8 +0.1	+0.1 -0.3
	0.050	0.513	± 2.1	+1.2 +0.8	+0.1 +0.1	+0.1 +0.4	+0.0 +0.0	+0.0 +0.3	+0.0 +0.0	+0.0 +0.0	+0.0 +0.7	+0.0 +0.8	+0.2 +0.2
	0.080	0.423	± 2.2	-3.2 +0.7	-0.1 +0.1	-0.0 +0.3	-0.0 +0.0	-0.0 +0.0	-0.0 -0.1	-3.1 -3.6	-0.6 +0.0	-1.4 +0.5	-1.5 +0.4
	0.130	0.352	± 2.3	-3.7 +1.1	-0.2 +0.2	-0.0 +0.3	-0.0 +0.0	-0.2 +0.5	-0.1 +0.0	-3.6 +0.0	-0.6 +0.6	-0.2 +0.6	-0.2 +0.7
	0.250	0.247	± 2.6	+1.1 -2.3	+0.2 -0.2	+0.3 -0.0	+0.0 -0.0	+0.5 -0.0	-0.1 -0.0	+0.0 -2.0	+0.0 +1.0	+0.6 +1.4	+0.7 -1.0
1500	0.021	0.724	± 3.4	+11.8 -1.9	+0.1 -0.1	+0.1 +0.3	+1.0 -1.0	+11.6 -0.0	+0.0 -0.1	+0.0 +0.0	+1.0 -1.4	+1.4 -0.9	+0.9 +0.6
	0.032	0.583	± 3.2	+4.5 -1.4	+0.0 -0.0	+0.3 -0.1	+0.0 -0.2	+4.3 -0.0	+0.0 -0.1	+0.0 -0.7	+1.1 +0.8	+1.2 -0.3	+0.4 -0.3
	0.050	0.532	± 2.8	+1.0 -2.2	+0.1 -0.2	+0.4 -0.0	+0.0 -0.0	+0.0 -0.7	+0.0 -0.1	+0.0 -1.8	+0.0 +0.7	+0.8 +0.4	-0.5 +0.4
	0.080	0.446	± 2.8	+1.0 -2.7	+0.2 -0.1	+0.1 -0.3	+0.0 -0.0	+0.5 -0.0	+0.0 -0.0	+0.0 -2.6	+0.0 +0.7	+0.7 +0.4	+0.4 -0.6
	0.130	0.373	± 3.3	+0.8 -2.3	+0.1 -0.1	+0.0 -0.6	+0.0 -0.0	+0.0 -0.1	+0.1 -0.0	+0.0 -2.2	+0.0 +0.5	+0.7 +0.5	+0.4 -0.2
	0.180	0.306	± 3.6	+1.0 -2.0	+0.1 -0.2	+0.4 -0.2	+0.0 -0.0	+0.6 -0.0	+0.0 -0.1	+0.0 -1.8	+0.0 +0.5	+0.5 +0.8	+0.5 -0.4
	0.250	0.242	± 4.4	+1.6 -1.3	+0.2 -0.2	+0.7 -0.2	+0.0 -0.0	+1.0 -0.0	+0.0 -0.0	+0.0 -1.1	+0.0 +0.7	+0.5 +1.7	+0.8 -0.3
2000	0.032	0.594	± 6.3	+2.0 +2.0	+0.1 +0.3	+0.0 +0.7	+0.0 +0.0	+0.0 +0.2	+0.0 +0.0	+0.0 -2.7	+0.0 +3.3	+1.4 +1.4	+1.5 -1.5
	0.050	0.495	± 3.8	-3.4 +11.3	-0.2 +0.1	-0.0 +0.8	-0.0 +0.9	-1.1 +10.6	-0.0 +0.0	-2.7 +3.3	+0.5 +1.4	+1.5 +1.4	-1.6 -1.5
	0.080	0.474	± 3.3	-2.0 +2.1	-0.0 +0.2	-0.9 +0.5	-0.9 +0.1	-0.0 +1.7	-0.0 +0.1	-0.0 +0.0	-1.4 +1.0	-0.8 +0.6	-0.8 +0.6
	0.130	0.352	± 4.1	-1.2 +0.9	-0.1 +0.2	-0.2 +0.4	-0.0 +0.1	-0.0 +0.0	-0.1 +0.0	-0.6 +0.0	-1.0 +0.8	-0.3 +0.2	-0.3 +0.2
	0.180	0.273	± 4.5	-4.0 +1.4	-0.1 +0.2	-0.0 +0.1	-0.1 +0.1	-0.3 +1.2	+0.0 +0.0	-3.9 +0.0	-0.7 +0.7	-0.4 +0.1	-0.4 +0.1
	0.250	0.247	± 5.1	-2.5 +1.0	-0.1 +0.1	-0.0 +0.2	-0.1 +0.7	-0.0 +0.0	-0.0 +0.0	-2.3 +0.0	-0.7 +0.6	-0.6 +0.2	-1.1 +0.2
	0.400	0.119	± 7.5	-2.6 +1.5	-0.2 +0.1	-0.3 +0.0	-0.0 +0.0	-0.1 +1.3	-0.1 +0.0	-2.2 +0.0	-0.6 +0.6	-0.6 +0.4	-0.5 +0.4
				-3.8 +2.5	-0.1 +0.2	-0.6 +0.0	-0.0 +0.0	-0.0 +2.0	-0.0 +0.0	-3.7 +0.7	-0.6 +0.5	-0.5 +1.2	-0.5 +1.2
				-0.8	+0.2	-0.2	-0.2	-0.0	-0.0	-0.0	-0.6	-0.6	-0.5

Table 8: Continuation 1.

Q_c^2 (GeV ²)	x_c	$\tilde{\sigma}$	stat. (%)	sys. (%)	δ_1 (%)	δ_2 (%)	δ_3 (%)	δ_4 (%)	δ_5 (%)	δ_6 (%)	δ_7 (%)	$\delta_8 - \delta_{13}$ (%)
3000	0.050	0.500	± 4.5	+2.4	+0.0	+1.0	+0.2	+1.9	+0.0	+0.0	+1.2	+0.2
		-2.4	-0.0	-0.0	-0.2	-0.0	-0.0	-2.0	-1.2	-0.6		
	0.080	0.429	± 4.2	+1.0	+0.1	+0.0	+0.0	+0.0	+0.0	+0.0	+0.8	+0.7
		-2.2	-0.1	-0.2	-0.0	-0.0	-1.9	-0.8	-0.9			
	0.130	0.366	± 4.7	+0.8	+0.1	+0.4	+0.0	+0.0	+0.0	+0.0	+0.7	+0.2
		-3.9	-0.2	-0.5	-0.0	-1.1	-0.0	-3.6	-0.7	-0.3		
	0.180	0.276	± 5.3	+1.6	+0.2	+0.1	+0.0	+0.6	+0.0	+1.3	+0.6	+0.4
-1.9		-0.2	-1.5	-0.0	-0.0	-0.0	-0.6	-0.9				
5000	0.250	0.243	± 5.9	+0.7	+0.1	+0.0	+0.0	+0.0	+0.0	+0.0	+0.6	+0.2
		-3.2	-0.1	-1.0	-0.0	-1.5	-0.0	-2.4	-0.6	-0.7		
	0.400	0.121	± 8.9	+3.0	+0.2	+0.0	+0.0	+3.0	+0.0	+0.0	+0.5	+0.2
		-2.3	-0.3	-0.2	-0.0	-0.0	-0.1	-2.1	-0.7	-0.7		
	0.650	0.015	± 21.6	+8.7	+0.5	+1.8	+0.0	+1.2	+0.1	+1.1	+0.7	+8.3
		-1.8	-0.0	-1.7	-0.0	-0.0	-0.0	-0.0	-0.5	-0.4		
	0.080	0.405	± 4.0	+4.1	+0.2	+0.0	+0.3	+3.9	+0.0	+0.0	+1.1	+0.6
-1.7		-0.2	-0.7	-0.3	-0.0	-0.0	-0.4	-1.1	-0.9			
8000	0.130	0.328	± 5.4	+1.0	+0.1	+0.0	+0.0	+0.0	+0.0	+0.0	+0.7	+0.7
		-3.9	-0.1	-0.4	-0.0	-0.0	-0.0	-3.8	-0.7	-0.7		
	0.180	0.286	± 5.5	+0.8	+0.1	+0.3	+0.0	+0.0	+0.0	+0.0	+0.7	+0.3
		-2.6	-0.1	-0.0	-0.0	-1.8	-0.0	-1.0	-0.7	-1.3		
	0.250	0.215	± 6.6	+1.0	+0.1	+0.4	+0.0	+0.7	+0.0	+0.0	+0.6	+0.2
		-2.5	-0.2	-0.7	-0.0	-0.0	-0.0	-2.3	-0.6	-0.7		
	0.400	0.135	± 8.5	+1.6	+0.3	+1.4	+0.0	+0.3	+0.0	+0.0	+0.6	+0.2
-1.7		-0.2	-0.0	-0.0	-0.0	-1.5	-0.6	-0.6				
12000	0.130	0.312	± 6.0	+3.3	+0.1	+0.4	+0.0	+3.0	+0.0	+0.0	+1.0	+0.6
		-3.9	-0.1	-2.7	-0.0	-0.0	-0.0	-2.2	-1.0	-1.3		
	0.180	0.239	± 7.9	+0.8	+0.1	+0.0	+0.0	+0.0	+0.0	+0.0	+0.7	+0.3
		-4.3	-0.1	-1.0	-0.0	-1.7	-0.0	-3.7	-0.7	-0.6		
	0.250	0.213	± 8.6	+1.9	+0.2	+0.5	+0.0	+0.0	+0.0	+0.0	+0.7	+1.7
		-3.1	-0.1	-0.0	-0.0	-0.9	-0.0	-2.6	-0.6	-1.3		
	0.400	0.104	± 12.3	+3.3	+0.2	+1.5	+0.0	+2.6	+0.0	+0.0	+0.6	+1.1
-2.9		-0.2	-1.5	-0.0	-0.0	-0.0	-2.1	-0.6	-1.2			
20000	0.650	0.017	± 25.5	+9.9	+0.4	+0.0	+0.0	+7.2	+0.0	+2.1	+0.7	+6.4
		-7.8	-0.8	-4.4	-0.0	-0.0	-0.1	-0.0	-0.5	-6.4		
	0.180	0.192	± 10.3	+1.9	+0.1	+1.0	+0.0	+0.0	+0.0	+0.0	+0.9	+1.3
		-3.0	-0.2	-0.3	-0.0	-0.2	-0.0	-2.2	-0.9	-1.7		
	0.250	0.152	± 13.4	+1.6	+0.1	+0.0	+0.0	+0.0	+0.0	+0.0	+0.7	+1.4
		-4.6	-0.1	-4.2	-0.0	-0.1	-0.0	-1.4	-0.7	-1.0		
	0.400	0.115	± 15.1	+3.2	+0.2	+1.7	+0.0	+1.3	+0.0	+0.0	+0.6	+2.3
-4.4		-0.2	-0.0	-0.0	-0.0	-0.0	-2.9	-0.6	-3.3			
30000	0.250	0.154	± 19.0	+7.8	+0.3	+2.0	+0.0	+6.1	+0.0	+0.0	+0.8	+4.2
		-16.2	-6.5	-0.2	-0.0	-0.0	-0.0	-5.6	-0.8	-3.2		
	0.400	0.064	± 25.5	+33.1	+7.1	+0.2	+4.6	+0.0	+0.0	+0.0	+0.7	+5.3
		-18.5	-0.2	-11.6	-0.0	-10.6	-0.0	-2.0	-0.7	-9.6		
	0.400	0.040	± 39.7	+59.7	+2.8	+0.3	+2.3	+0.0	+0.0	+0.0	+0.8	+1.5
		-39.7	-10.9	-0.3	-2.3	-0.0	-2.1	-0.0	-2.8	-0.8	-10.0	

Table 8: Continuation 2.

Q^2 range (GeV ²)	Q_c^2 (GeV ²)	x range	x_c	$x\tilde{F}_3 \times 10$
1300 – 1800	1500	0.017 – 0.025	0.021	$0.24 \pm 0.20^{+0.52}_{-0.14}$
	1500	0.025 – 0.037	0.032	$0.39 \pm 0.23^{+0.24}_{-0.08}$
	1500	0.037 – 0.06	0.050	$-0.15 \pm 0.29^{+0.11}_{-0.18}$
	1500	0.06 – 0.1	0.080	$0.76 \pm 0.41^{+0.17}_{-0.33}$
	1500	0.1 – 0.15	0.130	$0.14 \pm 0.69^{+0.35}_{-0.46}$
	1500	0.15 – 0.23	0.180	$0.36 \pm 0.86^{+0.40}_{-0.46}$
	1500	0.23 – 0.35	0.250	$1.81 \pm 1.19^{+0.51}_{-0.49}$
1800 – 2500	1500	0.35 – 0.53	0.400	$1.23 \pm 1.36^{+0.49}_{-0.96}$
	2000	0.023 – 0.037	0.032	$0.29 \pm 0.21^{+0.46}_{-0.10}$
	2000	0.037 – 0.06	0.050	$0.82 \pm 0.26^{+0.13}_{-0.08}$
	2000	0.06 – 0.1	0.080	$-0.27 \pm 0.37^{+0.18}_{-0.38}$
	2000	0.1 – 0.15	0.130	$0.68 \pm 0.59^{+0.18}_{-0.30}$
	2000	0.15 – 0.23	0.180	$1.57 \pm 0.74^{+0.14}_{-0.40}$
	2000	0.23 – 0.35	0.250	$0.02 \pm 1.02^{+0.33}_{-0.62}$
2500 – 3500	2000	0.35 – 0.53	0.400	$0.07 \pm 1.18^{+0.49}_{-0.50}$
	3000	0.037 – 0.06	0.050	$0.57 \pm 0.21^{+0.12}_{-0.09}$
	3000	0.06 – 0.1	0.080	$0.90 \pm 0.29^{+0.09}_{-0.13}$
	3000	0.1 – 0.15	0.130	$0.24 \pm 0.45^{+0.10}_{-0.29}$
	3000	0.15 – 0.23	0.180	$1.23 \pm 0.57^{+0.17}_{-0.18}$
	3000	0.23 – 0.35	0.250	$1.71 \pm 0.80^{+0.84}_{-0.89}$
	3000	0.35 – 0.53	0.400	$0.90 \pm 0.96^{+0.40}_{-0.37}$
3500 – 5600	3000	0.53 – 0.75	0.650	$0.24 \pm 0.41^{+0.26}_{-0.22}$
	5000	0.04 – 0.1	0.080	$0.82 \pm 0.16^{+0.13}_{-0.05}$
	5000	0.1 – 0.15	0.130	$1.52 \pm 0.29^{+0.07}_{-0.15}$
	5000	0.15 – 0.23	0.180	$0.87 \pm 0.35^{+0.06}_{-0.12}$
	5000	0.23 – 0.35	0.250	$0.65 \pm 0.46^{+0.10}_{-0.14}$
5600 – 9000	5000	0.35 – 0.53	0.400	$0.19 \pm 0.61^{+0.35}_{-0.36}$
	8000	0.07 – 0.15	0.130	$1.70 \pm 0.21^{+0.08}_{-0.11}$
	8000	0.15 – 0.23	0.180	$1.87 \pm 0.28^{+0.11}_{-0.15}$
	8000	0.23 – 0.35	0.250	$1.33 \pm 0.37^{+0.17}_{-0.19}$
	8000	0.35 – 0.53	0.400	$0.24 \pm 0.42^{+0.20}_{-0.20}$
9000 – 15000	8000	0.53 – 0.75	0.650	$0.06 \pm 0.22^{+0.08}_{-0.07}$
	12000	0.09 – 0.23	0.180	$1.72 \pm 0.22^{+0.04}_{-0.12}$
	12000	0.23 – 0.35	0.250	$1.77 \pm 0.31^{+0.09}_{-0.09}$
15000 – 25000	12000	0.35 – 0.53	0.400	$0.62 \pm 0.39^{+0.12}_{-0.12}$
	20000	0.15 – 0.35	0.250	$1.68 \pm 0.27^{+0.17}_{-0.11}$
25000 – 50000	20000	0.35 – 0.75	0.400	$1.01 \pm 0.27^{+0.09}_{-0.12}$
	30000	0.25 – 0.75	0.400	$1.13 \pm 0.24^{+0.09}_{-0.09}$

Table A.9: The structure function $x\tilde{F}_3$ extracted using the e^+p data set ($\mathcal{L} = 135.5\text{pb}^{-1}$, $P_e = 0$) and previously published NC e^-p DIS results ($\mathcal{L} = 169.9\text{pb}^{-1}$, $P_e = 0$). The bin range and bin centre for Q^2 and x , and measured $x\tilde{F}_3$ are shown. The first (second) error on the measurement refers to the statistical (systematic) uncertainties.

Q^2 (GeV ²)	x_c	$xF_3^{\gamma Z} \times 10$
1500	0.021	$2.85 \pm 1.21^{+1.57}_{-0.88}$
	0.032	$1.74 \pm 1.05^{+1.32}_{-0.62}$
	0.050	$3.35 \pm 0.84^{+0.46}_{-0.43}$
	0.080	$3.23 \pm 0.52^{+0.37}_{-0.21}$
	0.130	$4.91 \pm 0.50^{+0.17}_{-0.26}$
	0.180	$4.47 \pm 0.41^{+0.11}_{-0.22}$
	0.250	$3.86 \pm 0.41^{+0.20}_{-0.16}$
	0.400	$2.16 \pm 0.35^{+0.12}_{-0.14}$
	0.650	$0.32 \pm 0.73^{+0.28}_{-0.24}$

Table A.10: The structure function $xF_3^{\gamma Z}$ evaluated at $Q^2 = 1500\text{GeV}^2$ for x bins centred on x_c . The first (second) error on the measurement refers to the statistical (systematic) uncertainties.

Q^2 range (GeV ²)	Q_c^2 (GeV ²)	x range	x_c	$\tilde{\sigma}$	N_{data}	$N_{\text{bg}}^{\text{MC}}$
185 – 240	200	0.004 – 0.006	0.005	$(1.126 \pm 0.013^{+0.029}_{-0.018})$	7884	61.0
	200	0.006 – 0.010	0.008	$(0.944 \pm 0.010^{+0.008}_{-0.020})$	9129	22.3
	200	0.010 – 0.017	0.013	$(0.797 \pm 0.008^{+0.003}_{-0.022})$	9345	8.1
	200	0.017 – 0.025	0.021	$(0.682 \pm 0.008^{+0.013}_{-0.005})$	6504	3.0
	200	0.025 – 0.037	0.032	$(0.563 \pm 0.007^{+0.015}_{-0.001})$	5678	0.0
	200	0.037 – 0.060	0.050	$(0.512 \pm 0.007^{+0.011}_{-0.003})$	6074	0.7
	200	0.060 – 0.120	0.080	$(0.434 \pm 0.005^{+0.016}_{-0.001})$	8126	0.0
240 – 310	200	0.120 – 0.250	0.180	$(0.346 \pm 0.005^{+0.006}_{-0.008})$	5163	0.0
	250	0.006 – 0.010	0.008	$(0.939 \pm 0.013^{+0.020}_{-0.010})$	5432	20.1
	250	0.010 – 0.017	0.013	$(0.822 \pm 0.010^{+0.007}_{-0.035})$	6209	6.3
	250	0.017 – 0.025	0.021	$(0.711 \pm 0.010^{+0.003}_{-0.011})$	4663	2.6
	250	0.025 – 0.037	0.032	$(0.606 \pm 0.009^{+0.012}_{-0.013})$	4518	0.7
	250	0.037 – 0.060	0.050	$(0.514 \pm 0.008^{+0.013}_{-0.008})$	4529	0.0
	250	0.060 – 0.120	0.080	$(0.437 \pm 0.006^{+0.010}_{-0.005})$	5960	0.0
310 – 410	250	0.120 – 0.250	0.180	$(0.340 \pm 0.005^{+0.006}_{-0.009})$	4741	0.0
	350	0.006 – 0.010	0.008	$(0.963 \pm 0.017^{+0.030}_{-0.007})$	3313	15.5
	350	0.010 – 0.017	0.013	$(0.817 \pm 0.013^{+0.011}_{-0.010})$	4131	3.3
	350	0.017 – 0.025	0.021	$(0.689 \pm 0.012^{+0.010}_{-0.010})$	3088	0.7
	350	0.025 – 0.037	0.032	$(0.576 \pm 0.011^{+0.019}_{-0.003})$	2847	0.7
	350	0.037 – 0.060	0.050	$(0.520 \pm 0.009^{+0.011}_{-0.007})$	3181	0.7
	350	0.060 – 0.120	0.080	$(0.426 \pm 0.007^{+0.016}_{-0.005})$	4063	0.0
410 – 530	350	0.120 – 0.250	0.180	$(0.336 \pm 0.005^{+0.005}_{-0.008})$	3834	0.0
	450	0.006 – 0.010	0.008	$(1.044 \pm 0.020^{+0.020}_{-0.018})$	2718	26.0
	450	0.010 – 0.017	0.013	$(0.828 \pm 0.019^{+0.013}_{-0.018})$	1957	3.8
	450	0.017 – 0.025	0.021	$(0.715 \pm 0.018^{+0.014}_{-0.034})$	1607	1.3
	450	0.025 – 0.037	0.032	$(0.598 \pm 0.014^{+0.008}_{-0.022})$	1779	0.6
	450	0.037 – 0.060	0.050	$(0.504 \pm 0.011^{+0.005}_{-0.006})$	2087	0.0
	450	0.060 – 0.100	0.080	$(0.434 \pm 0.010^{+0.009}_{-0.008})$	1968	0.0
	450	0.100 – 0.170	0.130	$(0.382 \pm 0.009^{+0.005}_{-0.002})$	1891	0.0
	450	0.170 – 0.300	0.250	$(0.264 \pm 0.007^{+0.006}_{-0.008})$	1571	0.0

Table A.11: The reduced cross section $\tilde{\sigma}$ ($y < 0.9$, $y(1-x)^2 > 0.004$) ($\mathcal{L} = 78.8 \text{ textrmpb}^{-1}$, $P_e = +032$). The bin range, bin centre (Q_c^2) and measured cross section are shown. The first (second) error on the cross section corresponds to the statistical (systematic) uncertainties. The number of observed data events (N_{data}) and simulated background events ($N_{\text{bg}}^{\text{MC}}$) are also shown.

Q^2 range (GeV ²)	Q_c^2 (GeV ²)	x range	x_c	$\bar{\sigma}$	N_{data}	$N_{\text{bg}}^{\text{MC}}$
530 – 710	650	0.010 – 0.017	0.013	$(0.899 \pm 0.018^{+0.019}_{-0.025})$	2458	17.2
	650	0.017 – 0.025	0.021	$(0.763 \pm 0.019^{+0.007}_{-0.018})$	1551	0.0
	650	0.025 – 0.037	0.032	$(0.627 \pm 0.018^{+0.009}_{-0.025})$	1222	0.7
	650	0.037 – 0.060	0.050	$(0.520 \pm 0.015^{+0.003}_{-0.010})$	1199	0.0
	650	0.060 – 0.100	0.080	$(0.440 \pm 0.013^{+0.004}_{-0.011})$	1071	0.0
	650	0.100 – 0.170	0.130	$(0.320 \pm 0.011^{+0.006}_{-0.003})$	892	0.0
710 – 900	650	0.170 – 0.300	0.250	$(0.244 \pm 0.008^{+0.004}_{-0.004})$	869	0.0
	800	0.009 – 0.017	0.013	$(0.873 \pm 0.022^{+0.022}_{-0.027})$	1590	25.2
	800	0.017 – 0.025	0.021	$(0.748 \pm 0.023^{+0.008}_{-0.012})$	1039	1.9
	800	0.025 – 0.037	0.032	$(0.605 \pm 0.019^{+0.006}_{-0.020})$	1014	4.6
	800	0.037 – 0.060	0.050	$(0.534 \pm 0.015^{+0.004}_{-0.023})$	1192	0.7
	800	0.060 – 0.100	0.080	$(0.455 \pm 0.014^{+0.003}_{-0.017})$	1031	0.0
900 – 1300	800	0.100 – 0.170	0.130	$(0.363 \pm 0.012^{+0.008}_{-0.012})$	850	0.0
	800	0.170 – 0.300	0.250	$(0.243 \pm 0.010^{+0.006}_{-0.003})$	646	0.0
	1200	0.010 – 0.017	0.014	$(0.853 \pm 0.028^{+0.065}_{-0.038})$	994	21.5
	1200	0.017 – 0.025	0.021	$(0.758 \pm 0.023^{+0.017}_{-0.010})$	1090	7.1
	1200	0.025 – 0.037	0.032	$(0.641 \pm 0.019^{+0.006}_{-0.020})$	1114	0.0
	1200	0.037 – 0.060	0.050	$(0.531 \pm 0.015^{+0.009}_{-0.022})$	1334	0.0
1300 – 1800	1200	0.060 – 0.100	0.080	$(0.437 \pm 0.012^{+0.005}_{-0.013})$	1227	0.7
	1200	0.100 – 0.170	0.130	$(0.365 \pm 0.011^{+0.004}_{-0.012})$	1115	0.0
	1200	0.170 – 0.300	0.250	$(0.259 \pm 0.009^{+0.002}_{-0.010})$	893	0.0
	1200	0.300 – 0.530	0.400	$(0.133 \pm 0.007^{+0.002}_{-0.003})$	375	0.0
	1500	0.017 – 0.025	0.021	$(0.747 \pm 0.032^{+0.088}_{-0.013})$	556	10.5
	1500	0.025 – 0.037	0.032	$(0.585 \pm 0.025^{+0.040}_{-0.007})$	558	0.6
1800 – 2500	1500	0.037 – 0.060	0.050	$(0.562 \pm 0.020^{+0.005}_{-0.013})$	806	0.6
	1500	0.060 – 0.100	0.080	$(0.458 \pm 0.016^{+0.006}_{-0.012})$	780	0.0
	1500	0.100 – 0.150	0.130	$(0.387 \pm 0.017^{+0.003}_{-0.010})$	547	0.0
	1500	0.150 – 0.230	0.180	$(0.329 \pm 0.015^{+0.003}_{-0.007})$	496	0.0
	1500	0.230 – 0.350	0.250	$(0.249 \pm 0.014^{+0.004}_{-0.003})$	318	0.0
	1500	0.350 – 0.530	0.400	$(0.115 \pm 0.010^{+0.002}_{-0.004})$	142	0.0
1800 – 2500	2000	0.023 – 0.037	0.032	$(0.584 \pm 0.030^{+0.082}_{-0.011})$	402	7.1
	2000	0.037 – 0.060	0.050	$(0.522 \pm 0.024^{+0.006}_{-0.008})$	486	1.3
	2000	0.060 – 0.100	0.080	$(0.503 \pm 0.021^{+0.004}_{-0.020})$	582	0.7
	2000	0.100 – 0.150	0.130	$(0.355 \pm 0.019^{+0.003}_{-0.009})$	358	0.7
	2000	0.150 – 0.230	0.180	$(0.275 \pm 0.016^{+0.001}_{-0.008})$	294	0.0
	2000	0.230 – 0.350	0.250	$(0.254 \pm 0.017^{+0.004}_{-0.010})$	233	0.0
	2000	0.350 – 0.530	0.400	$(0.120 \pm 0.012^{+0.007}_{-0.001})$	106	0.0

Table 11: *Continuation 1.*

Q^2 range (GeV ²)	Q_c^2 (GeV ²)	x range	x_c	$\bar{\sigma}$	N_{data}	$N_{\text{bg}}^{\text{MC}}$
2500 – 3500	3000	0.037 – 0.060	0.050	$(0.497 \pm 0.029^{+0.013}_{-0.012})$	290	1.3
	3000	0.060 – 0.100	0.080	$(0.434 \pm 0.024^{+0.009}_{-0.009})$	338	0.0
	3000	0.100 – 0.150	0.130	$(0.380 \pm 0.023^{+0.003}_{-0.015})$	271	0.0
	3000	0.150 – 0.230	0.180	$(0.300 \pm 0.020^{+0.005}_{-0.004})$	225	0.0
	3000	0.230 – 0.350	0.250	$(0.264 \pm 0.020^{+0.002}_{-0.008})$	181	0.0
	3000	0.350 – 0.530	0.400	$(0.114 \pm 0.014^{+0.003}_{-0.003})$	70	0.0
3500 – 5600	3000	0.530 – 0.750	0.650	$(0.016^{+0.006}_{-0.004} \text{ } ^{+0.002}_{-0.000})$	13	0.0
	5000	0.040 – 0.100	0.080	$(0.450 \pm 0.023^{+0.017}_{-0.006})$	401	2.3
	5000	0.100 – 0.150	0.130	$(0.370 \pm 0.025^{+0.007}_{-0.015})$	224	0.0
	5000	0.150 – 0.230	0.180	$(0.326 \pm 0.022^{+0.002}_{-0.008})$	220	0.0
	5000	0.230 – 0.350	0.250	$(0.235 \pm 0.019^{+0.002}_{-0.007})$	147	0.0
	5000	0.350 – 0.530	0.400	$(0.149 \pm 0.016^{+0.003}_{-0.003})$	88	0.0
5600 – 9000	8000	0.070 – 0.150	0.130	$(0.339 \pm 0.026^{+0.010}_{-0.018})$	173	0.0
	8000	0.150 – 0.230	0.180	$(0.229 \pm 0.024^{+0.003}_{-0.009})$	89	0.0
	8000	0.230 – 0.350	0.250	$(0.241 \pm 0.026^{+0.004}_{-0.009})$	89	0.0
	8000	0.350 – 0.530	0.400	$(0.111^{+0.020}_{-0.017} \text{ } ^{+0.006}_{-0.003})$	41	0.0
	8000	0.530 – 0.750	0.650	$(0.020^{+0.008}_{-0.006} \text{ } ^{+0.002}_{-0.002})$	10	0.0
9000 – 15000	12000	0.090 – 0.230	0.180	$(0.218 \pm 0.028^{+0.007}_{-0.013})$	62	0.0
	12000	0.230 – 0.350	0.250	$(0.188^{+0.035}_{-0.030} \text{ } ^{+0.004}_{-0.013})$	40	0.0
	12000	0.350 – 0.530	0.400	$(0.148^{+0.030}_{-0.026} \text{ } ^{+0.003}_{-0.008})$	33	0.0
15000 – 25000	20000	0.150 – 0.350	0.250	$(0.135^{+0.039}_{-0.031} \text{ } ^{+0.020}_{-0.008})$	19	0.0
	20000	0.350 – 0.750	0.400	$(0.059^{+0.029}_{-0.020} \text{ } ^{+0.006}_{-0.008})$	8	0.0
25000 – 50000	30000	0.250 – 0.750	0.400	$(0.023^{+0.031}_{-0.015} \text{ } ^{+0.001}_{-0.022})$	2	0.0

Table 11: *Continuation 2.*

Q_c^2 (GeV ²)	x_c	$\tilde{\sigma}$	stat. (%)	sys. (%)	δ_1 (%)	δ_2 (%)	δ_3 (%)	δ_4 (%)	δ_5 (%)	δ_6 (%)	δ_7 (%)	$\delta_8 - \delta_{15}$ (%)	
200	0.005	1.126	± 1.1	+2.6 -1.6	+0.0 -0.0	+0.1 -0.1	+0.4 -0.5	+2.0 -0.0	+0.9 -1.5	+1.3 -0.0	+0.2 -0.0	+0.4 -0.3	
	0.008	0.944	± 1.0	+0.8 -2.1	+0.0 -0.1	+0.2 -0.0	+0.1 -0.1	+0.7 -0.0	+0.3 -0.9	+0.0 -1.9	+0.0 -0.0	+0.1 -0.2	
	0.013	0.797	± 1.0	+0.3 -2.7	+0.0 -0.1	+0.3 -0.2	+0.0 -0.1	+0.0 -0.0	+0.0 -1.5	+0.0 -2.3	+0.0 -0.1	+0.1 -0.2	
	0.021	0.682	± 1.2	+2.0 -0.7	+0.1 -0.1	+0.2 -0.2	+0.0 -0.0	+0.0 -0.3	+0.0 -0.5	+0.0 -0.0	+1.9 -0.0	+0.0 -0.1	
	0.032	0.563	± 1.3	+2.7 -0.2	+0.1 -0.1	+0.0 -0.1	+0.0 -0.0	+0.2 -0.0	+0.2 -0.0	+2.6 -2.0	+0.0 -0.0	+0.0 -0.2	
	0.050	0.512	± 1.3	+2.1 -0.5	+0.1 -0.1	+0.2 -0.0	+0.0 -0.0	+0.0 -0.1	+0.0 -0.5	+0.1 -0.0	+2.1 -0.0	+0.0 -0.0	+0.2 -0.1
	0.080	0.434	± 1.1	+3.6 -0.2	+0.1 -0.1	+0.2 -0.0	+0.0 -0.0	+0.6 -0.0	+0.0 -0.0	+0.6 -0.0	+3.6 -0.0	+0.0 -0.0	+0.1 -0.1
	0.180	0.346	± 1.4	+1.9 -2.4	+0.1 -0.1	+0.2 -0.0	+0.0 -0.0	+0.0 -0.0	+1.4 -0.0	+0.6 -0.0	+0.0 -2.3	+0.0 -0.0	+1.1 -0.4
250	0.008	0.939	± 1.4	+2.2 -1.1	+0.0 -0.0	+0.2 -0.1	+0.2 -0.2	+2.0 -0.0	+0.6 -0.3	+0.0 -1.0	+0.0 -0.0	+0.3 -0.3	
	0.013	0.822	± 1.3	+0.8 -4.2	+0.1 -0.1	+0.0 -0.0	+0.1 -0.0	+0.8 -0.0	+0.0 -1.0	+0.0 -4.1	+0.0 -0.0	+0.2 -0.2	
	0.021	0.711	± 1.5	+0.4 -1.6	+0.0 -0.1	+0.2 -0.0	+0.0 -0.1	+0.2 -0.0	+0.0 -0.0	+0.3 -0.0	+0.0 -0.1	+0.1 -0.2	
	0.032	0.606	± 1.5	+2.0 -2.1	+0.1 -0.1	+0.0 -0.2	+0.0 -0.0	+0.4 -0.0	+0.3 -0.0	+2.0 -0.0	+0.0 -0.0	+0.2 -0.3	
	0.050	0.514	± 1.5	+2.4 -1.6	+0.1 -0.1	+0.0 -0.1	+0.0 -0.0	+0.0 -0.6	+0.1 -1.5	+2.4 -0.0	+0.0 -0.0	+0.1 -0.2	
	0.080	0.437	± 1.3	+2.3 -1.2	+0.2 -0.1	+0.0 -0.0	+0.0 -0.0	+0.0 -0.1	+0.0 -1.1	+2.3 -0.0	+0.0 -0.0	+0.3 -0.1	
	0.180	0.340	± 1.5	+1.8 -2.5	+0.1 -0.1	+0.3 -0.0	+0.0 -0.0	+1.6 -0.0	+0.1 -1.0	+0.0 -1.2	+0.0 -0.0	+0.0 -0.4	+0.8 -0.4
	0.350	0.963	± 1.7	+3.1 -0.8	+0.1 -0.1	+0.1 -0.2	+0.2 -0.3	+1.8 -0.0	+0.0 -0.0	+2.4 -0.0	+0.5 -0.6	+0.4 -0.1	+0.4 -0.3
0.013	0.817	± 1.6	+1.3 -2.4	+0.1 -0.0	+0.1 -0.1	+0.3 -0.2	+0.0 -0.0	+1.2 -0.0	+0.6 -0.1	+0.0 -2.3	+0.1 -0.0	+0.2 -0.4	
0.021	0.689	± 1.8	+1.4 -1.5	+0.1 -0.0	+0.0 -0.3	+0.0 -0.0	+0.0 -0.0	+1.1 -0.0	+0.9 -0.0	+0.0 -1.4	+0.0 -0.0	+0.3 -0.4	
0.032	0.576	± 1.9	+3.3 -0.5	+0.2 -0.0	+0.4 -0.0	+0.0 -0.0	+0.7 -0.0	+0.0 -0.1	+2.7 -0.0	+1.7 -0.0	+0.1 -0.0	+0.6 -0.5	
0.050	0.520	± 1.8	+2.1 -1.3	+0.1 -0.1	+0.0 -0.0	+0.0 -0.0	+0.0 -0.0	+0.0 -0.9	+0.1 -0.0	+0.0 -0.1	+0.0 -0.1	+0.2 -0.6	
0.080	0.426	± 1.6	+2.5 -1.1	+0.1 -0.0	+0.1 -0.3	+0.0 -0.0	+0.0 -0.0	+0.0 -0.0	+0.0 -1.0	+0.0 -0.0	+0.0 -0.0	+0.1 -0.4	
0.180	0.336	± 1.6	+2.3 -1.6	+0.1 -0.0	+0.1 -1.2	+0.0 -0.0	+1.6 -0.0	+0.0 -1.0	+0.0 -0.0	+1.6 -0.0	+0.1 -0.0	+0.4 -0.2	
450	0.008	1.044	± 1.9	+1.9 -1.8	+0.5 -0.3	+0.1 -0.3	+0.5 -0.5	+1.2 -0.0	+0.0 -0.0	+0.0 -1.0	+0.0 -1.1	+1.1 -0.6	
	0.013	0.828	± 2.3	+1.5 -2.1	+0.0 -0.0	+0.3 -0.1	+0.1 -0.1	+1.3 -0.0	+0.1 -0.0	+0.0 -2.0	+0.8 -0.8	+0.3 -0.2	
	0.021	0.715	± 2.5	+1.9 -4.8	+0.1 -0.2	+0.4 -0.1	+0.0 -0.0	+1.9 -0.0	+0.0 -0.0	+0.0 -4.7	+0.1 -0.2	+0.1 -0.6	
	0.032	0.598	± 2.4	+1.3 -3.6	+0.0 -0.1	+0.1 -0.0	+0.0 -0.0	+1.2 -0.0	+0.0 -0.0	+0.0 -3.5	+0.0 -0.1	+0.0 -0.1	+0.3 -0.7
	0.050	0.504	± 2.2	+1.1 -1.3	+0.1 -0.1	+0.0 -0.9	+0.0 -0.0	+1.1 -0.0	+0.0 -0.1	+0.0 -0.7	+0.0 -0.1	+0.1 -0.0	+0.1 -0.6
	0.080	0.434	± 2.3	+2.1 -1.8	+0.1 -0.1	+0.3 -0.2	+0.0 -0.0	+2.0 -0.0	+0.0 -0.6	+0.0 -1.6	+0.0 -0.1	+0.0 -0.1	+0.3 -0.2
	0.130	0.382	± 2.3	+1.3 -0.5	+0.1 -0.0	+0.1 -0.0	+0.1 -0.0	+1.2 -0.0	+0.2 -0.0	+0.0 -0.4	+0.0 -0.1	+0.1 -0.1	+0.6 -0.2
	0.250	0.264	± 2.5	+2.2 -2.9	+0.1 -0.0	+0.2 -0.0	+0.0 -0.0	+2.2 -0.0	+0.0 -0.1	+0.0 -2.8	+0.0 -0.0	+0.0 -0.4	+0.2 -0.4

Table A.12: Systematic uncertainties for the reduced cross section $\tilde{\sigma}$ ($\mathcal{L} = 78.8\text{pb}^{-1}$, $P_e = +0.32$). The left five columns of the table contain the bin centres, Q_c^2 and x_c , the measured cross section, the statistical uncertainty and the total systematic uncertainty. The right eight columns of the table list the systematic uncertainties for $\delta_1 - \delta_7$, and the systematic uncertainties summed in quadrature for $\delta_8 - \delta_{15}$. The upper and lower uncertainties correspond to a positive or negative variation of a cut value. This table has two continuations.

Q_c^2 (GeV ²)	x_c	$\bar{\sigma}$	stat. (%)	sys. (%)	δ_1 (%)	δ_2 (%)	δ_3 (%)	δ_4 (%)	δ_5 (%)	δ_6 (%)	δ_7 (%)	$\delta_8 - \delta_{13}$ (%)
650	0.013	0.899	± 2.0	+2.1	+0.0	+0.2	+0.4	+1.6	+0.0	+0.0	+1.2	+0.3
				-2.8	-0.0	-0.0	-0.3	-0.0	-2.5	-1.1	-0.6	
	0.021	0.763	± 2.5	+0.9	+0.1	+0.3	+0.0	+0.2	+0.0	+0.0	+0.7	+0.3
				-2.3	-0.0	-0.0	-0.0	-0.0	-2.2	-0.7	-0.5	
	0.032	0.627	± 2.9	+1.4	+0.1	+0.0	+0.0	+1.2	+0.0	+0.0	+0.5	+0.5
				-4.0	-0.2	-0.3	-0.0	-0.0	-3.9	-0.6	-0.5	
0.050	0.520	± 2.9	+0.6	+0.1	+0.0	+0.0	+0.4	+0.0	+0.0	+0.4	+0.1	
			-2.0	-0.2	-0.6	-0.0	-0.0	-1.8	-0.4	-0.2		
0.080	0.440	± 3.1	+0.9	+0.2	+0.0	+0.0	+0.8	+0.1	+0.0	+0.3	+0.2	
			-2.4	-0.1	-0.6	-0.0	-0.0	-2.3	-0.3	-0.3		
0.130	0.320	± 3.3	+2.0	+0.1	+0.2	+0.0	+2.0	+0.1	+0.0	+0.2	+0.3	
			-0.8	-0.1	-0.3	-0.0	-0.0	-0.7	-0.2	-0.2		
0.250	0.244	± 3.4	+1.8	+0.2	+0.6	+0.0	+1.6	+0.0	+0.0	+0.2	+0.2	
			-1.6	-0.2	-0.5	-0.0	-0.0	-0.7	-0.2	-1.3		
800	0.013	0.873	± 2.5	+2.6	+0.3	+0.0	+0.8	+1.9	+0.3	+0.0	+1.3	+0.7
				-3.1	-0.2	-0.5	-0.6	-0.0	-2.8	-0.9	-0.7	
	0.021	0.748	± 3.1	+1.0	+0.1	+0.0	+0.1	+0.2	+0.0	+0.0	+0.9	+0.5
				-1.6	-0.0	-0.2	-0.1	-0.0	-1.2	-0.9	-0.5	
	0.032	0.605	± 3.2	+1.1	+0.1	+0.0	+0.3	+0.0	+0.1	+0.0	+0.7	+0.7
				-3.2	-0.1	-0.2	-0.2	-0.2	-3.2	-0.6	-0.4	
0.050	0.534	± 2.9	+0.7	+0.2	+0.2	+0.0	+0.3	+0.0	+0.0	+0.5	+0.2	
			-4.3	-0.1	-0.2	-0.0	-0.0	-4.3	-0.6	-0.1		
0.080	0.455	± 3.1	+0.7	+0.1	+0.0	+0.0	+0.0	+0.0	+0.0	+0.5	+0.4	
			-3.7	-0.2	-0.3	-0.0	-0.7	-1.1	-3.6	-0.6		
0.130	0.363	± 3.4	+2.2	+0.2	+0.3	+0.0	+2.0	+0.0	+0.0	+0.5	+0.5	
			-3.3	-0.0	-0.0	-0.0	-0.0	-3.2	-0.5	-0.2		
0.250	0.243	± 3.9	+2.3	+0.0	+0.8	+0.0	+2.1	+0.0	+0.0	+0.5	+0.2	
			-1.1	-0.1	-0.8	-0.0	-0.0	-0.3	-0.5	-0.5		
1200	0.014	0.853	± 3.2	+7.7	+0.3	+0.0	+1.1	+7.3	+0.1	+0.0	+1.1	+1.5
				-4.5	-0.3	-0.8	-1.8	-0.0	-3.6	-1.0	-1.3	
	0.021	0.758	± 3.0	+2.2	+0.0	+0.3	+0.3	+1.7	+0.0	+0.0	+1.1	+0.8
				-1.3	-0.0	-0.4	-0.3	-0.0	-0.6	-1.1	-0.1	
	0.032	0.641	± 3.0	+0.9	+0.1	+0.4	+0.0	+0.4	+0.0	+0.0	+0.7	+0.1
				-3.1	-0.1	-0.2	-0.0	-0.0	-2.9	-0.8	-0.8	
0.050	0.531	± 2.7	+1.7	+0.1	+0.4	+0.0	+1.5	+0.0	+0.0	+0.5	+0.2	
			-4.1	-0.2	-0.2	-0.0	-0.0	-4.1	-0.6	-0.3		
0.080	0.437	± 2.9	+1.0	+0.1	+0.2	+0.0	+0.8	+0.0	+0.0	+0.6	+0.1	
			-3.1	-0.1	-0.1	-0.0	-0.0	-3.0	-0.5	-0.3		
0.130	0.365	± 3.0	+1.1	+0.1	+0.5	+0.0	+0.8	+0.0	+0.0	+0.5	+0.4	
			-3.2	-0.2	-0.0	-0.0	-0.0	-3.1	-0.5	-0.6		
0.250	0.259	± 3.3	+0.7	+0.1	+0.3	+0.0	+0.0	+0.0	+0.0	+0.4	+0.5	
			-3.7	-0.2	-0.0	-0.0	-0.0	-3.6	-0.6	-0.4		
0.400	0.133	± 5.2	+1.5	+0.2	+0.3	+0.0	+1.1	+0.0	+0.0	+0.5	+1.0	
			-2.2	-0.2	-0.2	-0.0	-0.0	-2.0	-0.5	-0.7		
0.021	0.747	± 4.3	+11.8	+0.1	+0.2	+1.0	+11.6	+0.0	+1.0	+1.2	+1.0	
			-1.7	-0.0	-0.3	-1.0	-0.0	-1.2	-0.7	-0.7		
0.032	0.585	± 4.2	+6.8	+0.0	+0.4	+0.0	+6.7	+0.0	+0.0	+0.8	+0.7	
			-1.3	-0.1	-0.0	-0.2	-0.0	-1.1	-0.8	-0.9		
0.050	0.562	± 3.5	+0.8	+0.1	+0.5	+0.0	+0.0	+0.0	+0.0	+0.6	+0.4	
			-2.3	-0.2	-0.1	-0.0	-0.0	-2.3	-0.6	-0.6		
0.080	0.458	± 3.6	+1.2	+0.1	+0.2	+0.0	+0.9	+0.0	+0.0	+0.6	+0.5	
			-2.7	-0.1	-0.3	-0.0	-0.0	-2.5	-0.5	-0.6		
0.130	0.387	± 4.3	+0.7	+0.0	+0.0	+0.0	+0.0	+0.1	+0.0	+0.6	+0.3	
			-2.6	-0.1	-1.1	-0.0	-0.6	-2.2	-0.5	-0.2		
0.180	0.329	± 4.5	+1.0	+0.1	+0.5	+0.0	+0.7	+0.0	+0.0	+0.4	+0.3	
			-2.0	-0.2	-0.3	-0.0	-0.0	-1.8	-0.6	-0.5		
0.250	0.249	± 5.6	+1.6	+0.2	+0.9	+0.0	+0.5	+0.0	+0.0	+0.4	+1.1	
			-1.3	-0.2	-0.0	-0.0	-0.0	-1.1	-0.4	-0.6		
0.400	0.115	± 8.4	+1.6	+0.3	+0.5	+0.0	+0.0	+0.2	+0.0	+0.5	+1.4	
			-3.8	-0.2	-0.3	-0.0	-2.2	-0.0	-2.7	-0.4		
2000	0.032	0.584	± 5.1	+14.1	+0.1	+0.9	+0.9	+13.4	+0.0	+3.4	+1.2	+2.1
				-1.9	-0.0	-0.7	-0.9	-0.0	-1.3	-0.9	-0.9	
	0.050	0.522	± 4.5	+1.2	+0.2	+0.8	+0.1	+0.0	+0.1	+0.0	+0.7	+0.5
				-1.5	-0.1	-0.2	-0.0	-1.0	-0.0	-0.6	-0.7	
	0.080	0.503	± 4.1	+0.7	+0.1	+0.2	+0.1	+0.2	+0.0	+0.0	+0.6	+0.2
				-4.0	-0.1	-0.4	-0.1	-0.0	-3.9	-0.5	-0.4	
0.130	0.355	± 5.3	+0.8	+0.2	+0.2	+0.1	+0.1	+0.0	+0.0	+0.5	+0.4	
			-2.6	-0.1	-0.1	-0.1	-0.0	-2.3	-0.5	-1.1		
0.180	0.275	± 5.8	+0.5	+0.1	+0.0	+0.0	+0.0	+0.0	+0.0	+0.5	+0.2	
			-2.9	-0.2	-0.3	-0.0	-0.1	-2.2	-0.5	-1.8		
0.250	0.254	± 6.6	+1.4	+0.1	+0.0	+0.0	+1.2	+0.0	+0.0	+0.5	+0.4	
			-4.0	-0.1	-1.4	-0.0	-0.0	-3.7	-0.5	-0.4		
0.400	0.120	± 9.7	+5.8	+0.3	+0.0	+0.0	+5.6	+0.0	+0.7	+0.4	+1.2	
			-0.9	-0.3	-0.4	-0.0	-0.0	-0.5	-0.5	-0.5		

Table 12: *Continuation 1.*

Q_c^2 (GeV ²)	x_c	$\bar{\sigma}$	stat. (%)	sys. (%)	δ_1 (%)	δ_2 (%)	δ_3 (%)	δ_4 (%)	δ_5 (%)	δ_6 (%)	δ_7 (%)	$\delta_8 - \delta_{13}$ (%)	
3000	0.050	0.497	± 5.9	+2.7 -2.5	+0.0 -0.0	+1.2 -0.6	+0.2 -0.2	+2.1 -0.0	+0.0 -0.0	+0.0 -1.9	+0.9 -0.9	+0.7 -1.0	
	0.080	0.434	± 5.4	+2.1 -2.2	+0.1 -0.1	+0.1 -0.1	+0.0 -0.0	+1.8 -0.0	+0.0 -0.1	+0.0 -1.9	+0.6 -0.6	+0.7 -0.9	
	0.130	0.380	± 6.1	+0.7 -4.0	+0.1 -0.2	+0.0 -1.1	+0.0 -0.0	+0.0 -0.8	+0.0 -0.0	+0.0 -3.6	+0.5 -0.6	+0.4 -0.4	
	0.180	0.300	± 6.7	+1.5 -1.2	+0.2 -0.2	+0.0 -0.8	+0.0 -0.0	+0.5 -0.0	+0.0 -0.1	+0.0 -0.0	+1.3 -0.5	+0.5 -0.7	
	0.250	0.264	± 7.4	+0.8 -2.9	+0.2 -0.1	+0.0 -1.2	+0.0 -0.0	+0.4 -0.0	+0.0 -0.0	+0.0 -2.5	+0.0 -0.5	+0.6 -0.4	
	0.400	0.114	± 12.0	+2.3 -3.0	+0.2 -0.4	+1.1 -1.5	+0.0 -0.0	+2.0 -0.0	+0.0 -0.1	+0.0 -2.1	+0.0 -0.6	+0.3 -1.3	
5000	0.650	0.016	± 5.0	+36.1 -27.4	+10.4 -1.6	+0.6 -0.0	+1.9 -1.6	+0.0 -0.0	+1.2 -0.0	+0.1 -0.0	+1.2 -0.3	+10.0 -0.3	
	0.080	0.450	± 5.0	+3.8 -1.3	+0.2 -0.2	+0.0 -0.5	+0.3 -0.3	+3.6 -0.0	+0.0 -0.0	+0.0 -0.3	+0.8 -0.9	+0.8 -0.7	
	0.130	0.370	± 6.7	+1.9 -4.0	+0.1 -0.1	+0.0 -1.0	+0.0 -0.0	+1.7 -0.0	+0.0 -0.0	+0.0 -3.8	+0.6 -0.6	+0.5 -0.7	
	0.180	0.326	± 6.7	+0.8 -2.6	+0.1 -0.1	+0.1 -0.0	+0.0 -0.0	+0.0 -2.1	+0.0 -0.0	+0.0 -1.0	+0.6 -0.5	+0.5 -1.0	
	0.250	0.235	± 8.2	+0.9 -3.1	+0.1 -0.2	+0.5 -1.7	+0.0 -0.0	+0.4 -0.0	+0.0 -0.0	+0.0 -2.2	+0.5 -0.5	+0.3 -1.3	
	0.400	0.149	± 10.7	+1.9 -1.7	+0.3 -0.2	+1.4 -0.0	+0.0 -0.0	+1.0 -0.0	+0.0 -0.0	+0.0 -1.5	+0.5 -0.5	+0.5 -0.6	
8000	0.130	0.339	± 7.6	+2.8 -5.3	+0.1 -0.1	+1.0 -4.4	+0.0 -0.0	+2.4 -0.0	+0.0 -0.0	+0.0 -2.2	+0.8 -0.8	+0.7 -1.9	
	0.180	0.229	± 10.6	+1.3 -3.9	+0.1 -0.1	+0.0 -1.0	+0.0 -0.0	+0.3 -0.0	+0.0 -0.0	+0.0 -3.7	+0.6 -0.6	+1.2 -0.5	
	0.250	0.241	± 10.6	+1.5 -3.6	+0.1 -0.1	+0.1 -0.1	+0.0 -0.0	+0.0 -1.0	+0.0 -0.0	+0.0 -2.6	+0.5 -0.5	+1.4 -2.2	
	0.400	0.111	± 10.6	+18.2 -15.6	+5.3 -3.1	+0.2 -0.3	+3.3 -0.0	+0.0 -0.0	+3.5 -0.0	+0.0 -0.0	+0.0 -2.2	+0.5 -0.5	+1.9 -2.1
	0.650	0.020	± 10.6	+42.7 -31.1	+10.2 -10.2	+0.4 -0.9	+2.4 -2.8	+0.0 -0.0	+0.4 -0.0	+0.0 -0.1	+2.1 -0.0	+0.5 -0.4	+9.7 -9.8
	12000	0.180	0.218	± 12.7	+3.1 -5.9	+0.1 -0.2	+0.4 -1.4	+0.0 -0.0	+0.0 -3.9	+0.0 -0.0	+0.0 -2.2	+0.7 -0.7	+2.9 -3.5
20000	0.250	0.188	± 12.7	+18.4 -15.7	+2.1 -6.7	+0.1 -0.1	+0.0 -6.3	+0.0 -0.0	+0.2 -0.0	+0.0 -0.0	+0.0 -1.4	+0.6 -0.6	+2.0 -1.7
	0.400	0.148	± 12.7	+20.6 -17.3	+2.4 -5.2	+0.2 -0.2	+1.6 -1.4	+0.0 -0.0	+1.3 -0.0	+0.0 -0.0	+0.0 -2.9	+0.5 -0.5	+1.0 -4.0
	0.250	0.135	± 12.7	+28.6 -22.7	+14.7 -5.8	+0.3 -0.2	+2.0 -1.3	+0.0 -0.0	+13.8 -0.0	+0.0 -0.0	+0.0 -5.6	+0.7 -0.7	+4.8 -0.6
	0.400	0.059	± 12.7	+49.3 -34.6	+10.7 -14.4	+0.2 -0.2	+10.4 -10.7	+0.0 -0.0	+2.1 -0.0	+0.0 -0.0	+0.0 -1.9	+0.5 -0.5	+1.2 -9.3
	30000	0.400	0.023	+131.9	+2.8	+0.3	+2.3	+0.0	+0.0	+0.0	+0.0	+0.0	+1.5
				-64.6	-94.3	-0.3	-2.3	-0.0	-82.3	-0.0	-2.8	-0.6	-46.0

Table 12: Continuation 2.

Q^2 range (GeV ²)	Q_c^2 (GeV ²)	x range	x_c	$\tilde{\sigma}$	N_{data}	$N_{\text{bg}}^{\text{MC}}$
185 – 240	200	0.004 – 0.006	0.005	$(1.089 \pm 0.015^{+0.029}_{-0.015})$	5429	47.1
	200	0.006 – 0.010	0.008	$(0.947 \pm 0.012^{+0.010}_{-0.026})$	6518	16.5
	200	0.010 – 0.017	0.013	$(0.807 \pm 0.010^{+0.003}_{-0.022})$	6729	6.0
	200	0.017 – 0.025	0.021	$(0.679 \pm 0.010^{+0.013}_{-0.005})$	4603	2.1
	200	0.025 – 0.037	0.032	$(0.571 \pm 0.009^{+0.016}_{-0.003})$	4089	0.0
	200	0.037 – 0.060	0.050	$(0.510 \pm 0.008^{+0.011}_{-0.002})$	4301	0.5
	200	0.060 – 0.120	0.080	$(0.431 \pm 0.006^{+0.015}_{-0.001})$	5741	0.0
	200	0.120 – 0.250	0.180	$(0.346 \pm 0.006^{+0.006}_{-0.009})$	3660	0.0
240 – 310	250	0.006 – 0.010	0.008	$(0.916 \pm 0.015^{+0.026}_{-0.012})$	3758	14.8
	250	0.010 – 0.017	0.013	$(0.821 \pm 0.012^{+0.005}_{-0.034})$	4402	3.7
	250	0.017 – 0.025	0.021	$(0.667 \pm 0.012^{+0.009}_{-0.004})$	3107	3.7
	250	0.025 – 0.037	0.032	$(0.557 \pm 0.010^{+0.011}_{-0.009})$	2948	0.5
	250	0.037 – 0.060	0.050	$(0.513 \pm 0.009^{+0.012}_{-0.009})$	3211	0.0
	250	0.060 – 0.120	0.080	$(0.432 \pm 0.007^{+0.010}_{-0.004})$	4182	0.0
	250	0.120 – 0.250	0.180	$(0.334 \pm 0.006^{+0.004}_{-0.007})$	3301	0.0
	310 – 410	350	0.006 – 0.010	0.008	$(0.929 \pm 0.020^{+0.038}_{-0.009})$	2266
350		0.010 – 0.017	0.013	$(0.800 \pm 0.015^{+0.009}_{-0.018})$	2869	2.8
350		0.017 – 0.025	0.021	$(0.652 \pm 0.014^{+0.009}_{-0.010})$	2079	0.2
350		0.025 – 0.037	0.032	$(0.576 \pm 0.013^{+0.016}_{-0.006})$	2022	0.4
350		0.037 – 0.060	0.050	$(0.489 \pm 0.011^{+0.011}_{-0.004})$	2125	0.5
350		0.060 – 0.120	0.080	$(0.407 \pm 0.008^{+0.016}_{-0.003})$	2760	0.0
350		0.120 – 0.250	0.180	$(0.310 \pm 0.006^{+0.006}_{-0.003})$	2506	0.0
410 – 530		450	0.006 – 0.010	0.008	$(0.997 \pm 0.024^{+0.021}_{-0.023})$	1830
	450	0.010 – 0.017	0.013	$(0.802 \pm 0.022^{+0.010}_{-0.020})$	1347	2.9
	450	0.017 – 0.025	0.021	$(0.696 \pm 0.021^{+0.010}_{-0.034})$	1104	0.9
	450	0.025 – 0.037	0.032	$(0.563 \pm 0.016^{+0.007}_{-0.020})$	1183	0.5
	450	0.037 – 0.060	0.050	$(0.523 \pm 0.013^{+0.010}_{-0.003})$	1531	0.0
	450	0.060 – 0.100	0.080	$(0.415 \pm 0.011^{+0.007}_{-0.008})$	1337	0.0
	450	0.100 – 0.170	0.130	$(0.342 \pm 0.010^{+0.007}_{-0.002})$	1203	0.0
	450	0.170 – 0.300	0.250	$(0.248 \pm 0.008^{+0.009}_{-0.007})$	1041	0.0

Table A.13: The reduced cross section $\tilde{\sigma}$ ($y < 0.9$, $y(1-x)^2 > 0.004$) ($\mathcal{L} = 56.7\text{pb}^{-1}$, $P_e = -0.36$). The bin range, bin centre (Q_c^2) and measured cross section are shown. The first (second) error on the cross section corresponds to the statistical (systematic) uncertainties. The number of observed data events (N_{data}) and simulated background events ($N_{\text{bg}}^{\text{MC}}$) are also shown.

Q^2 range (GeV ²)	Q_c^2 (GeV ²)	x range	x_c	$\tilde{\sigma}$	N_{data}	$N_{\text{bg}}^{\text{MC}}$
530 – 710	650	0.010 – 0.017	0.013	$(0.822 \pm 0.021^{+0.033}_{-0.026})$	1587	11.8
	650	0.017 – 0.025	0.021	$(0.699 \pm 0.022^{+0.010}_{-0.019})$	1013	0.0
	650	0.025 – 0.037	0.032	$(0.587 \pm 0.020^{+0.010}_{-0.024})$	821	0.5
	650	0.037 – 0.060	0.050	$(0.503 \pm 0.017^{+0.004}_{-0.011})$	829	0.0
	650	0.060 – 0.100	0.080	$(0.426 \pm 0.016^{+0.002}_{-0.012})$	738	0.0
	650	0.100 – 0.170	0.130	$(0.358 \pm 0.013^{+0.003}_{-0.003})$	706	0.0
	650	0.170 – 0.300	0.250	$(0.232 \pm 0.010^{+0.002}_{-0.003})$	584	0.0
710 – 900	800	0.009 – 0.017	0.013	$(0.788 \pm 0.025^{+0.034}_{-0.028})$	1010	16.0
	800	0.017 – 0.025	0.021	$(0.734 \pm 0.027^{+0.012}_{-0.017})$	718	1.4
	800	0.025 – 0.037	0.032	$(0.620 \pm 0.023^{+0.012}_{-0.022})$	733	3.3
	800	0.037 – 0.060	0.050	$(0.489 \pm 0.018^{+0.010}_{-0.022})$	774	0.4
	800	0.060 – 0.100	0.080	$(0.456 \pm 0.017^{+0.005}_{-0.017})$	737	0.0
	800	0.100 – 0.170	0.130	$(0.320 \pm 0.014^{+0.005}_{-0.010})$	537	0.0
	800	0.170 – 0.300	0.250	$(0.244 \pm 0.011^{+0.007}_{-0.003})$	464	0.0
900 – 1300	1200	0.010 – 0.017	0.014	$(0.769 \pm 0.031^{+0.085}_{-0.037})$	637	14.9
	1200	0.017 – 0.025	0.021	$(0.715 \pm 0.027^{+0.019}_{-0.015})$	729	5.1
	1200	0.025 – 0.037	0.032	$(0.608 \pm 0.022^{+0.011}_{-0.020})$	749	0.0
	1200	0.037 – 0.060	0.050	$(0.490 \pm 0.017^{+0.007}_{-0.021})$	875	0.0
	1200	0.060 – 0.100	0.080	$(0.406 \pm 0.014^{+0.006}_{-0.013})$	810	0.5
	1200	0.100 – 0.170	0.130	$(0.336 \pm 0.012^{+0.003}_{-0.011})$	730	0.0
	1200	0.170 – 0.300	0.250	$(0.232 \pm 0.010^{+0.002}_{-0.008})$	566	0.0
	1200	0.300 – 0.530	0.400	$(0.125 \pm 0.008^{+0.002}_{-0.004})$	249	0.0
1300 – 1800	1500	0.017 – 0.025	0.021	$(0.699 \pm 0.037^{+0.083}_{-0.020})$	368	7.1
	1500	0.025 – 0.037	0.032	$(0.585 \pm 0.030^{+0.011}_{-0.011})$	394	0.9
	1500	0.037 – 0.060	0.050	$(0.496 \pm 0.022^{+0.007}_{-0.011})$	503	0.5
	1500	0.060 – 0.100	0.080	$(0.434 \pm 0.019^{+0.005}_{-0.012})$	523	0.0
	1500	0.100 – 0.150	0.130	$(0.356 \pm 0.019^{+0.005}_{-0.009})$	355	0.3
	1500	0.150 – 0.230	0.180	$(0.276 \pm 0.016^{+0.004}_{-0.005})$	293	0.0
	1500	0.230 – 0.350	0.250	$(0.234 \pm 0.016^{+0.005}_{-0.004})$	210	0.0
	1500	0.350 – 0.530	0.400	$(0.126 \pm 0.012^{+0.004}_{-0.004})$	109	0.0
1800 – 2500	2000	0.023 – 0.037	0.032	$(0.615 \pm 0.036^{+0.048}_{-0.015})$	299	5.1
	2000	0.037 – 0.060	0.050	$(0.463 \pm 0.027^{+0.029}_{-0.007})$	304	0.6
	2000	0.060 – 0.100	0.080	$(0.439 \pm 0.023^{+0.006}_{-0.018})$	358	0.4
	2000	0.100 – 0.150	0.130	$(0.351 \pm 0.022^{+0.011}_{-0.009})$	249	0.4
	2000	0.150 – 0.230	0.180	$(0.273 \pm 0.019^{+0.006}_{-0.007})$	205	0.0
	2000	0.230 – 0.350	0.250	$(0.239 \pm 0.019^{+0.005}_{-0.009})$	154	0.0
	2000	0.350 – 0.530	0.400	$(0.120 \pm 0.014^{+0.002}_{-0.004})$	74	0.0

Table 13: Continuation 1.

Q^2 range (GeV ²)	Q_c^2 (GeV ²)	x range	x_c	$\bar{\sigma}$	N_{data}	$N_{\text{bg}}^{\text{MC}}$
2500 – 3500	3000	0.037 – 0.060	0.050	$(0.511 \pm 0.035^{+0.012}_{-0.013})$	212	0.9
	3000	0.060 – 0.100	0.080	$(0.429 \pm 0.028^{+0.006}_{-0.015})$	237	0.0
	3000	0.100 – 0.150	0.130	$(0.350 \pm 0.026^{+0.005}_{-0.015})$	177	0.0
	3000	0.150 – 0.230	0.180	$(0.247 \pm 0.022^{+0.012}_{-0.008})$	131	0.0
	3000	0.230 – 0.350	0.250	$(0.217 \pm 0.021^{+0.003}_{-0.012})$	105	0.0
	3000	0.350 – 0.530	0.400	$(0.133 \pm 0.018^{+0.006}_{-0.004})$	57	0.0
	3000	0.530 – 0.750	0.650	$(0.014^{+0.007}_{-0.005} +^{+0.001}_{-0.000})$	8	0.0
3500 – 5600	5000	0.040 – 0.100	0.080	$(0.351 \pm 0.023^{+0.016}_{-0.010})$	227	1.7
	5000	0.100 – 0.150	0.130	$(0.276 \pm 0.025^{+0.005}_{-0.014})$	120	0.0
	5000	0.150 – 0.230	0.180	$(0.235 \pm 0.022^{+0.003}_{-0.007})$	113	0.0
	5000	0.230 – 0.350	0.250	$(0.191 \pm 0.021^{+0.004}_{-0.005})$	85	0.0
	5000	0.350 – 0.530	0.400	$(0.118 \pm 0.017^{+0.002}_{-0.003})$	49	0.0
5600 – 9000	8000	0.070 – 0.150	0.130	$(0.281 \pm 0.028^{+0.012}_{-0.009})$	104	0.0
	8000	0.150 – 0.230	0.180	$(0.258 \pm 0.030^{+0.003}_{-0.016})$	72	0.0
	8000	0.230 – 0.350	0.250	$(0.179 \pm 0.026^{+0.006}_{-0.005})$	47	0.0
	8000	0.350 – 0.530	0.400	$(0.096^{+0.023}_{-0.019} +^{+0.002}_{-0.007})$	25	0.0
	8000	0.530 – 0.750	0.650	$(0.014^{+0.010}_{-0.006} +^{+0.003}_{-0.003})$	5	0.0
9000 – 15000	12000	0.090 – 0.230	0.180	$(0.161^{+0.033}_{-0.028} +^{+0.012}_{-0.007})$	33	0.0
	12000	0.230 – 0.350	0.250	$(0.106^{+0.034}_{-0.026} +^{+0.002}_{-0.003})$	16	0.0
	12000	0.350 – 0.530	0.400	$(0.070^{+0.028}_{-0.021} +^{+0.008}_{-0.006})$	11	0.0
15000 – 25000	20000	0.150 – 0.350	0.250	$(0.185^{+0.053}_{-0.042} +^{+0.017}_{-0.020})$	19	0.0
	20000	0.350 – 0.750	0.400	$(0.073^{+0.040}_{-0.027} +^{+0.009}_{-0.026})$	7	0.0
25000 – 50000	30000	0.250 – 0.750	0.400	$(0.065^{+0.052}_{-0.031} +^{+0.026}_{-0.003})$	4	0.0

Table 13: Continuation 2.

Q_c^2 (GeV ²)	x_c	$\tilde{\sigma}$	stat. (%)	sys. (%)	δ_1 (%)	δ_2 (%)	δ_3 (%)	δ_4 (%)	δ_5 (%)	δ_6 (%)	δ_7 (%)	$\delta_8 - \delta_{15}$ (%)
200	0.005	1.089	± 1.4	+2.7	+0.1	+0.0	+0.5	+1.8	+1.4	+1.3	+0.2	+0.5
				-1.4	-0.0	-0.0	-0.4	-0.0	-1.3	-0.0	-0.0	-0.3
	0.008	0.947	± 1.2	+1.0	+0.1	+0.1	+0.1	+1.0	+0.0	+0.0	+0.1	+0.3
				-2.7	-0.0	-0.0	-0.1	-0.0	-2.0	-1.8	-0.0	-0.1
	0.013	0.807	± 1.2	+0.3	+0.1	+0.0	+0.0	+0.3	+0.0	+0.0	+0.0	+0.1
				-2.8	-0.1	-0.2	-0.1	-0.0	-1.7	-2.2	-0.1	-0.3
	0.021	0.679	± 1.5	+1.9	+0.1	+0.0	+0.0	+0.0	+0.1	+1.9	+0.0	+0.1
				-0.7	-0.1	-0.3	-0.0	-0.5	-0.0	-0.0	-0.1	-0.3
250	0.032	0.571	± 1.6	+2.7	+0.1	+0.0	+0.0	+0.0	+0.1	+2.7	+0.0	+0.1
				-0.4	-0.1	-0.1	-0.0	-0.4	-0.0	-0.0	-0.0	-0.1
	0.050	0.510	± 1.5	+2.2	+0.1	+0.0	+0.0	+0.4	+0.0	+2.1	+0.0	+0.1
				-0.3	-0.1	-0.1	-0.0	-0.0	-0.2	-0.0	-0.0	-0.1
	0.080	0.431	± 1.3	+3.6	+0.1	+0.1	+0.0	+0.0	+0.1	+3.5	+0.0	+0.1
				-0.3	-0.1	-0.0	-0.0	-0.1	-0.0	-0.0	-0.0	-0.2
	0.180	0.346	± 1.7	+1.7	+0.1	+0.0	+0.0	+1.3	+1.1	+0.0	+0.0	+0.3
				-2.6	-0.1	-0.3	-0.0	-0.0	-0.0	-2.3	-0.0	-1.0
350	0.008	0.916	± 1.6	+2.9	+0.0	+0.4	+0.2	+2.3	+1.6	+0.0	+0.0	+0.4
				-1.3	-0.0	-0.5	-0.2	-0.0	-0.6	-1.0	-0.1	-0.3
	0.013	0.821	± 1.5	+0.6	+0.1	+0.0	+0.0	+0.6	+0.1	+0.0	+0.0	+0.2
				-4.2	-0.0	-0.3	-0.1	-0.0	-1.1	-4.0	-0.0	-0.2
	0.021	0.667	± 1.8	+1.3	+0.2	+0.0	+0.1	+1.1	+0.7	+0.2	+0.0	+0.2
				-0.6	-0.1	-0.0	-0.0	-0.0	-0.6	-0.0	-0.0	-0.2
	0.032	0.557	± 1.8	+2.0	+0.1	+0.2	+0.0	+0.0	+0.0	+1.9	+0.0	+0.3
				-1.6	-0.1	-0.2	-0.0	-0.3	-1.6	-0.0	-0.0	-0.1
450	0.050	0.513	± 1.8	+2.4	+0.1	+0.0	+0.0	+0.0	+0.1	+2.4	+0.1	+0.3
				-1.8	-0.1	-0.0	-0.0	-0.2	-1.8	-0.0	-0.0	-0.1
	0.080	0.432	± 1.5	+2.3	+0.1	+0.2	+0.0	+0.0	+0.0	+2.3	+0.0	+0.3
				-1.0	-0.1	-0.5	-0.0	-0.0	-0.9	-0.0	-0.0	-0.2
	0.180	0.334	± 1.7	+1.1	+0.1	+0.2	+0.0	+1.0	+0.1	+0.0	+0.0	+0.4
				-2.0	-0.1	-0.2	-0.0	-0.0	-1.3	-1.1	-0.0	-1.0
	0.008	0.929	± 2.1	+4.1	+0.1	+0.0	+0.3	+3.2	+0.2	+2.5	+0.9	+0.3
				-1.0	-0.0	-0.3	-0.3	-0.0	-0.0	-0.0	-0.9	-0.3
200	0.013	0.800	± 1.9	+1.1	+0.0	+0.2	+0.0	+0.1	+1.1	+0.0	+0.1	+0.1
				-2.3	-0.1	-0.6	-0.0	-0.0	-0.0	-2.2	-0.1	-0.4
	0.021	0.652	± 2.2	+1.4	+0.0	+0.3	+0.0	+1.2	+0.5	+0.0	+0.1	+0.2
				-1.5	-0.0	-0.0	-0.0	-0.0	-0.1	-1.4	-0.0	-0.5
	0.032	0.576	± 2.2	+2.7	+0.0	+0.0	+0.0	+1.0	+1.9	+1.6	+0.0	+0.2
				-1.1	-0.1	-0.6	-0.0	-0.0	-0.1	-0.0	-0.1	-0.9
	0.050	0.489	± 2.2	+2.3	+0.1	+0.0	+0.0	+0.6	+1.4	+1.6	+0.0	+0.4
				-0.7	-0.0	-0.4	-0.0	-0.0	-0.5	-0.0	-0.0	-0.4
	0.080	0.407	± 1.9	+3.9	+0.1	+0.0	+0.0	+1.0	+0.6	+3.7	+0.0	+0.2
				-0.6	-0.1	-0.4	-0.0	-0.0	-0.2	-0.0	-0.1	-0.4
	0.180	0.310	± 2.0	+2.0	+0.1	+0.0	+0.0	+1.2	+0.0	+1.5	+0.0	+0.6
				-1.1	-0.0	-0.8	-0.0	-0.0	-0.6	-0.0	-0.0	-0.4
	0.008	0.997	± 2.4	+2.1	+0.4	+0.2	+0.5	+0.5	+0.0	+0.0	+1.8	+0.6
				-2.3	-0.4	-0.0	-0.5	-0.0	-0.0	-0.9	-1.7	-1.0
	0.013	0.802	± 2.7	+1.3	+0.1	+0.0	+0.1	+0.0	+0.0	+0.0	+1.2	+0.3
				-2.5	-0.0	-0.6	-0.1	-0.2	-0.0	-1.9	-1.3	-0.8
0.021	0.696	± 3.0	+1.4	+0.0	+0.0	+0.0	+1.3	+0.0	+0.0	+0.2	+0.1	
			-4.8	-0.1	-0.6	-0.0	-0.0	-0.0	-4.8	-0.3	-0.5	
0.032	0.563	± 2.9	+1.3	+0.1	+0.1	+0.0	+1.3	+0.0	+0.0	+0.1	+0.1	
			-3.6	-0.1	-0.4	-0.0	-0.0	-0.1	-3.4	-0.1	-1.0	
0.050	0.523	± 2.6	+2.0	+0.1	+0.3	+0.0	+1.9	+0.3	+0.0	+0.0	+0.3	
			-0.7	-0.1	-0.1	-0.0	-0.0	-0.0	-0.6	-0.1	-0.1	
0.080	0.415	± 2.7	+1.6	+0.1	+0.0	+0.0	+1.1	+0.0	+1.1	+0.0	+0.3	
			-1.9	-0.1	-0.2	-0.0	-0.0	-0.0	-1.6	-0.1	-1.1	
0.130	0.342	± 2.9	+2.1	+0.1	+0.3	+0.0	+1.0	+1.8	+0.0	+0.1	+0.4	
			-0.6	-0.0	-0.0	-0.0	-0.0	-0.0	-0.4	-0.0	-0.3	
0.250	0.248	± 3.1	+3.8	+0.0	+0.4	+0.0	+3.0	+1.2	+0.0	+0.0	+2.0	
			-3.0	-0.0	-0.1	-0.0	-0.0	-0.0	-3.0	-0.0	-0.5	

Table A.14: Systematic uncertainties for the reduced cross section $\tilde{\sigma}$ ($\mathcal{L} = 56.7\text{pb}^{-1}$, $P_e = -0.36$). The left five columns of the table contain the bin centres, Q_c^2 and x_c , the measured cross section, the statistical uncertainty and the total systematic uncertainty. The right eight columns of the table list the systematic uncertainties for $\delta_1 - \delta_7$, and the systematic uncertainties summed in quadrature for $\delta_8 - \delta_{15}$. The upper and lower uncertainties correspond to a positive or negative variation of a cut value. This table has two continuations.

Q_c^2 (GeV ²)	x_c	$\bar{\sigma}$	stat. (%)	sys. (%)	δ_1 (%)	δ_2 (%)	δ_3 (%)	δ_4 (%)	δ_5 (%)	δ_6 (%)	δ_7 (%)	$\delta_8 - \delta_{13}$ (%)
650	0.013	0.822	± 2.5	+4.0	+0.0	+0.7	+0.4	+3.5	+0.0	+0.0	+1.8	+0.2
				-3.1	-0.0	-0.1	-0.4	-0.0	-0.0	-2.5	-1.8	-0.6
	0.021	0.699	± 3.1	+1.5	+0.1	+0.3	+0.0	+0.0	+0.0	+0.0	+1.4	+0.4
				-2.7	-0.1	-0.0	-0.0	-0.4	-0.0	-2.2	-1.3	-0.7
	0.032	0.587	± 3.5	+1.7	+0.1	+0.0	+0.0	+1.2	+0.0	+0.0	+1.1	+0.3
				-4.1	-0.1	-0.2	-0.0	-0.0	-0.0	-3.9	-1.0	-0.2
	0.050	0.503	± 3.5	+0.9	+0.2	+0.3	+0.0	+0.1	+0.0	+0.0	+0.7	+0.4
				-2.1	-0.2	-0.2	-0.0	-0.0	-0.0	-1.9	-0.6	-0.7
800	0.080	0.426	± 3.7	+0.5	+0.1	+0.0	+0.0	+0.0	+0.0	+0.0	+0.4	+0.2
				-2.7	-0.2	-0.2	-0.0	-0.4	-0.0	-2.4	-0.4	-1.1
	0.130	0.358	± 3.8	+0.9	+0.1	+0.5	+0.0	+0.7	+0.0	+0.0	+0.3	+0.2
				-0.9	-0.1	-0.1	-0.0	-0.0	-0.0	-0.8	-0.2	-0.2
	0.250	0.232	± 4.1	+1.0	+0.1	+0.6	+0.0	+0.8	+0.0	+0.0	+0.2	+0.1
				-1.2	-0.2	-0.2	-0.0	-0.0	-0.1	-0.7	-0.3	-0.9
	0.013	0.788	± 3.2	+4.3	+0.3	+0.5	+0.7	+3.8	+0.0	+0.0	+1.7	+0.8
				-3.5	-0.3	-0.0	-0.0	-1.1	-0.0	-2.8	-1.8	-0.5
1200	0.021	0.734	± 3.7	+1.6	+0.0	+0.1	+0.1	+0.0	+0.0	+0.0	+1.5	+0.4
				-2.3	-0.1	-0.0	-0.1	-0.6	-0.0	-1.4	-1.5	-0.9
	0.032	0.620	± 3.7	+1.9	+0.1	+0.5	+0.2	+1.2	+0.2	+0.0	+1.3	+0.3
				-3.5	-0.1	-0.0	-0.2	-0.0	-0.0	-3.2	-1.2	-0.3
	0.050	0.489	± 3.6	+2.0	+0.2	+0.6	+0.0	+1.6	+0.0	+0.0	+1.0	+0.2
				-4.5	-0.1	-0.1	-0.0	-0.0	-0.0	-4.3	-1.0	-1.0
	0.080	0.456	± 3.7	+1.1	+0.1	+0.1	+0.0	+0.7	+0.0	+0.0	+0.8	+0.1
				-3.7	-0.1	-0.2	-0.0	-0.0	-0.0	-3.6	-0.9	-0.6
1500	0.130	0.320	± 4.3	+1.7	+0.1	+0.5	+0.0	+1.3	+0.0	+0.0	+0.8	+0.4
				-3.3	-0.1	-0.0	-0.0	-0.0	-0.0	-3.2	-0.7	-0.5
	0.250	0.244	± 4.6	+2.7	+0.2	+0.1	+0.0	+2.6	+0.0	+0.0	+0.7	+0.2
				-1.1	-0.1	-0.2	-0.0	-0.0	-0.0	-0.3	-0.7	-0.8
	0.014	0.769	± 4.1	+11.1	+0.1	+0.8	+1.1	+10.8	+0.0	+0.0	+1.7	+1.5
				-4.8	-0.4	-0.0	-1.4	-0.0	-0.1	-3.7	-1.8	-1.9
	0.021	0.715	± 3.7	+2.7	+0.0	+0.6	+0.4	+1.8	+0.0	+0.0	+1.7	+0.8
				-2.0	-0.0	-0.6	-0.4	-0.0	-0.0	-0.7	-1.7	-0.4
2000	0.032	0.608	± 3.7	+1.7	+0.1	+0.5	+0.0	+1.0	+0.0	+0.0	+1.3	+0.3
				-3.3	-0.1	-0.0	-0.0	-0.0	-0.0	-2.9	-1.3	-0.8
	0.050	0.490	± 3.4	+1.5	+0.1	+0.0	+0.0	+1.0	+0.0	+0.0	+1.1	+0.2
				-4.2	-0.1	-0.3	-0.0	-0.0	-0.0	-4.0	-1.1	-0.5
	0.080	0.406	± 3.5	+1.5	+0.1	+0.4	+0.0	+1.1	+0.0	+0.0	+0.9	+0.2
				-3.2	-0.1	-0.1	-0.0	-0.0	-0.0	-3.1	-0.9	-0.3
	0.130	0.336	± 3.7	+0.9	+0.1	+0.3	+0.0	+0.0	+0.0	+0.0	+0.8	+0.2
				-3.3	-0.1	-0.2	-0.0	-0.5	-0.0	-3.1	-0.7	-0.3
2500	0.250	0.232	± 4.2	+0.9	+0.1	+0.3	+0.0	+0.0	+0.0	+0.0	+0.7	+0.5
				-3.6	-0.1	-0.0	-0.0	-0.4	-0.0	-3.6	-0.7	-0.1
	0.400	0.125	± 6.3	+1.4	+0.2	+1.1	+0.0	+0.0	+0.0	+0.0	+0.7	+0.4
				-3.2	-0.1	-0.0	-0.0	-0.3	-0.0	-2.0	-0.7	-2.3
	0.021	0.699	± 5.3	+11.9	+0.1	+0.0	+1.0	+11.6	+0.0	+1.0	+1.7	+0.8
				-2.9	-0.1	-0.4	-1.0	-0.0	-0.1	-0.0	-1.8	-2.0
	0.032	0.585	± 5.0	+1.9	+0.1	+0.1	+0.1	+0.9	+0.0	+0.0	+1.5	+0.8
				-1.9	-0.0	-0.6	-0.1	-0.0	-0.0	-0.6	-1.5	-0.8
3000	0.050	0.496	± 4.5	+1.4	+0.1	+0.4	+0.0	+0.0	+0.0	+0.0	+1.2	+0.5
				-2.2	-0.1	-0.0	-0.0	-0.0	-0.0	-1.8	-1.2	-0.4
	0.080	0.434	± 4.4	+1.1	+0.2	+0.0	+0.0	+0.0	+0.0	+0.0	+0.9	+0.5
				-2.9	-0.1	-0.2	-0.0	-0.1	-0.0	-2.6	-0.9	-0.8
	0.130	0.356	± 5.3	+1.4	+0.2	+0.6	+0.1	+0.6	+0.1	+0.0	+0.8	+0.7
				-2.4	-0.1	-0.4	-0.1	-0.0	-0.0	-2.1	-0.8	-0.7
	0.180	0.276	± 5.8	+1.3	+0.1	+0.4	+0.0	+0.5	+0.0	+0.0	+0.7	+0.9
				-2.0	-0.1	-0.0	-0.0	-0.0	-0.1	-1.8	-0.8	-0.4
4000	0.250	0.234	± 6.9	+2.3	+0.2	+0.3	+0.0	+1.8	+0.0	+0.0	+0.7	+1.1
				-1.8	-0.1	-1.1	-0.0	-0.0	-0.0	-1.2	-0.7	-0.2
	0.400	0.126	± 9.6	+3.1	+0.4	+1.9	+0.0	+0.2	+0.1	+0.0	+0.9	+2.3
				-3.5	-0.3	-0.0	-0.0	-0.0	-0.0	-2.8	-0.5	-2.1
	0.032	0.615	± 5.9	+7.8	+0.1	+0.5	+0.9	+6.7	+0.0	+3.3	+1.8	+1.0
				-2.4	-0.0	-1.1	-0.9	-0.0	-0.0	-0.0	-1.7	-1.0
	0.050	0.463	± 5.7	+6.3	+0.1	+0.0	+0.1	+6.1	+0.1	+0.0	+1.4	+0.8
				-1.6	-0.2	-0.2	-0.0	-0.0	-0.1	-0.6	-1.3	-0.5
5000	0.080	0.439	± 5.3	+1.3	+0.2	+0.7	+0.1	+0.0	+0.0	+0.0	+1.0	+0.2
				-4.2	-0.1	-0.0	-0.1	-0.9	-0.0	-3.9	-1.0	-0.6
	0.130	0.351	± 6.3	+3.0	+0.2	+0.2	+0.1	+2.8	+0.0	+0.0	+0.9	+0.6
				-2.6	-0.1	-0.5	-0.1	-0.0	-0.0	-2.4	-0.9	-0.4
	0.180	0.273	± 7.0	+2.2	+0.1	+1.0	+0.0	+1.8	+0.0	+0.0	+0.7	+0.4
				-2.5	-0.2	-0.5	-0.0	-0.0	-0.1	-2.2	-0.8	-0.5
	0.250	0.239	± 8.1	+2.0	+0.1	+1.0	+0.0	+1.5	+0.0	+0.0	+0.7	+0.6
				-3.8	-0.2	-0.0	-0.0	-0.0	-0.0	-3.7	-0.7	-0.7
0.400	0.120	± 11.6	+1.6	+0.2	+0.1	+0.0	+0.0	+0.0	+0.8	+0.7	+1.2	
			-3.2	-0.2	-0.0	-0.0	-3.1	-0.0	-0.0	-0.7	-0.4	

Table 14: *Continuation 1.*

Q_c^2 (GeV ²)	x_c	$\tilde{\sigma}$	stat. (%)	sys. (%)	δ_1 (%)	δ_2 (%)	δ_3 (%)	δ_4 (%)	δ_5 (%)	δ_6 (%)	δ_7 (%)	$\delta_8 - \delta_{13}$ (%)	
3000	0.050	0.511	± 6.9	+2.4	+0.0	+0.7	+0.2	+1.6	+0.0	+0.0	+1.6	+0.4	
				-2.6	-0.0	-0.0	-0.2	-0.0	-0.0	-2.0	-1.6	-0.7	
	0.080	0.429	± 6.5	+1.3	+0.1	+0.0	+0.0	+0.0	+0.0	+0.0	+0.0	+1.1	+0.8
				-3.6	-0.1	-0.5	-0.0	-2.6	-0.0	-1.9	-0.9	-1.0	
	0.130	0.350	± 7.5	+1.5	+0.1	+1.1	+0.0	+0.0	+0.0	+0.0	+0.0	+0.9	+0.4
				-4.2	-0.2	-0.0	-0.0	-1.6	-0.0	-3.7	-0.9	-0.7	
	0.180	0.247	± 8.7	+1.9	+0.2	+0.5	+0.0	+0.0	+0.6	+0.0	+0.0	+1.3	+0.8
			-3.2	-0.2	-2.8	-0.0	-0.0	-0.0	-0.0	-0.8	-1.4		
0.250	0.217	± 9.8	+1.5	+0.1	+1.0	+0.0	+0.0	+0.0	+0.0	+0.0	+0.8	+0.7	
			-5.7	-0.2	-1.0	-0.0	-4.8	-0.0	-2.3	-0.8	-1.6		
5000	0.400	0.133	± 13.2	+4.7	+0.3	+1.6	+0.0	+4.2	+0.0	+0.0	+0.7	+0.9	
				-2.9	-0.2	-1.8	-0.0	-0.0	-0.1	-2.0	-0.8	-0.5	
	0.650	0.014	± 6.7	+49.3	+7.7	+0.5	+1.7	+0.0	+1.2	+0.0	+1.0	+0.6	+7.3
				-34.6	-2.1	-0.1	-1.9	-0.0	-0.0	-0.0	-0.0	-0.8	-0.6
	0.080	0.351	± 6.7	+4.6	+0.2	+0.2	+0.4	+4.3	+0.0	+0.0	+1.5	+0.5	+0.5
				-2.9	-0.1	-1.0	-0.4	-0.0	-0.0	-0.4	-1.4	-2.3	
	0.130	0.276	± 9.1	+1.7	+0.1	+0.6	+0.0	+0.0	+0.0	+0.0	+0.0	+1.0	+1.1
			-5.2	-0.1	-0.0	-0.0	-3.3	-0.0	-3.8	-1.0	-0.9		
0.180	0.235	± 9.4	+1.4	+0.1	+0.9	+0.0	+0.0	+0.0	+0.0	+0.0	+0.9	+0.6	
			-2.8	-0.1	-0.0	-0.0	-1.2	-0.0	-1.1	-0.9	-2.1		
8000	0.250	0.191	± 10.8	+1.9	+0.1	+1.1	+0.0	+1.1	+0.0	+0.0	+0.7	+0.8	
				-2.7	-0.1	-0.0	-0.0	-0.0	-0.1	-2.3	-0.8	-1.2	
	0.400	0.118	± 14.3	+1.8	+0.3	+1.4	+0.0	+0.0	+0.0	+0.0	+0.8	+0.7	
				-2.5	-0.2	-0.0	-0.0	-1.0	-0.0	-1.5	-0.7	-1.6	
	0.130	0.281	± 9.8	+4.3	+0.1	+0.1	+0.0	+3.9	+0.0	+0.0	+1.3	+1.2	
				-3.3	-0.1	-0.4	-0.0	-0.0	-0.0	-2.3	-1.3	-1.9	
	0.180	0.258	± 11.8	+1.0	+0.1	+0.0	+0.0	+0.0	+0.0	+0.0	+0.0	+1.0	+0.2
			-6.2	-0.1	-1.7	-0.0	-4.2	-0.0	-3.7	-0.9	-1.8		
12000	0.250	0.179	± 14.6	+3.2	+0.2	+1.1	+0.0	+0.0	+0.0	+0.0	+0.9	+2.8	
				-2.9	-0.1	-0.0	-0.0	-0.8	-0.0	-2.7	-0.8	-0.0	
	0.400	0.096	± 9.8	+24.3	+1.7	+0.2	+0.0	+0.0	+1.1	+0.0	+0.0	+0.8	+1.0
				-19.9	-6.8	-0.2	-6.5	-0.0	-0.0	-1.9	-0.7	-0.3	
	0.650	0.014	± 6.7	+67.6	+20.9	+0.4	+0.0	+0.0	+20.8	+0.1	+2.1	+0.9	+0.9
				-43.2	-18.1	-0.8	-18.0	-0.0	-0.0	-0.0	-0.7	-0.5	
	20000	0.180	0.161	± 10.8	+20.6	+7.5	+0.1	+2.1	+0.0	+6.7	+0.0	+0.0	+1.3
				-17.3	-4.1	-0.2	-0.0	-0.0	-0.0	-2.2	-1.2	-3.2	
0.250		0.106	± 11.8	+31.8	+2.3	+0.1	+1.3	+0.0	+0.0	+0.0	+0.0	+0.9	+1.6
				-24.7	-2.5	-0.1	-1.3	-0.0	-1.0	-0.0	-1.4	-0.9	-0.7
0.400		0.070	± 9.8	+40.2	+11.9	+0.2	+7.5	+0.0	+1.3	+0.0	+0.0	+0.8	+9.1
				-29.7	-8.9	-0.3	-0.0	-0.0	-0.0	-2.9	-0.8	-8.4	
0.250		0.185	± 10.8	+28.6	+9.0	+0.3	+3.9	+0.0	+0.0	+0.0	+0.0	+1.2	+8.0
			-22.7	-11.0	-0.2	-0.0	-0.0	-1.5	-0.0	-5.6	-1.2	-9.2	
30000	0.400	0.073	± 10.8	+53.9	+12.8	+0.2	+0.0	+0.0	+0.0	+0.0	+0.9	+12.8	
				-36.9	-35.9	-0.2	-12.5	-0.0	-27.1	-0.0	-2.0	-0.9	-19.8
	0.400	0.065	± 10.8	+79.1	+39.0	+0.3	+2.3	+0.0	+38.1	+0.0	+0.0	+1.1	+8.1
				-47.9	-5.0	-0.3	-2.4	-0.0	-0.0	-2.8	-1.1	-3.1	

Table 14: Continuation 2.

Q^2 range (GeV ²)	Q_c^2 (GeV ²)	$d\sigma/dQ^2$ (pb/GeV ²)	N_{data}	$N_{\text{bg}}^{\text{MC}}$
185.0 – 300.0	250	$(1.07 \pm 0.00^{+0.01}_{-0.01}) \times 10^1$	96158	149.8
300.0 – 400.0	350	$(4.74 \pm 0.03^{+0.07}_{-0.03})$	28667	33.6
400.0 – 475.7	440	$(2.73 \pm 0.03^{+0.05}_{-0.05})$	11858	36.2
475.7 – 565.7	520	$(1.83 \pm 0.02^{+0.03}_{-0.05})$	8698	22.7
565.7 – 672.7	620	$(1.19 \pm 0.02^{+0.02}_{-0.03})$	6108	22.4
672.7 – 800.0	730	$(8.02 \pm 0.11^{+0.10}_{-0.24}) \times 10^{-1}$	5859	20.0
800.0 – 1050.0	900	$(4.75 \pm 0.05^{+0.07}_{-0.17}) \times 10^{-1}$	7622	29.7
1050.0 – 1460.0	1230	$(2.11 \pm 0.03^{+0.05}_{-0.05}) \times 10^{-1}$	5875	32.9
1460.0 – 2080.0	1730	$(9.00 \pm 0.15^{+0.23}_{-0.13}) \times 10^{-2}$	3832	14.9
2080.0 – 3120.0	2500	$(3.28 \pm 0.07^{+0.07}_{-0.05}) \times 10^{-2}$	2298	6.1
3120.0 – 5220.0	3900	$(1.04 \pm 0.03^{+0.02}_{-0.02}) \times 10^{-2}$	1416	2.9
5220.0 – 12500.0	7000	$(1.73 \pm 0.07^{+0.02}_{-0.05}) \times 10^{-3}$	616	0.0
12500.0 – 51200.0	22400	$(2.03 \pm 0.26^{+0.02}_{-0.08}) \times 10^{-5}$	60	0.0

Table A.15: The single differential cross section $d\sigma/dQ^2$ ($y < 0.9$, $y(1-x)^2 > 0.004$) ($\mathcal{L} = 78.8\text{pb}^{-1}$, $P_e = +0.32$). The bin range, bin centre (Q_c^2) and measured cross section are shown. The first (second) error on the cross section corresponds to the statistical (systematic) uncertainties. The number of observed data events (N_{data}) and simulated background events ($N_{\text{bg}}^{\text{MC}}$) are also shown.

Q_c^2 (GeV ²)	$d\sigma/dQ^2$ (pb/GeV ²)	stat. (%)	sys. (%)	δ_1 (%)	δ_2 (%)	δ_3 (%)	δ_4 (%)	δ_5 (%)	δ_6 (%)	δ_7 (%)	$\delta_8 - \delta_{15}$ (%)
250	1.07×10^1	± 0.3	+0.7 -0.9	+0.2 -0.2	+0.1 -0.0	+0.1 -0.1	+0.6 -0.9	+0.2 -0.9	+0.1 -0.0	+0.0 -0.0	+0.2 -0.1
350	4.74	± 0.6	+1.5 -0.6	+0.3 -0.1	+0.0 -0.3	+0.1 -0.1	+1.1 -0.0	+0.7 -0.5	+0.7 -0.0	+0.2 -0.1	+0.2 -0.3
440	2.73	± 0.9	+1.8 -1.7	+0.1 -0.2	+0.1 -0.1	+0.1 -0.2	+1.8 -0.0	+0.2 -0.1	+0.0 -1.6	+0.3 -0.4	+0.2 -0.3
520	1.83	± 1.1	+1.5 -2.5	+0.3 -0.2	+0.0 -0.1	+0.1 -0.1	+1.3 -0.0	+0.1 -0.0	+0.0 -2.5	+0.5 -0.4	+0.4 -0.2
620	1.19	± 1.3	+1.8 -2.6	+0.3 -0.2	+0.1 -0.0	+0.2 -0.2	+1.6 -0.0	+0.0 -0.1	+0.0 -2.4	+0.6 -0.7	+0.5 -0.7
730	8.02×10^1	± 1.3	+1.3 -3.0	+0.2 -0.2	+0.0 -0.5	+0.2 -0.2	+1.0 -0.0	+0.0 -0.1	+0.0 -2.9	+0.7 -0.7	+0.2 -0.4
900	4.75×10^1	± 1.1	+1.4 -3.5	+0.1 -0.1	+0.3 -0.2	+0.2 -0.3	+1.2 -0.0	+0.0 -0.0	+0.0 -3.4	+0.7 -0.7	+0.2 -0.3
1230	2.11×10^1	± 1.3	+2.4 -2.3	+0.2 -0.1	+0.1 -0.1	+0.3 -0.2	+2.3 -0.0	+0.0 -0.0	+0.0 -2.2	+0.7 -0.7	+0.4 -0.1
1730	9.00×10^2	± 1.6	+2.5 -1.5	+0.1 -0.1	+0.0 -0.2	+0.2 -0.2	+2.4 -0.0	+0.0 -0.0	+0.0 -1.2	+0.7 -0.7	+0.3 -0.4
2500	3.28×10^2	± 2.1	+2.2 -1.6	+0.1 -0.1	+0.2 -0.1	+0.1 -0.1	+2.0 -0.0	+0.0 -0.0	+0.0 -1.4	+0.7 -0.7	+0.2 -0.2
3900	1.04×10^2	± 2.7	+2.1 -2.1	+0.2 -0.2	+0.0 -0.5	+0.1 -0.1	+1.9 -0.0	+0.0 -0.0	+0.0 -1.9	+0.7 -0.7	+0.0 -0.4
7000	1.73×10^3	± 4.0	+0.9 -2.7	+0.2 -0.2	+0.0 -1.6	+0.0 -0.0	+0.0 -0.2	+0.0 -0.0	+0.0 -1.9	+0.6 -0.6	+0.9 -0.5
22400	2.03×10^5	± 12.9	+1.1 -4.1	+0.2 -0.2	+0.2 -0.0	+0.0 -0.0	+0.0 -0.4	+0.0 -0.0	+0.0 -3.3	+0.6 -0.6	+0.9 -2.3

Table A.16: Systematic uncertainties for $d\sigma/dQ^2$ ($y < 0.9$, $y(1-x)^2 > 0.004$) ($\mathcal{L} = 78.8\text{pb}^{-1}$, corrected to $P_e = +0.32$). The left four columns of the table contain the bin centre (Q_c^2), the measured cross section, the statistical uncertainty and the total systematic uncertainty. The right eight columns of the table list the systematic uncertainties for $\delta_1 - \delta_7$, and the systematic uncertainties summed in quadrature for $\delta_8 - \delta_{15}$. The upper and lower uncertainties correspond to a positive or negative variation of a cut value.

$Q^2 >$ (GeV ²)	x range	x_c	$d\sigma/dx$ (pb)	N_{data}	$N_{\text{bg}}^{\text{MC}}$
185	$(0.63 - 1.00) \times 10^{-2}$	0.794×10^{-2}	$(8.80 \pm 0.06^{+0.12}_{-0.13}) \times 10^4$	20397	91.9
	$(0.10 - 0.16) \times 10^{-1}$	0.126×10^{-1}	$(5.88 \pm 0.04^{+0.06}_{-0.17}) \times 10^4$	23452	71.7
	$(0.16 - 0.25) \times 10^{-1}$	0.200×10^{-1}	$(3.69 \pm 0.02^{+0.03}_{-0.03}) \times 10^4$	23332	49.5
	$(0.25 - 0.40) \times 10^{-1}$	0.316×10^{-1}	$(2.12 \pm 0.01^{+0.02}_{-0.01}) \times 10^4$	22669	17.5
	$(0.40 - 0.63) \times 10^{-1}$	0.501×10^{-1}	$(1.25 \pm 0.01^{+0.01}_{-0.01}) \times 10^4$	19901	3.3
	$(0.63 - 1.00) \times 10^{-1}$	0.794×10^{-1}	$(6.98 \pm 0.05^{+0.08}_{-0.05}) \times 10^3$	18738	2.9
	0.10 - 0.16	0.126	$(3.97 \pm 0.03^{+0.03}_{-0.02}) \times 10^3$	18025	0.7
	0.16 - 0.25	0.200	$(2.09 \pm 0.02^{+0.04}_{-0.05}) \times 10^3$	11263	0.0
3000	$(0.40 - 0.63) \times 10^{-1}$	0.501×10^{-1}	$(1.81 \pm 0.11^{+0.08}_{-0.03}) \times 10^2$	269	0.6
	$(0.63 - 1.00) \times 10^{-1}$	0.794×10^{-1}	$(1.69 \pm 0.08^{+0.04}_{-0.02}) \times 10^2$	437	2.3
	0.10 - 0.16	0.126	$(1.28 \pm 0.06^{+0.01}_{-0.05}) \times 10^2$	542	0.0
	0.16 - 0.25	0.200	$(7.46 \pm 0.34^{+0.06}_{-0.19}) \times 10^1$	471	0.0
	0.25 - 0.40	0.316	$(3.41 \pm 0.18^{+0.08}_{-0.09}) \times 10^1$	350	0.0
	0.40 - 0.75	0.687	$(1.29 \pm 0.11^{+0.03}_{-0.02})$	151	0.0

Table A.17: The single differential cross section $d\sigma/dx$ ($y < 0.9$, $y(1-x)^2 > 0.004$) for $Q^2 > 185\text{GeV}^2$ and $Q^2 > 3000\text{GeV}^2$ ($\mathcal{L} = 78.8\text{pb}^{-1}$, corrected to $P_e = +0.32$). The Q^2 and bin range, bin centre (x_c) and measured cross section are shown. The first (second) error on the cross section corresponds to the statistical (systematic) uncertainties. The number of observed data events (N_{data}) and simulated background events ($N_{\text{bg}}^{\text{MC}}$) are also shown.

$Q^2 >$ (GeV ²)	x_c	$d\sigma/dx$ (pb)	stat. (%)	sys. (%)	δ_1 (%)	δ_2 (%)	δ_3 (%)	δ_4 (%)	δ_5 (%)	δ_6 (%)	δ_7 (%)	$\delta_8 - \delta_{15}$ (%)
185	0.794×10^{-2}	8.80×10^4	± 0.7	+1.3 -1.5	+0.2 -0.2	+0.1 -0.0	+0.1 -0.3	+1.2 -0.0	+0.2 -0.5	+0.0 -1.3	+0.3 -0.3	+0.2 -0.3
	0.126×10^{-1}	5.88×10^4	± 0.7	+1.1 -2.9	+0.1 -0.1	+0.1 -0.1	+0.1 -0.2	+1.0 -0.0	+0.2 -0.8	+0.0 -2.8	+0.3 -0.3	+0.1 -0.3
	0.200×10^{-1}	3.69×10^4	± 0.7	+0.9 -0.9	+0.1 -0.1	+0.1 -0.1	+0.1 -0.0	+0.8 -0.0	+0.1 -0.6	+0.0 -0.5	+0.2 -0.2	+0.2 -0.2
	0.316×10^{-1}	2.12×10^4	± 0.7	+0.6 -0.6	+0.1 -0.0	+0.0 -0.0	+0.0 -0.0	+0.4 -0.6	+0.4 -0.6	+0.6 -0.0	+0.2 -0.2	+0.1 -0.1
	0.501×10^{-1}	1.25×10^4	± 0.7	+1.1 -0.7	+0.1 -0.1	+0.0 -0.1	+0.0 -0.0	+0.4 -0.0	+0.1 -0.6	+1.0 -0.0	+0.2 -0.2	+0.1 -0.1
	0.794×10^{-1}	6.98×10^3	± 0.7	+0.4 -1.2	+0.1 +0.1	+0.1 +0.1	+0.0 +0.0	+0.0 +0.7	-0.4 +0.1	-0.0 +0.9	-0.1 +0.1	-0.1 +0.1
	0.126	3.97×10^3	± 0.7	+2.1 -0.5	+0.1 -0.1	+0.1 -0.2	+0.0 -0.0	+1.8 -0.0	+0.0 -0.5	+0.0 +0.0	+0.2 -0.1	+0.2 +0.1
	0.200	2.09×10^3	± 0.9	+2.6 +4.5	+0.1 +0.2	+0.3 +0.0	+0.0 +0.1	+4.3 +4.3	+0.0 +0.0	-2.4 +0.0	-0.2 +1.0	-0.8 +1.0
3000	0.501×10^{-1}	1.81×10^2	± 6.1	-1.7 +2.3	-0.2 +0.1	-0.7 +0.0	-0.1 +0.3	-0.0 +2.1	-0.0 +0.0	-0.7 +0.0	-1.0 +0.7	-0.9 +0.5
	0.794	1.69×10^2	± 4.8	-1.5 +0.8	-0.1 +0.1	-0.5 +0.0	-0.3 +0.0	-0.0 +0.5	-0.0 +0.0	-0.9 +0.0	-0.7 +0.6	-0.7 +0.3
	0.126	1.28×10^2	± 4.3	-3.6 +0.9	-0.1 +0.1	-1.1 +0.0	-0.0 +0.0	+0.5 +0.0	+0.0 +0.0	-3.3 +0.0	-0.6 +0.6	-0.6 +0.7
	0.200	7.46×10^1	± 4.6	-2.6 +2.3	-0.1 +0.1	-0.7 +0.0	-0.0 +0.0	-1.2 +2.1	-0.0 +0.0	-2.0 +0.0	-0.6 +0.5	-0.6 +0.8
	0.316	3.41×10^1	± 5.3	+2.3 -2.3	+0.1 -0.1	+0.0 +0.0	+0.0 +0.0	+2.1 -0.0	+0.0 -0.0	+0.0 -2.4	+0.5 -0.5	+0.8 -0.4
	0.687	1.29	± 8.1	+2.3 -1.9	+0.3 -0.3	+0.5 -0.0	+0.0 -0.0	+0.0 -0.3	+0.0 -0.0	+0.0 -0.0	+2.4 -0.5	+0.5 -1.8

Table A.18: Systematic uncertainties for $d\sigma/dx$ ($y < 0.9$, $y(1-x)^2 > 0.004$) for $Q^2 > 185\text{GeV}^2$ and $Q^2 > 3000\text{GeV}^2$ ($\mathcal{L} = 78.8\text{pb}^{-1}$, corrected to $P_e = +0.32$). The left five columns of the table contain the Q^2 range, bin centre (x_c), the measured cross section, the statistical uncertainty and the total systematic uncertainty. The right eight columns of the table list the systematic uncertainties for $\delta_1 - \delta_7$, and the systematic uncertainties summed in quadrature for $\delta_8 - \delta_{15}$. The upper and lower uncertainties correspond to a positive or negative variation of a cut value.

$Q^2 >$ (GeV ²)	y range	y_c	$d\sigma/dy$ (pb)	N_{data}	$N_{\text{bg}}^{\text{MC}}$
185	0.00 – 0.05	0.025	$(1.65 \pm 0.01^{+0.02}_{-0.01}) \times 10^4$	44541	0.0
	0.05 – 0.10	0.075	$(8.19 \pm 0.05^{+0.10}_{-0.05}) \times 10^3$	29853	4.4
	0.10 – 0.15	0.125	$(5.73 \pm 0.04^{+0.03}_{-0.05}) \times 10^3$	20723	5.3
	0.15 – 0.20	0.175	$(4.40 \pm 0.04^{+0.02}_{-0.14}) \times 10^3$	15423	15.0
	0.20 – 0.25	0.225	$(3.66 \pm 0.03^{+0.03}_{-0.21}) \times 10^3$	12419	11.7
	0.25 – 0.30	0.275	$(2.96 \pm 0.03^{+0.03}_{-0.03}) \times 10^3$	9588	10.2
	0.30 – 0.35	0.325	$(2.58 \pm 0.03^{+0.04}_{-0.03}) \times 10^3$	8283	25.2
	0.35 – 0.40	0.375	$(2.26 \pm 0.03^{+0.03}_{-0.03}) \times 10^3$	7167	24.7
	0.40 – 0.45	0.425	$(2.01 \pm 0.03^{+0.03}_{-0.02}) \times 10^3$	6164	35.7
	0.45 – 0.50	0.475	$(1.76 \pm 0.02^{+0.05}_{-0.02}) \times 10^3$	5223	28.7
	0.50 – 0.55	0.525	$(1.56 \pm 0.02^{+0.04}_{-0.01}) \times 10^3$	4534	32.9
	0.55 – 0.60	0.575	$(1.46 \pm 0.02^{+0.04}_{-0.03}) \times 10^3$	4079	38.4
	0.60 – 0.65	0.625	$(1.31 \pm 0.02^{+0.03}_{-0.04}) \times 10^3$	3415	37.2
	0.65 – 0.70	0.675	$(1.22 \pm 0.02^{+0.05}_{-0.05}) \times 10^3$	2788	25.1
	0.70 – 0.75	0.725	$(1.13 \pm 0.02^{+0.07}_{-0.05}) \times 10^3$	2097	28.8
0.75 – 0.90	0.825	$(9.76 \pm 0.19^{+0.69}_{-0.46}) \times 10^2$	2685	58.5	
3000	0.05 – 0.10	0.075	$(3.50 \pm 0.34^{+0.05}_{-0.03}) \times 10^1$	109	0.0
	0.10 – 0.15	0.125	$(5.86 \pm 0.41^{+0.08}_{-0.14}) \times 10^1$	201	0.0
	0.15 – 0.20	0.175	$(6.38 \pm 0.43^{+0.04}_{-0.13}) \times 10^1$	225	0.0
	0.20 – 0.25	0.225	$(6.32 \pm 0.42^{+0.08}_{-0.22}) \times 10^1$	226	0.0
	0.25 – 0.30	0.275	$(5.59 \pm 0.39^{+0.03}_{-0.21}) \times 10^1$	204	0.0
	0.30 – 0.35	0.325	$(5.66 \pm 0.40^{+0.05}_{-0.14}) \times 10^1$	206	0.0
	0.35 – 0.40	0.375	$(3.90 \pm 0.33^{+0.07}_{-0.20}) \times 10^1$	142	0.0
	0.40 – 0.45	0.425	$(3.56 \pm 0.31^{+0.05}_{-0.10}) \times 10^1$	130	0.0
	0.45 – 0.50	0.475	$(3.62 \pm 0.32^{+0.14}_{-0.10}) \times 10^1$	131	0.0
	0.50 – 0.55	0.525	$(2.89 \pm 0.29^{+0.03}_{-0.14}) \times 10^1$	103	0.0
	0.55 – 0.60	0.575	$(3.19 \pm 0.30^{+0.23}_{-0.04}) \times 10^1$	112	0.0
	0.60 – 0.65	0.625	$(2.55 \pm 0.26^{+0.04}_{-0.04}) \times 10^1$	93	2.3
	0.65 – 0.70	0.675	$(2.69 \pm 0.28^{+0.05}_{-0.15}) \times 10^1$	92	0.0
	0.70 – 0.75	0.725	$(2.39 \pm 0.27^{+0.07}_{-0.18}) \times 10^1$	79	0.0
	0.75 – 0.80	0.775	$(2.17 \pm 0.26^{+0.10}_{-0.11}) \times 10^1$	71	0.0
0.80 – 0.85	0.825	$(2.16 \pm 0.26^{+0.28}_{-0.07}) \times 10^1$	68	0.6	
0.85 – 0.90	0.875	$(1.98 \pm 0.28^{+0.22}_{-0.20}) \times 10^1$	52	0.0	

Table A.19: The single differential cross section $d\sigma/dy$ ($y < 0.9$, $y(1-x)^2 > 0.004$) for $Q^2 > 185\text{GeV}^2$ and $Q^2 > 3000\text{GeV}^2$ ($\mathcal{L} = 78.8\text{pb}^{-1}$, corrected to $P_e = +0.32$). The Q^2 and bin range, bin centre (x_c) and measured cross section are shown. The first (second) error on the cross section corresponds to the statistical (systematic) uncertainties. The number of observed data events (N_{data}) and simulated background events ($N_{\text{bg}}^{\text{MC}}$) are also shown.

$Q^2 >$ (GeV ²)	y_c	$d\sigma/dy$ (pb)	stat. (%)	sys. (%)	δ_1 (%)	δ_2 (%)	δ_3 (%)	δ_4 (%)	δ_5 (%)	δ_6 (%)	δ_7 (%)	$\delta_8 - \delta_{15}$ (%)
185	0.025	1.65×10^4	± 0.5	+1.4 -0.6	+0.1 -0.1	+0.1 -0.1	+0.0 -0.0	+0.8 -0.8	+0.0 -0.6	+1.1 -1.0	+0.0 -0.0	+0.5 -0.2
	0.075	8.19×10^3	± 0.6	+1.2 -0.7	+0.1 -0.1	+0.0 -0.2	+0.0 -0.0	+0.4 -0.0	+0.3 -0.6	+1.0 -0.0	+0.1 -0.1	+0.1 -0.2
	0.125	5.73×10^3	± 0.7	+0.6 -0.9	+0.1 -0.1	+0.2 -0.2	+0.0 -0.0	+0.3 -0.0	+0.4 -0.8	+0.0 -0.3	+0.0 -0.1	+0.1 -0.1
	0.175	4.40×10^3	± 0.8	+0.5 -3.1	+0.1 -0.1	+0.1 -0.1	+0.0 -0.1	+0.4 -0.0	+0.1 -0.9	+0.0 -2.9	+0.0 -2.9	+0.1 -0.1
	0.225	3.66×10^3	± 0.9	+0.7 -5.7	+0.1 -0.1	+0.2 -0.1	+0.1 -0.0	+0.6 -0.0	+0.0 -0.6	+0.0 -5.6	+0.0 -5.6	+0.1 -0.2
	0.275	2.96×10^3	± 1.0	+1.0 -1.1	+0.1 -0.0	+0.1 -0.0	+0.1 -0.1	+0.9 -0.0	+0.2 -0.3	+0.0 -1.0	+0.0 -1.0	+0.2 -0.2
	0.325	2.58×10^3	± 1.1	+1.5 -1.2	+0.1 -0.1	+0.0 -0.0	+0.1 -0.2	+0.5 -0.0	+2.5 -0.8	+0.0 -0.9	+0.0 -0.9	+0.2 -0.3
	0.375	2.26×10^3	± 1.2	+1.5 -1.1	+0.0 -0.0	+0.2 -0.1	+0.2 -0.3	+1.0 -0.0	+1.0 -0.9	+0.0 -0.2	+0.0 -0.2	+0.3 -0.3
	0.425	2.01×10^3	± 1.3	+1.6 -1.3	+0.0 -0.1	+0.1 -0.1	+0.3 -0.4	+1.2 -0.0	+0.5 -0.5	+0.8 -0.0	+0.8 -0.5	+0.4 -0.5
	0.475	1.76×10^3	± 1.4	+1.4 -1.4	+0.0 -0.9	+0.1 -0.0	+0.0 -0.4	+0.3 -0.2	+2.5 -2.0	+0.2 -0.1	+1.6 -0.7	+0.7 -0.4
	0.525	1.56×10^3	± 1.5	+1.5 -1.5	+0.1 -0.7	+0.1 -0.0	+0.5 -0.3	+0.4 -0.0	+2.3 -0.0	+1.1 -0.9	+0.7 -0.0	+0.7 -0.5
	0.575	1.46×10^3	± 1.6	+1.6 -1.6	+0.3 -2.3	+0.3 -0.1	+0.5 -0.3	+2.5 -0.0	+0.5 -0.0	+2.5 -2.2	+0.0 -2.2	+0.0 -0.7
	0.625	1.31×10^3	± 1.7	+1.7 -1.7	+0.6 -2.8	+0.5 -0.6	+0.5 -0.6	+1.9 -0.0	+1.9 -0.1	+0.0 -2.4	+0.0 -2.4	+0.0 -0.8
	0.675	1.22×10^3	± 1.9	+1.9 -1.9	+3.8 -3.7	+1.3 -1.0	+0.2 -0.3	+3.4 -0.0	+0.1 -0.0	+0.0 -3.4	+0.0 -3.4	+0.0 -0.9
	0.725	1.13×10^3	± 2.2	+2.2 -2.2	+6.6 -4.6	+2.4 -2.1	+0.4 -1.2	+0.7 -0.7	+5.9 -0.0	+0.0 -0.1	+0.0 -3.7	+0.0 -1.1
	0.825	9.76×10^2	± 2.0	+2.0 -1.9	+7.1 -4.8	+3.1 -2.7	+0.0 -0.6	+0.8 -1.5	+6.1 -0.0	+0.2 -0.1	+0.0 -3.3	+0.0 -0.7
3000	0.075	3.50×10^1	± 9.6	+1.5 -1.0	+0.3 -0.3	+1.1 +0.0	+0.0 -0.0	+0.7 -0.0	+0.0 -0.0	+0.0 -0.1	+0.0 -0.1	+0.5 -0.8
	0.125	5.86×10^1	± 7.1	+1.3 -2.4	+0.2 -0.1	+0.0 -0.8	+0.0 -0.0	+1.0 -0.0	+0.0 -0.0	+0.0 -2.1	+0.0 -0.5	+0.7 -0.2
	0.175	6.38×10^1	± 6.7	+0.7 -2.0	+0.1 -0.2	+0.3 -0.8	+0.0 -0.0	+0.0 -0.4	+0.0 -0.1	+0.0 -0.0	+0.0 -0.6	+0.4 -1.6
	0.225	6.32×10^1	± 6.7	+1.3 -3.5	+0.2 -0.2	+0.2 -0.5	+0.0 -0.0	+1.1 -0.0	+0.0 -0.0	+0.0 -3.2	+0.0 -0.6	+0.5 -0.9
	0.275	5.59×10^1	± 7.0	+0.6 -3.8	+0.1 -0.2	+0.0 -0.5	+0.0 -0.0	+0.0 -1.9	+0.0 -0.1	+0.0 -3.2	+0.0 -0.6	+0.1 -0.5
	0.325	5.66×10^1	± 7.0	+0.8 -2.5	+0.2 -0.1	+0.2 -0.6	+0.0 -0.0	+0.0 -0.0	+0.0 -0.0	+0.0 -2.1	+0.0 -0.5	+0.6 -1.0
	0.375	3.90×10^1	± 8.4	+1.7 -5.2	+0.1 -0.1	+0.0 -0.9	+0.0 -0.0	+1.2 -0.0	+0.0 -0.0	+0.0 -5.1	+0.0 -0.5	+0.6 -0.4
	0.425	3.56×10^1	± 8.8	+1.4 -2.9	+0.1 -0.1	+0.0 -1.0	+0.0 -0.0	+0.0 -0.7	+0.0 -0.0	+0.0 -2.5	+0.0 -0.6	+0.6 -0.5
	0.475	3.62×10^1	± 8.7	+3.8 -2.7	+0.1 -0.1	+0.5 -1.1	+0.0 -0.0	+3.7 -0.0	+0.0 -0.0	+0.0 -1.8	+0.0 -0.6	+0.6 -1.7
	0.525	2.89×10^1	± 9.9	+1.1 -4.9	+0.1 -0.1	+0.0 -2.5	+0.0 -0.0	+0.0 -3.8	+0.0 -0.0	+0.0 -1.5	+0.0 -0.7	+0.7 -0.8
	0.575	3.19×10^1	± 9.4	+7.1 -1.2	+0.0 -0.1	+0.0 -0.3	+0.0 -0.0	+7.0 -0.0	+0.0 -0.1	+0.0 -0.4	+0.0 -0.7	+0.8 -0.7
	0.625	2.55×10^1	± 10.4	+5.2 -1.7	+0.1 -0.1	+1.0 -0.6	+1.3 -1.3	+3.6 -0.0	+0.0 -0.1	+1.5 -0.0	+0.8 -0.8	+3.0 -0.7
	0.675	2.69×10^1	± 10.4	+1.7 -5.7	+0.0 -0.0	+0.9 -1.1	+0.0 -0.0	+0.0 -4.4	+0.1 -0.0	+0.0 -3.2	+0.0 -0.9	+0.9 -0.8
	0.725	2.39×10^1	± 11.3	+2.8 -7.5	+0.0 -0.0	+0.0 -6.3	+0.0 -0.0	+2.5 -0.0	+0.0 -0.0	+0.0 -3.3	+0.0 -1.0	+1.0 -2.2
	0.775	2.17×10^1	± 11.9	+4.6 -5.2	+0.0 -0.1	+0.0 -2.6	+0.0 -0.0	+4.3 -0.0	+0.0 -0.1	+0.0 -4.2	+0.0 -1.1	+1.1 -1.4
	0.825	2.16×10^1	± 12.1	+12.8 -3.3	+0.1 -0.1	+0.7 -0.0	+0.5 -0.5	+11.9 -0.0	+0.0 -0.0	+0.0 -1.3	+0.0 -1.1	+1.2 -2.7
0.875	1.98×10^1	± 13.9	+11.2 -10.0	+1.5 -1.1	+0.0 -2.3	+0.0 -0.0	+7.0 -0.0	+0.0 -0.0	+8.2 -0.0	+1.1 -1.1	+2.4 -9.7	

Table A.20: Systematic uncertainties with for $d\sigma/dy$ ($y < 0.9$, $y(1-x)^2 > 0.004$) for $Q^2 > 185\text{GeV}^2$ and $Q^2 > 3000\text{GeV}^2$ ($\mathcal{L} = 78.8\text{pb}^{-1}$, corrected to $P_e = +0.32$). The left five columns of the table contain the Q^2 range, bin centre (x_c), the measured cross section, the statistical uncertainty and the total systematic uncertainty. The right eight columns of the table list the systematic uncertainties for $\delta_1 - \delta_7$, and the systematic uncertainties summed in quadrature for $\delta_8 - \delta_{15}$. The upper and lower uncertainties correspond to a positive or negative variation of a cut value.

Q^2 range (GeV ²)	Q_c^2 (GeV ²)	Asymmetry A^+ $\times 10$
185.0 – 300.0	250	0.18 ± 0.07
300.0 – 400.0	350	0.57 ± 0.14
400.0 – 475.7	440	0.59 ± 0.21
475.7 – 565.7	520	0.54 ± 0.25
565.7 – 672.7	620	0.95 ± 0.30
672.7 – 800.0	730	0.71 ± 0.30
800.0 – 1050.0	900	1.09 ± 0.27
1050.0 – 1460.0	1230	0.73 ± 0.30
1460.0 – 2080.0	1730	1.27 ± 0.38
2080.0 – 3120.0	2500	0.77 ± 0.48
3120.0 – 5220.0	3900	2.82 ± 0.63
5220.0 – 12500.0	7000	2.74 ± 0.95
12500.0 – 51200.0	22400	0.76 ± 2.96

Table A.21: The polarisation asymmetry measured using positively and negatively polarised e^+p beams ($\mathcal{L} = 78.8\text{pb}^{-1}$, $P_e = +0.32$ and $\mathcal{L} = 56.7\text{pb}^{-1}$, $P_e = -0.36$, respectively). The bin range, bin centre (Q_c^2) and measured Asymmetry A^+ are shown. Only the statistical uncertainties on the measurement are shown as systematic uncertainties are assumed to cancel.

Q^2 range (GeV ²)	Q_c^2 (GeV ²)	$d\sigma/dQ^2$ (pb/GeV ²)	N_{data}	$N_{\text{bg}}^{\text{MC}}$
185.0 – 300.0	250	$(1.06 \pm 0.00^{+0.01}_{-0.01}) \times 10^1$	67629	112.2
300.0 – 400.0	350	$(4.55 \pm 0.03^{+0.07}_{-0.03})$	19579	25.5
400.0 – 475.7	440	$(2.62 \pm 0.03^{+0.05}_{-0.04})$	8079	27.6
475.7 – 565.7	520	$(1.77 \pm 0.02^{+0.02}_{-0.05})$	5919	15.2
565.7 – 672.7	620	$(1.11 \pm 0.02^{+0.03}_{-0.03})$	4058	17.0
672.7 – 800.0	730	$(7.64 \pm 0.12^{+0.19}_{-0.25}) \times 10^{-1}$	3969	15.0
800.0 – 1050.0	900	$(4.41 \pm 0.06^{+0.09}_{-0.16}) \times 10^{-1}$	4994	19.7
1050.0 – 1460.0	1230	$(2.01 \pm 0.03^{+0.04}_{-0.05}) \times 10^{-1}$	3948	22.3
1460.0 – 2080.0	1730	$(8.25 \pm 0.17^{+0.27}_{-0.14}) \times 10^{-2}$	2485	10.9
2080.0 – 3120.0	2500	$(3.11 \pm 0.08^{+0.05}_{-0.06}) \times 10^{-2}$	1541	4.4
3120.0 – 5220.0	3900	$(8.54 \pm 0.30^{+0.15}_{-0.20}) \times 10^{-3}$	826	2.1
5220.0 – 12500.0	7000	$(1.43 \pm 0.08^{+0.02}_{-0.03}) \times 10^{-3}$	361	0.0
12500.0 – 51200.0	22400	$(1.93^{+0.35}_{-0.30} \text{ } ^{+0.11}_{-0.15}) \times 10^{-5}$	41	0.0

Table A.22: The single differential cross section $d\sigma/dQ^2$ ($y < 0.9$, $y(1-x)^2 > 0.004$) for the reaction $e^+p \rightarrow e^+X$ ($\mathcal{L} = 56.7\text{pb}^{-1}$, $P_e = -0.36$). The bin range, bin centre (Q_c^2) and measured cross section corrected to the electroweak Born level are shown. The first (second) error on the cross section corresponds to the statistical (systematic) uncertainties. The number of observed data events (N_{data}) and simulated background events ($N_{\text{bg}}^{\text{MC}}$) are also shown.

Q_c^2 (GeV ²)	$d\sigma/dQ^2$ (pb/GeV ²)	stat. (%)	sys. (%)	δ_1 (%)	δ_2 (%)	δ_3 (%)	δ_4 (%)	δ_5 (%)	δ_6 (%)	δ_7 (%)	$\delta_8 - \delta_{15}$ (%)
250	1.06×10^1	± 0.4	+0.7 -0.8	+0.2 -0.2	+0.0 -0.1	+0.1 -0.1	+0.6 -0.0	+0.3 -0.8	+0.1 -0.0	+0.0 -0.0	+0.2 -0.2
350	4.55	± 0.7	+1.6 -0.6	+0.2 -0.2	+0.0 -0.2	+0.1 -0.1	+1.1 -0.0	+0.7 -0.3	+0.7 -0.0	+0.2 -0.2	+0.3 -0.4
440	2.62	± 1.1	+2.1 -1.6	+0.2 -0.2	+0.0 -0.1	+0.2 -0.1	+1.8 -0.0	+0.7 -0.0	+0.0 -1.5	+0.5 -0.5	+0.5 -0.3
520	1.77	± 1.3	+1.2 -2.7	+0.2 -0.3	+0.1 -0.1	+0.1 -0.1	+0.9 -0.0	+0.0 -0.0	+0.0 -2.5	+0.7 -0.7	+0.3 -0.5
620	1.11	± 1.6	+2.3 -2.7	+0.3 -0.2	+0.5 -0.0	+0.2 -0.2	+1.8 -0.0	+0.1 -0.0	+0.0 -2.4	+1.2 -1.2	+0.4 -0.4
730	7.64×10^1	± 1.6	+2.4 -3.2	+0.2 -0.2	+0.2 -0.1	+0.2 -0.2	+2.1 -0.0	+0.0 -0.0	+0.0 -2.9	+0.0 -1.2	+0.3 -0.7
900	4.41×10^1	± 1.4	+2.0 -3.6	+0.2 -0.2	+0.2 -0.0	+0.2 -0.3	+1.6 -0.0	+0.0 -0.0	+0.0 -3.4	+1.2 -1.2	+0.2 -0.3
1230	2.01×10^1	± 1.6	+2.2 -2.5	+0.2 -0.1	+0.5 -0.0	+0.3 -0.3	+1.8 -0.0	+0.0 -0.0	+0.0 -2.2	+1.1 -1.1	+0.4 -0.2
1730	8.25×10^2	± 2.0	+3.3 -1.7	+0.2 -0.1	+0.1 -0.1	+0.2 -0.2	+3.1 -0.0	+0.0 -0.0	+0.0 -1.2	+1.1 -1.1	+0.4 -0.4
2500	3.11×10^2	± 2.5	+1.6 -1.8	+0.1 -0.1	+0.2 -0.0	+0.1 -0.1	+1.0 -0.0	+0.0 -0.0	+0.0 -1.4	+1.1 -1.1	+0.2 -0.4
3900	8.54×10^3	± 3.5	+1.7 -2.3	+0.1 -0.2	+0.1 -0.0	+0.1 -0.0	+1.3 -0.0	+0.0 -0.0	+0.0 -1.9	+1.1 -1.1	+0.3 -0.7
7000	1.43×10^3	± 5.3	+1.4 -2.3	+0.2 -0.2	+0.4 -0.3	+0.0 -0.3	+0.6 -0.0	+0.0 -0.0	+0.0 -1.9	+1.1 -1.0	+0.4 -0.6
22400	1.93×10^5	± 18.2 -15.6	+5.8 -7.6	+0.2 -0.2	+0.8 -0.5	+0.0 -0.0	+1.9 -0.0	+0.0 -0.0	+0.0 -3.3	+1.1 -1.0	+5.3 -6.7

Table A.23: Systematic uncertainties for $d\sigma/dQ^2$ ($y < 0.9$, $y(1-x)^2 > 0.004$) ($\mathcal{L} = 56.7\text{pb}^{-1}$, corrected to $P_e = -0.36$). The left four columns of the table contain the bin centre (Q_c^2), the measured cross section, the statistical uncertainty and the total systematic uncertainty. The right eight columns of the table list the systematic uncertainties for $\delta_1 - \delta_7$, and the systematic uncertainties summed in quadrature for $\delta_8 - \delta_{15}$. The upper and lower uncertainties correspond to a positive or negative variation of a cut value.

$Q^2 >$ (GeV ²)	x range	x_c	$d\sigma/dx$ (pb)	N_{data}	$N_{\text{bg}}^{\text{MC}}$
185	$(0.63 - 1.00) \times 10^{-2}$	0.794×10^{-2}	$(8.61 \pm 0.07^{+0.16}_{-0.16}) \times 10^4$	14173	69.1
	$(0.10 - 0.16) \times 10^{-1}$	0.126×10^{-1}	$(5.79 \pm 0.05^{+0.07}_{-0.17}) \times 10^4$	16410	50.8
	$(0.16 - 0.25) \times 10^{-1}$	0.200×10^{-1}	$(3.54 \pm 0.03^{+0.03}_{-0.03}) \times 10^4$	15901	33.4
	$(0.25 - 0.40) \times 10^{-1}$	0.316×10^{-1}	$(2.07 \pm 0.02^{+0.02}_{-0.01}) \times 10^4$	15715	12.7
	$(0.40 - 0.63) \times 10^{-1}$	0.501×10^{-1}	$(1.21 \pm 0.01^{+0.01}_{-0.01}) \times 10^4$	13656	2.3
	$(0.63 - 1.00) \times 10^{-1}$	0.794×10^{-1}	$(6.84 \pm 0.06^{+0.08}_{-0.03}) \times 10^3$	13087	2.1
	0.10 - 0.16	0.126	$(3.79 \pm 0.03^{+0.04}_{-0.01}) \times 10^3$	12219	0.7
	0.16 - 0.25	0.200	$(1.97 \pm 0.02^{+0.03}_{-0.06}) \times 10^3$	7505	0.0
3000	$(0.40 - 0.63) \times 10^{-1}$	0.501×10^{-1}	$(1.61 \pm 0.12^{+0.04}_{-0.05}) \times 10^2$	171	0.5
	$(0.63 - 1.00) \times 10^{-1}$	0.794×10^{-1}	$(1.50 \pm 0.09^{+0.05}_{-0.03}) \times 10^2$	277	1.7
	0.10 - 0.16	0.126	$(1.05 \pm 0.06^{+0.01}_{-0.05}) \times 10^2$	317	0.0
	0.16 - 0.25	0.200	$(5.81 \pm 0.36^{+0.11}_{-0.15}) \times 10^1$	259	0.0
	0.25 - 0.40	0.316	$(3.02 \pm 0.21^{+0.04}_{-0.09}) \times 10^1$	217	0.0
	0.40 - 0.75	0.687	$(1.10 \pm 0.12^{+0.04}_{-0.02})$	89	0.0

Table A.24: The single differential cross section $d\sigma/dx$ ($y < 0.9$, $y(1-x)^2 > 0.004$) for $Q^2 > 185\text{GeV}^2$ and $Q^2 > 3000\text{GeV}^2$ ($\mathcal{L} = 56.7\text{pb}^{-1}$, corrected to $P_e = -0.36$). The Q^2 and bin range, bin centre (x_c) and measured cross section are shown. The first (second) error on the cross section corresponds to the statistical (systematic) uncertainties. The number of observed data events (N_{data}) and simulated background events ($N_{\text{bg}}^{\text{MC}}$) are also shown.

$Q^2 >$ (GeV ²)	x_c	$d\sigma/dx$ (pb)	stat. (%)	sys. (%)	δ_1 (%)	δ_2 (%)	δ_3 (%)	δ_4 (%)	δ_5 (%)	δ_6 (%)	δ_7 (%)	$\delta_8 - \delta_{15}$ (%)	
185	0.794×10^{-2}	8.61×10^4	± 0.8	+1.9 -1.8 +1.3	+0.2 -0.1 +0.1	+0.1 -0.0 +0.0	+0.2 -0.2 +0.2	+1.7 -0.0 +1.2	+0.5 -1.2 +0.2	+0.0 -1.2 +0.0	+0.5 -0.5 +0.4	+0.3 -0.2 +0.1	
	0.126×10^{-1}	5.79×10^4	± 0.8	-2.9 +1.0 +0.8	-0.1 +0.1 +0.1	-0.2 +0.0 -0.1	-0.2 +0.1 -0.1	-0.0 +0.9 -0.0	-0.9 +0.2 -0.4	-2.7 +0.0 -0.5	-0.5 +0.4 -0.4	-0.3 +0.1 -0.3	
	0.200×10^{-1}	3.54×10^4	± 0.8	+0.8 -0.5 +1.1	-0.1 +0.1 +0.1	-0.1 +0.0 +0.0	-0.1 +0.0 +0.0	-0.0 +0.4 +0.8	-0.4 +0.3 -0.3	-0.5 +0.5 -0.0	-0.4 +0.3 +0.6	-0.4 +0.3 +0.3	-0.3 +0.1 +0.1
	0.316×10^{-1}	2.07×10^4	± 0.8	-0.6 +1.1 +1.1	-0.1 +0.1 +0.1	-0.0 +0.0 +0.0	-0.0 +0.0 +0.0	-0.0 +0.4 +0.8	-0.5 +0.1 -0.2	-0.0 +1.0 -0.0	-0.0 +0.2 +0.9	-0.3 +0.2 +0.2	-0.2 +0.1 +0.1
	0.501×10^{-1}	1.21×10^4	± 0.9	-0.4 +1.0 -0.3	-0.1 +0.1 -0.1	-0.2 +0.0 -0.1	-0.0 +0.0 -0.0	-0.0 +0.3 -0.0	-0.0 +0.1 -0.2	-0.0 +0.9 -0.0	-0.0 +0.2 +0.2	-0.2 +0.2 +0.2	-0.2 +0.1 +0.1
	0.794×10^{-1}	6.84×10^3	± 0.9	+1.6 -3.0 -3.0	+0.1 -0.1 -0.0	+0.0 -0.0 -0.0	+0.0 -0.0 -0.0	+1.5 +0.1 -0.5	+0.1 +0.0 -2.5	+0.0 +0.0 -2.5	+0.0 +0.0 -0.2	+0.2 +0.2 -0.2	+0.6 +0.6 -1.6
		0.126	3.79×10^3	± 0.9	+1.0 -0.3 +1.6	+0.1 -0.1 +0.1	+0.0 -0.1 +0.0	+0.0 -0.0 +0.0	+0.3 -0.0 +1.5	+0.1 -0.2 +0.1	+0.9 -0.0 +0.0	+0.2 -0.2 +0.2	+0.1 -0.2 +0.6
		0.200	1.97×10^3	± 1.2	-3.0 -2.7 -2.9	-0.1 +0.2 -0.2	-0.0 +0.7 -1.2	-0.0 +0.1 -0.1	-0.0 +1.9 -0.0	-0.5 +0.0 -0.0	-2.5 +0.0 -0.8	-0.2 +1.6 -1.6	-1.6 +0.5 -1.9
	3000	0.501×10^{-1}	1.61×10^2	± 7.6	+3.4 -1.8 +1.2	+0.1 -0.1 +0.1	+0.1 -0.0 +0.3	+0.3 -0.3 +0.0	+3.0 -0.0 +0.0	+0.0 -0.0 +0.0	+0.0 -0.9 +0.0	+1.3 -1.3 +1.0	+1.1 -0.7 +0.6
		0.794	1.50×10^2	± 6.0	-4.8 +1.9 -2.6	-0.1 +0.1 -0.1	-0.1 +0.2 -0.1	-0.0 +0.0 -0.0	-3.1 +1.6 -0.0	-0.0 +0.0 -2.0	-3.4 +0.0 +0.0	-1.0 +0.9 -0.9	-1.3 +0.4 -1.4
0.126		1.05×10^2	± 5.6	+1.3 -1.3 +3.5	+0.1 -0.1 +0.3	+0.3 +0.8 -0.0	+0.0 +0.0 -0.0	+0.0 +0.0 -1.3	+0.0 +0.0 -0.0	+0.0 +0.0 -2.5	+0.0 +0.8 -0.8	+1.0 +0.8 -0.5	
0.200		5.81×10^1	± 6.2	+3.5 -2.1 -0.3	+0.3 -0.3 -0.4	+0.4 -0.4 -0.0	+0.0 -0.0 -0.0	+3.3 -0.0 -0.0	+0.0 +0.1 -0.0	+0.1 +0.1 -0.0	+0.8 +0.8 -0.7	+1.0 +1.0 -1.9	
0.316		3.02×10^1	± 6.8	-2.1 -0.2 +0.3	-0.3 -0.2 +0.4	-0.4 -0.0 +0.0	-0.0 +0.0 +0.0	-0.0 -1.3 +3.3	-0.0 +0.0 +0.1	-0.0 -2.5 +0.1	-0.0 +0.8 +0.1	-0.7 +0.8 +0.8	
0.687		1.10	± 10.6	-2.1 -0.2 +0.3	-0.3 -0.2 +0.4	-0.4 -0.0 +0.0	-0.0 +0.0 +0.0	-0.0 -1.3 +3.3	-0.0 +0.0 +0.1	-0.0 -2.5 +0.1	-0.0 +0.8 +0.1	-0.7 +0.8 +0.8	

Table A.25: Systematic uncertainties for $d\sigma/dx$ ($y < 0.9$, $y(1-x)^2 > 0.004$) for $Q^2 > 185\text{GeV}^2$ and $Q^2 > 3000\text{GeV}^2$ ($\mathcal{L} = 56.7\text{pb}^{-1}$, corrected to $P_e = -0.36$). The left five columns of the table contain the Q^2 range, bin centre (x_c), the measured cross section, the statistical uncertainty and the total systematic uncertainty. The right eight columns of the table list the systematic uncertainties for $\delta_1 - \delta_7$, and the systematic uncertainties summed in quadrature for $\delta_8 - \delta_{15}$. The upper and lower uncertainties correspond to a positive or negative variation of a cut value.

$Q^2 >$ (GeV ²)	y range	y_c	$d\sigma/dy$ (pb)	N_{data}	$N_{\text{bg}}^{\text{MC}}$
185	0.00 – 0.05	0.025	$(1.60 \pm 0.01^{+0.02}_{-0.01}) \times 10^4$	30773	0.0
	0.05 – 0.10	0.075	$(7.98 \pm 0.06^{+0.09}_{-0.04}) \times 10^3$	20679	3.0
	0.10 – 0.15	0.125	$(5.53 \pm 0.05^{+0.03}_{-0.04}) \times 10^3$	14221	6.3
	0.15 – 0.20	0.175	$(4.34 \pm 0.04^{+0.03}_{-0.14}) \times 10^3$	10814	9.7
	0.20 – 0.25	0.225	$(3.55 \pm 0.04^{+0.03}_{-0.20}) \times 10^3$	8555	8.1
	0.25 – 0.30	0.275	$(2.89 \pm 0.04^{+0.05}_{-0.05}) \times 10^3$	6666	7.6
	0.30 – 0.35	0.325	$(2.47 \pm 0.03^{+0.04}_{-0.04}) \times 10^3$	5636	19.4
	0.35 – 0.40	0.375	$(2.24 \pm 0.03^{+0.01}_{-0.03}) \times 10^3$	5035	19.1
	0.40 – 0.45	0.425	$(1.95 \pm 0.03^{+0.04}_{-0.02}) \times 10^3$	4238	26.9
	0.45 – 0.50	0.475	$(1.68 \pm 0.03^{+0.06}_{-0.02}) \times 10^3$	3538	21.8
	0.50 – 0.55	0.525	$(1.52 \pm 0.03^{+0.04}_{-0.02}) \times 10^3$	3127	21.5
	0.55 – 0.60	0.575	$(1.38 \pm 0.03^{+0.04}_{-0.04}) \times 10^3$	2715	25.8
	0.60 – 0.65	0.625	$(1.26 \pm 0.03^{+0.06}_{-0.04}) \times 10^3$	2308	25.8
	0.65 – 0.70	0.675	$(1.18 \pm 0.03^{+0.03}_{-0.05}) \times 10^3$	1883	10.5
	0.70 – 0.75	0.725	$(1.11 \pm 0.03^{+0.07}_{-0.05}) \times 10^3$	1445	19.5
0.75 – 0.90	0.825	$(9.24 \pm 0.22^{+0.86}_{-0.46}) \times 10^2$	1748	45.3	
3000	0.05 – 0.10	0.075	$(2.99 \pm 0.37^{+0.09}_{-0.04}) \times 10^1$	65	0.0
	0.10 – 0.15	0.125	$(5.21 \pm 0.47^{+0.15}_{-0.14}) \times 10^1$	125	0.0
	0.15 – 0.20	0.175	$(5.33 \pm 0.46^{+0.15}_{-0.07}) \times 10^1$	132	0.0
	0.20 – 0.25	0.225	$(4.73 \pm 0.43^{+0.09}_{-0.25}) \times 10^1$	119	0.0
	0.25 – 0.30	0.275	$(4.19 \pm 0.40^{+0.06}_{-0.15}) \times 10^1$	108	0.0
	0.30 – 0.35	0.325	$(4.47 \pm 0.42^{+0.07}_{-0.12}) \times 10^1$	115	0.0
	0.35 – 0.40	0.375	$(3.54 \pm 0.37^{+0.21}_{-0.26}) \times 10^1$	91	0.0
	0.40 – 0.45	0.425	$(3.24 \pm 0.35^{+0.04}_{-0.19}) \times 10^1$	84	0.0
	0.45 – 0.50	0.475	$(3.61 \pm 0.37^{+0.06}_{-0.24}) \times 10^1$	93	0.0
	0.50 – 0.55	0.525	$(2.77 \pm 0.33^{+0.06}_{-0.07}) \times 10^1$	70	0.0
	0.55 – 0.60	0.575	$(2.64 \pm 0.33^{+0.31}_{-0.06}) \times 10^1$	66	0.0
	0.60 – 0.65	0.625	$(2.26 \pm 0.29^{+0.16}_{-0.06}) \times 10^1$	59	1.7
	0.65 – 0.70	0.675	$(1.72^{+0.31}_{-0.27} \text{ } ^{+0.07}_{-0.09}) \times 10^1$	42	0.0
	0.70 – 0.75	0.725	$(2.32 \pm 0.31^{+0.05}_{-0.11}) \times 10^1$	55	0.0
	0.75 – 0.80	0.775	$(2.05 \pm 0.30^{+0.19}_{-0.14}) \times 10^1$	48	0.0
0.80 – 0.85	0.825	$(1.55^{+0.31}_{-0.26} \text{ } ^{+0.27}_{-0.07}) \times 10^1$	35	0.5	
0.85 – 0.90	0.875	$(1.87^{+0.37}_{-0.32} \text{ } ^{+0.19}_{-0.12}) \times 10^1$	35	0.0	

Table A.26: The single differential cross section $d\sigma/dy$ ($y < 0.9$, $y(1-x)^2 > 0.004$) for $Q^2 > 185\text{GeV}^2$ and $Q^2 > 3000\text{GeV}^2$ ($\mathcal{L} = 56.7\text{pb}^{-1}$, corrected to $P_e = -0.36$). The Q^2 and bin range, bin centre (x_c) and measured cross section are shown. The first (second) error on the cross section corresponds to the statistical (systematic) uncertainties. The number of observed data events (N_{data}) and simulated background events ($N_{\text{bg}}^{\text{MC}}$) are also shown.

$Q^2 >$ (GeV ²)	y_c	$d\sigma/dy$ (pb)	stat. (%)	sys. (%)	δ_1 (%)	δ_2 (%)	δ_3 (%)	δ_4 (%)	δ_5 (%)	δ_6 (%)	δ_7 (%)	$\delta_8 - \delta_{15}$ (%)
185	0.025	1.60×10^4	± 0.6	+1.3 -0.4	+0.1 -0.1	+0.0 -0.1	+0.0 -0.0	+0.6 -0.2	+0.1 -0.2	+1.1 -0.0	+0.0 -0.1	+0.4 -0.3
	0.075	7.98×10^3	± 0.7	+1.2 -0.5	+0.1 -0.1	+0.0 -0.0	+0.0 -0.0	+0.3 -0.0	+0.2 -0.4	+1.1 -0.0	+0.1 -0.1	+0.1 -0.1
	0.125	5.53×10^3	± 0.8	+0.5 -0.7	+0.1 -0.1	+0.0 -0.2	+0.0 -0.0	+0.3 -0.0	+0.4 -0.6	+0.0 -0.2	+0.0 -0.2	+0.2 -0.2
	0.175	4.34×10^3	± 1.0	+0.6 -3.2	+0.1 -0.1	+0.1 -0.2	+0.0 -0.1	+0.5 -0.0	+0.2 -1.3	+0.0 -2.9	+0.2 -0.2	+0.1 -0.4
	0.225	3.55×10^3	± 1.1	+0.8 -5.6	+0.1 -0.0	+0.0 -0.2	+0.0 -0.0	+0.7 -0.0	+0.2 -0.5	+0.0 -5.6	+0.3 -0.2	+0.3 -0.1
	0.275	2.89×10^3	± 1.2	+1.6 -1.9	+0.0 -0.1	+0.2 -0.2	+0.1 -0.0	+1.5 -0.0	+0.3 -1.6	+0.0 -0.9	+0.4 -0.3	+0.2 -0.2
	0.325	2.47×10^3	± 1.3	+1.6 -1.4	+0.1 -0.0	+0.2 -0.1	+0.2 -0.1	+1.4 -0.0	+0.5 -0.9	+0.0 -0.9	+0.4 -0.4	+0.2 -0.4
	0.375	2.24×10^3	± 1.4	+1.4 -1.4	+0.0 -0.0	-0.3 -0.3	-0.2 -0.2	-0.0 -0.0	-1.2 -1.2	-0.2 -0.2	-0.5 -0.5	-0.1 -0.1
	0.425	1.95×10^3	± 1.6	+2.0 -1.5	+0.0 -0.0	+0.2 -0.2	+0.3 -0.3	+1.1 -0.0	+1.3 -0.0	+0.8 -0.0	+0.7 -0.7	+0.2 -0.7
	0.475	1.68×10^3	± 1.7	+1.7 -1.7	+0.1 -0.0	+0.1 -0.0	+0.3 -0.0	+2.3 -2.5	+1.6 -0.0	+1.7 -0.0	+0.8 -0.0	+0.4 -0.4
	0.525	1.52×10^3	± 1.8	+1.8 -1.8	+0.1 -0.0	+0.4 -0.4	+0.3 -0.4	+2.5 -0.0	+0.7 -0.1	+0.7 -0.0	+1.0 -1.0	+0.5 -0.4
	0.575	1.38×10^3	± 1.8	+1.8 -1.9	+0.2 -2.6	+0.3 -0.2	+0.5 -0.3	+2.8 -0.0	+0.1 -0.0	+0.0 -2.2	+1.3 -1.1	+0.6 -0.5
	0.625	1.26×10^3	± 1.9	+1.9 -2.1	+0.3 -0.7	+0.4 -0.0	+0.6 -0.5	+4.6 -0.0	+0.0 -0.1	+0.0 -2.3	+1.4 -1.4	+0.6 -1.1
	0.675	1.18×10^3	± 2.0	+2.0 -2.3	+0.7 -4.3	+1.3 -1.2	+0.1 -0.0	+0.9 -0.2	+0.0 -0.1	+0.0 -3.5	+0.0 -1.7	+0.7 -1.6
	0.725	1.11×10^3	± 2.1	+2.1 -2.3	+0.7 -4.3	+1.3 -1.2	+0.1 -0.0	+0.9 -0.2	+0.0 -0.1	+0.0 -3.5	+0.0 -1.7	+0.7 -1.6
	0.775	1.11×10^3	± 2.1	+2.1 -2.3	+0.7 -4.3	+1.3 -1.2	+0.1 -0.0	+0.9 -0.2	+0.0 -0.1	+0.0 -3.5	+0.0 -1.7	+0.7 -1.6
0.825	9.24×10^2	± 2.2	+2.2 -2.4	+0.7 -4.9	+1.3 -2.7	+0.1 -0.0	+0.9 -1.3	+0.0 -0.0	+0.0 -3.5	+0.0 -1.4	+0.7 -0.9	
3000	0.075	2.99×10^1	± 12.4	+3.1 -4.9	+0.3 -2.7	+1.4 -0.0	+0.0 -1.3	+2.3 -0.0	+0.0 -0.0	+0.0 -3.5	+0.0 -1.4	+1.2 -0.9
	0.125	5.21×10^1	± 8.9	+0.9 -2.8	+0.2 -0.2	+0.4 -1.1	+0.0 -0.0	+0.2 -0.0	+0.0 -0.1	+0.0 -2.1	+0.0 -0.7	+0.2 -1.2
	0.175	5.33×10^1	± 8.7	+2.8 -1.4	+0.1 -0.1	+2.0 -0.4	+0.0 -0.0	+1.7 -0.0	+0.0 -0.0	+0.1 -0.0	+0.8 -0.8	+0.4 -1.0
	0.225	4.73×10^1	± 9.2	+1.9 -5.3	+0.1 -0.2	+1.1 -0.0	+0.0 -0.0	+0.0 -4.0	+0.0 -0.0	+0.0 -3.2	+0.8 -0.9	+1.3 -0.9
	0.275	4.19×10^1	± 9.6	+1.5 -3.5	+0.1 -0.2	+0.0 -0.0	+0.0 -0.0	+0.2 -0.0	+0.0 -0.0	+0.0 -3.4	+0.9 -0.9	+1.2 -0.9
	0.325	4.47×10^1	± 9.3	+1.5 -2.7	+0.1 -0.1	+0.2 -0.0	+0.0 -0.0	+0.0 -0.5	+0.0 -0.0	+0.0 -2.1	+1.0 -1.0	+1.3 -1.3
	0.375	3.54×10^1	± 10.5	+1.7 -5.9	+0.1 -0.1	+0.2 -1.0	+0.0 -0.0	+0.0 -0.7	+0.0 -0.0	+0.0 -5.1	+0.0 -1.0	+1.0 -2.4
	0.425	3.24×10^1	± 10.9	+1.3 -6.0	+0.1 -0.1	+0.2 -0.1	+0.0 -0.0	+0.0 -4.8	+0.0 -0.0	+0.0 -2.4	+0.0 -1.1	+0.7 -2.4
	0.475	3.61×10^1	± 10.4	+1.7 -6.6	+0.1 -0.1	+0.2 -0.1	+0.0 -0.0	+0.0 -6.2	+0.0 -0.0	+0.0 -1.8	+0.0 -1.2	+1.2 -0.3
	0.525	2.77×10^1	± 12.0	+2.0 -2.6	+0.0 -0.1	+0.3 -0.1	+0.0 -0.0	+1.4 -0.0	+0.0 -0.0	+0.0 -1.8	+0.0 -1.2	+0.8 -0.3
	0.575	2.64×10^1	± 12.3	+1.5 -2.2	+0.1 -0.1	+0.0 -1.4	+0.0 -0.0	+0.0 -0.0	+0.0 -0.0	+0.0 -0.5	+1.0 -1.3	+1.7 -1.0
	0.625	2.26×10^1	± 13.0	+7.0 -2.6	+0.1 -0.1	+1.7 -0.0	+1.4 -1.4	+5.8 -0.0	+0.0 -0.0	+1.5 -0.0	+1.4 -1.4	+2.4 -1.7
	0.675	1.72×10^1	± 13.5	+17.9 -15.7	+4.1 -5.0	+0.0 -0.0	+3.4 -0.2	+0.0 -0.0	+1.6 -0.0	+0.0 -0.0	+0.0 -3.4	+1.5 -1.4
	0.725	2.32×10^1	± 13.5	+2.0 -4.6	+0.0 -0.0	+1.0 -0.0	+0.0 -0.0	+0.3 -0.0	+0.0 -0.0	+0.0 -3.4	+0.0 -1.6	+0.6 -2.6
	0.775	2.05×10^1	± 14.4	+9.3 -6.7	+0.1 -0.1	+0.0 -0.1	+0.0 -0.0	+0.0 -0.0	+9.1 -0.0	+0.0 -4.3	+0.0 -1.7	+1.1 -1.8
	0.825	1.55×10^1	± 14.4	+19.9 -16.8	+17.5 -4.5	+0.1 -0.1	+3.5 -1.4	+0.7 -0.7	+16.7 -0.0	+0.0 -0.0	+0.0 -1.1	+1.8 -1.8
0.875	1.87×10^1	± 14.4	+19.8 -17.1	+10.2 -6.5	+1.4 -1.1	+2.2 -2.4	+0.0 -0.0	+4.1 -0.0	+0.0 -0.1	+8.2 -0.0	+1.7 -1.7	

Table A.27: Systematic uncertainties with for $d\sigma/dy$ ($y < 0.9$, $y(1-x)^2 > 0.004$) for $Q^2 > 185\text{GeV}^2$ and $Q^2 > 3000\text{GeV}^2$ ($\mathcal{L} = 56.7\text{pb}^{-1}$, corrected to $P_e = -0.36$). The left five columns of the table contain the Q^2 range, bin centre (x_c), the measured cross section, the statistical uncertainty and the total systematic uncertainty. The right eight columns of the table list the systematic uncertainties for $\delta_1 - \delta_7$, and the systematic uncertainties summed in quadrature for $\delta_8 - \delta_{15}$. The upper and lower uncertainties correspond to a positive or negative variation of a cut value.

Bibliography

- [1] ZEUS Collab., S. Chekanov et al., *Measurement of High- Q^2 Neutral Current Deep Inelastic e^-p Scattering Cross Sections with a Longitudinally Polarised Electron Beam at HERA*, Eur. Phys. J C 62, 625 (2008).
- [2] Fukuda, Y., et al., *Measurements of the Solar Neutrino Flux from Super-Kamiokande's First 300 Days*, Phys. Rev. Lett. 81 (6), 1158 (1998).
- [3] Q. R. Ahmad et al., *Direct Evidence for Neutrino Flavor Transformation from Neutral-Current Interactions in the Sudbury Neutrino Observatory*, Phys. Rev. Lett. 89, 011301 (2002).
- [4] W. Prout, *On the relation between the specific gravities of bodies in their gaseous state and the weights of their atoms*, Annals of Philosophy, 6 321 (1815).
- [5] N. Lockyer, *The Chemistry of the Sun*, Macmillan and co., (1887).
- [6] W. Crookes, *The Bakerian Lecture: On the Illumination of Lines of Molecular Pressure, and the Trajectory of Molecules*, Phil. Trans. R. Soc. 170, 135 (1879).
- [7] J.J. Thomson, *On the Structure of the Atom: an Investigation of the Stability and Periods of Oscillation of a number of Corpuscles arranged at equal intervals around the Circumference of a Circle; with Application of the Results to the Theory of Atomic Structure*, Cambridge Philosophical Magazine Series 6 7, 237 (1904).
- [8] H. Geiger and E. Marsden, *On a Diffuse Reflection of the α -Particle*, Proc. R. Soc. A82, 495 (1909).

- [9] E. Rutherford, *The Scattering of α Particles by Matter and the Structure of the Atom*, Phil. Mag. 6, 21 (1911).
- [10] J. Chadwick, *Possible Existence of a Neutron*, Nature 129, 312 (1932)
- [11] R. W. McAllister, R. Hofstadter, *Elastic Scattering of 188-Mev Electrons from the Proton and the Alpha Particle*, Phys. Rev. 102, 851 (1956).
- [12] M. Gell-Mann, *A schematic model of baryons and mesons*, Phys. Lett., 8 (3), 214 (1964).
- [13] E.D. Bloom et al., *High-Energy inelastic e-p scattering at 6 and 10 degrees*, Phys. Rev. Lett. 23 (16) 930 (1969).
- [14] M. Breidenbach, J. I. Friedman, and H. W. Kendall, *Observed Behavior of Highly Inelastic Electron-Proton Scattering*, Phys. Rev. Lett. 23, 935 (1969)
- [15] K. Nakamura et al. (Particle Data Group), *The Review of Particle Physics*, J. Phys. G 37, 075021 (2010).
- [16] F. Halzen, A. D. Martin, *Quarks and Leptons: An introductory course in modern particle physics*, John Wiley & sons (1984).
- [17] J. D. Bjorken, *Asymptotic Sum Rules at Infinite Momentum*, Phys. Rev. 179, 1547 (1969)
- [18] J. I. Friedman, H. W. Kendall, *Deep inelastic electron scattering*, Ann. Rev. Nucl. Part. Sci. 22 203 (1972).
- [19] R. P. Feynman, *Very High-Energy Collisions of Hadrons*, Phys. Rev. Lett. 23 1415 (1969)
- [20] J. D. Bjorken, E. A. Paschos, *Inelastic Electron-Proton and γ -Proton Scattering and the Structure of the Nucleon*, Phys. Rev. 185 (5) 1975 (1969).
- [21] C. G. Callan, D. J. Gross, *High-Energy Electroproduction and the Constitution of the Electric Current*, Phys. Rev. Lett. 22 156 (1969).

- [22] A. Bodek et al., *Experimental studies of the neutron and proton structure functions*, Phys. Rev. D *20* 1471 (1979).
- [23] T. Eichten et al., *Measurement of the neutrino-nucleon and antineutrino-nucleon total cross sections*, Phys. Lett. B *46* 281 (1973).
- [24] TASSO Collab., R. Brandelik et al., *Evidence for Planar Events in e+e- Annihilation at High Energies*, Phys. Lett. B *86* 243 (1979).
- [25] MARK J Collab., D. Barber et al., *Discovery of Three-Jet Events and a Test of Quantum Chromodynamics at PETRA*, Phys. Rev. Lett. *43* 830 (1979).
- [26] JADE Colla., W. Bartel et al., *Observation of planar three-jet events in e+e- annihilation and evidence for gluon bremsstrahlung*. Phys. Lett. B *91* 142 (1980).
- [27] PLUTO Collab., C. Berger et al., *Evidence for gluon bremsstrahlung in e+e- annihilations at high energies*. Phys. Lett. B *86* 418 (1979).
- [28] R. Devenish, A. Cooper-Sarkar, *Deep Inelastic Scattering*, Oxford University Press (2004).
- [29] V. N. Gribov, L. N. Lipatov, *Deep inelastic e p scattering in perturbation theory*, Sov. J. Nucl. Phys. *15* 438 (1972).
- [30] Yu. L. Dokshitzer, *Calculation of the Structure Functions for Deep Inelastic Scattering and e+ e- Annihilation by Perturbation Theory in Quantum Chromodynamics*, Sov. Phys. JETP *46* 641 (1977).
- [31] G. Altarelli, G. Parisi, *Asymptotic Freedom in Parton Language*, Nucl. Phys. B *126* 298 (1977).
- [32] D. J. Gross, C. H. Llewellyn-Smith, *High-energy neutrino-nucleon scattering, current algebra and partons*, Phys. Rev. Lett. *80* (17) 3715 (1969).
- [33] CTEQ Collab., Hung-Liang Lai et. al., *New parton distributions for collider physics*, Phys.Rev.D *82* 074024 (2010).

- [34] MRST Collab., A. D. Martin et. al., *Parton distributions for the LHC*, Eur.Phys.J.C 63 189 (2009).
- [35] H1 and ZEUS Collaboration, F.D. Aaron et al., *Combined Measurement and QCD Analysis of the Inclusive e^+p Scattering Cross Sections at HERA*, JHEP 1001 109 (2010).
- [36] S.L. Glashow, *Partial Symmetries of Weak Interactions*, Nucl.Phys. 22 579 (1961).
- [37] S. Weinberg, *A Model of Leptons*, Phys. Rev. Lett. 19 1264 (1967).
- [38] P.W. Higgs, *Broken Symmetries and the Masses of Gauge Bosons*, Phys. Rev. Lett. 13 16 508 (1964).
- [39] F.J. Hasert et al., *Search For Elastic Muon-Neutrino Electron Scattering*, Phys. Lett. B 46 121 (1973).
- [40] UA1 Collab., G. Arnison et. al., *Further evidence for charged intermediate vector bosons at the SPS collider*
- [41] UA2 Collab., M. Banner et al., *Observation of Single Isolated Electrons of High Transverse Momentum in Events with Missing Transverse Energy at the CERN anti- $p p$ Collider*, Phys. Lett. B 122 476 (1983).
- [42] UA1 Collab., G. Arnison et. al., *Experimental Observation of Lepton Pairs of Invariant Mass Around 95-GeV/c² at the CERN SPS Collider*, Phys. Lett. B 126 398 (1983).
- [43] UA2 Collab., M. Banner et al., *Evidence for $Z_0 \rightarrow e^+ e^-$ at the CERN anti- $p p$ Collider.*, Phys. Lett. B 129 130 (1983).
- [44] *HERA - A proposal for a large electron proton colliding beam facility at DESY*, DESY Report HERA 81-10, Hamburg, Germany (1981).

- [45] G. Hemmie J. R. Maidment, *DESY III, The New Proton Injector for HERA*, 12th IEEE Particle Accelerator Conference (1987).
- [46] H1 Collab., *The H1-Detector at HERA*, Status Report (unpublished), DESY (1996), available on <http://www-h1.desy.de/h1/www/h1det/detpaper/contents.html>
- [47] Zeus Collab., U. Holm (ed.), *The ZEUS Detector*, Status Report (unpublished) (1993), available on <http://www-zeus.desy.de/bluebook/bluebook.html>
- [48] M. Minty, *Summary of Recent High Luminosity Experiments after the HERA-II Luminosity Upgrade and Future Prospects*, HERA-03-25 Internal Report (2003).
- [49] U. Schneekloth (ed.), *The HERA Luminosity Upgrade*, DESY-HERA-98-05 Internal Report (1998).
- [50] A. A. Sokolov, I. M. Ternov, *On polarization and spin effects in the theory of synchrotron radiation*, Sov. Phys. Dokl. 8 1203 (1964).
- [51] A. W. Chao, *POLARIZATION OF A STORED ELECTRON BEAM*, SLAC-PUB-2781 Internal Report/Lecture given in the 1981 Summer School on High Energy Particle Accelerators (1981).
- [52] D. P. Barber et. al., *The first achievement of longitudinal spin polarization in high energy electron storage ring*, Phys. Lett. B 343 436 (1995).
- [53] S. R. Mane, Y. M. Shatunov, K. Yokoya, *Spin-polarized charged particle beams in high-energy accelerators*, Reports on Progress in Physics, 68 1997 (2005).
- [54] D. Möhl, B.W. Montague, *Depolarisation in large electron storage rings*, Nuclear Instruments and Methods 137 3 423 (1976).
- [55] R. F. Schwitters, *Spin Motion in e^+e^- Storage Rings*, SLAC-PUB-1348 Internal Report (1973).

- [56] D. P. Barber et al., *The HERA polarimeter and the first observation of electron spin polarisation at HERA*, Nucl. Instrum. Meth. A *329* 79 (1993).
- [57] M. Beckmann et al., *The longitudinal polarimeter at HERA*, Nucl. Instrum. Meth. A *479* 334 (2002).
- [58] F. Lipps, H. A. Tolhoek, *Polarization phenomena of electrons and photons. II: Results for Compton scattering*, Physica *20* 85 and 385 (1954).
- [59] [A. Polini et al., *The design and performance of the ZEUS Micro Vertex detector*, Nucl. Instrum. Meth. A *581* 656 (2007).
- [60] N. Harnew et al., *Vertex triggering using time difference measurements in the ZEUS Central Tracking Detector*, Nucl. Inst. Meth. A *279* 290 (1989).
- [61] B. Foster et al., *The design and construction of the ZEUS central tracking detector*, Nucl. Inst. Meth. A *338* 254 (1994).
- [62] J. A. Kadyk, *Wire chamber aging*, *300* 3 436 (1991). John A. Kadyk
- [63] B. Foster, et. al., *The performance of the ZEUS central tracking detector z-by-timing electronics in a transputer based data acquisition system*, Nucl. Phys. B (Proc Suppl.) *32* 181 (1993).
- [64] R.Hall-Wilton, N.McCubbin, P.Nylander, M.Sutton, M.Wing, *The CTD Tracking Resolution*, ZEUS-NOTE 99-024 Internal Report (1999).
- [65] F. Barreiro et al., *Design, construction and test results of the ZEUS forward tracking detector*, Nucl. Inst. Meth. A *344* 335 (1994).
- [66] ZEUS Collab., *A Straw-Tube Tracker for ZEUS*, ZEUS-NOTE 98-046 Internal Report (1998).
- [67] F. Karstens, A. Stifoutkin, J. Tandler, *Performance tests of the ZEUS straw-tube tracker*, Nuclear Science Symposium Conference Record IEEE *2* 1122 (2005)

- [68] M. Derrick et. al, *Design and construction of the ZEUS barrel calorimeter*, Nucl. Inst. Meth. A 309 77 (1991).
- [69] A. Andresen et. al., *Construction and beam test of the ZEUS forward and rear calorimeter*, Nucl. Inst. Meth. A 309 101 (1991).
- [70] B. Bernstein et. al., *Beam tests of the ZEUS barrel calorimeter*, Nucl. Inst. Meth. A 336 23 (1993).
- [71] A. Dwurazni et. al., *Experimental study of electron-hadron separation in calorimeters using silicon diodes*, Nucl. Inst. Meth. A 277 176 (1989).
- [72] ZEUS Collab., *Measurement of w photoproduction at HERA* Z. Phys. C 73 73 (1996).
- [73] A. Bamberger, et al., *The Presampler for the Forward and Rear Calorimeter in the ZEUS Detector*, Nucl. Inst. Meth. A 382 419 1996
- [74] H. Bethe, W. Heitler, *On the Stopping of Fast Particles and on the Creation of Positive Electrons*, Proc. Roy. Soc. A 146 83 (1934).
- [75] J. Andruszkow et. al., *Luminosity Measurement in the ZEUS Experiment*, Acta Physica Polonica B 32 7-8 2025 (2001).
- [76] M. Helbich et. al., *The Spectrometer System for Measuring ZEUS Luminosity at HERA*, ZEUS-NOTE 06-002 Internal Report (2006).
- [77] R. Carlin et. al., *The trigger of ZEUS, a flexible system for a high bunch crossing rate collider*, Nucl. Inst. Meth. A 379 542 (1996).
- [78] M. Moritz, *Measurement of the High Q^2 Neutral Current DIS Cross Section at HERA*, Ph.D Thesis, Universitat Hamburg, DESY-THESIS-02-009 (2001).
- [79] J. Goncalo, *Measurement of the high- Q^2 neutral current deep inelastic scattering cross sections with the ZEUS detector at HERA*, DESY-THESIS-03-022 (2003).

- [80] G. A. Schuler and H. Spiesberger, *DJANGO: The interface for the event generators for HERACLES and LEPTO.*, Proceedings, Physics at HERA, vol. 3 1419 (1991).
- [81] H. Spiesberger, *An Event Generator for ep Interactions at HERA Including Radiative Processes (Version 4.6)*, available on <http://www.desy.de/hspiesb/heracles.html> (1996).
- [82] G. Zech, *Comparing Statistical Data to Monte Carlo Simulation: Parameter Fitting and Unfolding*, DESY-95-113 (1995).
- [83] L. Lonnblad, *ARIADNE version 4 - a program for simulation of QCD cascades implementing the colour dipole model*, Comp. Phys. Comm. 71, 15 (1992).
- [84] G. Ingelman, A. Edin and J. Rathsmann, *LEPTO 6.5 - A Monte Carlo Generator for Deep Inelastic Lepton-Nucleon Scattering*, Comp. Phys. Comm. 101, 108 (1997).
- [85] T. Sjostrand, *The Lund Monte Carlo for jet fragmentation and e^+e^- physics: JETSET VERSION 6.2*, Comp. Phys. Comm. 39, 347 (1986).
- [86] J. Jung, *Hard diffractive scattering in high energy ep collisions and the Monte-Carlo generator RAPGAP*, Comp. Phys. Comm. 39, 347 (1986).
- [87] G. Marchesini, et. al., *Herwig 5.1 - a Monte Carlo event generator for simulating hadron emission reactions with interfering gluons*, Comp. Phys. Comm. 67, 465 (1992).
- [88] C. Catterall, *Understanding MOZART*, available at <http://www-zeus.desy.de/lectures>.
- [89] CERN Application Software Group, *GEANT Detector description and simulation tool. CERN Program Library Long Writeup W5013*, available on <http://wwwasdoc.web.cern.ch/wwwasdoc/>.

- [90] B. Straub, *Introduction to orange*, available at <http://www-zeus.desy.de/lectures>.
- [91] ROOT development team, *ROOT - and object-oriented data analysis framework*, available at <http://root.cern.ch>.
- [92] S. Bentvelsen, J. Engelen and P. Kooijman, *Reconstruction of (x, Q^2) and extraction of structure functions in neutral current scattering at HERA.*, NIKHEF-H-92-02, Published in DESY HERA Workshop, 23 (1992).
- [93] Y. Ri, *Measurement of neutral current deep inelastic e-p scattering cross sections with longitudinally polarized electrons with ZEUS at HERA* Ph.D Thesis (2009).
- [94] G. F. Hartner, *VTRACK Briefing: Program and math (unpublished)*, ZEUS-NOTE 98-058, Internal report (1998).
- [95] A. Spiridonov, *Mathematical Framework for Fast and Rigorous Track Fit for the ZEUS Detector*, ZEUS-NOTE 08-003, Internal report (2008).
- [96] R. E. Kalman, *A new approach to linear filtering and prediction problems*. Journal of Basic Engineering 82, 35 (1960).
- [97] R. Frühwirth and A. Strandlie, *Track fitting with ambiguities and noise: a study of elastic tracking and non-linear filters*, Comp.Phys.Comm. 120 197 (1999).
- [98] R. Frühwirth and A. Strandlie, *Track and vertex reconstruction: From classical to adaptive methods*, Rev. Mod. Phys. 82, 1420 (2010).
- [99] H. Stadie, *DAF Primary Vertex Reconstruction (unpublished)*. Talk at ZEUS Collaboration Meeting, June (2006).
- [100] A. Lopez-Duran and S. Schlenstedt, *A Comparison Between SINISTRA95, EM and EMNET (unpublished)*, ZEUS-NOTE 99-077, internal report (1999).
- [101] B. Straub, *The EM Electron Finder*, available at http://www-zeus.desy.de/straub/ZEUS_ONLY/doc/em.ps

- [102] G. M. Briskin, *Diffractive Dissociation in ep Deep Inelastic Scattering*, Ph.D Thesis (1998).
- [103] T. C. Awes et. al., *A simple method of shower localization and identification in laterally segmented showers*, Nucl. Instr. Meth. A 311, 130 (1992).
- [104] J. Grosse-Knetter, *Corrections for the Hadronic Final State (unpublished)*, ZEUS-NOTE 98-031, internal report (1998).
- [105] A. Andresen et. al., *RESPONSE OF A URANIUM-SCINTILLATOR CALORIMETER TO ELECTRONS, PI AND PROTONS IN THE MOMENTUM RANGE 0.5-10 GeV/c*, Nucl. Inst. Meth. A 290 95 (1990).
- [106] S. Chekanov et al., *Measurement of the Longitudinal Proton Structure Function at HERA*, Phys. Lett. B 682 8 (2009).
- [107] Y. Yamazaki, *S30cor*, internal report.
- [108] A. Tapper, *Hadronic energy scale studies*, http://www-zeus.desy.de/tapperad/ZEUS_ONLY/nc/escale_had.php
- [109] A. Bernstein et. al., *Beam Test of the ZEUS Barrel Calorimeter*, Nucl. Inst. Meth. A 336 23 (1993).
- [110] R. Sinkus, T. Voss, *Particle identification with neural networks using a rotational invariant moment representation*, Nucl. Inst. Meth. A 389 160 (1997).
- [111] M. Wlasenko, *Measurement of neutral current deep inelastic e^+p scattering cross sections with longitudinally polarized positrons with ZEUS at HERA*, Ph.D Thesis (2007).
- [112] L. Lyons, *Statistics for nuclear and particle physicists*, Cambridge University Press (1986).
- [113] S. Chekanov et al., *High- Q^2 neutral current cross section in e^+p deep inelastic scattering at $\sqrt{s}=318$ GeV*, Phys. Rev. D 70 052001 (2004).